C. Senthil Kumar · R. Sujatha ·
R. Muthukumar · K. Balaji Rao ·
Raghu V. Prakash ·
Prabhakar V. Varde   *Editors*

Advances in Reliability and Safety Assessment for Critical Systems

Proceedings of the 5th National
Conference on Reliability and Safety
(NCRS 2022)

Springer

Lecture Notes in Mechanical Engineering

Lecture Notes in Mechanical Engineering (LNME) publishes the latest developments in Mechanical Engineering—quickly, informally and with high quality. Original research reported in proceedings and post-proceedings represents the core of LNME. Volumes published in LNME embrace all aspects, subfields and new challenges of mechanical engineering.

Topics in the series include:

- Engineering Design
- Machinery and Machine Elements
- Mechanical Structures and Stress Analysis
- Automotive Engineering
- Engine Technology
- Aerospace Technology and Astronautics
- Nanotechnology and Microengineering
- Control, Robotics, Mechatronics
- MEMS
- Theoretical and Applied Mechanics
- Dynamical Systems, Control
- Fluid Mechanics
- Engineering Thermodynamics, Heat and Mass Transfer
- Manufacturing
- Precision Engineering, Instrumentation, Measurement
- Materials Engineering
- Tribology and Surface Technology

To submit a proposal or request further information, please contact the Springer Editor of your location:

Europe, USA, Africa: Leontina Di Cecco at Leontina.dicecco@springer.com
China: Ella Zhang at ella.zhang@springer.com
India: Priya Vyas at priya.vyas@springer.com
Rest of Asia, Australia, New Zealand: Swati Meherishi at swati.meherishi@springer.com

Indexed by SCOPUS, EI Compendex, and INSPEC

All books published in the series are evaluated by Web of Science for the Conference Proceedings Citation Index (CPCI)

To submit a proposal for a monograph, please check our Springer Tracts in Mechanical Engineering at https://link.springer.com/bookseries/11693

C. Senthil Kumar · R. Sujatha · R. Muthukumar ·
K. Balaji Rao · Raghu V. Prakash ·
Prabhakar V. Varde
Editors

Advances in Reliability and Safety Assessment for Critical Systems

Proceedings of the 5th National Conference on Reliability and Safety (NCRS 2022)

Springer

Editors
C. Senthil Kumar
Atomic Energy Regulatory Board,
Government of India
Chennai, India

R. Muthukumar
Ministry of Electronics and Information
Technology, Government of India
Chennai, India

Raghu V. Prakash
Department of Mechanical Engineering
Indian Institute of Technology Madras
Chennai, India

R. Sujatha
Department of Mathematics
Shiv Nadar University Chennai
Chennai, India

K. Balaji Rao
CSIR-Structural Engineering Research
Center
Chennai, India

Prabhakar V. Varde
Homi Bhabha National Institute
Mumbai, India

Contents

About the Editors

Dr. C. Senthil Kumar joined the Atomic Energy Regulatory Board (AERB) in 1990 and is presently the officer-in-charge of the Southern Regional Regulatory Centre of AERB in Chennai. His areas of specialization include reliability engineering, probabilistic safety assessment (PSA), software reliability, seismic safety, statistical analysis, remote sensing and GIS applications. He has performed the reliability analysis of shutdown system, decay heat removal system, power supply system and passive system reliability analysis as part of Level-1 PSA for the Prototype Fast Breeder Reactor which is under construction at Kalpakkam. His contribution in the seismic re-evaluation of Fast Breeder Test Reactor earned him the AERB group achievement award. His current research is in the development of a methodology for performing multi-unit PSA at Indian nuclear sites. He is also a member of AERB's regulatory review committee on PSA for nuclear facilities. He has earned the Erasmus-Mundus EURECA fellowship for post-doctoral research in the area of 'Software reliability for computer-based systems in safety critical operations' at Sweden in 2009–2010.

Dr. R. Sujatha is currently an associate professor, Mathematics, School of Science and Humanities, Shiv Nadar University, Chennai, India. She has pursued her M.Sc. and Ph.D. from Indian Institute of Technology (IIT) Madras and M.Phil. at Ramanujan Institute of Advance Studies in Mathematics. She was awarded CSIR-UGC fellowship for doing Ph.D. Her research interests include algebraic coding theory, fuzzy theory and its applications, and reliability studies. She has 25 years of experience in teaching and research. She has guided seven Ph.D. students and two are under progress. She has authored four books, 78 papers in peer-reviewed journals and 22 in international conference proceedings. She has completed three research projects funded by DST-SERB and AERB.

Dr. R. Muthukumar is the director, Centre for Reliability, STQC Directorate, Ministry of Electronics and I.T., Government of India, Chennai. He obtained his Bachelor's degree in Electronics and Communication Engineering from Government College of Engineering, Tirunelveli, and Master's degree, M.S. in Electronics

and Communication Engineering from the College of Engineering, Anna University, India. He also has a post-graduate Diploma in Business Administration from Pondicherry Central University. He obtained his doctoral degree in Embedded Systems Reliability from the Faculty of Engineering, M.S. University, Tirunelveli. He has to his credit over 23 research papers in international and national journals/conferences and magazines. He has guided many research scholars, doing their Ph.D. in Electronics and Reliability Engineering.

Dr. K. Balaji Rao completed his M.E. and Ph.D. from Indian Institute of Science (IISc) Bangalore, in 1984 and 1990, respectively. He joined CSIR-Structural Engineering Research Centre (CSIR-SERC), Chennai, in 1990. Currently, he is an emeritus scientist at CSIR-SERC and is a faculty of AcSIR. He worked at CSIR-SERC in various capacities from 1990 to June 2020. He was identified as a mentor at CSIR-SERC. He retired as a chief scientist and an advisor (M) of CSIR-SERC. He has led a number of in-house and sponsored R&D projects. Important among the sponsored projects are: (i) A methodology for risk informed in-service inspection for safety related systems, (ii) Seismic vulnerability analysis of brick masonry buildings, (iii) Development of probabilistic seismic hazard map of India. He has guided six Ph.D. candidates (one under progress) and about 35 B.Tech./M.E. students. He has published more than 100 papers in refereed journals and more than 100 papers in conferences.

Dr. Raghu V. Prakash is currently working as a senior professor in the Department of Mechanical Engineering, Indian Institute of Technology (IIT) Madras. He specializes in the areas of fatigue, fracture of materials (metals, composites, hybrids), structural integrity assessment, remaining life prediction of critical components used in transportation, energy sectors, apart from new product design. He has more than 25 years of professional experience in the field of fatigue and fracture and has more than 100 journals, chapter publications and 100 conference publications, and has edited six book volumes. He headed sponsored research for Boeing, Aeronautical Development Agency while at National Aerospace Laboratories, Bangalore; he has developed test systems for use in academia, R&D and industry during his tenure as a technical director at BiSS Research, Bangalore; at IIT Madras, he teaches courses relating to Fracture Mechanics, Design with Advanced Engineering Materials, Product Design and DFMA apart from being a researcher and consultant to several Industries.

Dr. Prabhakar V. Varde is a mechanical engineer by education, a nuclear engineer by profession and a well-known expert in the area of probabilistic risk assessment and its application as part of risk-based engineering. He started his carrier at Bhabha Atomic Research Centre in 1983 as nuclear engineering trainee of BARC Training School and after completion of training joined erstwhile Reactor Operations and Maintenance Group now Reactor Group, served as operations engineering for Dhruva—a 100 MW research reactor at BARC and rose through the administrative ladder and retired in 2019 as an associated director, Reactor Group. During his

service, he completed his Ph.D. from Indian Institute of Technology (IIT) Bombay in 1996 and later focused his research in nuclear safety in general and risk-based engineering in particular, along with reactor related services responsibilities.

Event Identification in Indian Standard PHWR NPP Using Machine Learning Technique

Subhadeep Sen

1 Introduction

Nuclear power plants operation is extremely complex with more than 14,000 input/output parameters. Under steady-state condition all the thermal–hydraulic parameters like pressure, temperature, flow, level of primary heat transport system, steam generator level, radioactivity inside reactor building, reactor power remains within very stringent range within least standard deviation. Nuclear power plants world-wide conduct high quality training program to sensitize its operators about plant healthiness monitoring, despite that, operator instinct limitation sometimes diverts the operating crew attention off target under stressful transient condition. Rapidly fluctuating parameters under abnormal operations are often confusing, difficult to correlate and indecisive to act. At times diagnosing initiating event takes lot of time. This paper as demonstration of scope of machine learning in predicting real time plant status, which could be useful for future implementation of frontier technologies like artificial intelligence, Internet of Things into process industry which continuously generates data but hardly harness the might of data science. During the study, many machine learning techniques were tried but eventually logistic regression appears to be the simplest, fastest and optimised algorithm to bring result with highest precision. To develop the model 5000 datapoints with 18 feature set has been selected, however in industry implementation these datapoints will be continuous seeding data for those 18 features. Six scenarios consisting of five anomalies and one normal state of operation has been considered in this paper for the sake of simplification. Those five events are so chosen that their symptoms are very close to differentiate but the model has been robust enough to draw clear classification with 100% recall and precision.

S. Sen (✉)
Nuclear Power Corporation of India Limited, Kaiga, Karnataka, India
e-mail: subhadeep.sen87@gmail.com

2 Data Generation

A sample size of 5000 data instances for 18 feature set have been retrieved from plant Computer Based System (CB System) and around 1% of accidental condition data generated in plant simulator has been mixed to develop the final training dataset. Followings are the parameters in 18 feature set.

1. Reactor Power
2. Steam Generator (SG) Pressure
3. Reactor Building (RB) V-1 area Pressure
4. Primary Heat Transport (PHT) Pressure
5. SG-1 level
6. SG-2 level
7. SG-3 level
8. SG-4 level
9. RB Exhaust Duct Radioactivity
10. Neutronic Signal in linear scale
11. Neutronic Signal in logarithmic scale
12. PHT Storage Tank level
13. SG blowdown line radioactivity
14. Reactor Trip parameter
15. Emergency Core Cooling System (ECCS) injection (Phase-I)
16. Emergency Core Cooling System (ECCS) injection (Phase-II)
17. Auto Crash cool down
18. Plant Status.

Out of approximately 14,000 input parameter, these features have been judiciously selected with domain specific knowledge to bring sufficient identifier in the model at the same time limit multi-collinearity. So, a Python dataframe of 5000 rows with optimized 18 columns has been created. Since normal operation parameters maintains within a narrow band of values so requirement of stratified sampling is ruled out (Fig. 1).

Within these 18 features only '*Plant Status*' is selected as dependent variable other 17 are independent variables. Dependent feature is the target feature for this paper. '*Plant Status*' is the feature intended to be predicted under transient scenario. Following six proximate '*Plant Status*' (accident condition) has been selected for classification which can be time consuming and error prone to diagnose if left on human instinct.

1. Normal (100% power operation)
2. Small Loss of Coolant Accident (LOCA)
3. Large break LOCA
4. Blind LOCA
5. (Main Steam Line Break) MSLB inside Reactor Building with SG tube leak
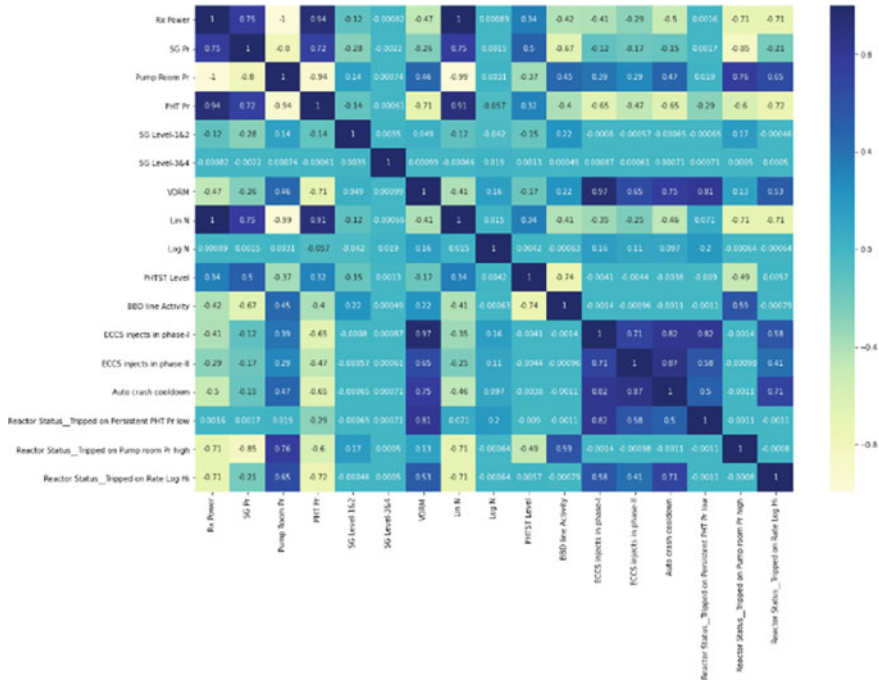
Fig. 1 Correlation between features. *Note* Multicollinearity has minimal impact on accuracy of the model but may rise ambiguity in determining the effects of individual independent features on the dependent feature in model and that can be a problem in interpreting model

6. MSLB inside Reactor Building without SG tube leak.

Combination of feature values will be distinct for different '*Plant Status*' (accident condition), e.g. Large break LOCA will have higher Neutronic signal compared to small break LOCA. Likewise, Reactor trip parameter for MSLB will differ from LOCA. So these feature set combinations will be the differentiator between scenarios with each other in the model.

3　Data Pre-processing

3.1　Dealing with Categorical Variable

In Nuclear power plant various CB system generates lot of process parameter every second both in analog as well as in digital form, out of those parameters, 18 selected features can be seeded and used for the model after some specific feature engineering to fit in the algorithm. Continuous variables can be directly fed to the model, but categorical variable needs to be converted into binary form. For the sake of that *get_*

dummies () function in Python has been used to convert '*Reactor Trip parameter', 'ECCS injection (Phase-I)', 'ECCS injection (Phase-II)', 'Auto Crash cooldown'* into binary value.

3.2 Setting Target Variable

'*Plant Status*' column has been set as target variable and selected from the 5000 * 18 dataframe using 'pop ()' function in Python and assigned as target variable '*y*'. The rest of 17 columns (features) are set as '*X*'.

3.3 Test-Train Split

Machine Learning model needs to be trained on a training dataset and the credibility of the model is tested on a test dataset. For the sake of building the model, generated data has been split into test and train set with 70:30 ratio using '*test_train_split*' function from Python '*sklearn*' library. While implementing in industry, training data can be generated in plant simulator or though accident analysis code. The model which performed well on validation data is expected to match in real test. Here feature train set and target variable is assigned as X_train, X_test and y_train, y_test respectively. Both test and train data set has been shuffled using '*shuffle = True*' command in Python. Shuffling reduces bias in model.

3.4 Oversampling Technique

Since accident condition is uncommon compared to normal operation, the model may not learn the accident condition fully during training. To avoid this class imbalanced skewness, rare datapoints are oversampled to artificially make them more common to model. '*RandomOverSampler()*'(ROS) function is used here for the purpose. Machine learning models can be misleadingly show great accuracy on skewed dataset. Oversampling addresses the issue. Training data size increased 6 times after oversampling (Figs. 2 and 3).

3.5 Scaling

As the values of features has wide range, e.g., numerically PHT pressure could be many times of RB V-1 area pressure, PHT pressure will have more impact on the model if the data is fed as it is, which may mislead the model because model needs

Fig. 2 Dataset before oversampling

```
np.asarray(np.unique(y_train, return_counts=True)).T

array([['Blind LOCA', 4],
       ['Large LOCA', 2],
       ['MSLB with SG tube leak', 4],
       ['MSLB without SG tube leak', 3],
       ['Normal', 3484],
       ['Small LOCA-Feeder Break', 3]], dtype=object)
```

Fig. 3 Dataset after oversampling

```
np.asarray(np.unique(y_train_ros, return_counts=True)).T

array([['Blind LOCA', 3484],
       ['Large LOCA', 3484],
       ['MSLB with SG tube leak', 3484],
       ['MSLB without SG tube leak', 3484],
       ['Normal', 3484],
       ['Small LOCA-Feeder Break', 3484]], dtype=object)
```

to value all its independent feature on a same scale with same gravity. Therefore 'StandardScaler' function from 'sklearn' library of Python has been used to scale all the feature value with mean = 0 and scales the data to unit variance. This is a kind of centering the data.

4 Modelling

Many supervised learning approach has been tried for accident condition prediction like Logistic Regression, KNN, SVM, Random Forest, Decision Tree, Artificial Neural Network, but logistic regression stroke the best balance between prediction precision, computational time and model complexity, hence Logistic regression has been adopted for model development and feature evaluation. LogisticRegression().fit() function from sklearn library of Python has been used to get a multivariate predictive model. The model came up with absolute accuracy of 100% along with 100% precision, recall and f-1 score. With more versatile training with more simulated data for accidental operation and real time data from CB system the model is expected to maintain same level of robustness in industrial implementation. Model regularization hasn't been applied here instead features are chosen carefully.

5   Model Evaluation

Here the hypothesis testing of the result is being introspected, where a Type-I error is misinterpreting a '*normal*' plant status as event and the Type-II error is failing to interpret event as a event precisely. For the business problem of this paper where Type-II error could be detrimental rather than type-I error because even if a '*normal*' plant status gets misinterpreted as event that can be confirmed by further checks by the operating crew without taking any corrective action but if a type-II error is commenced that may mislead the operating crew in a different scenario loosing initial period of action time. General convention in statistical approach is to assign rare find as positive and abundant find as negative (Fig. 4).

There are several important matrixes used to judge the prediction efficacy such as *Precision, Recall, Sensitivity, Specificity*. According to business requirement any of these is given preference over others as improving all of them may be impractical in well spread data. As in this case detecting all positive case as positive is of prime importance, the matrix *Recall* seems the best to describe our model effectiveness. Specifically, for this paper, '*events*' are classified as positive case, '*Normal*' state is classified as negative case.

The formula for *Recall* can be given as,

$$\text{Recall} = \text{TP}/(\text{TP} + \text{TN})$$

So, *Recall* gives an idea of How many of Actual Positive (TP) cases are being detected as positive within whole pool of positive case. For binary output prediction there will be 2 * 2 = 4 possibilities whereas for this paper's six scenarios here will be 6 * 6 = 36 possibilities, such as '*Large LOCA*' misinterpreted as '*MSLB*', '*Small LOCA*' misinterpreted as '*Blind LOCA*'. Diagonals represent '*True Positive (TP)*' (Fig. 5).

The result shows all the '*Plant Status*' has been correctly detected by the model. Out of 1500 test result all rare events such as both '*Blind LOCA*', both '*MSLB with*

Fig. 4   Confusion matrix

```
#Predict and calculate the accuracy and auc score
y_pred_logreg = logregmodel.predict(X_test_scaled)
# Print the prediction accuracy
print ('Model Accuracy: ', metrics.accuracy_score(y_test, y_pred_logreg))
# Printing confusion matrix
print('\n confusion_matrix:\n', confusion_matrix(y_test,y_pred_logreg))
```

```
Model Accuracy:  1.0

 confusion_matrix:
[[   2    0    0    0    0    0]
 [   0    1    0    0    0    0]
 [   0    0    2    0    0    0]
 [   0    0    0    1    0    0]
 [   0    0    0    0 1493    0]
 [   0    0    0    0    0    1]]
```

```
print(classification_report(y_test,y_pred_logreg))
```

```
                           precision   recall  f1-score   support

               Blind LOCA       1.00     1.00      1.00         2
               Large LOCA       1.00     1.00      1.00         1
       MSLB with SG tube leak   1.00     1.00      1.00         2
    MSLB without SG tube leak   1.00     1.00      1.00         1
                   Normal       1.00     1.00      1.00      1493
       Small LOCA-Feeder Break  1.00     1.00      1.00         1

                 accuracy                          1.00      1500
                macro avg       1.00     1.00      1.00      1500
             weighted avg       1.00     1.00      1.00      1500
```

Fig. 5 Classification report

SG tube leak', single cases of *'Large LOCA', 'MSLB without SG tube leak', 'Small LOCA'* has been detected precisely by the model, hence '*Recall*' value came as good as 1, suggesting a perfect model for present dataset. With more practical data generated from simulator will strengthen the model learning further during industry implementation hence model performance is expected to remain satisfactory.

6 Model Interpretation

The model predicts the 'Plant Status' with a probability. So, to capture that probability and use that in decision making, the six '*Plant Status'* are numerically represented as 0 to 5. But those should be seen as mere tagging and not be misunderstood with ranking. LabelEncoder.fit_transform() command has been used from 'preprocessing' module of 'sklearn' library in Python (Fig. 6).

```
# Import label encoder
from sklearn import preprocessing

# label_encoder object knows how to understand word labels.
label_encoder = preprocessing.LabelEncoder()

# Encode labels in column 'Plant Status'.
y_train_ros_mapped= label_encoder.fit_transform(y_train_ros)
dict(zip(y_train_ros,y_train_ros_mapped))
```

```
{'Normal': 4,
 'MSLB with SG tube leak': 2,
 'Blind LOCA': 0,
 'MSLB without SG tube leak': 3,
 'Large LOCA': 1,
 'Small LOCA-Feeder Break': 5}
```

Fig. 6 Event labels

```
import statsmodels.api as sm

X_train_sm = sm.add_constant(X_train_scaled)
logm2 = sm.GLM (y_train_ros_mapped,X_train_sm)
res = logm2.fit()
```

```
y_train_predict = res.predict(X_train_sm)
print('Prediction Probability: \n\n', y_train_predict)
```

```
Prediction Probability:

 [3.99108124 3.97982597 3.98883438 ... 4.98682785 5.00593948 4.98682785]
```

Fig. 7 Prediction probability

Test set prediction probabilities has been retrieved using 'predict ()' command from 'statsmodels.api' library in Python. Prediction value with threshold tolerance of 10% can be assigned as nearest possible 'event'. e.g., if prediction probability is between 2.7 and 3.3, the 'event' will be classified as 'MSLB without SG tube leak' event. Similar method to be followed with other events (Fig. 7).

7 Decision Making

As during transients in Nuclear Power Plant, the plant parameters fluctuates rapidly before it reaches a quasi-steady state, Prediction probability also fluctuates rapidly causing confusion to the operating crew. Therefore, it is proposed to freeze prediction

once prediction probability stays in range-bound for certain time delay. Once prediction is frozen thus confirmed, operating crew can verify the '*Plant Status'* using their 'Emergency Operating Procedure' and proceed with its protocol.

8 Conclusion and Future Work

Historically, one of the biggest hurdle for nuclear power roll out has been public anxiety, governments discomfort pertaining to design failure, human error led nuclear event. Therefore, an AI based cutting-edge operator support solutions for operational problems like this paper can be harnessed by the nuclear community to gain more preparedness against odds. The demonstration in this paper provides a potential automated mechanism for guiding operating crew to take a decisive call on the most probable event happened during transient. The selected Computer Based Systems generated values, outputs (In this case 18 parameters) can be seeded to the model to get a data driven decision with fast yet absolute precision. This operator support system could become useful for the operating crew which are anyway depending on their experience-based judgment and can improve the way man and machines work together.

In the backdrop of success of this model, instead of six 'Plant Status', all probable anticipated operational occurrences will be included in the dataset and model's credibility will be tested to prepare a full-fledged Operator Support System Module. Unsupervised learning method like Clustering will be tried to detect any off-normal deviation from the known event and alert through the same Operator Support System Module.

Bibiliography

1. Hanna B, Son TC, Dinh N (2019) AI-guided reasoning-based operator support system for the nuclear power plant management, pp 7–11
2. Swaton E, Neboyan V, Lederman L (1987) Human factors in the operation of NPPs. IAEA Bull 4
3. Nuclear Power Engineering Section, International Atomic Energy Agency, Operator support systems in nuclear power plants, IAEA TECDOC-762 (1994)
4. Kim J, Lee D, Yang J, Lee S (2019) Conceptual design of autonomous emergency operation system for nuclear power plants and its prototype. Nucl Eng Technol
5. Luger G (2005) Artificial intelligence: structures and strategies for complex problem solving. Pearson Education
6. Ayo-Imoru RM, Cilliers AC (2018) Continuous machine learning for abnormality identification to aid condition-based maintenance in nuclear power plant. Ann Nucl Energy 118:61–70

Adaptive Kriging Metamodel Based Reliability Analysis of Tunnel

Axay Thapa, Atin Roy, and Subrata Chakraborty

1 Introduction

The design and analysis of tunnel is a complex task due to the inadequacy of the knowledge of ground behaviour under excavation procedure and insufficient data on the state of stress of the ground condition. Tunnel is subjected to uncertainties caused by the innate variations in the rockmass and the imprecision of measurement and modelling. In case of conventional design, the unpredictability is generally taken in a deterministic way by assigning a value with safety factor, which uses the mean values of deformation characteristics of rock/soil-mass. A deterministic analysis gives the margin of safety to a very limited extent because the parametric uncertainties and their effect on the design are not taken into account. On the other hand, a probabilistic analysis approach provides a rational perspective to such problem. It also distinguishes between minor and major uncertainties. Therefore, the proposed research study focussed on safety assessment of tunnel in probabilistic format with due importance to the various parameters that affects the tunnel behaviour. Oreste presented a probabilistic numerical approach applicable for the design of primary tunnel supports based on the hyper-static reaction method by Monte Carlo simulation (MCS) [1]. Mollon presented response surface method (RSM) based reliability analysis of a shallow circular tunnel driven by pressurized shield in soil following Mohr–Coulomb (M–C) failure criterion [2]. Lü and Low implemented first order reliability method (FORM) to calculate the reliability index of a circular tunnel under hydrostatic stress field and compared with the result achieved by MCS method. They used an approach based on RSM and second order reliability method (SORM) to find the reliability of

A. Thapa (✉) · A. Roy · S. Chakraborty
Indian Institute of Engineering Science and Technology, Shibpur 711103, India
e-mail: axay.t@smit.smu.edu.in

A. Thapa
Sikkim Manipal Institute of Technology, Sikkim Manipal University, Sikkim 737132, India

the tunnel based on M–C failure criterion and Hoek–Brown (H–B) yield criterion [3]. Lu et al. [4] performed probabilistic ground-support interaction analysis of deep rock excavation using artificial neural network (ANN) and uniform design (UD) based on the convergence–confinement method. The least squares support vector machines (LS-SVM) based RSM combined with FORM [5] has also been used in tunnel reliability analysis of elastic-perfectly-plastic rockmass. The moving least square method (MLSM) and FORM/SORM are also used for probabilistic analysis of rock tunnel excavation [6]. Apart from the mentioned method, Kriging model is known to be very efficient and flexible in dealing with cases involving numerical modelling [7]. The accuracy of the metamodel can be further improved by adding a new sample by means of a learning function, the augmentation of which can be stopped by means of a stopping criterion or stopping function. Bichon et al. [8] introduced an active learning method on the threshold of Kriging metamodel, the learning function called the Expected Feasibility Function (EFF). Echard et al. [9] introduced an efficient active learning function for probabilistic analysis combining Kriging and MCS for structural. In the AK-MCS, a candidate sample set was introduced to represent the whole simulation domain for an approximate result to update the Kriging model. The sampling concept for active learning in AK-MCS is further modified for rare events e.g., brute force MCS is replaced by importance sampling in AK-IS [10] and by subset simulation in AK-SS [11]. Learning functions implementing an active sparse polynomial chaos expansion applicable to system reliability analysis are also developed [12]. AK-MCS method are also adapted for small failure probabilities [13]. The method however is seldom used in safety assessment of deep tunnel. Following the same framework, an adaptive technique is proposed in the present work based on the maximin distance criterion from the reduced space considering the prediction uncertainties of Kriging model. The application potential of the proposed approach is elucidated by considering reliability analysis of a tunnel example problem. The accuracy and efficiency of the proposed approach is studied by comparing the reliability results obtained by the proposed approach with the most accurate reliability estimates obtained by brute force MCS technique.

2   Performance Function

The convergence confinement method is a simplified and rational approach for analysing the ground-support interaction [14]. The simplicity of the approach is due to the hypothesis based on which the method is based. For example, the tunnel is assumed to be circular and deep, subjected to hydrostatic lithospheric stress, in a continuous and homogeneous/isotropic soil/rock mass condition. Thus, the problem is reduced to a two-dimensional plain strain problem. The approach is extensively used as a basic tool for estimation of support requirement for stabilization and for final convergence estimate of tunnel wall. The underground tunnel is assumed to be subjected to hydrostatic insitu stress. During construction, with the progress of excavation, the rockmass is subjected to redistribution of stress due to loss of confinement

Fig. 1 A circular deep tunnel subjected to hydrostatic insitu stress
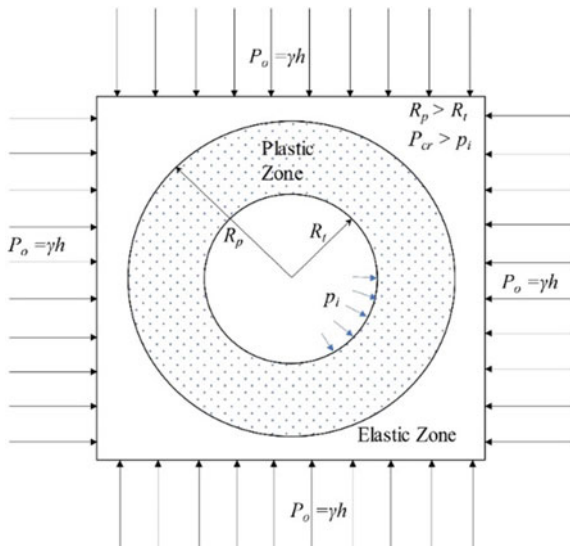
caused by excavation. The failure during the initial phase can be broadly classified into structurally influenced instability considering discontinuity of rockmass and stress induced instability considering continuity of rockmass. In the present study, the continuity of rockmass is assumed and according to the stress induced instability criteria, two possible failure mechanism are considered. A circular tunnel section subjected to hydrostatic insitu stress po and applied internal stress pi, having an internal radius of R_t and effective plastic zone radius R_p is shown in Fig. 1.

The M–C failure criterion presents the failure of an isotropic material by a set of equations in terms of principal stress neglecting the intermediate principal stress [15]. The criterion may be expressed as the relationship between the principal stresses or in terms of shear and normal stress on the failure plane. In terms of shear stress (τ), and normal stress (σ), the equation is given by Labuz and Zang [16] as,

$$|\tau| = c + \sigma \tan \phi \tag{1}$$

The given equation can be written in terms of principal stresses, σ_1 and σ_3 as,

$$(\sigma_1 - \sigma_3) = (\sigma_1 + \sigma_3)c + 2c.\cos \varphi \tag{2}$$

In terms of radial stress (σ_r) and circumferential stress (σ_θ) in cylindrical co-ordinate system, the above equation can be written as,

$$(\sigma_\theta - \sigma_r) = (\sigma_\theta + \sigma_r)\sin \varphi + 2c.\cos \varphi \tag{3}$$

Here, c is the cohesion of rockmass and φ is the friction angle of the rock mass.

At the plastic-elastic interface where r = R_p (from Eqs. (2) and (3) and), we get:

$$\sigma_r = p_{cr} \tag{4}$$

Inserting the values in the equation for failure criterion:

$$p_{cr} = \frac{2p_o - \sigma_{cm}}{1 + K_p} \tag{5}$$

where $K_p = \frac{1+\sin\varphi}{1-\sin\varphi}$ and, $\sigma_{cm} = \frac{2c.\cos\varphi}{1-\sin\varphi}$

The radius of the plastic zone [3] is given by:

$$R_p = R_t \left(\frac{2(p_o(K_p - 1) + \sigma_{cm})}{(K_p + 1)(K_p - 1)p_i + \sigma_{cm}} \right) \tag{6}$$

The displacement in the plastic zone [3] is given by:

$$u_{rp} = \frac{R_t}{2G_r} \left[2(1 - v)(p_o - p_{cr}) \left(\frac{R_p}{r} \right)^2 - (1 - 2v)(p_o - p_i) \right] \tag{7}$$

G_r is the shear modulus and v is Poisson's ratio of the rockmass, respectively.

The performance functions of circular unlined tunnel can now be constructed according to the above two solutions (Eqs. (6) and (7)) as followings,

$$g_1(x) = \lambda - \frac{R_p}{R_t} \tag{8}$$

$$g_2(x) = \varepsilon - \frac{u_{rp}}{R_t} \tag{9}$$

The performance threshold λ in Eq. (8) is the maximum value of the ratio between the radius of plastic zone and the tunnel opening radius. It depends directly on the maximum radius of the plastic zone which is in face derived by applying the least internal stress i.e., zero. In Eq. (9), ε is the ratio of the maximum radial convergence of the tunnel wall and the radius of tunnel, which is achieved by not applying any internal stress in the tunnel wall.

3 Kriging Model

Let, the input variable x is l-dimensional vector with n number of sample sets. The variable is written in $n \times l$ matrix form with l being the number of variables and n being the total sample set generated. The Kriging model can be written as,

$$g(x_i) = \sum_{j=1}^{p} f_j(x_i)\beta_j + Z(x_i) = (f(x_i))^T\beta + Z(x_i) \tag{10}$$

where $\beta^{\mathrm{T}} = [\beta_1, \beta_2, \beta_3, \ldots, \beta_p]$ is the vector of regression-coefficient, very similar to the regression-coefficient vector used in polynomial model in response surface method and $f_j(x_i)_{i=1}^{p}$ is a set of known function. $Z(x)$ is a stationary Gaussian process (an assortment of random variable such that every finite collection from the collection follows a multivariate normal-distribution). The following statistical property is used to define the Gaussian process:

$$E(Z(\boldsymbol{x})) = 0 \text{ and } \mathrm{Var}(Z(\boldsymbol{x})) = \sigma_Z^2$$

$$\mathrm{Cov}[Z(\boldsymbol{x}), Z(\boldsymbol{w})] = \sigma_Z^2 R_\theta(\boldsymbol{x}, \boldsymbol{w})$$

σ_Z^2 is the unknown variance between two points of $\mathbf{x}$ and $\mathbf{w}$ space of the stochastic field $Z(\mathbf{x})$. R is the correlation matrix of dimension ($n \times n$) and as the correlation-parameter vector of length n. There are variety of functional form defining the correlation [17, 18]. The following correlation model (anisotropic Gaussian model) is considered here:

$$R_\theta(\boldsymbol{x}, \boldsymbol{w}) = \prod_{i=1}^{n} \exp\left[-\theta_i |x_i - w_i|^2\right] \tag{11}$$

x_i and w_i are the ith co-ordinate point of $\mathbf{x}$ and $\mathbf{w}$. The values of β and σ^2 are evaluated by Jones et al. [19],

$$\hat{\beta} = \frac{F^T R^{-1} g}{F^T R^{-1} F} \tag{12}$$

$$\hat{\sigma}^2 = \frac{(g - F\beta)^T R^{-1}(g - F\beta)}{n} \tag{13}$$

Since the value of $\hat{\beta}$ and $\hat{\sigma}^2$ are dependent upon the value of θ, hence θ is first evaluated using the maximum likelihood estimation by minimising $\Psi(\theta) = |R(\theta)|^{\frac{1}{n}}\sigma(\theta)^2$. The achieved predictor $G(x)$ with parameters: $\beta = \hat{\beta}$; $\sigma^2 = \hat{\sigma}^2$ and $\theta = \widehat{\theta}$; is known as the maximum likelihood empirical 'best linear unbiased predictor' (BLUP) $\widehat{G}(\boldsymbol{x})$, and is evaluated by,

$$\widehat{G}(\boldsymbol{x}) = \beta + r_o^T R_\theta^{-1}(g - \beta) \tag{14}$$

where $r_o = \{R(\boldsymbol{x}, \boldsymbol{x}_1), R(\boldsymbol{x}, \boldsymbol{x}_2), \ldots, R(\boldsymbol{x}, \boldsymbol{x}_n)\}$. Here, the optimal choice of the parameters θ is obtained as the maximum likelihood estimator using the "dacefit"

algorithm of the DACE toolbox [17]. The least value of the mean square error between the predicted value $\widehat{G}(\boldsymbol{x})$ and the response value $G(\mathrm{x})$, also known as the Kriging variance $\sigma^2_{\widehat{G}}(\boldsymbol{x})$ is given by,

$$\sigma^2_{\widehat{G}}(\boldsymbol{x}) = \hat{\sigma}^2 \left[1 + \boldsymbol{u}^T (F^T R^T F)^{-1} \boldsymbol{u} - r_o^T R_\theta^{-1} r_o \right] \tag{15}$$

where $\boldsymbol{u} = F^T R^{-1} r_o - f(\boldsymbol{x})$.

4   Adaptive Kriging Approach of Reliability Analysis

The applications of Adaptive Kriging Based MCS (AK-MCS) for reliability analysis of structures are enormous. However, it is not applied in reliability analysis of tunnel. The present study attempts to explore an adaptive Kriging approach on the basis of the Max–min distance concept. The proposed approach is built primarily on the basis of AK-MCS approach. Thus, the AK-MCS based approach is explained in this section and the proposed adaptive Kriging is presented in the next section. The failure probability of a structural system having performance function $g(x)$ is given by:

$$P_f = \int_F f_X(x)\mathrm{d}x = \int_{\mathbb{R}^n} I_F(x) f_X(x)\mathrm{d}x \tag{16}$$

where $f_X(\mathbf{x})$ is the joint probability distribution function (PDF) of random variable $\mathbf{x} = \{x_1, \ldots, x_n\}$, F is the region of failure given by $F = \{\mathbf{x}|g(\mathbf{x}) < 0\}$, the indicator function, $I_F(\mathbf{x})$ becomes 1 if $\boldsymbol{x} \in F$ and 0 otherwise. For MCS, the failure probability is:

$$P_f \approx \widehat{P}_f = \frac{1}{N_{MCS}} \sum_{i=1}^{N_{MCS}} I_F(x_i) \tag{17}$$

For, $\{\mathbf{x}_i, i = 1, 2, \ldots, N_{MC}\}$ are samples drawn from the PDF. In case of MCS, the entire population are to be evaluated with the performance function. The tedious process of evaluating the entire population with the performance function is reduced by applying AK-MCS based on active learning method. The Kriging model is trained with fewer possible samples by applying the active learning function on the MCS population. The refined Kriging model then evaluates the MCS population instead of the predefined limit state function. The active learning process dynamically updates and refine the Kriging model based on adopted DOE which is iteratively enriched by adding new sample identified by an active learning function. The active learning function continues to enrich and refine the Kriging model until a prescribed stopping condition is attained. It is to be noted that the mean Kriging (i.e., the regression part

in Eq. 10 contains a constant only) is considered. The steps followed in AK-MCS are outlined below.

1. *Generation of a standard Monte Carlo population in the prescribed design space*:

   The population S consists of N numbers of MCS samples following the respective PDF in the parameter space. The population S is only used as a pool for drawing and identifying the next best sample which is assessed on the defined performance function.

2. *Initial design of experiments (DOE) definition*:

   N_1 samples are randomly selected from the population S and evaluated with the true performance function. The DOE is generally preferred to be less to reduce the number of calls to the true performance function.

3. *Construction of the Kriging model based on initial DOE*:

   The Kriging model is constructed based on the current DOE.

4. *Prediction by Kriging and failure probability estimation*:

   Kriging predictions (Eq. (14)) are obtained using the DACE MATLAB toolbox. Then, the failure probability is assessed with the signs of these predictions as the ratio of the points in the population S with a negative Kriging prediction and the total number of points in *S*.

5. *Recognition of the suitable next point to evaluate on the defined performance function*:

   The next best sample is identified using the learning function. Here the learning function $U(x)$ [9] is used:

   $$U(x) = \frac{\left|\mu_g(x)\right|}{\sigma_g(x)} \tag{18}$$

   The sample is given by:

   $$\breve{x} = \underset{x \in S}{\arg\min}\, U(x) \tag{19}$$

   The sample with minimum $U(x)$ are either located near the limit state $((\mu_g(x) \approx 0))$ or have high prediction uncertainty $((\sigma_g(x) \gg 0))$, or both. The sample so drawn will have high potential to cross the prediction separator. Hence should be included in the DOE.

6. *Definition of stopping condition for learning*:

   The Kriging model is updated by the augmented DOE. The iteration process is stopped when the stopping condition is outreached. The stopping condition is defined as:

   $$\min(U(x)) \geq 2, \forall x \in S \tag{20}$$

which means that the probability of executing a wrong sign prediction is $\Phi(-2) < 0.023$

7. *Update of the previous DOE with the best suitable point*:

The active learning process is continued if the stopping condition given in step (6) is not satisfied. The best sample achieved is computed on the performance function and added to DOE. The method goes back to step (3) and the Kriging model is updated with the updated/augmented DOE.

8. *Calculation of the coefficient of variation (COV_{pf}) of the probability of failure*:

If the stopping condition in step (7) is achieved, the learning process is stopped and the metamodel is considered accurate enough on the performance function's signs of the N_{MC} points. The next step is to check whether the Monte Carlo population S is sufficiently large to give low COV_{pf} on the Kriging estimation of the failure probability (step (4)). Values of COV_{pf} less than 5% is taken considered acceptable.

$$COV_{\hat{P}_f} = \sqrt{\frac{1 - \hat{P}_f}{\hat{P}_f N_{MC}}} \tag{21}$$

9. *Updating of the initial population*:

If the estimated COV_{pf} is high than prescribed value (5%), S is updated with new set of points from another Monte Carlo population (generated like in step (1)). It is then followed by (step (4)) to predict the new population and the active learning method continues till the stopping condition is achieved. No information about the previous evaluations is lost.

10. *End of the AK-MCS*:

The COV$_{pf}$ is calculated and if it is small enough then the method is stopped, the failure probability is assessed. The estimate is the final result of AK-MCS.

5 Proposed Adaptive Kriging Approach

An adaptive Kriging approach is proposed here based on the maximin distance concept. A reduced space is constructed first by the proposed approach. Then a new training point is selected based on the maxmin distance criterion. This process goes on iteratively, the details of which are given below.

A population S consisting of N_{MC} samples in the input parameter space is generated following the respective PDF. The selection of initial training samples and searching of the next best training sample are limited to the population space S only. To build an initial DOE, N_1 samples are selected randomly from the population space S and evaluated with the true performance function. The number N_1 is generally preferred to be less for reduction of the total number of calls on the true

performance function. Once the initial DOE is built, the Kriging model is constructed based on it. Kriging prediction and its variance at N_{MC} samples are obtained using the Kriging model. Then, the failure probability is assessed with the signs of these predictions as the ratio of the points in the population S with a negative prediction and the total number of points in S.

Now, to construct the reduced space, first, $U(\mathbf{x})$ function is evaluated at all points in S based on the Kriging predictions and its variance obtained from the Kriging model. Then, samples, which are satisfying $U(\mathbf{x}) < 2$, are selected to construct a reduced space (denoted by R). This implies that all MCS samples having the probability of executing a wrong sign prediction greater than 0.023 (i.e., $\Phi(-2)$) is included in the reduced space. Like active learning-based AK-MCS method, the sign of predicted performance function at any point having probability of executing a wrong sign prediction less than 0.023 is considered as accurate. After that, a new training sample is selected by maximin distance criterion. For this, the scaled Euclidian distance of each point in the reduced space from its corresponding nearest training sampling is calculated as,

$$D(\mathbf{x}) = \|\mathbf{x}_r - \mathbf{x}_{nearest}\| \tag{22}$$

where $\|\ \|$ represents the scaled Euclidian distance, $\mathbf{x}_r$ is a point of the reduced space and $\mathbf{x}_{nearest}$ is the nearest training sample of the point $\mathbf{x}_r$. The point in the reduced space having the maximum value of such calculated distance is selected as the next training sample. The next training sample is given by:

$$\breve{\mathbf{x}} = \arg\max_{\mathbf{x} \in R} D(\mathbf{x}) \tag{23}$$

The sample $\breve{\mathbf{x}}$ is included into the DOE. The sample with maximum $D(\mathbf{x})$ improve the space-filling property of the new augmented samples. Hence increases the efficiency of the model. The Kriging model is updated by the augmented DOE. Subsequently, the Kriging prediction and its variance at MCS samples are updated. Based on the updated prediction, the updated failure probability is obtained. In addition, the reduced space R is reconstructed based on the updated value of U-function at the MCS points. Again, a new training point is selected based on Eq. (23) and Kriging model is updated. Thus, the failure probability is updated iteratively. It can be noted here that no new training point can be added if there is no new sample in the reduced space. Thus, this is treated as the stopping condition for adaptive sampling. Alternatively, the stopping condition can also be expressed as,

$$\min_{x \in S} U(\mathbf{x}) \geq 2 \tag{24}$$

The next step is to check whether the Monte Carlo population S is sufficiently large to give low COV_{pf} on the Kriging estimation of the failure probability. The COV_{pf} is calculated (ref. Eq. (21)) and the COV_{pf} value below 5% is considered to

be acceptable. If the estimated COV_{pf} is higher than the prescribed value (5%), S is enriched with new set of N_{MC} points generated from the associated PDF of the input variables. The prediction of the new population is done and the adaptive sampling continues till the stopping condition is achieved. No information about the previous evaluations is lost. The COV_{pf} is calculated and if the value is very high, then the method again enriches the Monte Carlo population space S. Once, the COV_{pf} is small enough (i.e., less than 5%), the method is stopped, and the failure probability is assessed.

6   Reliability Analysis of Unlined Circular Tunnel Subjected to Hydrostatic Insitu Stress

The effectiveness of the AK-MCS and the proposed adaptive Kriging approach for reliability analysis of underground tunnel is demonstrated by considering an unlined-circular tunnel subjected to hydrostatic insitu stress, p_o and applied internal stress, p_i. The reliability analysis is performed based on the analytical formulation framework defined in Sect. 2. The results of the AK-MCS and the proposed approach are compared and validated with the results obtained by MCS. The M–C failure criterion is applied to assess the plastic radius of the tunnel. The cohesion, elastic modulus, angle of internal friction and Poisson ratio of the rockmass defines the elasto-plastic behaviour of the tunnel. The statistical properties of the parameters considered to be random are provided in Table 1.

The performance function is defined by Eqs. (8) and (9). The performance threshold λ and ε are taken as 3 and 0.02 [3]. The Poisson ratio is taken as 0.22. A parametric study is made by varying the applied internal stress, hydrostatic insitu stress, and performance threshold. The number of random samples (N_1) taken to initially start the Kriging model is 12. Three cases are considered for each performance function, in the first case (Case 1) the value of p_o is taken as 2.5 N/mm^2 with varying values of p_i. In the second case (Case 2), the value of p_i is taken as 0.5 N/mm^2 with varying values of p_o. In the third case (Case 3) the value of p_i and p_o are taken as 0.25 N/mm^2 and 2.5 N/mm^2 for $g_1(x)$ and 0.5 N/mm^2 and 3.25 N/mm^2, respectively for $g_2(x)$ with variation in the values of the performance functions. The variation of failure probability (p_f) for all the three cases are shown in Fig. 2.

It may be noted that both the AK-MCS and the proposed approach can estimate the failure probability with reasonable accuracy. The accuracy and efficiency of the

Table 1 Statistical properties of the parameters [3]

Sl. No.	Property		Units	Distribution	Mean
1	Elastic modulus	E	MPa	Normal	1185
2	Cohesion	C	MPa	Normal	0.28
3	Angle of internal friction	ϕ	Degree	Normal	23.7
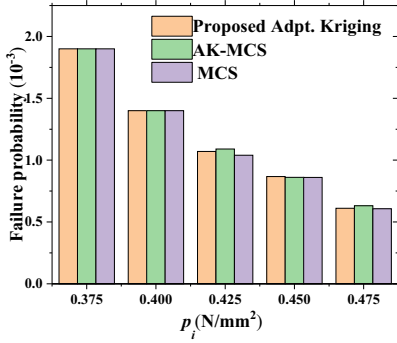
(a) $p_0 = 2.5$ N/mm^2; for $(g_1(x))$
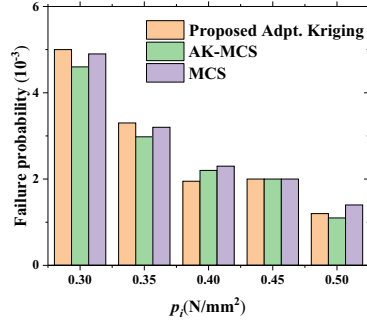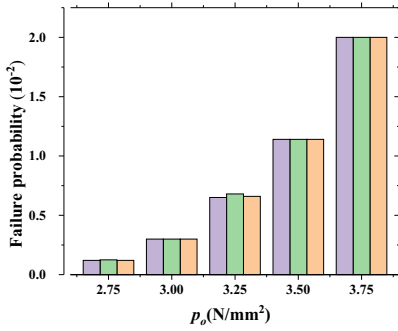
(b) $p_0 = 2.5$ N/mm^2; for $(g_2(x))$

(c) $p_i = 0.5$ N/mm^2; for $(g_1(x))$
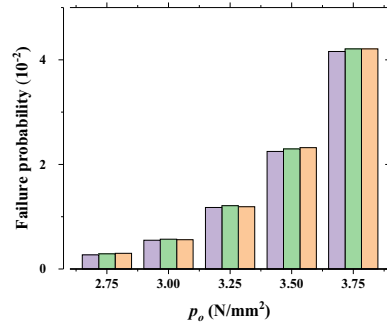
(d) $p_i = 0.5$ N/mm^2; for $(g_2(x))$
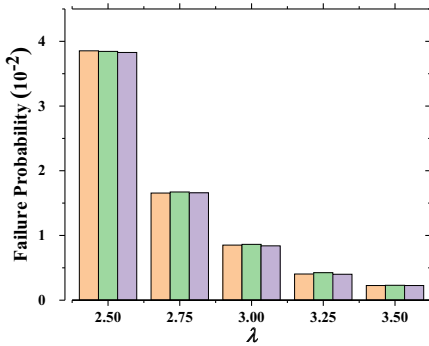
(e) $p_i = 0.25$ N/mm^2; $p_o = 2.5$ N/mm^2; for $(g_1(x))$
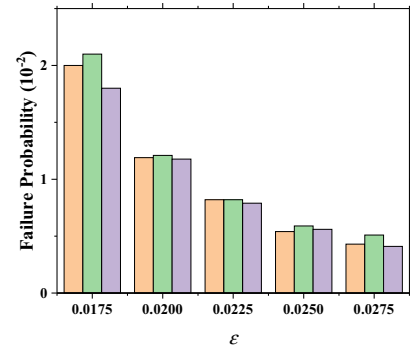
(f) $p_i = 0.5$ N/mm^2; $p_o = 3.25$ N/mm^2; for $(g_2(x))$

Fig. 2 Variation in failure probability (p_f) due to change in **a** internal stress for $g_1(x)$; **b** internal stress for $g_2(x)$; **c** insitu stress for $g_1(x)$; **d** insitu stress for $g_2(x)$; **e** performance function λ in $g_1(x)$ and **f** performance function ε in $g_2(x)$

Table 2 Average number of samples required and average absolute percentage error for $g_1(x)$

Method	Case 1 (Fig. 2a)		Case 2 (Fig. 2c)		Case 3 (Fig. 2e)	
	Average no. of samples	Average % error	Average no. of samples	Average % error	Average no. of Samples	Average % error
Proposed adaptive Kriging	29	0.87	24	0.31	24	0.70
AK-MCS	27	1.78	22	1.76	21	2.29

Table 3 Average number of samples required and average absolute percentage error for $g_2(x)$

Method	Case 1 (Fig. 2b)		Case 2 (Fig. 2d)		Case 3 (Fig. 2f)	
	Average no. of samples	Average % error	Average no. of samples	Average % error	Average no. of samples	Average % error
Proposed adaptive Kriging	60	6.93	47	3.68	51	4.89
AK-MCS	61	7.75	47	3.43	48	10.60

proposed method and the AK-MCS is compared in terms of the percentage error in the failure probability with respect to direct MCS. The average percentage error and the average number of samples required are enlisted in Tables 2 and 3 for the first and second performance functions respectively.

Both the method shows good accuracy and efficiency for the first performance function. The total number of samples required are also similar for the two methods. For the second performance function, as the equation is highly non-linear, at some instances the accuracy is moderate for both the methods. However, the proposed method shows better accuracy than the AK-MCS in majority of the cases.

7 Conclusion

The proposed adaptive Kriging method is applied to assess the safety of tunnel based on the allowable plastic radius and tunnel wall displacement criteria. The proposed adaptive Kriging approach is noted to provide comparatively better accuracy. When highly nonlinear performance function is involved, the method showed moderate accuracy, similar to the AK-MCS. As random sampling was adopted in the both the methods, therefore it can be concluded that there is high chance of increasing the accuracy and efficiency of the proposed approach if better DOE framework is adopted. There is scope of improvement in the adaptive technique based on the stopping criteria. The applicability of the proposed adaptive Kriging method in reliability analysis of tunnel is studied for simple problem and needs to verify for more realistic tunnel reliability analysis problem involving finite element response analysis.

References

1. Oreste P (2009) The convergence-confinement method: roles and limits in modern geomechanical tunnel design. J Am Sci Appl Publ Sci 6:757–771
2. Mollon G, Dias D, Soubra AH (2009) Probabilistic analysis of the face stability of circular tunnels. Geotech Spec Publ:348–355.https://doi.org/10.1061/41022(336)45
3. Lü Q, Low BK (2011) Probabilistic analysis of underground rock excavations using response surface method and SORM. Comp Geotech 38:1008–1021. https://doi.org/10.1016/j.compgeo.2011.07.003
4. Lü Q, Chan CL, Low BK (2012) Probabilistic evaluation of ground-support interaction for deep rock excavation using artificial neural network and uniform design. Tunn Undergr Sp Technol. 32:1–18. https://doi.org/10.1016/j.tust.2012.04.014
5. Zhao H, Ru Z, Chang X et al (2014) Reliability analysis of tunnel using least square support vector machine. Tunnell Undergr Space Technol 41:14–23. https://doi.org/10.1016/j.tust.2013.11.004
6. Lü Q, Xiao ZP, Ji J et al (2017) Moving least squares method for reliability assessment of rock tunnel excavation considering ground-support interaction. Comp Geotech 84:88–100. https://doi.org/10.1016/j.compgeo.2016.11.019
7. Gaspar B, Teixeira AP, Guedes Soares C (2017) Adaptive surrogate model with active refinement combining Kriging and a trust region method. Reliab Eng Syst Saf 165:277–291. https://doi.org/10.1016/j.ress.2017.03.035
8. Bichon BJ, Eldred MS, Swiler LP, Mahadevan S, McFarland JM (2008) Efficient global reliability analysis for nonlinear implicit performance functions. AIAA J 46(10):2459–2468. https://doi.org/10.2514/1.34321
9. Echard B, Gayton N, Lemaire M (2011) AK-MCS: an active learning reliability method combining Kriging and Monte Carlo simulation. Struct Saf 33(2):145–154. https://doi.org/10.1016/j.strusafe.2011.01.002
10. Zhang J, Xiao M, Gao L, Chu S (2019) A combined projection-outline-based active learning Kriging and adaptive importance sampling method for hybrid reliability analysis with small failure probabilities. Comp Meth Appl Mech Eng 344:13–33. https://doi.org/10.1016/j.cma.2018.10.003
11. Zhang J, Xiao M, Gao L (2019) An active learning reliability method combining Kriging constructed with exploration and exploitation of failure region and subset simulation. Reliab Eng Syst Saf 188:90–102. https://doi.org/10.1016/j.ress.2019.03.002
12. Zhou Y, Lu Z, Yun W (2020) Active sparse polynomial chaos expansion for system reliability analysis. Reliab Eng Syst Saf 202:107025. https://doi.org/10.1016/J.RESS.2020.107025
13. Xu C, Chen W, Ma J et al (2020) AK-MSS: An adaptation of the AK-MCS method for small failure probabilities. Struct Saf 86:101971. https://doi.org/10.1016/J.STRUSAFE.2020.101971
14. Panet M, Coyne AB, Bruno B et al (2001) Recommendations on the convergence-confinement method. Aftes 11
15. Zhao J (2000) Applicability of Mohr-Coulomb and Hoek-Brown strength criteria to the dynamic strength of brittle rock. Int J Rock Mech Min Sci 37:1115–1121. https://doi.org/10.1016/S1365-1609(00)00049-6
16. Labuz JF, Zang A (2012) Mohr-Coulomb failure criterion. Rock Mech Rock Eng 45:975–979. https://doi.org/10.1007/s00603-012-0281-7
17. Lophaven SN, Nielsen HB, Søndergaard J, Nielsen HB (2002) DACE—A Matlab Kriging toolbox (Version 2.0). IMM Informatics and mathematical modelling
18. Panda SS, Manohar CS (2008) Applications of meta-models in finite element based reliability analysis of engineering structures. CMES—Comp Model Eng Sci 28:161–184. https://doi.org/10.3970/cmes.2008.028.161
19. Jones DR, Schonlau M, Welch WJ (1998) Efficient global optimization of expensive black-box functions

Estimation of Corrosion Initiation Time Considering Fractal Nature of Concrete Pores

N. J. Yogalakshmi and K. Balaji Rao

1 Modelling the Chloride Ingress into Concrete as Sub-diffusion Process

Diffusion, permeation, capillary suction, absorption and migration are the common transport mechanisms of chlorides in concrete [1]. The mechanism by which chloride ion is transported depends on the exposure condition, temperature, pore-structure and moisture content in the concrete. In most cases, wherein the marine structures are exposed to atmospheric or splash zone or where the structures are exposed to de-icing salts, diffusion will be the governing transport mechanism. In this case, chloride ingress into concrete cover is modelled using a time dependent diffusion coefficient, to account for pore structure modification due to hydration. However, while modelling, there is also a need to take into account the topological form of the pore structure. Studies on the pore structure of cement-based material reveals fractal characteristics at some length scales [2]. Hence, Konkol and Prokopski [3] and Jin et al. [4] characterized the pore structure of concrete as a fractal structure.

A master equation which has a fractional time derivative (later given in Eq. (1)), was used as the mathematical model for explaining the process of diffusion on complex fractal space by Janett [5]. Principle of thermodynamics relates the fractal space to fractional time [6]. Taking the analogy of entropy of a physical system which increases by becoming increasingly disordered, the arrow of time can only move forward but the speed of occurrence can be relative. This has led to a power-law variation of waiting time. The same concept is applied for chloride diffusion into concrete to account for the fractal topology of pore-structure. A detailed review

N. J. Yogalakshmi (✉) · K. B. Rao
CSIR-Structural Engineering Research Centre, Taramani, Chennai, India
e-mail: yoga.engg10@gmail.com

K. B. Rao
e-mail: balaji@serc.res.in

related to diffusion of chlorides into cover concrete that has led the selection of the model presented in this paper can be obtained from RMIT University repository [7].

The diffusion through the concrete pores retards with time due to hydration and the same as been considered/recognized by Bazant [8] and Takewaka and Matusumoto [9]. The anomalous exponent of time should lie between 0 and 1, and is classified as a sub-diffusion process. A time fractional partial differential equation is used as the tool to describe the process. The same is considered in this paper and is given by,

$$\frac{\partial c}{\partial t} = D_\alpha \mathbb{D}_t^{1-\alpha} \frac{\partial^2 c}{\partial x^2} \tag{1}$$

where c is the chloride ion concentration, x and t are space and time, α is fractional exponent of time $0 < \alpha < 1$; D_α is the chloride sub-diffusion coefficient; $\mathbb{D}_t^{1-\alpha}$ is the Riemann–Liouville fractional operator. Metzler and Klafter [10] present an approximate analytical solutions of time fractional diffusion equation. However, the analytical solution cannot be used to represent the chloride ingress into the cover concrete (where the boundary condition is $c(0, t) = c_s$ and $\frac{\partial c}{\partial x}\big|_{x=boundary} = 0$). Therefore, a numerical solution is adopted in this study.

1.1 Numerical Solution

An explicit finite difference scheme is used as a solution for Eq. (1). Grunwald–Letnikov difference operator is used as the discretization scheme of Riemann–Liouville fractional operator. Similar discretization using Caputo operator was performed by Wei et al. [11]. It is important to note that fractional operator in the fractional diffusion equation is of significance in modelling the transport behavior. Using Caputo differential operator, the process is modelled as normal diffusion at smaller times and gets transformed into confined diffusion at larger times. The use of Riemann–Liouville operator, on the other hand, models the mean square displacement as power-law function of time, and waiting time as a power-law distribution [12].

The numerical representation of fractional derivative defined by Grunwald–Letnikov is given as [13],

$$\mathbb{D}_t^{1-\alpha} f(t) = \lim_{h \to 0} \frac{1}{h^{1-\alpha}} \sum_{k=0}^{m} w_k^{1-\alpha} f(t - kh) \tag{2}$$

where h is the time interval and m is number of time steps and $w_0^{1-\alpha} = 1$; $w_k^{1-\alpha} = \left(\frac{k-2+\alpha}{k}\right) w_{k-1}^{1-\alpha}$.

A forward time and centered space scheme is used and the resulting numerical solution for chloride concentration is given by,

$$C_j^{m+1} = C_j^m + S_a \sum_{k=0}^{m} w_k^{1-\alpha} \left[C_{j-1}^{m-k} - 2C_j^{m-k} + C_{j+1}^{m-k} \right] \tag{3}$$

where C_j^m denotes the chloride concentration at mth time step (m.Δt) and jth step length (j.Δx) and $S_a = \frac{D_\alpha (\Delta t)^\alpha}{(\Delta x)^2}$.

It is noted that this explicit numerical solution is conditionally stable and the bounds are given by $0 \le S_a \le \frac{1}{2^{(2-\alpha)}}$ [13]. The time step and step length should be carefully chosen such that S_a is within specified bounds. For example, when $\alpha = 0.8$ and $D_\alpha = 5.08 \times 10^{-11} \, \text{m}^2/\text{s}^\alpha$, considering $\Delta t = 0.04$ years and $\Delta x = 0.002$ m; leads to an unstable solution because $\frac{D_\alpha (\Delta t)^\alpha}{(\Delta x)^2} > \frac{1}{2^{(2-\alpha)}}$. In such a case either Δt has to be decreased or Δx has to be increased so that stability condition is satisfied. For the application of sub diffusion to chloride ingress problem, Δx should not be more than 0.01 m because chloride concentration profiles are usually established from core samples that are sliced into 10 mm thick intervals for chemical analysis. On the other hand, Δt can be 3 months to 1 year.

1.2 Numerical Procedure Adopted in This Study

The numerical procedure adopted in the present study for estimating the chloride concentration at a given time along the cover depth is as follows:

1. The time step, Δt, and jump length, Δx, are taken as 0.04 years and 0.005 m, respectively. The value of Δt and Δx are fixed such that $0 \le S_a \le \frac{1}{2^{(2-\alpha)}}$, for the numerical solution to be stable. (It is noted that for values of α obtained for the case studies considered in this study, the values of $\Delta t = 0.04$ years and $\Delta x = 0.005$ m ensures the stability condition).
2. The initial condition is set as $c(x, 0) = c_s \delta(x)$
3. The boundary conditions are set as $c(0, t) = c_s$ and $\frac{\partial c(x,t)}{\partial x}\Big|_{x=L} = 0$; where x = 0 is the left boundary which is supplied with chloride source and x = L is the right boundary which is the thickness of the structure. In this study, the left boundary is treated using Dirishlet boundary condition and the right boundary is treated using Neumann boundary condition.
4. The concentration values at every other time step and jump length is calculated using Eq. (3). For this purpose MATLAB code presented by Ali et al. [14] is used with some modification. The code was amended for imposing Neumann boundary condition to the right boundary and considering that the diffusion occurs along one direction from the source (i.e., diffuses from left to right).

The outcome of the above procedure is a matrix containing rows that represent the variations in chloride concentration over time at a particular depth and columns that represent the variations in chloride concentration along the depth at a particular time.

2 Corrosion Initiation Time

The time at which the chloride concentration at the level of reinforcement equals or exceeds the critical chloride concentration is the corrosion initiation time, T_i [7]. At this time the alkaline environment surrounding the steel reinforcement is destroyed by the presence of chloride ions. Thus,

$$c(\tilde{c}, T_i) = c_{cr} \tag{4}$$

where $\tilde{c}$ is the cover depth of concrete (in m), T_i is the corrosion initiation time (in years) and c_{cr} is the critical chloride concentration (in % by weight of cement).

The initiation time of corrosion is estimated by scanning the row of matrix generated using numerical procedure given in previous section for variation in chloride concentration with time at the location of reinforcement. The time at which the chloride concentration value in that row equals or becomes greater than the critical chloride concentration is the initiation time of corrosion.

2.1 Model Parameters

The parameters c_s, α and D_α involved in Eq. (3) are estimated by fitting the chloride concentration values obtained from the numerical solution with the measured values at different depths taken from chloride profiles. Two or more chloride profiles measured at different times, can be collectively used for this purpose to cater to the variations observed in parameters with respect to time. For example, it is observed from the literature that the surface chloride concentration increases with the time of exposure, this variation is indirectly considered since c_s is fitted based on chloride profile at different times.

A Genetic algorithm-based optimization technique is used to perform the least square fitting in MATLAB. The least square error, whose expression is given below, is specified as the objective function for the optimization.

$$\text{LSE} = \sum_{i=1}^{n} \left[\frac{c_i^d(t)}{c^n(x_i, t)} - 1 \right]^2 \tag{5}$$

where c_i^d is the chloride concentration of samples exposed to real marine environment measured at laboratory; $c^n(x_i, t)$ is the chloride concentration at depth x_i calculated using the numerical procedure adopted in this study; n is the number of data points. Iterations are carried out till the average change in the fitness value of the objective function is less than $1.0e-20$. The details of the same can be found in [7].

2.2 Performance of Adopted Numerical Procedure

The performance of the numerical procedure adopted in this study is checked by comparing the results with data obtained from the field investigations. The chloride profiles considered, in this study for this purpose, are chloride profiles of concrete samples drawn from existing structure exposed to tidal/splash zone in marine environment. Only one experimentally measured chloride profile at a particular age was available. The parameters involved in the solution are estimated using one chloride profile (earliest in time) and the predicted corrosion initiation times are compared with the reported visual field observations.

For demonstration chloride profiles of samples reported by Liam et al. [15], and Michael [16] are considered. These samples are taken from a 24-year-old pile of jetty structure in Singapore by Liam and a 54-year-old Jetty structure in Shute Harbour, Australia, by Michael. For samples of Liam et al., the salinity of the sea water at a depth 2 m, ranged from 26.0 to 32.0%. Average temperature and relative humidity, were in the range of 24.2–32 °C and 62.4–94.6%, respectively. In case of Michael's data, the core samples were collected from lower part of western desk. The average temperature in a day near Shute harbour was around 24.4–25.5 °C and the mean annual humidity was between 74 and 78%. Since, the chloride profiles of real structures are available at only one age, the profiles are used for fitting the parameters and performance of the model is checked with the predictions of initiation time of corrosion and relating to the visual field observations with respect to the corrosion state of the structure. The model parameters that are fitted to the chloride profiles are given in Table 1. The fitted chloride profiles are shown in Fig. 1.

The estimated corrosion initiation times for real structures are presented in Table 2. It can be noted from this table that in case of Liam data and Michael data, the predictions by sub-diffusion model are realistic as the results of initiation time are comparable with field observations. The corrosion initiation time being higher than 34.34 and 56.57 years indicates that the quality of concrete and of the construction practice adopted was good. Therefore, the proposed model without considering time dependent surface chloride concentration, is suitable for estimating the initiation time of corrosion of real structure even when initiation time of corrosion is long.

Table 1 Values of C_s, α, D_α of the proposed model for real structures exposed to marine environment

Investigation	Sub-diffusion model parameters		
	C_s (% by weight of cement)	A	D_α (m^2/s$^\alpha$)
Liam et al. [15] Jetty pile	1.26	0.88	2.32×10^{-11}
Michael [16] Jetty deck	1.54	0.73	8.15×10^{-11}
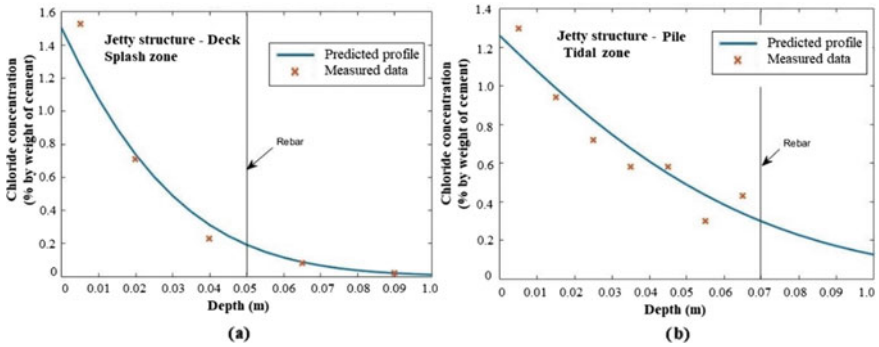
Fig. 1 Chloride profiles of real structures exposed to real marine environment predicted by the proposed model: **a** Michael's data; **b** Liam et al. data

Table 2 Estimated initiation times of corrosion for real structures exposed to marine environment

Sample	Exposure	Cover depth (mm)	C_{cr} (% by weight of cement)	Initiation time (years)	Remarks related to field observation
Liam et al. [15] Jetty pile	Mean tidal zone	70	0.4	34.34	No delamination observed at 24 years in mean tidal zone. Initiation time reported by Liam et al. is 35 years
Michael [16] Jetty deck	Splash zone	50	0.2	56.57	No delamination observed at 54 years

3 Probabilistic Analysis of Corrosion Initiation Time

The model presented so far results in a deterministic value of corrosion initiation time. However, the corrosion initiation time should be treated as a random variable represented by a probability density function because of the statistical nature of diffusion process, the inherent heterogeneities of the concrete matrix and critical chloride content [17]. This can be achieved by carrying out probabilistic analysis of the corrosion initiation time. In this study, Monte Carlo Simulation technique is used to obtain the histogram of corrosion initiation time. In each simulation cycle, the deterministic value of corrosion initiation time is calculated using a set of drawn samples of basic variables. As numerical solution of sub-diffusion process take a significant time for each simulation compared to analytical solution, Latin hypercube sampling technique is used to draw the samples of each the basic variables. Therefore, by adopting this sampling technique lesser of number of simulation cycles are sufficient to obtain the corrosion initiation time distribution.

3.1 Illustrative Example

A typical Indian bridge girder of span 10 m, by the MORT&H [18] is considered for this purpose. MORT&H provides standard plans for highway bridges in India. The cross-section of the girder is shown in Fig. 2. The design compressive strength of concrete and yield strength of stirrups are 25 MPa and 415 MPa, respectively. The stirrups in the girder are spaced at 100 mm c/c upto 3.3 m, from the support on either side of girder. The structure is assumed to be located in a coastal environment and hence subjected to deterioration due to chloride induced corrosion of reinforcement. The random variables considered in the study are given in Table 3 and 250 simulation cycles are considered.

The deterministic value of model parameters, α and D_α, for this case is assumed based on the specimens of Chalee et al. [21]. The OPC specimens had a water-cement ratio of 0.65 (compressive strength at 28 days varying between 17 and 29 MPA) and were exposed to tidal environment in the Gulf of Thailand. The chloride concentration in the sample were measured at different depths after 2, 3, 4, 5 and 7 years of exposure.

Fig. 2 Standard cross-section of T-Girder recommended by IRC for 10 m span
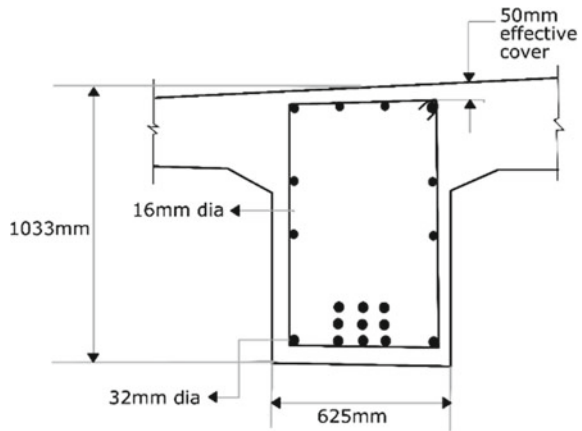
Table 3 Statistical details of random variables involved in the study

Variables	Units	Distribution	Mean	COV	References
Concrete cover thickness for stirrups	M	Lognormal	0.005	0.10	[19]
Surface chloride concentration	% weight of concrete	Uniform	0.306 (0.211–0.401)	0.18	[20]
Critical chloride concentration	% weight of concrete	Uniform	0.1275 (0.073–0.182)	0.25	[20]
Chloride sub diffusion co-efficient	m^2/s^α	Lognormal	2.08×10^{-11}	0.257	[20]
Fractional exponent	–	–	0.94	–	
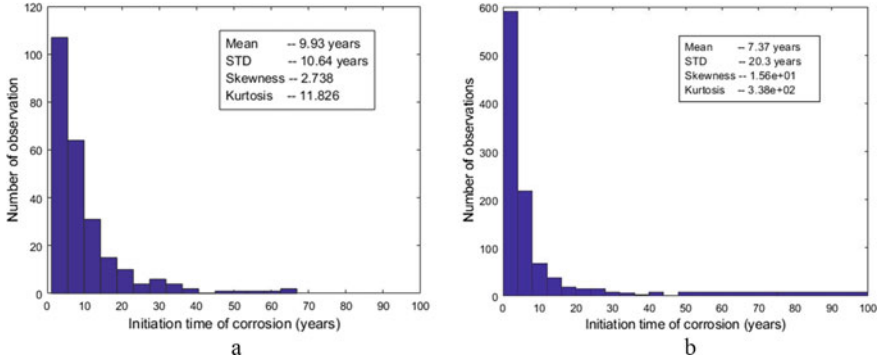
Fig. 3 Histogram of corrosion initiation time obtained using: **a** proposed model; **b** Fickian model

The values of modal parameters are fitted using these chloride profile. While D_α is considered to be a random variable, α is considered to be constant for guaranteeing the stability of numerical solution. However, there is a scope for addressing this limitation in the future.

Results and Discussion. The histogram of corrosion initiation time of stirrups is shown in Fig. 3a. The mean corrosion initiation time for stirrups is found to be 9.9 years and the standard deviation is found to be 10.64 years. For comparison the histogram of corrosion initiation time of stirrups obtained using the Fickian model with time variant chloride diffusion coefficient is shown in Fig. 3b. The expression used for prediction is given in Eq. (6).

$$T_i = \left[\frac{\bar{c}^2 t_m^{-q}}{4 m_D D_{Cl}(t_m)} \left\{ erf^{-1} \left(\frac{c_s - c_{cr}}{c_s} \right) \right\}^{-2} \right]^{\frac{1}{1-q}} \tag{6}$$

where $D_{Cl}(t_m)$ is the time dependent chloride ion diffusion coefficient at reference time t_m; m_D is the modeling error associated with prediction of diffusion coefficient at any time t; q is an exponent involved in prediction of diffusion coefficient which depends on the type of concrete mix. The statistical property of $D_{Cl}(t_m)$, m_D and q can be found in [20].

The mean corrosion initiation time obtained by Fickian model is around 7.37 years. A higher value for mean corrosion initiation time is obtained from the proposed sub-diffusion model because it takes into consideration the tortuous path of concrete pores due to its fractal nature. Hence, using the proposed the model in design leads to a lesser conservative and a more economical structure.

Lognormal distribution for corrosion initiation time obtained using sub-diffusion model passes the Chi-square test at 5% significance level. The obtained chi-square value is 6.3 and degree of freedom is 3. The analogy to sub-diffusion process can be brought from continuous time random walk accompanied by long rests represented in [8]. The long rests are the outcome of clogging of pores due to hydration products,

making the path tortuous for ions to diffuse. Hence, the time spent by the chloride ion in a state follows a fat tailed distribution. The histogram shown in Fig. 3 also has fat tail.

Thus, the study brings out the importance of considering the fractal nature of concrete pore-structure when modelling the phenomenon of chloride ingress into cover concrete.

4 Conclusion

The ingress of chlorides into the cover concrete is often modelled using Fick's second law of diffusion. However, it is important for the prediction model to take into account the nature of the concrete pore structure. A sub-diffusion model, which accounts for the fractal topology of concrete pore structure by considering fractional time derivative, is proposed in this paper. The performance of the model with reference to the measured chloride profiles from actual structures, suggests that although the surface chloride concentration is assumed constant, the proposed model does not underestimate concentration values when the time of prediction is close to the maximum time used in data fitting. Even otherwise when the time of prediction is high, the concentration near the level of reinforcement is predicted satisfactorily by the model. Therefore, the initiation time predicted using proposed model is more realistic.

Further, for the application of the proposed model in durability designs, probabilistic analysis of corrosion initiation time is carried out. Here, the parameter involved in the numerical solution for sub-diffusion equation (i.e., fractional order) is estimated by data fitting using the chloride profiles obtained from literature. However, the same can be predicted using its relationship with fractal dimension of pore structure through experimental studies. This becomes the scope of future work.

References

1. Claisse PA (2014) Transport properties of concrete: measurements and applications. Elsevier. Science & Technology
2. Tang SW, Chen E, Li ZJ (2012) Fractal model for pore structure in cement-based materials. In: 2nd International conference on microstructural-related durability of cementitious composites. RILEM Publications SARL, pp 997–1004
3. Konkol J, Prokopski G (2014) The effect of concrete mix composition on the character of fracture of set concrete. J Geogr Geol 6(4):29–41
4. Jin X, Li B, Tain Y, Jin N, Duan A (2013) Study on fractal characteristics of cracks and pore structure of concrete based on digital image technology. Res J Appl Sci Eng Technol 5(11):3165–3171
5. Janett, P.: Diffusion on fractals and space-fractional diffusion equations. Technical University of Chemnitz, Faculty of science, Dissertation (2010).

6. West BJ (2016) Fractional calculus view of complexity. In: Tomorrow's science. CRC Press, London
7. Yogalakshmi NJ (2020) Stochastic service life prediction of RC girders subjected to chloride induced corrosion—shear limit state. PhD thesis, RMIT University
8. Bazant ZP (1979) Physical model for steel corrosion in concrete sea structures-theory. ASCE J Struct Div 105(6):1137–1153
9. Takewaka K, Mastumoto S (1988) Quality and cover thickness of concrete based on the estimation of chloride penetration in marine environments. ACI Spcl Publ 109:381–400
10. Metzler R, Klafter J (2000) The random walk's guide to anomalous diffusion: a fractional dynamics approach. Phys Rep 339(1):1–77
11. Wei S, Chen W, Zhang J (2017) Time-fractional derivative model for chloride ions sub-diffusion in reinforced concrete. Eur J Environ Civ Eng 21(3):319–331
12. Tateishi A, Ribeiro HV, Lenzi EK (2017) The role of fractional time-derivative operators on anomalous diffusion. Front Phys 5:52
13. Yuste SB, Luis A (2005) An explicit finite difference method and a new von Neumann-type stability analysis for fractional diffusion equations. SIAM J Numer Anal 42(5):1862–1874
14. Ali I, Nadeem AM, Bilal C (2016) Solutions of time-fractional diffusion equation with reflecting and absorbing boundary conditions using Matlab. In: Mathematical and computational approaches in advancing modern science and engineering. Springer, Cham, pp 15–25
15. Liam KC, Roy SK, Northwood DO (1992) Chloride ingress measurements and corrosion potential mapping study of a 24-year-old reinforced concrete jetty structure in a tropical marine environment. Mag Concr Res 44(160):205–215
16. Michael L (2016) Physical testing: chloride ingress, Lloyd Roberts Jetty, Shute Harbour. Prepared for Cardno NSW Water and Environment, Australia
17. Shi X, Xie N, Fortune K, Gong J (2012) Durability of steel reinforced concrete in chloride environments: an overview. Constr Build Mater 30:125–138
18. Standard Plans for Highway Bridges, RCC beam and slab superstructure: Indian Roads Congress, Ministry of Surface Transport, Roads Wing (1993)
19. Enright MP, Frangopol DM (1998) Probabilistic analysis of resistance degradation of reinforced concrete bridge beams under corrosion. Eng Struct 20(11):960–971
20. Balaji Rao K, Anoop MB (2014) Stochastic analysis of reinforced concrete beams with corroded reinforcement. Proc Inst Civ Eng Constr Mater 167(1):26–35
21. Chalee W, Jaturapitakkul CA, Chindaprasirt P (2009) Predicting the chloride penetration of fly ash concrete in seawater. Mar Struct 22(3):341–353

Robust Design Optimization of Telecommunication Tower Under Extreme Load in Dual Response Surface Method

Sujit Das , **Gaurav Datta, and Soumya Bhattacharjya**

1 Introduction

It is well established now that optimization disregarding uncertainty may lead to unsafe design leading to catastrophic failure consequences. This is due to the undesirable deviation of structural performance caused by uncertainty. To minimize such unwanted deviation, and also to maintain economy of structural cost, a suitable scheme of uncertainty-based-optimization is needed. In fact, in mechanical and production engineering, to yield the best quality products by ensuring minimum undesirable deviation from their design performances in the presence of uncertainty, a technique popularly known as robust design optimization (RDO) is used [1–4]. An RDO simultaneously minimizes the dispersion of structural performance under uncertainty and cost. Besides production engineering, the application of RDO is also becoming popular in aircraft engineering to design aeroplane wings, ensuring minimum chance of flutter and resonance under extremely uncertain wind turbulence [5]. In the last decade, RDO has also paved its path in structural engineering to ensure minimum deviation of structural performance (thus the minimum chance of failure), maintaining simultaneously the budget under extremely uncertain loads [1, 6]. The present paper focuses on the RDO of a telecommunication tower structure as substantial deviations of structural performance for such a structure is highly anticipated when subjected to extremely uncertain wind environment.

In this regard, it is worth mentioning that a reliability-based design optimization (RBDO) is the most popular approach to uncertainty-based-optimization. The RBDO

S. Das (✉) · G. Datta · S. Bhattacharjya
Department of Civil Engineering, Indian Institute of Engineering Science and Technology, Shibpur, Howrah, West Bengal 711103, India
e-mail: sujitdas.rs2020@civil.iiests.ac.in

S. Bhattacharjya
e-mail: soumya@civil.iiests.ac.in

brings specified reliability of structure by yielding a design which has reliability index more than a user-specified target reliability index value [7, 8]. But, there are two major drawbacks of RBDO. Firstly, the system may still be sensitive to input parameter variation due to uncertainty, leading to large undesirable deviations, even though the target reliability index criteria are satisfied. Secondly, the RBDO is only applicable when sufficient statistical data, such as mean, standard deviation, and probability density function (PDF), is available for all the parameters. The RBDO is fully hinged on the reliability index calculation, which cannot be done unless one has the mean, standard deviation, or PDF information about the uncertain parameters.

In fact, most often, sufficient realistic statistical data of involved system parameters like load, temperature difference, etc., are not available to characterize an uncertain system and construct probability density function to conduct a reliability analysis. Instead, only a range of variation of the parameters due to uncertainty is available, by which parameters can be treated as uncertain-but-bounded (UBB) type. Dynamic wind load is an extremely stochastic phenomenon characterized by many uncertain parameters. Lift coefficient, drag coefficient, wind speed, gradient height, the Power law exponent, dead load of antenna, dimensions and thicknesses of the tower members—for all these parameters a definite mean, standard deviation or PDF is not available. Only a set of upper and lower bounds can be constituted based on the findings of the previous researchers or from experience. The dynamic wind load signatures vary significantly over time and show different fluctuating behaviour at different realizations even for same set of input parameters [9, 10] Thus, it is more logical to set lower and upper bounds of the parameters so that all possible variations within that range can be suitably considered.

Thus, it is clear that the RBDO cannot be applied with UBB parameters as reliability calculation is impossible under the above-mentioned circumstances. However, the RDO, since it does not depend on the reliability information, and works fine with UBB parameters (as noted for seismic load in [3]), is an elegant approach in this regard. Also, the RDO makes the structural performance least sensitive to uncertainty effects. Thereby, the drawbacks of the RBDO mentioned above gets circumvented. Thus, the present paper focuses on the RDO of tower structure under UBB-type uncertainty.

The RDO with UBB parameters is generally executed using a first-order perturbation approach [11], which is only valid for the low level of uncertainty. Also, this approach often leads to uneconomic and very conservative design since it is based on worst-case propagation of uncertainty [12]. In this regard, the convex programming (CP) approach [13] is gaining increasing attention, where the UBB parameters constitute a convex set. In the CP, the design parameters are so selected that provides a so-called 'safety measure' more than the target one [13]. It may be noted here that the term 'safety measure' is not the same as the 'reliability index' used for probabilistic parameters. Rather, it is a term that denotes the largest variation of the UBB parameters that the system can withstand.

The state-of-the-art on mathematical formulation of RDO with probabilistic parameters is quite advanced [7]. Available techniques enable one to formulate RDO problem in presence of higher uncertainty level, mixed probability distribution

and correlation. In this regard, there is enough scope to explore RDO formulation with UBB parameters. Ben-Tal and Nemirovski [6] detailed the concept of convex modelling to treat UBB uncertainty. Since then, researchers have tried various extension of the convex modelling to effectively solve RDO problem. Au et al. [6] proposed an unsatisfactory degree function following the concept of Physical Programming to express the feasibility of constraints under undesirable variation of UBB parameters. Wang et al. [14] applied convex modelling for optimization of a simple semi-active tuned mass damper system. Chen et al. [13] presented hyper-ellipsoidal CP approach for RDO of structural system, where the authors proposed a sub-optimization scheme to efficiently yield RDO solution. Meng et al. [15] proposed a super-parametric approach of convex modelling which is a general case of ellipsoidal model. In this regard, the theoretical review of Jiang et al. [16] on probability-interval hybrid uncertainty analysis for structures with both aleatory and epistemic uncertainties is of worth mentioning. In this paper, the wind effect is simulated by generating the artificial wind field while using weighted amplitude wave superposition technique. In this regard, Kaimal's power spectral density function (PSDF) [17] is used. This approach of artificial wind force generation has been successfully used in wind fragility analysis of structures [1, 18]. One can also obtain wind force distribution over height, space and time by using wind tunnel experiments or by computational fluid dynamics. But, such approaches will require execution of a large number of experimentations (or computer simulations) and thus it takes high simulation time to generate the random wind field. Hence, in the present study, random wind field is simulated by numerically generating artificial wind force time-histories considering uncertainty in related parameters.

It is now well conceived that RDO under stochastic dynamic load becomes extensively onerous in context of computational time and hazards by conventional direct Monte Carlo simulation based approach [19, 20]. To circumvent this, use of response surface method (RSM) is quite popular [2]. The usual RSM yields an explicit equation for mean value of response as functions of input parameters. Once the explicit equation of response quantity under interest becomes available, the RDO problem can be easily cast and solved as one does for simple structural systems [13]. However, such single level RSM is not sufficient to capture the highly stochastic nature of extreme wind, as this approach does not focus on the performance dispersion values. In fact, under extremely uncertain wind load, the wind force time-history signatures vary even for the same set up of wind speed, wind incidence angle and other parameters of wind. Due to this reason, the record-to-record variation of wind force time-history cannot be considered using a single RSM [1]. In this regard, Datta et al. [9] adopted a dual RSM concept, where this variation time-history signatures are taken into account through another response surface, which is for standard deviation of response. By this approach, for the same set up of input parameters, a number of wind speed time-histories are generated. So, at each design of experiment (DOE) point, it will create two response surfaces, one for the mean response and another for the standard deviation (SD) of the response. It is quite clear that the application of single RSM in RDO may be erroneous as it does not consider the record-to-record variation of wind speed time-histories. However, work on Datta et al. [9] was confined for

probabilistic parameters only and attains its limitation for UBB parameters. Thus, this present work is more general as it considers UBB parameters as well. In doing so, the CP-based RDO formulation is posed in dual RSM framework, which is not attempted earlier in the existing literature.

Thus, the unique contribution of this paper is to propose a new RDO formulation with UBB parameters under dual RSM, which is hinged on the concept of imposing the record-to-record variation of wind speed time-histories. The improvement by the proposed approach is elucidated by optimizing a steel telecommunication tower problem, and the results are compared with the existing formulations of CP.

2   Conventional CP Based RDO

The concept of CP is first described with the help of Fig. 1. Let us suppose that, U_1 and U_2 are two UBB parameters which can be represented by a general ellipse defined by their ranges $\bar{U}_1$ and $\bar{U}_2$ shown in Fig. 1. Since, these have dimensions; it will be quite advantageous to transform the system in non-dimensional space. It is done by changing the scale of U_i^L (lower bound) to U_i^U (upper bound) to (-1) (lower bound) to $(+1)$ (upper bound). Thereby, the ellipse becomes a circle as shown in Fig. 2. Thus, by this normalization, the UBB parameters are transformed from $\mathbf{U}$ space to $\mathbf{u}$ space. It can be written that $U_i = \bar{U}_i + (u_t + \Delta U_i)$, where $\bar{U}_i = \frac{(U_i^L + U_i^U)}{2}$ and $\Delta U_i = \max(|U_i^U - \bar{U}|, |\bar{U} - U_i^L|)$ $\bar{U}_t = \frac{(U_i^L + U_i^U)}{2}$. By this operation, the variation of the interval variables will lie in the interval $[-1, 1]$.

Now, the structure is said to be in reliable state if the constraint function $g(\mathbf{u})$ < 0. On the other hand, $g(\mathbf{u}) > 0$ indicates the failure of the structure. $g(\mathbf{u}) = 0$ defines the critical condition or limiting state of the structures. These conditions are depicted in Fig. 3. The safety region and the failure region are indicated by yellow and blue fill, respectively, in Fig. 3. In this figure, η defines the safety of the structures. Higher the values of η, more will be the tolerance of the structures to uncertainty, and

Fig. 1 Convex ellipsoidal space
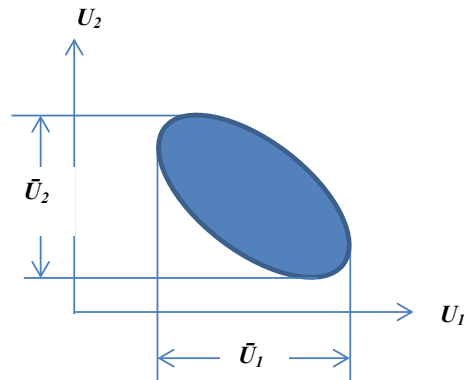
Fig. 2 Unit radius circle case
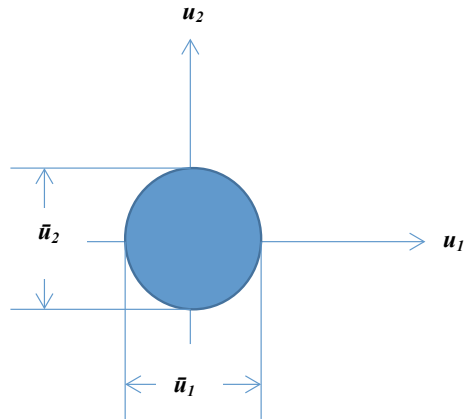
hence, more will be the robustness. Chen et al. [13] formulated robust optimization problem such as to make η more than a target value η_{target} (shown in Fig. 3). In this proposition, the original unit circle is allowed to increase in size whose radius depicts the uncertainty. $\eta = 1$ presents the case of highest variation of UBB parameters i.e. $\Delta U_i = 1.0$. η_{target} is generally taken as 1.0. But, by proper selection of design variables (DVs), if it becomes possible to achieve $\eta > 1$, the design is said to be more robust since it can endure substantial amount of undesirable variations which is unprecedented. But, in this case, for $\eta < 1$, the curve touches or becomes inside the circle which implies the failure of the system. At $\eta = 1$, the curve cuts the unit circle tangentially that implies the critical state of the structures.

Fig. 3 Concept of η
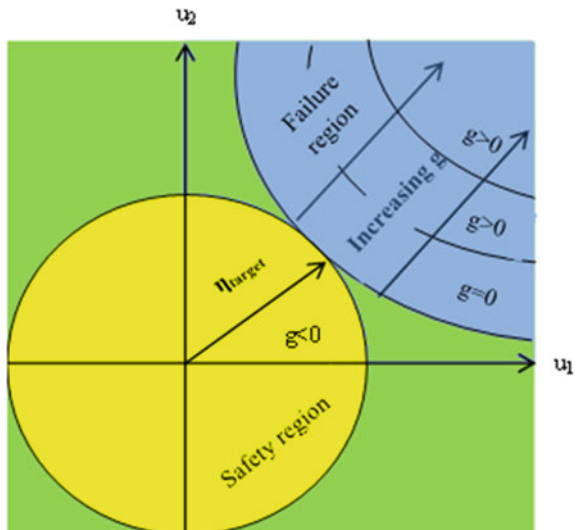
Chen et al. [13] proposed a two-step optimization process for the RDO. The main Optimization problem is to find the DVs **X** as,

$$\text{find } X \text{ such as to minimize } f(X, U)$$
$$\text{such that, } g_j(X, U) \leq 0, \forall j \in M, X \in \left[X^L, X^U \right] \tag{1}$$

A sub-optimization problem is defined at each update of **X** to find out the maximum deviation of UBB parameters **U** that the system can tolerate. This optimization formulation finds **U**, such as to,

$$\text{minimize } g_j(X, U), \forall j \in n$$
$$\text{such that, } n_j = \max(|u_1|, |u_2|, \ldots, |u_m|) \geq \eta_{\text{target}} \tag{2}$$

The constraint function is minimized in the sub-optimization problem to find the most probable failure point or the set-up of **U** for which $g(\mathbf{U})$ is just critical or becomes an active constraint.

3   Dual RSM

Let us suppose the response Y_a is to be considered by the RSM for the a-th wind force time-histories. Consider, $u_i^{(m)}$ as the m-th observation of the i-th input variable, u_i, in the DOE space whereas $Y_l^{(m)}$ is the output response of m-th DOE point under a-th wind force time histories. The relationship between the predicted response ($\hat{Y}$) and the input variables (**U**) can be expressed by the quadratic polynomial form as:

$$\hat{Y} = \beta_0 + \sum_{i=1}^{n} \beta_i u_i + \sum_{i=1}^{n} \sum_{j=1}^{n} \beta_{ij} u_i u_j \tag{3}$$

where, n is the total number of variables and $\mathbf{u} = [\mathbf{x}\ \mathbf{z}]$. The parameters, β_0, β_i and β_{ij} are the unknown coefficients which are obtained by the least-squares method. Based on the obtained response values at all the DOE points, the relationship between structural response and input random variables can be put into the matrix form as follows:

$$\hat{Y} = Q\beta \tag{4}$$

where **Q** is known as the design matrix. The unknown polynomial coefficient vector (**β**) is to be obtained by minimising an error, Δ_y, which is defined as:

$$\Delta_y = \sum_{i=1}^{m} \left(Y_i - \beta_0 - \sum_{i=1}^{n} \beta_i u_i^{(m)} - \sum_{i=1}^{n} \sum_{j=1}^{n} \beta_{ij} u_i^{(m)} u_j^{(m)} \right)^2$$

$$= \left(Y - \hat{Y} \right)^T \left(Y - \hat{Y} \right) = (Y - Q\beta)^T (Y - Q\beta) \qquad (5)$$

The least-squares estimate of $\boldsymbol{\beta}$ is then obtained as:

$$\beta = \left[Q^T Q \right]^{-1} Q^T Y \qquad (6)$$

Once $\boldsymbol{\beta}$ is obtained by the Eq. (5), $\hat{Y}$ can easily obtained for any set of input variables by using Eq. (3). Now stochasticity due to the wind analysis is obtained by using the wind force time-histories to consider the record-to-record variations. In case of the dual RSM, at first for each DOE point (each DOE point corresponds to a particular wind speed), a number of wind speed time-histories are generated. Then, the mean and SD of response are obtained for each DOE point. This process is to be repeated for all the DOE points (which include a set of different wind speeds). Due to this, two vectors, viz. a mean vector and a SD vector, of the desired responses '$\hat{\mathbf{Y}}$' are generated. Then the response surface for mean and SD are obtained for the considered responses as,

$$\hat{Y}_\mu = g_1(U) \text{ and } \hat{Y}_\sigma = g_2(U) \qquad (7)$$

4 Generation of Wind Load

In general, the along-wind component of wind force acting at ith level at height z from the ground can be written as [9]:

$$F_D(z, t) = \frac{1}{2} \rho [V(z, t)]^2 C_D A_i \qquad (8)$$

In above Eq. (8), A_i is the tributary area of the node under consideration. C_D is the drag coefficient, which is invariant over height. In the present study, the value of C_D is obtained from IS 875(III) (2015) [21] since the structure considered is regular in shape and size. It may be noted that under dynamic condition and due to various uncertainty effects the drag coefficient may vary. Thus, C_D is considered as a UBB parameter (see Table 2). The wind speed, $V(z, t)$ is composed of time-invariant mean component $\bar{V}(z)$, and a fluctuating component $v(t)$, known as gust. i.e.,

$$V(z, t) = \overline{V}(z) + v(t). \qquad (9)$$

The mean wind speed profile is expressed by the Power law [22] as:

$$\overline{V}(z) = V_G(z/z_G)^{1/\varsigma} \tag{10}$$

where, V_G is the gradient wind speed, z_G is the gradient height, and ς is the exponential coefficient. The values of z_G and ς depend on ground surface roughness and terrain categories. z_G and ς values are taken as 270 m and 7 as per ANSI (1982) [23] for terrain category 2 in the present study. In fact, these parameters are also uncertain with no definite distribution. Hence, in the present study these parameters are taken as UBB parameters. Their ranges are provided in Table 2. In the numerical study, z_G = 270 m and ς = 7 have been considered.

In this study, the gust component is generated by using Kaimal's PSDF [17] which can be expressed as:

$$S_u(\Omega, z) = 50u_*^2 z / \left\{ \pi \overline{V}(z) \left[1 + 50 \left(|\Omega| z / 2\pi \overline{V}(z) \right) \right]^{5/3} \right\} \tag{11}$$

where $\Omega(=2\pi f)$ is the frequency in rad/s, and f is in Hz. The shear velocity u_* is computed by logarithmic law of mean velocity as,

$$u_* = \kappa \overline{V} / \ln(z/z_o) \tag{12}$$

in which, κ is the von Karman constant, taken as 0.4, and z_o is the roughness length of the surface which depends on the surface properties only and can be taken as 0.01 for smooth surface.

It is important to note here that for telecommunication tower like structures, the effect of vortex shedding must have to be considered in addition to the along-wind effect. The time-varying vortex shedding force can be expressed as [9],

$$F_L(z, t) = \frac{1}{2}\rho[V(z, t)]^2 C_L(z, t) A_i \tag{13}$$

In above Eq. (10), the stochastic lift force co-efficient, $C_L(z, t)$ is obtained by weighted aptitude wave superposition technique with the PSDF of $C_L(z, t)$ as [24],

$$S_{C_L}(z, \omega)/\sigma_{C_L}^2(z) = \left\{ (1/\omega_0)/2\sqrt{\pi}\beta(z) \right\} exp \left\{ -[1 - \omega/\omega_0]^2/\beta^2(z) \right\} \tag{14}$$

where $\omega_0 = 2\pi f_0$ is the vortex shedding frequency and $f_0 = S_t V(z)/D(Z)$. S_t is the Strouhal number, assumed as 0.20 (for $D \times V < 6$ m^2/s) and 0.25 (for $D \times V \geq 6$ m^2/s) [21]. $\beta(z)$ is the band-width parameter of the PSDF assumed as 0.25. $\sigma_{C_L}(z)$ is the standard deviation of C_L which is assumed as invariant over height and taken as 0.4. $D(z)$ is the outside width of the tower at height z from the ground level. Finally, the along-wind force and across-wind force are combined as,

$$F(z, t) = \sqrt{\left\{ F_D(z, t)^2 + F_L(z, t)^2 \right\}} \tag{15}$$

Note that As per Eq. (8), the along-wind component of wind force depends on the drag coefficient (C_D) and from Eq. (13) the across-wind component depends upon the lift force coefficient (C_L). The C_D values are more near the ground surface and decrease as the elevation increases; but, the C_L values increase as the elevation increases. Accordingly, for realizing drag forces and lift forces by Eqs. (8) and (13), at first, using the uniform design method, the values of C_D and C_L are realized and sorted in descending and ascending order, respectively. Then, these sorted values of C_D and C_L are assigned with increasing heights. As a result, at higher elevation, lower C_D and higher C_L got assigned in the design of DOE, and vice-versa. Since, the whole RDO approach is based on these DOE, this issue is taken care of right at the wind field simulation stage.

It may be further noted here that overturning moment may be also checked to ensure stability and design of foundations. Though, in this study, dimensioning of main members due to stress constraints under extremely uncertain wind load is of main concern, the methodology can be easily applied for checking stability of the tower against overturning. In such a case, in addition to tensile stress and compressive stress in tower members, the overturning moment should be also included as one of the response quantity. It will vary over time and should be obtained as, $M(t) = \sum_i F_i(t) \times z_i$ where, F_i is the wind force at i-th elevation from ground level at height z_i and obtained through Eq. (15).

5 Dual RSM Based Proposed RDO

As mentioned, the conventional CP based RDO is one of the most viable alternative when dealing with the uncertain parameters. But, one of the important disadvantages for the conventional CP based approach of RDO is that, it is proven incompetent when it comes to consider the random fluctuations in case of stochastic dynamic loadings such as earthquake load, blast load, wind load etc. as the approach only consider only the mean in terms of constraint function. Thus, the proposed dual RSM based modified CP approach may seem to be a potential choice as it not only takes up the record to record variation of stochastic load, but also reduces the constraint boundary. The proposed approach considers the mean as well as the standard deviation in the constraint function and is given as follows:

Find **X** such as to,

Minimize, $f(X, U)$

Subject to, $\begin{aligned} \overline{g_j}(X, U) + k * \Delta \overline{g_j}(X, U) \leq 0, \text{ if } \overline{g_j}(X, U) \leq 0 \\ \overline{g_j}(X, U) - k * \Delta \overline{g_j}(X, U) \leq 0, \text{ if } \overline{g_j}(X, U) \geq 0 \end{aligned}$, $j = 1, 2, \ldots M, X_L \leq X + \Delta X \leq X_U$

$$(16)$$

where $\overline{g_j}(X, U)$ and $\Delta \overline{g_j}(X, U)$ are the RS meta-models of mean and standard deviation of constraints, respectively and k is the penalty factor.

$$\text{Minimize, } a_j = \overline{g_j}(X, U), \quad j = 1, 2, \dots M,$$
$$\text{Such that, } \eta_j = \max(|u_1|, |u_2|, \dots, |u_n|) \geq \eta_{\text{target}} \tag{17}$$

6 Numerical Study

A 80 m tall steel telecommunication tower is modeled to analyze the efficiency of the present RDO. The tower is made up of angle sections, and square in plan. The tower consists of 16 panels at each face. The top five panels are straight with panel-height of 2 m. Thereafter, the batter starts at a slope of 6.85 degree from the vertical. The supports are fixed. The telecommunication tower carries the weight of the antennas and equipment for the functioning of the telecom services. These loads are equally shared between the topmost nodes. The modeling and analysis of the tower are done in STAAD.Pro software. A linear elastic analysis is performed.

To ensure stability, it is customary to design the leg members such that the lower legs have greater thickness and widths compared to upper leg members. To effectively economize the tower, the tower members are grouped in five categories, shown in Table 1 and Fig. 4. A deterministic design is first carried out following IS:875(III) (2015) considering wind load along with gust. The optimal sections obtained are shown in Table 1. The modulus of elasticity (E) and density (ρ) of the steel are taken as 2×10^5 N/mm^2 and 7850 kg/m^3, respectively. The deterministic optimization is posed to minimize material cost of tower subjected to stress constraints.

The major impact on the cost of a telecommunication tower is weight of the tower. Due to this significance of the weight, the objective function is chosen as to minimize the weight of the tower (W):

$$W = \sum \rho.L_i.A_i \tag{18}$$

where ρ the unit weight of steel, L_i and A_i is the length and area of the i-th member of the tower, respectively. The constraints are framed to limit the maximum tensile and compressive stress in each group within allowable tensile stress or compressive stress.

Table 1 Geometry and properties of telecommunication tower

Sl. No.	Properties	Value
1	Top dimension	2 m × 2 m
2	Bottom dimension	8 m × 8 m
3	Angle sections	Group 1: ISA 50 × 50 × 8
		Group 2: ISA 65 × 65 × 8
		Group 3: ISA 100 × 100 × 8
		Group 4: ISA 150 × 150 × 20
		Group 5: ISA 200 × 200 × 25

Table 2 Details of the UBB parameters

Design and UBB parameters (Unit)	Lower limit	Upper limit	Nominal value
Wind speed (m/sec)($\overline{V}$)	40	60	50
Dead weight of antenna (kN)	1	2	1.5
Drag coefficient (C_D)	0.9	1.2	1.05
Lift force coefficient (C_L)	0.6	1	0.8
Gradient height (z_G) (m)	240	300	270
Power law exponent (ζ)	6	8	7
Width of group 1 members (mm)	50	130	90
Width of group 2 members (mm)	55	150	102.5
Width of group 3 members (mm)	60	150	105
Width of group 4 members (mm)	100	200	150
Width of group 5 members (mm)	150	200	175
Thickness of group 1 members (mm)	6	12	9
Thickness of group 2 members (mm)	6	12	9
Thickness of group 3 members (mm)	6	10	8
Thickness of group 4 members (mm)	6	25	15.5
Thickness of group 5 members (mm)	12	25	18.5

The allowable stresses are calculated using IS: 802 (I) (1992) [25]. The maximum slenderness ratios of tower members are also constrained by allowable slenderness ratio as per IS: 802 (I) (1992) [25]. The design variables are the widths and thicknesses of angle sections of the five groups (i.e. total 10 design variables for the five groups). All the design variables are taken as UBB parameters. The basic wind speed, dead weight of antenna, etc., C_D, C_L, z_G, ζ are all taken as UBB parameters. The dead weight of antenna and associated attachments are taken as UBB parameters. This is taken uncertain as these antennas may be changed in future based on availability of more technologically advanced systems, which may have different weights. $\overline{V}$, that is the time-invariant component of wind speed at 10 m elevation, is taken as UBB parameter. $\overline{V}(z)$ can be found in Eq. (9).The ranges and the nominal values of the UBB parameters are listed in Table 2.

Now, the DOE space is constituted by the UD scheme [26] with these UBB parameters. To consider the record-to-record variation of stochastic wind load, a suite of 10 wind load time-histories is generated at each set up of the DOE points. The variations of the mean along wind drag force and lift force over height are presented in Fig. 5. Both the forces increase over height. Drag force is observed to be more than the lift force here.

The response quantities (maximum tensile stresses and compressive stresses for all the groups here) are obtained for these wind load time-histories at each DOE point using linear elastic time-history analysis in STAAD.Pro. Mean and SD of each response quantity at each DOE point are then obtained. These data are in-turn used to generate the dual response surfaces ($\hat{Y}_\mu$ and $\hat{Y}_\sigma$) for each response quantity through
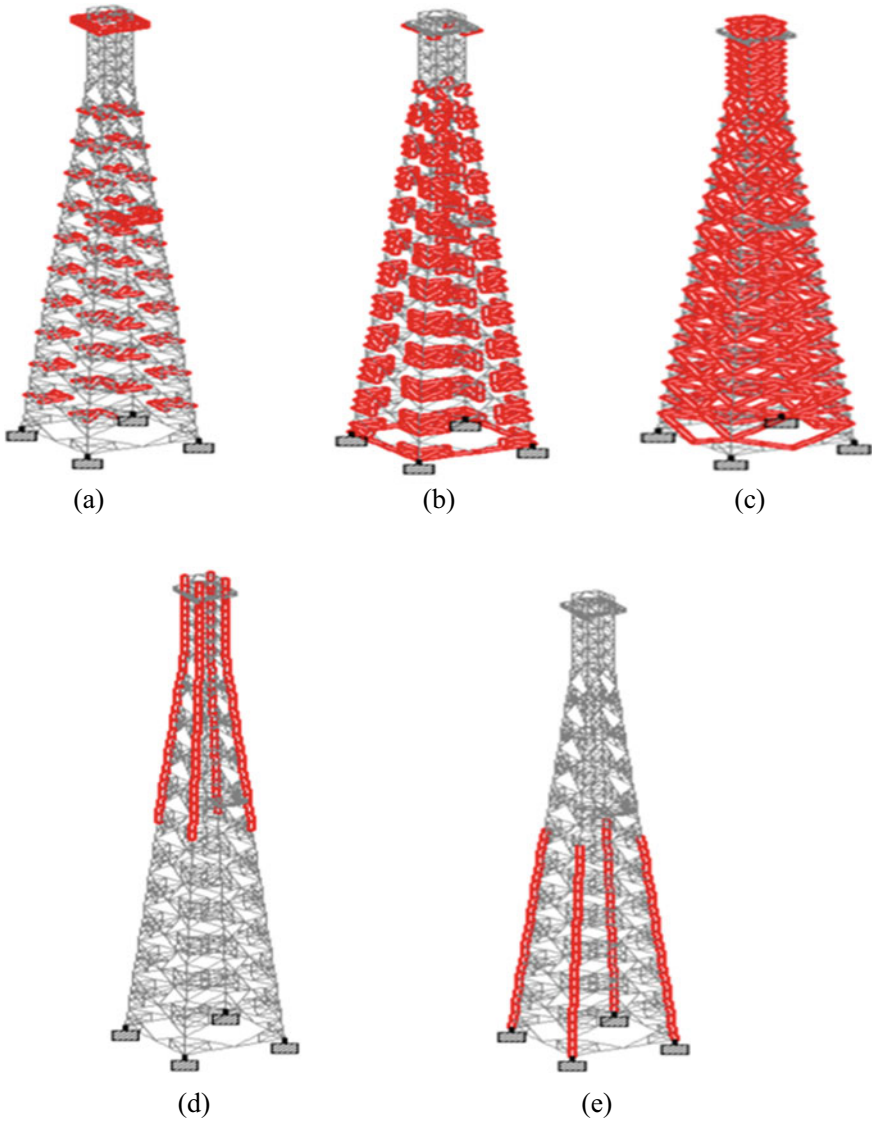
Fig. 4 Telecommunication tower members: **a** Group 1, **b** Group 2, **c** Group 3, **d** Group 4, and **e** Group 5

Eq. (7). The RDO is posed using Eqs. (16) and (17) using the CP and solved by the sequential quadratic programming method in MATLAB.

The RDO results by the formulation of CP [13] and the proposed RDO over the conventional formulation of [13] are presented in Figs. 6 and 7 for varying range of uncertainty level of the UBB parameters. Value of η is considered as 1.0 to develop

Fig. 5 Variation of along and across wind force component for varying height of the tower
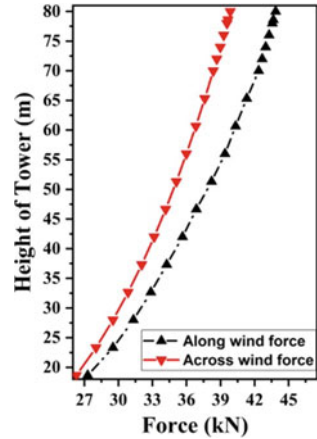
these figures. Figure 6 is plotted by varying all the UBB parameters, simultaneously; whereas, in Fig. 7, the optimal weight is plotted for increasing uncertainty range of wind speed only. These plots are so done to envisage the effect of uncertainty of wind with respect to combined effect of uncertainty in all the UBB parameters. Here, uncertainty range is defined by ΔU_i of Sect. 2. By comparing Figs. 6 and 7, it can be observed that the increase in robust optimal weight due to all UBB parameters uncertainty with respect to uncertainty due to wind is only 12% to 20%. Thus, wind speed constitutes the major source of uncertainty in this system.

In Fig. 7, the robust optimal weight is further plotted for η equals to 1.0, 2.0, and 3.0. As expected, that the highest values of optimal weights are required for $\eta = 3.0$, that is when the system demands more tolerance to uncertainty. The safety circle of Fig. 3 in such a case can grow to a larger extent without failure. However, even

Fig. 6 Optimal weight of the tower for varying dispersion of UBB parameters
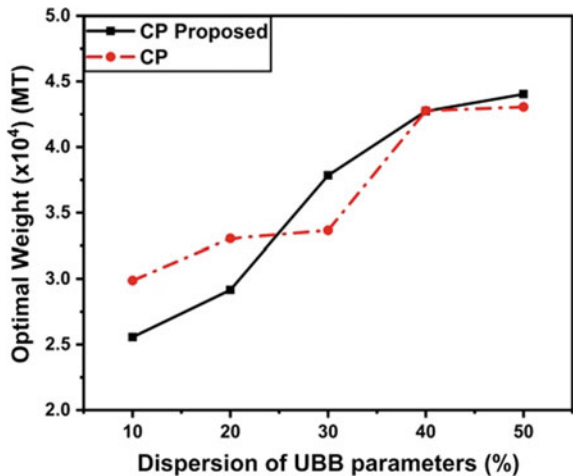
Fig. 7 Optimal weight of the tower for varying dispersion of wind speed
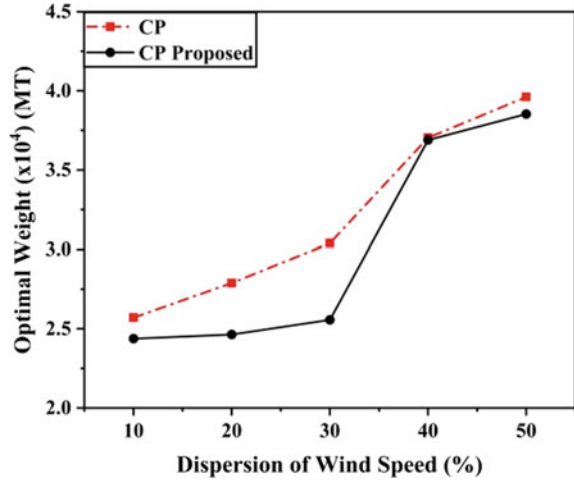
though there is a trend of optimal weight increment for higher η, in the present case, the difference between the RDO results for η equals to 1.0, 2.0, and 3.0, is marginal, especially for the proposed CP case. This may be due to the fact, that higher growing of the safety circle than that achieved at η equals to 1.0, is not possible, owing to the random fluctuations of wind load. In fact, the safety circle cannot grow indefinitely in size denoting an indefinite tolerance to uncertainty. This issue has been correctly identified through the proposed dual RSM-based CP formulation, which considers more detailed uncertainty description of wind load time-histories.

It can be observed from Figs. 6, 7 and 8 that the proposed RDO approach requires lesser optimal weight than the existing approaches in the most cases. However, when uncertainty range is higher, the proposed RDO approach requires marginally higher optimal weight (1–5%) than the existing approaches. The higher optimal weight requirement may be due to consideration of detailed uncertainty description of wind load through dual RSM to make the system insensitive to undesirable variation of UBB parameters.

7   Conclusions

An improved RDO formulation with UBB parameter is proposed using CP, where the robustness of the system is imposed through a dual RSM-based metamodelling approach. The improvement by the proposed approach is elucidated by optimizing weight of a telecommunication tower subjected to axial stress and slenderness ratio constraints. It has been observed that even at the same set-up of hazard parameters, wind speed time-histories vary significantly due to the effect of randomness in the wind field. In such situations, the conventional single RSM-based approach is inadequate as it considers only one sample of wind speed time-history, neglecting

Fig. 8 Optimal weight of the tower for varying η
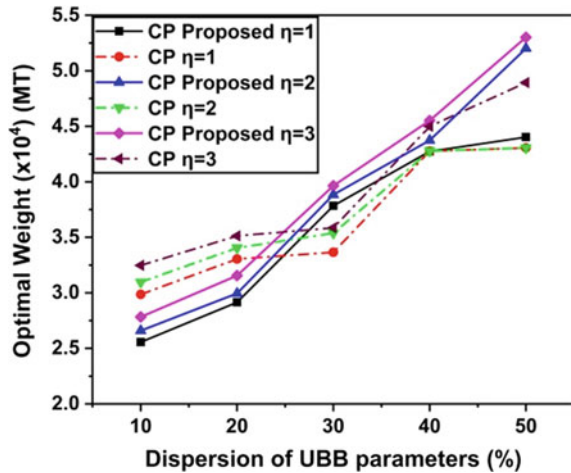
record-to-record variation. On the other hand, sufficient wind speed time-history records are taken in dual RSM for capturing the variation of wind speed in a more detailed way. As a result, the proposed RDO approach yields optimal solution with a detailed consideration of wind uncertainty. The proposed approach yields lesser optimal weight in most of the cases. Thus, the proposed approach is cost-economic as well. In some cases, the proposed approach demands marginally higher optimal weight than the usual CP-based RDO. However, irrespective of whether the proposed RDO will yield lesser optimal weight or marginally higher optimal weight, the main merit of the proposed approach is incorporation of uncertainty in a more detailed way through UBB parameter modeling and the convex programming in the dual RSM framework. The proposed approach yields optimal results in a computationally efficient way. The proposed RDO, though have been presently applied on wind-excited steel tower, can be applied to other structures under various other uncertain loads, as well. This is under consideration at this stage.

References

1. Bhandari A, Datta G, Bhattacharjya S (2018) Efficient wind fragility analysis of RC high rise building through metamodeling. Wind Struct 27(3):199–211
2. Chakraborty S, Bhattacharjya S (2011) Robust optimization of structures subjected to stochastic earthquake with limited information on system parameter uncertainty. Eng Optim 43(12):1311–1330. https://doi.org/10.1080/0305215X.2011.554545
3. Bhattacharjya S, Datta G, Aravapalli HGS (2022) Robust design optimization of concrete circular underground pipes considering seismic effects. J Pipeline Syst Eng Pract 13(2):05022003. https://doi.org/10.1061/(ASCE)PS.1949-1204.0000648
4. Gur S, Ray-Chaudhuri S (2014) Vulnerability assessment of container cranes under stochastic wind loading. Struct Infrastruct Eng 10(12):1511–1530

5. Öztürk B, Saab A (2021) Optimal aircraft design decisions under uncertainty using robust signomial programming. AIAA J 59(5). https://doi.org/10.2514/1.J058724
6. Au FTK, Cheng YS, Tham LG, Zeng GW (2003) Robust design of structures using convex models. Comput Struct 81(28–29):2611–2619
7. Haldar A, Mahadevan S (2000) Reliability assessment using stochastic finite element analysis. John Wiley & Sons, US
8. Tu J, Choi KK, Park YH (1999) A new study on reliability-based design optimization. J Mech Des 121(4):557–564. https://doi.org/10.1115/1.2829499
9. Datta G, Sahoo A, Bhattacharjya B (2020) Wind fragility analysis of RC chimney with temperature effects by dual response surface method. Wind Struct 31(1):59–73. https://doi.org/10.12989/was.2020.31.1.59
10. Fang Z, Wang Z, Zhu R, Huang H (2022) Study on wind-induced response of transmission tower-line system under downburst wind. Buildings 12:891. https://doi.org/10.3390/buildings12070891
11. Wu J, Luo Z, Zhang N, Zhang Y (2015) A new interval uncertain optimization method for structures using Chebyshev surrogate models. Comput Struct 146:185–196
12. Ben-Tal A, Nemirovski A (1998) Robust convex optimization. Math Oper Res 23(4):769–1024
13. Chen X, Fan J, Bian X (2017) Structural robust optimization design based on convex model. Results Phys 7:3068–3077
14. Wang L, Wang XJ, Wang RX, Chen X (2016) Reliability-based design optimization under mixture of random, interval and convex uncertainties. Arch Appl Mech 86(7):1341–1367
15. Meng Z, Hu H, Zhou H (2018) Super parametric convex model and its application for non-probabilistic reliability-based design optimization. Appl Math Modell 55:354–370
16. Jiang C, Zheng J, Han X (2018) Probability-interval hybrid uncertainty analysis for structures with both aleatory and epistemic uncertainties: a review. Struct Multidisc Optim 57:2485–2502
17. Kaimal JC, Wyngaard JC, Izumi Y, Cote OR (1972) Spectral characteristics of surface-layer turbulence. Q J R Meteorol Soc 98(417):563–589
18. Chakraborty S, Bhattacharjya S, Halder A (2012) Sensitivity importance-based robust optimization of structures with incomplete probabilistic information. Int J Numer Meth Eng 90(10):1207–1320
19. Venanzi I, Materazzi AL, Ierimonti L (2015) Robust and reliable optimisation of wind-excited cable-stayed masts. J Wind Eng Ind Aerod 147:368–379. https://doi.org/10.1016/j.jweia.2015.07.011
20. Xu J, Spencer BF Jr, Lu X, Chen X, Lu L (2017) Optimisation of structures subject to stochastic dynamic loading. Comput-Aided Civ Inf 32:657–673. https://doi.org/10.1111/mice.12274
21. IS: 875 (Part 3): 2015, Design loads (other than earthquake) for buildings and structures—code of practice
22. Simiu E, Scanlan HR (1986) Wind effects on structure, 2nd edn. Wiley, New York
23. ANSI Code (1982), ANSI A58.1-1982. Minimum design loads for buildings and other structures. American National Standards Institute
24. Vickery BJ, Basu RI (1983) Across-wind vibrations of structures of circular cross-section. Part I. Development of a mathematical model for two-dimensional conditions. J Wind Eng Indus Aerod 12(1):49–73
25. IS: 802 (Part 1): 1992, Use of structural steel in overhead transmission line towers—code of practice
26. Fang KT, Lu X, Tang Y, Yin J (2004) Constructions of uniform designs by using resolvable packings and coverings. Discret Math 274(1–3):25–40

Statistical Characterisation of Service Life of Corroded RC Bridge Pier

Gheyasuddin Ahmad and P. Kamatchi

1 Introduction

Bridge structures are one of the important lifelines of the transportation system in India. It plays an important role to connect people, places, and transporting goods. Reinforced concrete is the widely used material for bridge infrastructure all over the world because of their durability and price effectiveness [1]. Reinforcements embedded in the reinforced concrete are protected by the passive layer of the thin oxide film. Once chloride present in the environment diffused into the concrete, it reduces the pH value of concrete [2]. Reduction of the pH value of the concrete leads to loss of the protective cover around the reinforcements and the reinforcement get exposed to corrosive environmental condition. Degradation due to corrosion in the concrete is mainly caused due to ingress of carbonation and chloride ions [3]. Chloride is the major cause of the degradation of bridge structures situated in the marine environment. Degradation of concrete structures due to corrosion leads to a gradual decrease in the performance of the structures [4]. The residual service life of the structures is based on the ingress of chloride ions inside the concrete. Garg et al. [5] analysed the failure of bridge structures from 1977 to 2017 and found that the average age of failure of the bridge structures is 34.53 years, which is much less than the IRC 2011 recommendation of a design life of 100 years. Service life estimation is not only necessary for the structural design, but also for the maintenance of the structure over time, life cycle analysis, and for the prediction of risk associated with the structure [6].

G. Ahmad (✉)
Academy of Scientific and Innovative Research, Ghaziabad, Uttar Pradesh, India
e-mail: gheyasuddin.serc18a@acsir.res.in

P. Kamatchi
CSIR-Structural Engineering Research Centre, Chennai, India

Numerous studies are reported in the literature on service life prediction of the structures exposed to chloride-induced corrosion [7, 8]. The number of deterministic models for corrosion initiation is reported in literature viz., Bazant, Cady wayers model, IRC models, Guirguies models, Hookman models, and Morinaga model [9–14]. Despite the corrosion initiation time, there are some models reported in the literature [9, 14–17] to predict the time for cracking of cover concrete. Enright et al. [18] calculated the service life of highway bridges by considering the degradation of the structural performance of corroded structures after the initiation of corrosion.

Liang et al. [19] suggested a simplified methodology to calculate the service life and classified it into three steps viz., corrosion initiation time, de-passivation time, and corrosion propagation time. Wang and Liu [20] offered a streamlined methodology capable of calculating the remaining life of corroded RC beams; this method makes use of the material's damaged qualities and takes partial corrosion's duration and amounts into account. Verma et al. [4] suggested a method to calculate the residual service life of deterioration based on the measured value of depth of chloride content, carbonation depth, and cover concrete for different failure extent. Zhang et al. [21] have classified the service life into corrosion initiation, concrete cracking, serviceable limit, and ultimate limit. Many uncertainties are associated in including the effect of corrosion on the prediction of the service life of RC bridges and deterministic models couldn't account for the uncertainties associated with the different parameters. Huge variations can be seen in the estimated values of service life using deterministic models. Probabilistic models are accounting for the uncertainties in different parameters and hence can lead to rational estimation of service life. To account for the uncertainties associated with the different parameters affecting the service life of structures, researchers [22, 23] suggested different methodologies for the calculation of the service life of structures, but it is very important to account for the service life of the bridge structure situated in the different exposure conditions like mild moderate severe and extreme severe.

In this paper, an effort has been made to identify the random variable associated with the service life of RC bridge piers due to corrosion which includes, the time for initiation of the corrosion, time for the first crack to occur due to corrosion, and time for propagation after first crack for different water-cement ratio and curing condition and for different exposure conditions. Expected values of service life and suitable distribution functions are determined.

2 Service Life Model

Among the various models for service life prediction, one of the widely adopted service life models viz., Tuutti's service life model [24], has been chosen in the present study for characterizing the uncertainty in the service life of bridges. According to Tuutti's model, the service life of the structure before the repair is represented as the summation of Corrosion initiation time and Corrosion propagation time as presented in Eq. 1.

Fig. 1 Schematic diagram
of service life model
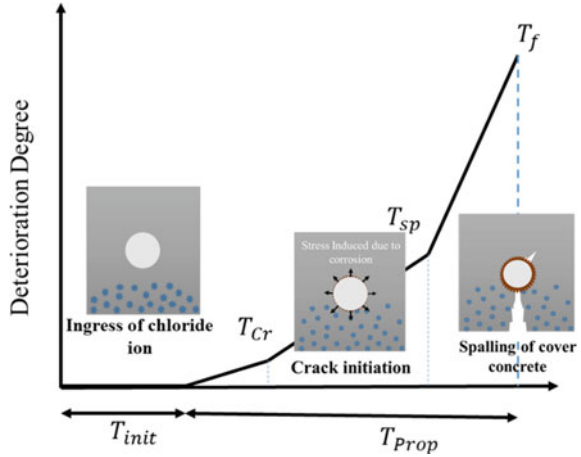
$$T = T_{init} + T_{Prop} \tag{1}$$

where T is the service life of the structure, T_{init} is the corrosion initiation time and T_{Prop} is the corrosion propagation time. The corrosion initiation time depends upon cover depth, water-cement ratio, environmental exposure conditions, material properties as well as curing time, whereas propagation time depends upon the availability of oxygen, water, and chloride ion concentration.

Furthermore, after the initiation of corrosion, it propagates throughout the structure and leads to a reduction in the cross-section as well as changes in the mechanical properties of the reinforcement. Corrosion propagation is the stage where the rusting of reinforcement takes place which imparts sudden changes in the volume of reinforcement, due to the sudden change in the volume the stress-induced inside the concrete causes crack initiation inside the cover concrete. After the initiation of the crack, it widens throughout the cover concrete and leads to spalling of concrete. To study the above effect, corrosion propagation time in Tuutti's models is divided into two parts viz., time for the first crack to occur due to corrosion and time from the first crack formation after initiation of corrosion and upto spalling of cover concrete as shown in Fig. 1.

2.1 Calculation of Corrosion Initiation Time (T_{init})

Researchers [9, 14, 25, 26], have attempted to develop a simple mathematical model for predicting the service life of a structure based on the diffusion of the chloride ion inside the cover concrete for the period of time *t*. Chloride is one of the major causes of concrete degradation. The corrosion initiation depends upon the rate of diffusion of chloride ions through the cover concrete and the diffusion coefficient of materials.

Once the chloride ion penetrates inside the concrete cover and reaches the surface of the reinforcement, the passive layer around the reinforcement gets broken and the corrosion initiation takes place. The diffusion of chloride ion or carbon dioxide ion inside the concrete structure is modeled based on Fick's second law of linear diffusion as presented in Eq. 2 [27].

$$\frac{\partial C}{\partial t} = D \cdot \frac{\partial^2 C}{\partial x^2} \tag{2}$$

where D is the diffusion coefficient of the chloride ions. After solving the above Eq. 2 using Laplace transformation with the initial and boundary condition as presented in Eqs. 3–5. Chloride concentration at depth x over time t is as given in Eq. 6.

$$C(x, 0) = C_i \tag{3}$$

$$C(0, t) = C_s \tag{4}$$

$$C(x \to \infty, t) = C_i \tag{5}$$

$$C(x, t) = C_i + (C_s - C_i)\left\{1 - erf\left(\frac{x}{2\sqrt{Dt}}\right)\right\} \tag{6}$$

where $C(x, t)$ is the concentration of chloride ion at depth x at time t, C_s is the surface chloride concentration, erf is error function and C_i is the initial chloride ion concentration which can be taken as zero.

Once the chloride ion reaches the surface of the reinforcement it initiates the process of corrosion. The time taken for the chloride to reach the surface of the reinforcement is called corrosion initiation time which is estimated using Eq. 7. [28]

$$T_{init} = \frac{d_c^2}{4D}\left\{erf^{-1}\left(1 - \frac{C_{cr}}{C_s}\right)\right\}^{-2} \tag{7}$$

where d_c is the depth of clear cover of concrete, $C(d_c, T_{init}) = C_{cr}$ is the critical chloride concentration at depth of d_c, and D is the diffusion coefficient which depends upon the water-cement ratio, environmental exposure conditions, material properties as well as curing time. As reported by Castaneda et al. [23], uncertainties associated with the diffusion coefficient can be modeled as given in Eq. 8.

$$\log[D(t, \theta)] = \log[D'(t, \theta_c, \alpha_c) + \sigma \tag{8}$$

where $\theta = (\theta_c, \alpha_c, \sigma)$ denote the set of unknown parameter to be estimated by Bayesian Methodology and $\theta_c = (\theta_1, \theta_2, \theta_3 \ldots)$ which are the set of unknown parameters for the calculation of diffusion coefficient, $\alpha_c = \alpha_1, \alpha_2, \alpha_3, \ldots$ are the set

of parameters which are used as correction factors for exposure condition, material properties, curing time water-cement ratio, which are estimated using Bayesian Methodology.

Castaneda et al. [23], have modeled diffusion coefficient D as defined in Eq. 9.

$$[D(t, \theta)] = \exp(\sigma).\alpha_1.\alpha_2.\theta_1, (\theta_2/t)^{\theta_3} \tag{9}$$

Hence, the calculation of Corrosion initiation Time T_{init} (Eq. 7) is modified as specified in Eq. 10.

$$T_{init} = \left[\frac{d_c^2}{4.S.\alpha_1\alpha_2\theta_1\theta_2^{\theta_3}} \left\{ erf^{-1}\left(1 - \frac{C_{cr}}{C_c}\right) \right\}^{-2} \right]^{\frac{1}{1-\theta_3}} \tag{10}$$

2.2 Time for the First Crack to Occur After Initiation of Corrosion (T_cor)

After the initiation of corrosion of the reinforcement, the volumetric expansion of the reinforcement takes place. Concrete surrounded by the reinforcement surface opposes the volumetric expansion of the reinforcement and causes hoop stress in the concrete around the reinforcement as shown in Fig. 2.

Once the hoop stress caused due to corrosion of reinforcement exceeds the tensile strength of concrete the hairline crack is initiated. The time from corrosion initiation time to the first crack to initiate is comparatively low and it can be calculated using

Fig. 2 Initiation of the first crack around the reinforcement
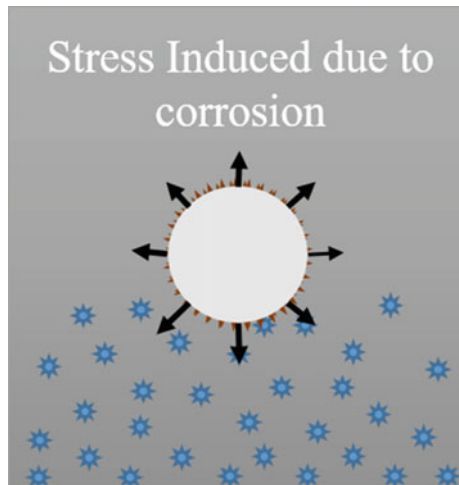
the equation presented by Maaddawy and Soudki [17], as given in Eq. 11.

$$T_{cr} = \left[\frac{7117.5(D_0 + 2d_0)(1 + \vartheta + \varphi)}{i_{corr} E_{eff}} \right] \cdot \left[\frac{2d_c f_t}{D_0} + \frac{2d_0 E_{eff}}{(D_0 + 2d_0).(1 + \vartheta + \varphi)} \right]$$

(11)

where D_0 is the diameter of reinforcement, d_0 is the thickness of porous zone, ϑ is poison's ratio of concrete which is taken as 0.18. φ factor which depends on, D_0, d_c (depth of cover concrete), and d_0 is the thickness of the porous zone is taken in the range of 10–20 μm [17]. φ is calculated using Eq. 12. i_{corr} is corrosion current density and is calculated by using Eq. 13, and φ_{cr} is the creep coefficient the value of the same is taken as 2.35 as suggested in literature[17]. E_{eff} is the effective elastic modulus of concrete and is calculated using Eq. 14.

$$\varphi = \frac{(D_0 + 2d_0)^2}{2d_c(d_c + D_0 + 2d_0)}$$

(12)

$$i_{corr} = \frac{37.8\left(1 - \frac{w}{c}\right)^{-1.64}}{d_c}$$

(13)

$$E_{eff} = \frac{E}{1 + \emptyset_{cr}}$$

(14)

$$\frac{w}{c} = \frac{27}{f_c + 13.5}$$

(15)

where w/c is water content and is calculated by using Bolomey's formula [29–31] as given in Eq. 15. E is the modulus of elasticity of concrete and is obtained as suggested in Indian standard for reinforced concrete structures as $5000\sqrt{f_c}$ [32], $\emptyset_{cr}$ is the creep coefficient of concrete. f_c is the characteristic compressive strength of concrete, f_t is the tensile strength of concrete which is equal to $0.7\sqrt{f_c}$.

2.3 Time from the First Crack Formation After Initiation of Corrosion and Upto Spalling of Cover Concrete (T_{sp})

It has been reported in the literature [33, 34], that 1 mm crack width is sufficient for the delamination of cover concrete. Once the delamination of the cover happens then the reinforcement gets directly exposed to the environment and hence the reduction rate of the cross-section area significantly increases and the structure is assumed to have reached its service life as shown in Fig. 3.

Vu and Steward [33], have proposed Eq. 16 for estimation of time taken from the first crack to spalling of concrete cover.

Fig. 3 Schematic diagram for delamination of cover concrete
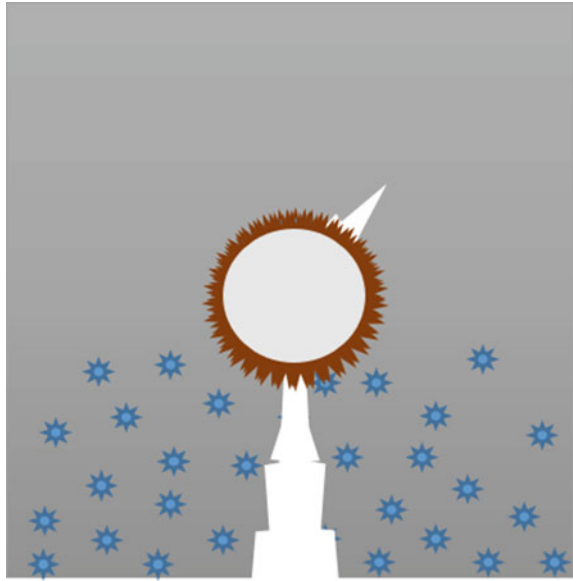
$$T_{sp} = 0.0167 i_{corr}^{-1.1} \left[42.9 \left(\frac{w/c}{d_c} \right)^{-0.54} + \left(\frac{w_{lim} - 0.3}{0.0062} \right)^{1.5} \right] \quad (16)$$

where w_{lim} is the limiting width of cover for cracking and spalling of concrete which is taken as 1 mm.

3 Bridge Pier Considered for Service Life Estimation

A typical bridge pier from the nine-span bridge situated in Chennai (Fig. 4) is considered for the calculation of service life in the present study. The diameter of the bridge pier is 1500 mm, with 50 mm clear cover, compressive strength of concrete used in the pier is M40, and there are 70 numbers of 32 mm diameter reinforcements with 16 mm diameter stirrups at 200 mm C/C spacing.
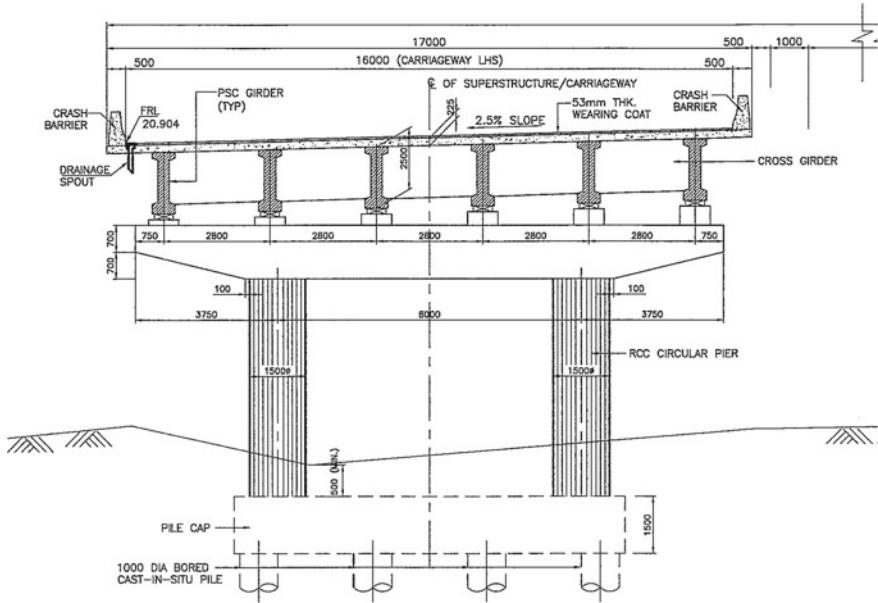
Fig. 4 Reference bridge piers chosen for service life estimation

4 Statistical Modeling of Service Life

4.1 Modelling Uncertainties Associated with T_{init}

In the present study, the clear cover of concrete, critical chloride concentration, surface chloride concentration, and diffusion coefficient are chosen as random variables to account for uncertainties in time for initiation of corrosion. Based on surface chloride concentration, four different severity levels of corrosion are considered in the present study. To model the uncertainty in the diffusion coefficient, five additional random variables are identified from the literature. The mean and standard deviation of different random variables and their distribution function as adopted in the present study are given in Table 1. As reported in the literature water-cement ratio and curing time are the important parameters that influence the corrosion initiation time. In the present study, corrosion initiation times for different water-cement ratios viz., 0.46, 0.53, 0.76, and for different curing times viz., 1 day, 3 days, and 7 days, are considered and the corrosion initiation times have been obtained for four severity levels of corrosion. Depending on the water-cement ratio and curing time nine cases are considered in the present study as given in Table 2. Ten thousand random samples are generated for various random variables using Monte Carlo simulation and corrosion initiation times are estimated. The mean (μ) and standard deviation (σ) of corrosion initiation time obtained for different levels of corrosion for different cases are given in Table 3. The distribution of corrosion initiation time for different severity cases for

the water-cement ratio of 0.46 and curing time of 1 day is typically shown in Fig. 5. Fitting lognormal distribution is found to be passing the goodness of fit hypothesis Chi-Square test for 95% percent confidence level as shown in Fig. 6.

Table 1 Random variable is chosen in the calculation of T_{init}

Parameter	Mean	Standard deviation	Distribution	References	Comments
d_c	50	2.5	Normal	[22]	
Σ	0.008	0.002	Normal	[18]	
θ_1	46	1.001	Normal		
θ_2	1.88	0.339	Normal		
θ_3	0.0547	0.001	Normal		
α_1	1	0.4	Normal		W/c = 0.46
	2.283	0.673	Normal		W/c = 0.53
	2.783	0.984	Normal		W/c = 0.76
α_2	1.265	0.221	Normal		C_d = 24 h
	0.716	0.073	Normal		C_d = 3 days
	0.875	0.090	Normal		C_d = 7 days
C_{cr}	0.04	0.004	Lognormal	[22]	
C_s	0.1	0.01	Lognormal		Mild
	0.2	0.02	Lognormal		Moderate
	0.3	0.03	Lognormal		Severe
	0.4	0.04	Lognormal		Extreme. Severe

Table 2 Different cases considered based on water-cement ratio and curing time

Case	Water cement ratio (w/c)	Curing time (C_d) (days)
1	0.46	1 day
2	0.53	1 day
3	0.76	1 day
4	0.46	3 days
5	0.53	3 days
6	0.76	3 days
7	0.46	7 days
8	0.53	7 days
9	0.76	7 days

Table 3 Mean (μ) and standard deviation (σ) of T_{init} time for different cases in years

Case	Mild		Moderate		Severe		Extreme severe	
	μ	σ	μ	σ	μ	σ	μ	Σ
1	46.19	32.88	18.12	11.17	12.93	8.18	10.65	6.77
2	18.40	11.89	7.24	4.20	5.15	1.57	4.23	2.42
3	16.11	14.63	6.33	5.28	4.51	3.83	3.71	3.12
4	81.92	53.75	32.26	19.28	22.97	13.53	18.92	11.21
5	32.91	21.03	12.93	7.41	9.21	5.23	7.57	4.21
6	28.73	25.30	11.28	8.95	8.04	6.49	6.60	5.27
7	66.48	44.90	26.17	16.00	18.63	11.19	15.34	9.27
8	26.65	17.19	10.47	6.01	7.46	4.23	6.13	3.44
9	23.20	20.11	9.11	7.14	6.5	5.16	5.33	4.2
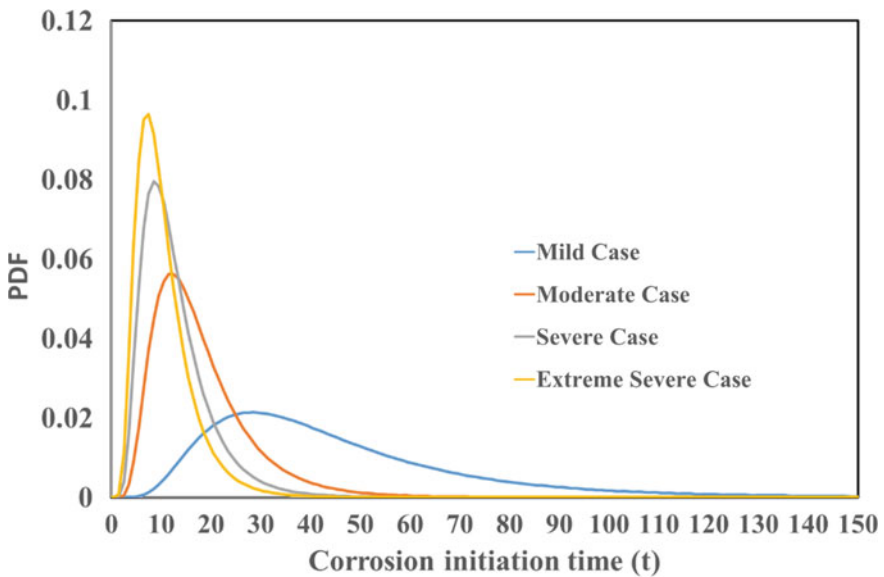
Fig. 5 Case-1 Corrosion initiation time in years for different severity levels for w/c = 0.46 for C_d = 1 day

4.2 Modelling Uncertainties Associated with T_{cr}

In the estimation of time for the first crack to occur after initiation of corrosion, the diameter of reinforcement, compressive strength of concrete (f_c), creep coefficient ($\emptyset_{cr}$), and thickness of porous zone (d_0) around reinforcement are chosen as random variables. The mean, standard deviation, and distribution function as adopted from the literature are given in Table 4. It may be noted that the time before the first crack
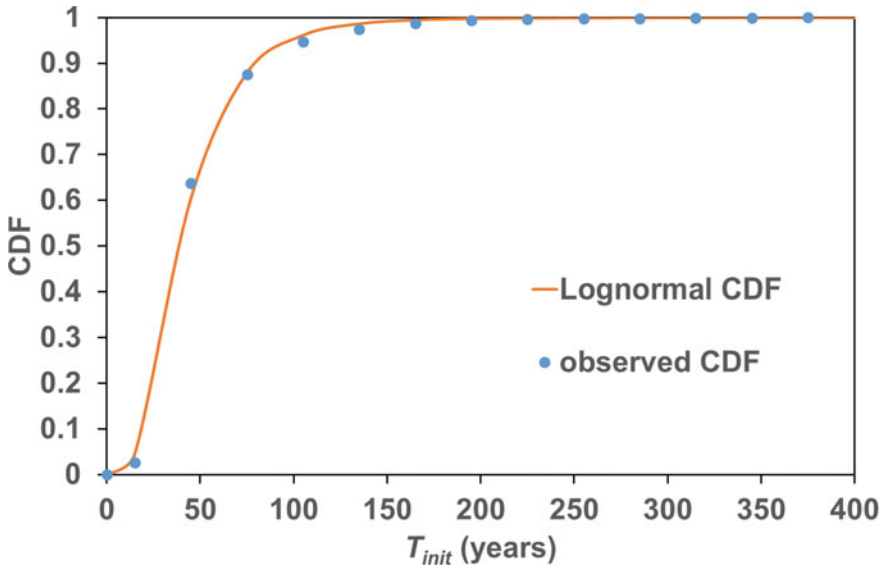
Fig. 6 Goodness of fit hypothesis test for Case-1 w/c $= 0.46$ for $C_d = 1$ day

Table 4 Random variable chosen in the calculation of T_{cr}

Parameter	Mean	Standard deviation	Distribution	References
f_c	40	5	Lognormal	[2]
d_0	0.002	0.0002	Normal	[19]
$\emptyset_{cr}$	2.0	0.02	Normal	[19]

is independent of the severity level of corrosion. Ten thousand random samples for the random variables are generated and T_{cr} values are obtained. Both normal and lognormal distributions are found to be passing the goodness of fit hypothesis Chi-Square test for T_{cr} for 95% percent confidence as shown in Fig. 7.

4.3 Modelling uncertainties associated with T_{sp}

In the modeling of uncertainties in the time from the first crack formation after initiation of corrosion and up to spalling of cover concrete (T_{sp}) corrosion current density, water-cement ratio, and effective area of reinforcement are chosen as random variables. Wherein, water-cement ratio and effective area of reinforcement are derived random variables from the compressive strength of concrete and diameter of the reinforcement. Ten thousand random samples are generated for the random variables and the T_{sp} values are estimated. Both normal and lognormal distributions are found to
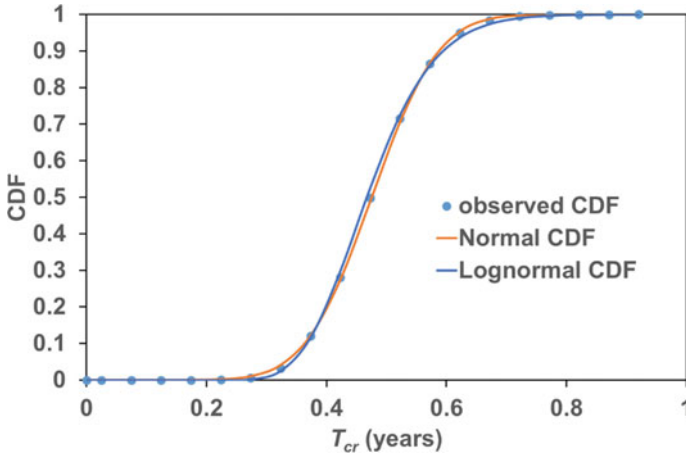
Fig. 7 Goodness of fit hypothesis test for T_{cr} (in years)
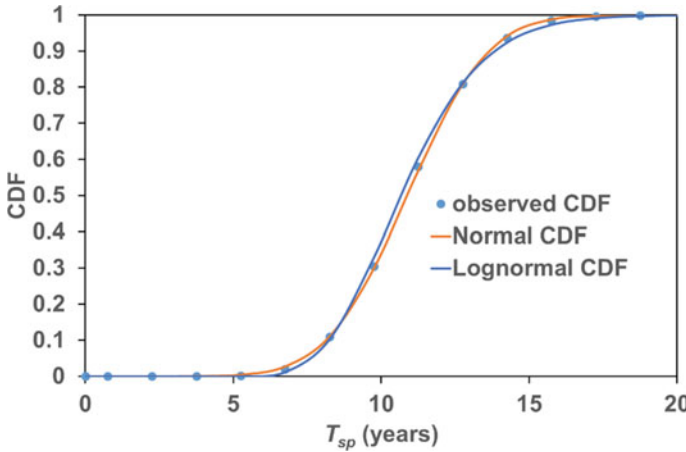
Fig. 8 Goodness of fit hypothesis test for T_{sp} (in years)

be passing the goodness of fit hypothesis Chi-Square test for 95% percent confidence for T_{sp} as shown in Fig. 8.

5   Total Service Life of the Structure

As discussed in the earlier section that the total service life of the structure is obtained as the summation of T_{init}, T_{cr}, and T_{sp} for different severity exposure conditions. Typically, the mean and standard deviation for the total service life of bridge piers

Table 5 Mean (μ) and standard deviation (σ) of the service life of bridge piers in years

Exposure condition	μ	σ
Mild	57.55	33.04
Moderate	29.53	12.01
Severe	24.29	8.58
Extreme severe	22.01	7.01

for the four corrosion severity conditions for $w/c = 0.46$ for $C_d = 1$ day are presented in Table 5.

6 Comparison of Probabilistic Service Life with Deterministic Service Life Model

Bažant's Model [35] has been chosen to calculate the total service life of the structure deterministically. According to Bazant's model, the service life of the structure represented as the summation of corrosion initiation time and corrosion propagation time as presented in Eq. 1.

Bažant [35] proposed a numerical model (Eq. 17) to calculate the corrosion initiation time and the corrosion propagation time. Corrosion initiation time (t_{init}) depend upon the diffusion of the chloride (D) inside the concrete cover to break the passive layer and exposure condition based on the surface chloride concentration (C_s).

$$t_{init} = \frac{1}{12D} \cdot \left(\frac{d_c}{1 - \sqrt{\frac{C_{cr}}{C_{cs}}}} \right)^2 \tag{17}$$

Liang et al. [19] has proposed a numerical model (Eq. 18) to calculate the corrosion initiation time by modifying the Bažant [35] method (Eq. 17).

$$t_{init} = \frac{1}{4D} \cdot \left(\frac{d_c}{1 - \sqrt{\frac{C_{cr}}{C_{cs}}}} \right)^2 \tag{18}$$

where D is calculated from the Eq. 9 by considering the mean of each parameters and d_c, C_s, and C_{cr} are taken as the mean values of the respective parameters from Table 1.

Liang et al. [36] has modified the Bazant's model for calculation of the corrosion propagation time as given in Eq. 19.

$$t_{corr} = \rho_{cor} \cdot \frac{D \cdot \Delta D}{s \cdot J_r} \tag{19}$$

Table 6 Comparison of probabilistic and the deterministic values of service life (in years) calculated for the different exposure conditions

Exposure condition	Probabilistic mean(σ)	Mean − SD $\mu - \sigma$	Mean + SD $\mu + \sigma$	Deterministic Bažant [35]	Deterministic Liang et al. [19]
Mild	57.55	24.51	90.59	29.63	80.42
Moderate	29.53	17.52	41.54	15.46	37.91
Severe	24.29	15.71	32.87	12.74	29.77
Extremesevere	22.01	15.0	29.02	11.57	26.24

where ρ_{cor} is density of the corrosion product, $\rho_{cor} = 3600\,\text{kg/m}^3$ and D is diameter of the longitudinal reinforcement, ΔD is increase in diameter of rebar due to formation of rust, s is spacing between longitudinal reinforcement taken as 30 mm for this case. J_r is the instantaneous corrosion rate calculated from Eq. 20 [3].

$$J_r = \frac{W.i_{corr}}{F} \tag{20}$$

where W—equivalent weight of reinforcement (27.925 g/mol) F—Faraday's constant (96,483.33 Coulombs/mol)

Total service life is computed based on the Bazant et al. deterministic model and the comparison has been made with the values obtained from present study through probabilistic analyses (Table 6).

7 Conclusion

In this paper, the procedure for inclusion of uncertainties in modelling service life of RC bridge piers due to corrosion has been demonstrated by identifying the random variables associated with time for initiation of the corrosion, time for the first crack to occur due to corrosion, and time for propagation after the first crack. Four exposure conditions viz., Mild, Moderate, Severe and Extreme severe are considered for service life estimation, and mean values of service life for the four cases are obtained as 22.03 years, 24.31 years, 29.55 years, and 57.57 years respectively. Fitting lognormal distribution is found to be passing the goodness of fit hypothesis Chi-Square test for 95% percent confidence for time for initiation of the corrosion. Both normal and lognormal distribution is found to be passing the goodness of fit hypothesis Chi-Square test for 95% percent confidence for first crack to occur due to corrosion, and time for propagation after first crack. A comparison of probabilistic and the deterministic values of service life (in years) calculated for the different exposure conditions has also been made. Since huge variations are seen in the estimated values of service life using different deterministic models, probabilistic approach can be adopted for rational estimation of service life of bridge piers. The procedure demonstrated in the study can be adopted for modeling uncertainty in the evaluation

of service life due to corrosion for other components of bridges and also for other critical infrastructure.

References

1. Borah MM, Dey A, Sil A (2020) Service life assessment of chloride affected bridge located in coastal region of India considering variation in the inherent structural parameters. In: Structures, vol 23. Elsevier, pp 191–203
2. Wan X-M, Wittmann FH, Zhao T-J, Fan H (2013) Chloride content and pH value in the pore solution of concrete under carbonation. J Zhejiang Univ Sci A 14(1):71–78
3. Ranjith A, Balaji Rao K, Manjunath K (2016) Evaluating the effect of corrosion on service life prediction of RC structures–a parametric study. Int J Sustain Built Environ 5(2):587–603
4. Verma SK, Bhadauria SS, Akhtar S (2013) Estimating residual service life of deteriorated reinforced concrete structures. Am J Civ Eng Architec 1(5):92–96
5. Garg RK, Chandra S, Kumar A (2022) Analysis of bridge failures in India from 1977 to 2017. Struct Infrastruct Eng 18(3):295–312
6. Vesikari E (2009) Carbonation and chloride penetration in concrete with special objective of service life modeling by factor approach. Research Report VTT-R-04771-09
7. Silvestro L, Andrade JJO, Dal Molin DCC (2019) Evaluation of service-life prediction model for reinforced concrete structures in chloride-laden environments. J Build Pathol Rehabil 4(1):1–11
8. Marques PF, Costa A, Lanata F (2012) Service life of RC structures: chloride induced corrosion: prescriptive versus performance-based methodologies. Mater Struct 45(1):277–296
9. Bažant ZP (1979a) Physical model for steel corrosion in concrete sea structures—theory. ASCE J Struct Div 105(6):1137–1153
10. Cady PD, Weyers RE (1984) Deterioration rates of concrete bridge decks. J Transp Eng 110(1):34–44
11. IRC (2002) An approach document for assessment of remaining life of concrete bridges. Spcl Publ 60-2002
12. Guirguis S (1987) Basis for determining minimum cover requirement for durability. Spcl Publ 100:447–468
13. Hookman CJ (1990) Rehabilitation of Great Lakes steel's No. One Dock. Spcl Publ 122:385–400
14. Morinaga S (1988) Prediction of service lives of reinforced concrete buildings based on rate of corrosion of reinforcing steel. Special report of institute of technology, Shimizu corporation, 23
15. Liu Y, Weyers RE (1998) Modeling the time-to -corrosion cracking in chloride contaminated reinforced concrete structure. ACI Mater J 95(4):445–453
16. Bhargava K, Ghosh AK, Mori Y, Ramanujam S (2006) Analytical model for time to cover cracking in RC structures due to rebar corrosion. Nucl Eng Design 236(11):1123–1139
17. El Maaddawy T, Soudki K (2007) A model for prediction of time from corrosion initiation to corrosion cracking. Cement Concr Composites 29(3):168–175
18. Enright MP, Frangopol DM (1998) Service-life prediction of deteriorating concrete bridges. J Struct Eng 124(3):309–317

19. Liang MT, Huang R, Feng SA, Yeh CJ (2009) Service life prediction of pier for the existing reinforced concrete bridges in chloride-laden environment. J Marine Sci Technol 17(4):312–319
20. Wang X-H, Liu X-L (2010) Simplified methodology for the evaluation of the residual strength of corroded reinforced concrete beams. J Perform Constructed Facilities 24(2):108–119
21. Zhang D, Zeng Y, Fang M, Jin W (2019) Service life prediction of precast concrete structures exposed to chloride environment. Adv Civ Eng
22. Asadi P, Hamed Ranjkesh S, Zeinal Hamedani A (2021) Life-cycle cost analysis of RC bridges subjected to multiple hazards. Scientia Iranica 28(2):629–644
23. Castaneda H, Karsilaya A, Okeil A, Taha MR (2018) A comprehensive reliability-based framework for corrosion damage monitoring and repair design of reinforced concrete structures
24. Tuutti K (1982) Corrosion of steel in concrete. Doctoral dissertation, Lund University
25. Weyers RE (1998) Service life model for concrete structures in chloride-laden environments. Mater J 95(4):445–453
26. Bentz DP, Guthrie WS, Jones SZ, Martys NS (2014) Predicting service life of steel-reinforced concrete exposed to chlorides. Concrete Int 36(9):55–64
27. Liang MT, Huang R, Fang SA (2013) Carbonation service life prediction of existing concrete viaduct/bridge using time-dependent reliability analysis. J Marine Sci Technol 21(1):13
28. Thoft-Christensen P, Jensen FM, Middleton CR, Blackmore A (1996) Assessment of the reliability of concrete slab bridges
29. Vu KAT, Stewart MG (2000) Structural reliability of concrete bridges including improved chloride-induced corrosion models. Struct Saf 22(4):313–333
30. Song S, Qian Y, Liu J, Xie X, Wu G (2019) Time-variant fragility analysis of the bridge system considering time-varying dependence among typical component seismic demands. Earthq Eng Eng Vibr 18(2)
31. Ma Y, Guo Z, Wang L, Zhang J (2020) Probabilistic life prediction for reinforced concrete structures subjected to seasonal corrosion-fatigue damage. J Struct Eng 146(7):04020117
32. Indian Standard (2000) Plain and reinforced concrete-code of practice. Bureau of Indian Standards, New Delhi
33. Vu KA, Stewart MG (2005) Predicting the likelihood and extent of reinforced concrete corrosion-induced cracking. J Struct Eng 131(11):1681–1689
34. Ma Y, Wang L, Zhang J, Xiang Y, Peng T, Liu Y (2015) Hybrid uncertainty quantification for probabilistic corrosion damage prediction for aging RC bridges. J Mater Civ Eng 27(4):04014152
35. Bažant ZP (1979b) Physical model for steel corrosion in concrete sea structures—application. J Struct Div 105(6):1155–1166
36. Liang M-T, Lin L-H, Liang C-H (2002) Service life prediction of existing reinforced concrete bridges exposed to chloride environment. J Infrastruct Syst 8(3):76–85

Deep Neural Network for Time Dependent Reliability Analysis of Structures

Rajyasri Roy, Atin Roy, and Subrata Chakraborty

1 Introduction

The large amount of uncertainty in the occurrence of events like earthquakes, winds, sea storms, etc. are well known. Not only the physical parameters those characterized such loads vary stochastically in both time and space; the structural parameters also show sufficient variability. Stochastic dynamic analysis studies the internal forces, deformations or any other responses to study the behavior of a system. It is important to know whether these responses are within a specified limit to understand the safety of the structure at present and in the long run. The computational techniques leading to uncertainty quantification of stochastic loads involves detailed analysis of a system considering uncertainty in both the load as well as structural parameters. The problem of structural reliability analysis under stochastic dynamic loads is to obtain reliability of the system where the limit state function (LSF) acts as the safety margin.

Monte Carlo Simulation (MCS) technique is the versatile, clear, and accurate method for structural reliability analysis where no partial derivatives of the LSF is required [1]. However, it may become inefficient as the evaluation of LSF needs to be repeated several times. The required number of evaluations to obtain the probability of failure (P_f) may be very large for small order of P_f. These analyses are usually performed with the help of finite element (FE) codes which requires a very high the computation time and cost, especially when the structure exhibits non-linear behaviour or the numerical model is complex.

The application of metamodeling technique to reduce the time consumption for implicit LSFs is notable in this regard. Several approaches have been proposed to construct surrogate model of implicit LSFs e.g., polynomial regression model based response surfaces [2], artificial neural networks (ANNs) [3], support vector machine

R. Roy (✉) · A. Roy · S. Chakraborty
Indian Institute of Engineering Science and Technology, Shibpur, Howrah 711103, India
e-mail: rajyasri0309@gmail.com

(SVM) techniques [4], Kriging technique [5], etc. The application of metamodels to time dependent reliability analysis problems, especially those involving nonlinear dynamic response approximation using FE analysis are not so easy. It is a difficult task as the numbers of input parameters required to approximate the entire input–output relationship is very large. The mentioned metamodels are usually applied to approximate one/few outputs for an input, but unable to deal with time series or spatiotemporal problems involving large number of outputs. They tend to give insufficient accuracy when it comes to complex systems due to their simplicity and attempt to approximate highly nonlinear behavior by lower order polynomials. Hence, these metamodeling techniques are broadly limited to linear or lower order polynomial systems under stationary conditions where applying these methods of modelling highly nonlinear structures is not practically feasible.

Various deep neural network (DNN) algorithms are noted to be quite effective to approximate time varying responses of structures subjected to stochastic dynamic loads. Wu et al. [6] suggested a Convolutional Neural Network (CNN) based approach to estimate the dynamic response of a linear and nonlinear steel frame system. Zhang et al. [7] proposed the use of long short-term memory (LSTM) based model for sequence-to-sequence learning in time series prediction of nonlinear structural response. Oh et al. [8] implemented CNN in predicting seismic response of a building structure by training it through recorded ground motion histories. Kim et al. [9] developed a DNN model in a Bayesian framework in order to quantify the uncertainties rising from varying seismic demand of a structure considering nonlinear behavior under a specific ground motion intensity level. Xiang et al. [10] propose an active learning method that combines the DNN model and weighted sampling method to address the improper selection of experimental points that are used to train the surrogate model. However, majority of the prevailing studies are based on by considering the dynamic load as the only random input parameter assuming the structural system parameters as deterministic. Recently, Kundu et al. [11] proposed an LSTM based DNN algorithm for seismic reliability analysis considering maximum response as the failure criteria.

This study explores an LSTM based DNN algorithm for time dependent reliability analysis of a structure by appropriately considering the random nature of dynamic load as well parameters characterizing the structure.

The feature of functional application program interface available in Keras permits the allocation of various neural network layers aiding in the formation of more complex models. This feature of functional API has been exploited in this study to help incorporate both the stochastic sequence of dynamic excitation as well as the uncertainty of structural parameters. The present approach is illustrated by considering time dependent response approximation and reliability analysis of a corroded beam under random loading. The effectiveness and accuracy of the LSTM model-based approximation is judged with regard to the actual evaluation of the limit state function defining the beam failure. For this, the test samples that are kept aside from the total dataset and never involved in training process are used. For each of the time-dependent response pairs (i.e., the prediction by the proposed approach and the real one), the Pearson's correlation co-efficient is obtained. The reliability analysis

of the beam is conducted by the present approach and also by the more accurate direct MCS method and found to match quite well.

2 Time-Varying Safety Assessment of Structures

Reliability analysis of structure basically considers a load effect S resisted by a resistance R. S and R both are represented by some known probability density function (PDF): $f_S()$ and $f_R()$, respectively and the probability of structural failure is given by:

$$P_f = P[G(R, S) < 0] = \iint\limits_{G<0} f_{RS}(R, S)\mathrm{d}R\mathrm{d}S \tag{1}$$

where G is the LSF, $P[]$ denotes the probability, $f_{RS}()$ represents joint density function and $G < 0$ denotes failure. In time variant domain, the resistance R and the load effect S becomes functions of time t, represented as $R(t)$ and $S(t)$, respectively. The time-dependent LSF is usually expressed in a generalised way as,

$$G(t) = g(\mathbf{X}, \mathbf{F}(t)) \tag{2}$$

where $\mathbf{X}$ is an n-dimensional vector of time-invariant input variables $[X_1, X_2, \ldots, X_n]$ and $\mathbf{F}(t) = [F_1(t), F_2(t), \ldots, F_m(t)]$ is an m-dimensional input random processes as a function of t. $P_f(t) = P[G(t) < 0]$ is indicated as the probability of instantaneous failure at time t. However, this is meaningful only when $G(t)$ decreases with time or if the random load effect is re-applied precisely i.e., the structure experiences a failure cannot be safe again at any future time t. One of the ways of dealing with such problems is to check the probability when $G(t)$ becomes a non-positive number in the lifetime of the structure. The P_f over the time period $[0, T]$ is defined as:

$$P_f(T) = P[g(\mathbf{X}, \mathbf{F}(t), t) < 0 \quad \forall t \in [0, T]] \tag{3}$$

This is based on the first-passage failure probability, i.e., the probability that a stochastic process (here, $G(t)$) crosses a prescribed threshold level (here, zero) at least once during a finite duration (here, $[0, T]$).

The MCS technique is widely used as reliability method for obtaining failure probability. It can directly consider any type of PDF f_x and can be used to compute the P_f with the desired precision. In the MCS technique, N random samples for each random variable of input vector, $\mathbf{X}$ are generated according to the corresponding probability distribution. Then, the number of samples that falls into the failure domain (N_f) (i.e. where $G(X) < 0$) helps in estimating the P_f as,

$$P_f = \frac{1}{N} \sum_{i=1}^{N} I\big(G(X^i)\big) = \frac{N_f}{N} \tag{4}$$

where $I(G(X))$ is indication function which has value 1 if $G(X) < 0$ and 0, otherwise. In case of time-dependent reliability analysis, indication function equals to 1 if $g(X, F(t), t) < 0 \quad \forall t \in [0, T]$ and 0, otherwise.

As already discussed, the repetitive evaluation of LSF is a challenging task for large complex problems and is replaced by a metamodel. DNN based algorithms are found suitable for approximating time-dependent LSF vector. An LSTM model, basically a DNN based algorithm is explored here for this. The related background of DNN is presented first in the next section followed by the proposed LSTM algorithm.

3 Deep Neural Network

3.1 General

Deep Neural Network or Deep Learning is a sub-domain of machine learning based on Artificial Neural Networks and uses algorithms inspired by the structure and function of the brain's neural network. The main advantage of deep learning is the high representational ability of input data, by using various layers to train huge quantity of data and the back-propagation algorithm that indicates how a machine should adjust its internal parameters to successfully apply to the representation. The DNN algorithms in used majorly are the Multilayer Perceptron (MLP), CNNs, Recurrent Neural Networks (RNN) etc. The LSTM algorithm is basically a special case of RNN. Thus, RNN is briefly introduced in the next section for better presentation of the proposed LSTM algorithm.

3.2 Recurrent Neural Network

RNN are a family of DNN for processing sequential data. The sequences can be of variable length. Each element of these sequences is interdependent on each other. RNN memories its action at immediate previous steps to make recurrent connections. In detail, RNN undergoes temporal feedback loops by employing the output of the preceding step as an input for the present step. Thereby, RNN can process sequences of inputs without losing track. The hidden layers comprising the loop related activities are sandwiched between the input layer and the output layer. Each hidden layer treated as an input to produce an output that will be treated as an input in the next layer (*feed-forward passes*). In this process, different hidden layers adapt different weights for their neurons and incrementally a kind of function is built to transform the input layer to the input layer. Then, the error function can be calculated based on

Fig. 1 Typical RNN network
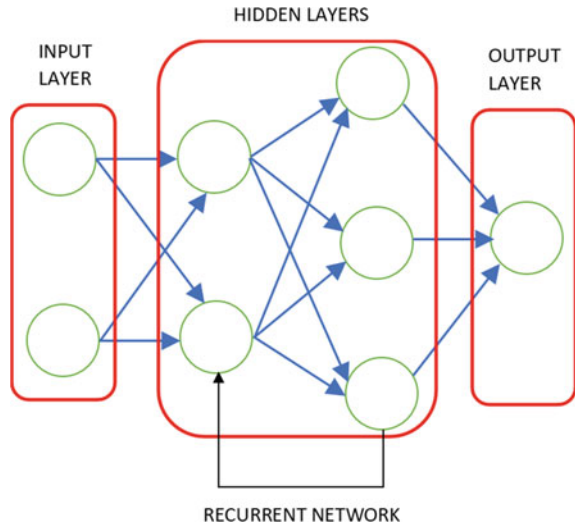
the difference between the values of the approximation function and the actual observation. In the training process, an optimal set of weights is obtained by minimizing their corresponding gradient of error function. The gradient calculation of this error function based on the chain rule method propagates backward from the output layer to the input layer through hidden layers (back-propagation). This process adjusts the synapse weights of different hidden layers and recalibrates with new weights to increase the training accuracy. Figure 1 shows a typical RNN structure.

It can easily be understood from the chain rule method that the gradient of any layer depends on the product of partial derivative of all successive layers. If some of those derivatives approaches a value close to zero then the gradient may vanish (negligible). Further, the multiplication of the gradient with the learning rate (ranging between 0.1 and 0.001) produces a smaller value that practically made no alteration in weights in successive iterations. The issue is known as the vanishing gradient problem. In the same way, the exploding gradient occurs accumulating large gradients that update weights extremely large. Due to the vanishing gradient problem or the exploding gradient problem, is an ordinary RNN is not able to retain the useful gradient information for many time steps. The LSTM algorithm developed by Hochreiter and Schmidhuber [12] tried to solve this problem and to avoid this scaling effect by saving the information for later preventing the older inputs from gradually vanishing during processing. The present study explores LSTM algorithm for response approximation of time-dependent reliability analysis problems. The detail of the LSTM algorithm is presented in the next sub-section.

3.3 Long Short-Term Memory Network

LSTMs are an extension of RNNs that are capable of retaining a long-term memory and are employed for learning patterns in long sequences of dataset. They introduce loops which are able to generate long-duration gradients unlike ordinary RNNs where the memory could retain information only of the preceding steps.

LSTM Cell. A typical deep LSTM architecture consists of multiple hidden layers between the input and output layers. A group of LSTM cells are present in the LSTM layer for mapping the series input sequence to the output sequence. An LSTM cell consists of an independent set of weights and biases in each layer. There are three gates and two states in each cell similar to an ordinary RNN, viz, an input state, a hidden state, an input gate, a forget gate and an output gate. In addition to these, there is an internal recurrence or self-loop which makes up the cell state. The movement of input activation into the internal cell state is controlled by the input gate whereas on the other end, the movement of output activation into the output cell of LSTM is controlled by the output gate. The forget gate regulates the LSTM cell to overlook or reset the memory of the cell as and when required. The most important component of an LSTM cell is the state unit or the cell state which helps to memorize the information obtained in the preceding time step through the internal recurrent loop.

Let us consider a time step t where $t = 1, 2, ..., n$ ($n =$ total number of time steps); and the l-th LSTM module. The corresponding states and gates are denoted as: input state: x_t^l; forget gate: f_t^l; input gate: i_t^l; output gate: o_t^l; cell state: c_t^l; hidden state: h_t^l. The above variables are related to each with the help of various weights and biases. The relationships can be summed up as follows.

$$f_t^l = \sigma\left(W_{xf}^l x_t^l + W_{hf}^l h_{t-1}^l + b_f^l\right)$$
$$i_t^l = \sigma\left(W_{xi}^l x_t^l + W_{hi}^l h_{t-1}^l + b_i^l\right)$$
$$\tilde{c}_t^l = \tanh\left(W_{xc}^l x_t^l + W_{hc}^l h_{t-1}^l + b_c^l\right)$$
$$o_t^l = \sigma\left(W_{xo}^l x_t^l + W_{ho}^l h_{t-1}^l + b_o^l\right)$$
$$c_t^l = f_t^l \odot c_{t-1}^l + i_t^l \odot \tilde{c}_t^l \quad h_t^l = o_t^l \odot \tanh\left(c_t^l\right) \tag{5}$$

where $W_{\alpha\beta}^l$ represents the weight matrices corresponding to different inputs to different gates, b_β^l represents the corresponding bias vectors, $\tilde{c}_t^l$ denotes a vector of intermediate candidate values created by a tan$h$ (hyperbolic tangent function) layer, σ is the logistic sigmoid function, and $\odot$ denotes the Hadamard or element-wise product.

Figure 2 show a typical LSTM cell. The input to the LSTM cell comprises x_t^l, c_{t-1}^l, h_{t-1}^l and the output comprises c_t^l, h_t^l which signifies that the lth layer of an LSTM cell feeds on the input data at the current step (which is the output data of the preceding step) as well as the cell state and hidden state data of the previous step; and the hidden state and cell state data of the current step is provided as output. The cell inputs x_t^l and h_{t-1}^l eventually passes through the forget gate (sigmoid function)
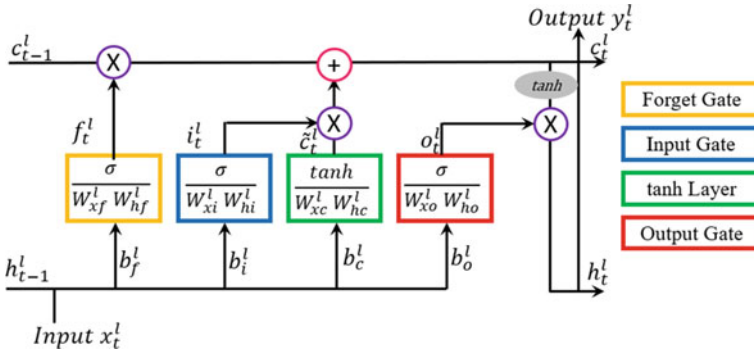
Fig. 2 An LSTM cell

and generates a vector with values ranging from 0 to 1. This vector guides whether the information from the cell state (c_{t-1}^l) is to be retained or forgotten. 0 implies that the information is completely forgotten and 1 implies that the complete information is still memorised. New information, if required, is then added to the cell state (c_{t-1}^l) through both input gate (sigmoid function) and a hyperbolic tangent function and the new cell state is updated by adding the two subsequent parths together. The new cell state (c_t^l) is then scaled within $[-1, 1]$ by a hyperbolic tangent function (tan$h$) and controlled by a sigmoid function through the output gate in order to output the hidden state h_t^l of the LSTM cell.

LSTM Architecture. An LSTM network is consisting of LSTM layer(s) along with the fully connected (FC) or dense layers. A typical LSTM layer consists of many LSTM cells or nodes. Each such node in the layer is exposed to the input data from the input order and associated output.

A representative sequential LSTM architecture consists of an input series which is processed one step at a time. Each input node results into an output which is passed to the following LSTM cell at the next layer. It also results into an internal cell state which is carried forward to the next cell of the same layer. The cell state remains fixed within a particular layer. The dense or FC layers enables the LSTM network to map the target output from the LSTM layer to the output layer. Dropout layer may be added where there may be a problem of overfitting. During the time of defining the architecture of LSTM in Keras, a finite number of nodes is allocated in a particular layer which functions as the size of a window of the memory which apprehend the dependence of linear and nonlinear behaviour of the sequence and slides along the sequence length. The number of nodes in the layer is unrelated to the length of the time steps in the input sequence though node number decides the dimension of the feature of the generated output of the corresponding LSTM layer. By default, in Keras, only the last output from the end of the sequence is treated as the output which can be changed such that the output is generated from each input time step, resulting a sequence of outputs. This is called the sequence-to-sequence learning.

4 Time-Dependent Reliability Analysis of a Corroded Beam by LSTM Based Metamodeling Approach

4.1 Problem Definition

The problem under study considers reliability analysis of a steel corroded beam [13]. The length of the beam (L) is taken as 10 m. The beam is assumed to be corroding with time. The corrosion is considered to be isotropic around the rectangular cross section of the beam. Schematic diagram of the corroded beam is shown in Fig. 3.

The dimension of the cross-section decreases with time which can be modelled as follows

$$a(t) = a_0 - 2\omega t, \quad b(t) = b_0 - 2\omega t \tag{6}$$

where a_0 and b_0 are the initial cross section of the beam, $\omega = 5 \times 10^{-5}$ m/year is the rate of corrosion. The beam experiences gravitational load and a time variant stochastic load. The unit weight of the material of the beam is $\rho_{st} = 7.85 \times 10^{-4}$ N/m^3. The beam failed when the maximum bending moment exceeds the allowable bending moment. The corresponding LSF becomes,

$$G(X, F(t), t) = \frac{a(t)b^2(t)}{4}\sigma_u - \left(\frac{F(t)L}{4} + \frac{\rho_{st}a_0b_0L^2}{8}\right) \tag{7}$$

where σ_u is the yield strength of steel and $\mathbf{X} = [\sigma_u, a_0, b_0]^T$. In the above problem, the variables σ_u, a_0, b_0 and $F(t)$ are considered random; the probabilistic characteristic of which are furnished in Table 1. The distributions of variables, a_0, b_0 and σ_u are truncated between thrice standard deviation from their mean. The co-variance matrix for the time dependant stochastic load is given as:

$$\sum (t_i, t_j) = 700 \exp\left(-(t_i - t_j)^2\right) \tag{8}$$

The time interval is uniformly discretised into 101 time instants between [0, 20], i.e., $t_0 = 0$, $t_{101} = 20$, and $t_k - t_{k-1} = 0.2$ where ($k = 1, 2, ..., K$).

Fig. 3 Schematic diagram of the corroded beam

Table 1 Statistical characteristics of random variables

Variable	Type of distribution	Mean	Standard deviation	Co-variance matrix
σ_u (Pa)	Lognormal	2.4×10^8	2.4×10^7	–
a_0 (m)	Lognormal	0.2	0.01	–
b_0 (m)	Lognormal	0.04	0.004	–
$F(t)$ (N)	Gaussian process	3500	–	Equation (8)

4.2 Proposed LSTM Model

In the proposed LSTM model, there are four input vectors. The first input is a time variant stochastic load vector of length n denoted as $X^1 = \left[x_1^1, x_2^1, ..., x_n^1\right]^T \in \mathbb{R}$. The output is the response to the LSF denoted as $Y = \left[y_1^1, y_2^1, ..., y_n^1\right]^T \in \mathbb{R}$. The primary concern with the multiple input parameters is the variation in the dimension and nature of the input space. The stochastic inputs of the LSF are single point scalar quantities unlike the stochastic time variant load. Each of these are transformed to a vector having size of *n*. They include the remaining three input vectors, X^2, X^3 and X^4.

The sequential API feature of Keras has been utilized in the proposed LSTM model. This feature allows to create models layer-by-layer. A sequential model of a typical LSTM network is unidirectional, having layers starting from an input layer followed by the multiple LSTM-layers stacked over each other, and each consists of definite numbers of LSTM cells. Dropout layer follows the LSTM layers to check over-fitting, followed by an output layer.

In the present study, a dynamic load vector of time step of 101 is considered. Now, two successive LSTM layers are considered each having 100 LSTM cells/nodes. Number of cells represents the number of recurrent unrolling operation of the LSTM module. The parameters governing the LSF viz. initial depth (a_0), initial width (b_0) and the yield strength (σ_u) are incorporated as vectors of length 101. These scalar inputs are also fed into the two successive LSTM layers similar to the first input. The outputs obtained from the 4 set of LSTM layers are then concatenated so that the parameters of the LSTM and dense layers can be shared. This concatenation results in a vector of size 101 × 400 which is followed by two dense layers, the first one reduces the feature dimension to 101 × 100. A third dense layer reduces it to 101 × 1 i.e. the output vector dimension. The Proposed LSTM Architecture is shown in Fig. 4. To feed the data into the network, the data set is arranged in three-dimensional format to represent the number of samples for training phase, number of time steps and number of features.

The training is done on the Google Colaboratory platform which is a free Jupyter Notebook environment that runs entirely on cloud. LSTM models require Graphics Processing Units (GPUs) for faster training. The Google Colaboratory comes with free limited GPU which not only helps in cutting down the cost of expensive GPUs required, but also makes the performance/training much faster. It can be accessed
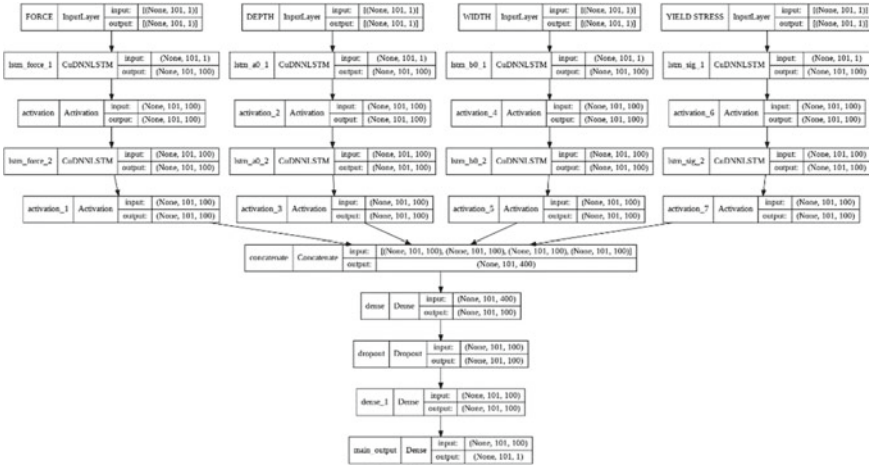
Fig. 4 Proposed LSTM architecture

from any computer with an installed browser and with a proper internet connection. Keras is applied to train the neural network model. This high-level open-source library is designed for easy human interpretation of deep neural networks using Python programming language. It acts as an interface for TensorFlow library, which is an open-source machine learning platform offering in easy numerical computation fast prototyping of neural networks, developed by Google Brain Team.

It offers flexibility of data flow architecture that enables high-performance training of different types of neural networks in a variety of platforms e.g., CPUs, GPUs and TPUs.

4.3 Data Preparation

The stochastic time variant load vector $F(t)$ and the corresponding response of the LSF have been generated using MATLAB platform. The co-variance matrix given by Eq. (8) is first constructed. The discretisation of the stochastic process is performed by Optimal Linear Estimation (OLE) method [14]. It is based on the OLE and is proved to be more efficient than the commonly adopted midpoint method, spatial averaging method, shape function method, series expansion method, etc. Optimal estimation is a regularized matrix inverse method based on Bayes' theorem. The efficiency of the method can be greatly improved by using spectral decomposition of the nodal co-variance matrix; the corresponding method is known as the expansion OLE (EOLE) [13].

Let us denote the mean function and co-variance function of the stochastic process (here, the time variant load $F(t)$) by $\mu^{(m)}(t)$ and $\Sigma^{(m)}(t, t')$. Here, m signifies a random stochastic process from a pool of M stochastic processes. Let the m-th load vector

be denoted as $F^{(m)}(t)$. According to the principle of Gaussian Processes, $\overline{F}^{(m)} = \left[F^{(m)}(t_0), \ldots, F^{(m)}(t_K)\right]$ is subjected to a multivariate normal distribution with the mean vector $\mu_{\overline{F}^{(m)}}(t) = \left[\mu^{(m)}(t_0), \ldots, \mu^{(m)}(t_K)\right]$ and co-variance matrix $C_{\overline{F}^{(m)}(t)}$ given by Eq. (8). Now, $K + 1$ time instants are selected to discretise the process $[F^{(m)}(t)]$. The EOLE expansion gives [13]:

$$F^{(m)}(t) \approx \mu^{(m)}(t) + \sum_{i=1}^{r} \frac{\zeta_i}{\sqrt{\lambda_i}} \phi_i^T C_{\overline{F}^{(m)}(t)} \tag{9}$$

Here, $i = 1, 2, \ldots, r \leq K + 1$. ζ_i are mutually independent and subjected to standard normal distribution. ϕ_i and λ_i are the eigenvectors and eigenvalues of the co-variance matrix $C_{\overline{F}^{(m)}(t)}$. After obtaining the load vector, $F(t)$ from Eq. (9), it is fed into the LSF, $G(t)$ given by Eq. (7).

Dataset consisting of 500 input–output pairs are prepared for training. In doing this, 500 samples for each scalar parameter (i.e., σ_u, a_0, b_0) are generated using Latin Hypercube Sampling (LHS) technique as random uniform variables within their truncation limits [15]. These variables are distrusted as truncated lognormal to ensure good prediction performance over the entire input space. It can be noted here that a good prediction performance at each location of the input space is important as the failure plane is not known a priori. Now, 500 load vectors are generated to get corresponding vectors of the LSF. The input data and output data so prepared is represented in the form of a 3-D array for proper feeding into the LSTM network. A flow chart of data preparation is shown in Fig. 5.
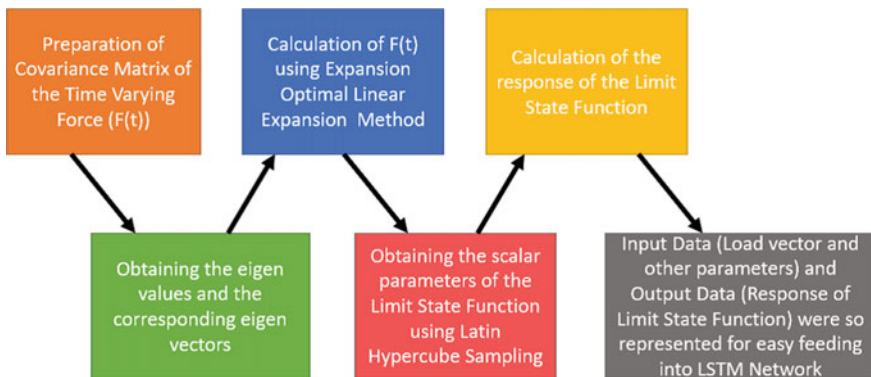
Fig. 5 Flow chart of data preparation

4.4 Training of the LSTM Model

Proper training of the neural (here, LSTM) network described in Sect. 4.2 is an important task. It requires meticulous selection of the hyperparameters required for training the neural network. The hyperparameters include the number of LSTM layers, presence of dropout layer (if required), number of LSTM cells per layer, the type of optimiser, the learning rate, the decay rate, batch size, etc. With the help of the MinMaxScaler available in the SciKit-Learn Library, the entire dataset was scaled in the range of [0, 1]. SciKit-Learn is a Library that features various machine learning algorithms. In the initial stage of the study, the training has been done with the help of arbitrary values of these parameters within the acceptable range. The activation function considered was ReLU. A learning rate of 0.001 and decay rate of 0.00001 is adopted as suggested as default in the Keras Library. A batch size of 32 is used for the first set of training. A batch size of n implies n samples of the training dataset will be shown to the network at a time to evaluate the gradient of the loss function and the learnable parameters (e.g., weights and biases) will be updated accordingly. The number of neurons is taken as 100 for the initial training. Number of neurons adopted in a layer controls the network's representational capacity. Dropout layer is not provided in the initial round of training. Using an epoch of 4000, the validation loss obtained is 2.7484×10^{-5}.

4.5 Results and Observations

The initial dataset is divided into three parts for the purpose of training, validation and test. From the 500 data generated, 10% (i.e., 50 data) is kept aside for the purpose of test. The remaining 90% of the dataset is further divided into 2 parts in the ratio of 8:1 to make the training dataset and the validation dataset. After the model is trained with the help of the training dataset and the validation dataset, the initially kept aside test dataset is used to test the model. For a particular input from the test dataset, the original response and the predicted response are compared. Four such comparisons are shown in Fig. 6. A good match between predicted response and original response is observed over the entire time span. The similar observations are also noted in case of other test data.

The cross-correlation function or Pearson's correlation function [16] commonly used to study the matching between two time series is further obtained. For two time-series $\{a_1, \ldots, a_n\}$ and $\{b_1, \ldots, b_n\}$, the cross-correlation coefficient (r) is defined as,

$$r = \frac{\sum_{i=1}^{n} (a_i - \overline{a})(b_i - \overline{b})}{\sqrt{\left(\sum_{i=1}^{n} (a_i - \overline{a})^2\right)\left(\sum_{i=1}^{n} (b_i - \overline{b})^2\right)}}, \quad \overline{a} = \sum_{i=1}^{n} a_i, \ \overline{b} = \sum_{i=1}^{n} b_i \qquad (10)$$
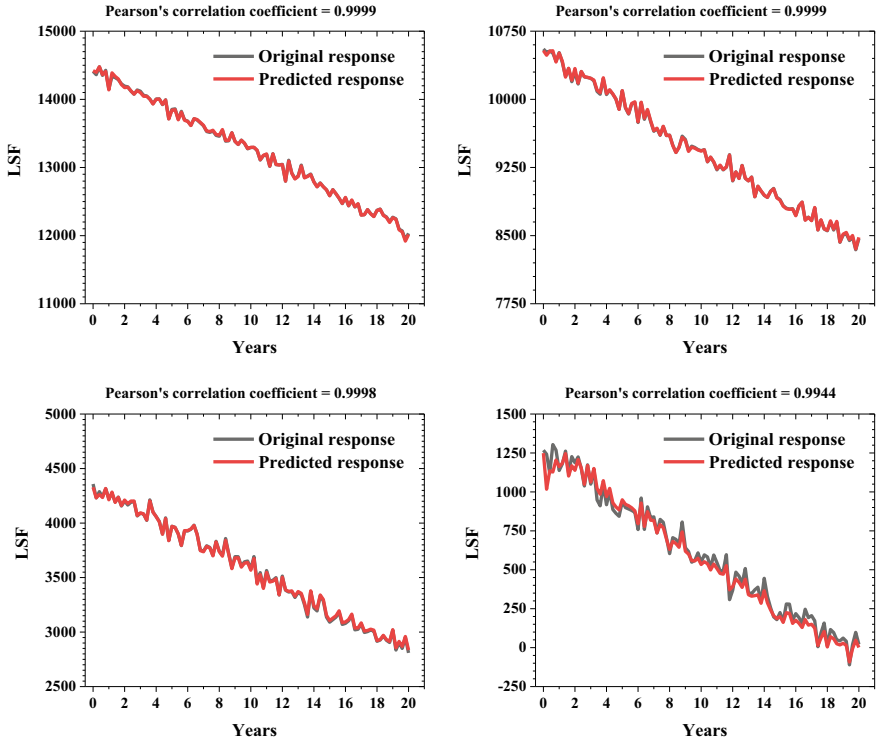
Fig. 6 Comparison of predicted response with original response at four different test data

The cross-correlation coefficient or Pearson's correlation coefficient is calculated for each of the fifty-test data. A histogram of Pearson's correlation coefficient is presented in Fig. 7. A closer value of Pearson's correlation coefficient to unity indicates a better quality of approximation. Out of 50 test data, 42 pairs of original and predicted time series of LSF are between 0.9995 and 1.0. The minimum value of Pearson's correlation coefficient is noted as 0.9944. This clearly indicate the capability of the proposed approach to approximate stochastic dynamic responses.

To study the performance of the proposed LSTM model for time-dependent reliability analysis, the failure probability is obtained based on the LSF values predicted by the proposed LSTM model. In doing so, one lakh samples are generated for each random truncated lognormal variable, σ_u, a_0, b_0. Using Eq. (9), one lakh random load vectors are generated according to distribution as described in Table 1. The reliability results are also obtained by the direct MCS method. The P_f values over time interval of [0, T] obtained by both the methods are presented in Table 2 for T = 15, 16, 17, 18, 19 and 20 years. It is observed from the table that failure probabilities of both methods are close for different time intervals.

Fig. 7 A histogram of
Pearson's correlation
coefficient for 50 test data
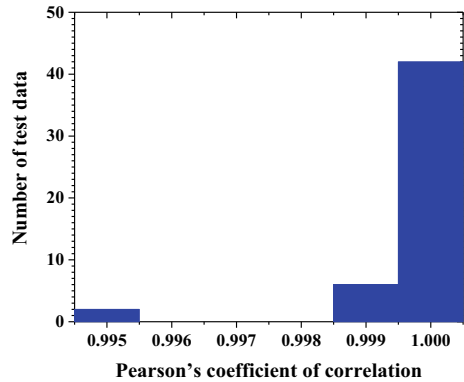
Table 2 Comparison of reliability results

Method	P_f over time interval of [0, T] years					
	15	16	17	18	19	20
Direct MCS	0.0018	0.00202	0.00231	0.0026	0.0028	0.00311
Proposed LSTM	0.0015	0.00172	0.00196	0.00236	0.00267	0.00282

5   Conclusion

An LSTM model is developed to approximate the time-dependent LSF of a corroded
steel beam. A satisfactory accuracy of LSTM model prediction is observed on test
data which is not used in the training process. For those test data, the Pearson's
correlation coefficient is calculated and found to be excellent. A good accuracy in
predicting response time history of the beam is noted for all the test samples. Finally,
P_f values over different time span are obtained based on the proposed LSTM model
predictions. Results are quite close to the reference results obtained by the direct
MCS method clearly reveals its capability of estimating time dependent reliability of
structures. However, the present study is restricted to a simple beam problem having
explicit LSF. It needs to be explored for more realistic non-linear dynamic response
analysis and reliability estimate problems involving FE analysis of structure.

References

1. Ditlevsen O, Madsen HO (2005) Structural reliability methods. Wiley, 372
2. Box GEP, Wilson KB (1951) On the experimental attainment of optimum conditions. J R Stat
   Soc Ser B 13:1–38
3. Hosni Elhewy A, Mesbahi E, Pu Y (2006) Reliability analysis of structures using neural network
   method. Probabilistic Eng Mech 21:44–53

4. Ghosh S, Roy A, Chakraborty S (2018) Support vector regression based metamodeling for seismic reliability analysis of structures. Appl Math Model 64:584–602
5. Ghosh S, Roy A, Chakraborty S (2021) Kriging metamodeling-based Monte Carlo simulation for improved seismic fragility analysis of structures. J Earthq Eng 25:1316–1336
6. Wu R-T, Jahanshahi MR, Asce AM (2018) Deep convolutional neural network for structural dynamic response estimation and system identification. J Eng Mech 145:04018125
7. Zhang R, Chen Z, Chen S, Zheng J, Büyüköztürk O, Sun H (2019) Deep long short-term memory networks for nonlinear structural seismic response prediction. Comput Struct 220:55–68
8. Oh BK, Park Y, Park HS (2020) Seismic response prediction method for building structures using convolutional neural network. Struct Control Heal Monit 27:e2519
9. Kim T, Song J, Kwon OS (2020) Probabilistic evaluation of seismic responses using deep learning method. Struct Saf 84:101913
10. Xiang Z, Chen J, Bao Y, Li H (2020) An active learning method combining deep neural network and weighted sampling for structural reliability analysis. Mech Syst Signal Process 140:106684
11. Kundu A, Ghosh S, Chakraborty S (2022) A long short-term memory based deep learning algorithm for seismic response uncertainty quantification. Probabilistic Eng Mech 67:103189
12. Hochreiter S, Schmidhuber J (1997) Long short-term memory. Neural Comput 9:1735–1780
13. Wang J, Cao R, Sun Z (2021) Importance sampling for time-variant reliability analysis. IEEE Access 9:20933–20941
14. Chun-Ching Li B, Der Kiureghian A (1993) Optimal discretization of random fields. J Eng Mech 119:1136–1154
15. Santner TJ, Williams BJ, Notz WI (2018) Space-filling designs for computer experiments. In: The design and analysis of computer experiments. Springer, New York, NY, pp 145–200
16. Cassisi C, Montalto P, Aliotta M, Cannata A, Pulvirenti A (2012) Similarity measures and dimensionality reduction techniques for time series data mining. In: Advances in data mining knowledge discovery and applications. InTech, Rijeka, Croatia, pp 71–96

Crack Growth Life Prediction in API 5L X46 Grade Steel Pipes Subjected to Cyclic Internal Pressure

S. Vishnuvardhan, A. Ramachandra Murthy, M. Saravanan, and P. Gandhi

1 Introduction

Oil and gas transportation pipelines experience cyclic pressure leading to failure by fatigue. Welded joints in the pipelines are the regions where fatigue cracks are expected to initiate and propagate due to increased stress concentration in view of inclusions and weld defects. In general, pipelines are prone to different failure modes such as plastic collapse by gross plastic deformation, fatigue failure due to cyclic internal pressure, buckling and post buckling instability under external pressure as well as interaction of stress corrosion and defects [1, 2]. The main problem associated with oil and gas transportation pipelines are (a) sweet corrosion, (b) sour corrosion and (c) microbiologically influence corrosion (MIC), which leads to pitting corrosion [3, 4]. Zheng et al. [5] studied the fatigue crack initiation life and the influence of pre-deformation on fatigue crack initiation life using single edge notch specimens machined from deformed X60 steel pipeline. Azevedo [6] investigated crack nucleation and propagation in API X46 grade crude oil pipeline and found that the crack nucleation on the internal surface of the pipeline was promoted by the presence of welding defects and corrosion pits, and propagated in a stable manner in both longitudinal and radial direction and later along the heat affected zone of the pipeline. The nucleation of the primary crack was found to be promoted.

Liu et al. [7] proposed a finite element method and evaluated the fatigue life of X65 steel buried natural gas pipeline under cyclic internal pressure and vibrating loads. Liu et al. [8] conducted failure analysis on API X65 steel natural gas pipeline buried at a depth of 1200 mm with diameter and thickness of 813 and 12.5 mm and predicted the load-bearing capacity of the pipeline by 3D finite element analysis using ABAQUS. Hasan et al. [9] studied the failure of an 18-inch diameter gas pipeline caused by

S. Vishnuvardhan (✉) · A. Ramachandra Murthy · M. Saravanan · P. Gandhi
CSIR—Structural Engineering Research Centre, Chennai 600 113, India
e-mail: svvardhan@serc.res.in

83

stress corrosion cracking (SCC) influenced by the coal-tar based coating. Hamid Reza Hajibagheri et al. [10] carried out inspection of a 6-inch diameter seamless steel pipeline, which was primarily used for transmitting oil and was later repurposed for transmitting gas. Cracks up to a depth of 100 µm were observed on the surface and propagated inwardly and no cracks of stress corrosion cracking (SCC) and hydrogen induced cracking (HIC) type were present. Nguyen et al. [11] conducted fracture toughness and fatigue crack growth rate (FCGR) tests on X70 pipeline steel base and weld metals under 10 MPa of a natural/hydrogen gas mixture with 1% H_2 blend. A significant reduction in the fracture toughness and accelerated fatigue crack growth rates were observed in both the metals under the gas mixture with 1% H_2 blend compared with the tests conducted in ambient air. Jiao and Shuai [12] conducted cyclic pressure studies on long distance transmission pipelines and it was observed that the cyclic pressure is one of the main reasons of pipeline damage. Rainflow counting method could be used to resolve the pressure cycles and an appropriate pipeline maintenance scheme could be adopted for considering the cyclic pressure.

Ghaednia et al. [13] studied the effect of crack depth on burst strength of X70 pipeline with combined dent-crack defect. It was observed that the combined dent-crack defect with crack depth of 75% of wall thickness could reduce the pressure capacity by 54%. A pipeline material fatigue crack growth database was developed using fatigue crack growth rate tests conducted on base and weld materials of different pipeline steel grades ranging from X46 to X70 under two different stress ratios. It was reported that the crack growth rates in the pipeline steels tested were two to three times lower than the crack growth rates recommended in BS 7910 [14]. Tewari and Agarwal [15] investigated the failure of an in-service pipeline. Pipeline failed from its longitudinal seam, failure initiated from heat affected zone (HAZ) when the pipeline was in operation. The failure occurred much below the maximum allowable operating pressure (MAOP) of the Pipeline. The pipeline was operating pressure at 77 kg/cm^2 against the MAOP was 91.4 kg/cm^2. After examination, the pipe seam weld was reported to be affected by fatigue and that the failure might have initiated from a crack at the internal surface of the pipe.

In the present studies, crack growth life of API 5L X46 grade steel in-service pipes subjected to cyclic internal pressure was evaluated experimentally. Numerical studies were carried out on the pipes under cyclic internal pressure and stress intensity factor was evaluated by varying crack length and depth. SIF for different crack depths was also evaluated analytically using the expressions available in API 579/ASME FFS-1 and ASME B&PV Code Section XI Division I. Employing Paris' crack growth model and crack growth constants reported in the literature for API 5L X46 grade steel, number of cycles to failure was predicted both numerically and analytically.

2 Details of Pipe Specimens

The pipe specimens used in the present studies were made of API 5L X46 Grade steel conforming to API 5L [16]. The pipe specimens of 4.0 m length with different defect profiles cut removed from in-service pipe line were used. The nominal outer diameter and thickness of the pipe specimens were 14″ (355.6 mm) and 7.14 mm respectively. Based on the intelligent pigging measurements carried out in the field, one pipe was detected to contain a longitudinal seam crack of 32 mm length and 2 mm depth and the other pipe was detected to contain two lamination defects of different sizes. Length and width of one lamination was 644 mm and 121 mm respectively. Length and width of the other lamination was 967 mm and 228 mm respectively.

3 Experimental Studies

The pipe specimens were welded with curved blind flanges at both the ends. Two threadolets were provided in the pipe specimens at a distance of 200 mm from the weld centre. Threadolet is an opening given in the specimen with threads inside and a bolt is used for opening or closing it. This provision was used to fill the specimen with hydraulic oil and apply the desired internal pressure. The pipe specimens were instrumented with two element rosette strain gauges to study the variation of strains during cyclic pressure test. Strain gauges were mounted on the pipe specimen at two different cross-sections along the length of the pipe viz, centre of defect location and middle of pipe specimen. In the case of pipe specimen containing lamination defect, strain gages were also mounted at the edge of defect. Figure 1 shows details of pipe specimens, defect details and location of strain gauges.

The pipe specimens were filled with hydraulic oil and subjected to a cyclic pressure of 5–77 kg/cm^2 and then back to 5 kg/cm^2. The pressure cycle simulates one day of actual operation in a typical oil pipeline in India. The cyclic pressure was applied on the pipe specimen using a slave hydraulic cylinder connected to the $\pm$ 500 kN capacity servo-hydraulic Universal Testing Machine. Figure 2 shows the set-up for cyclic pressure test on a pipe specimen. Figure 3 shows a typical pressure cycle. The rate of loading was one cycle per minute. The cyclic pressure tests were carried out till failure of the pipe specimens. During the cyclic pressure tests, load, load-line displacement and strains at different locations were monitored using a high-speed data acquisition system.
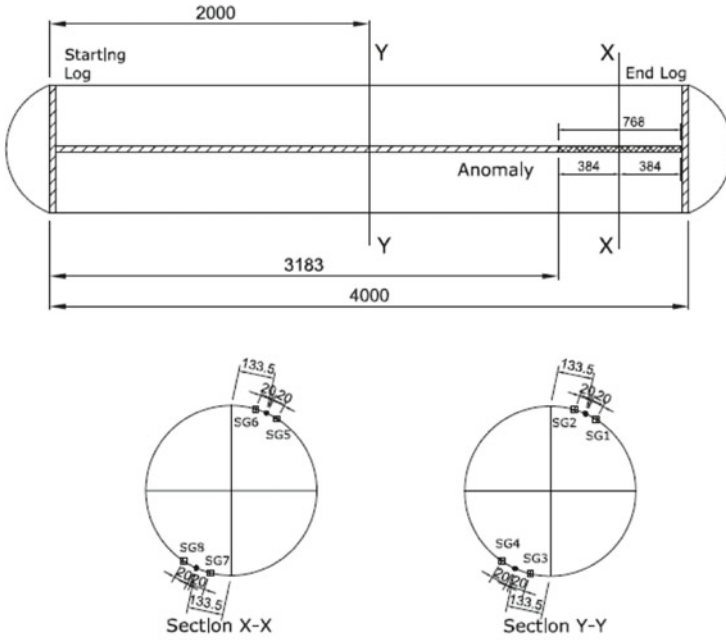
(a) Specimen with longitudinal seam crack
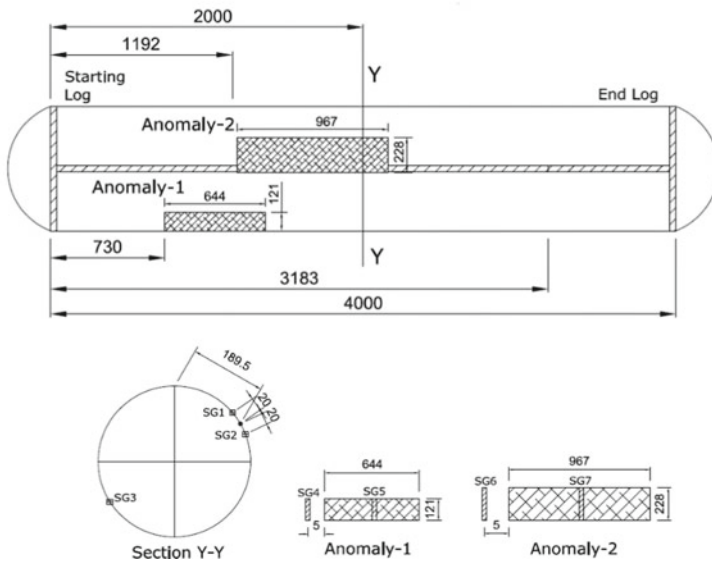
(b) Specimen with lamination defects

Fig. 1 Details of pipe specimens, defect details and location of strain gauges

Fig. 2 Set-up for cyclic pressure test on a pipe specimen
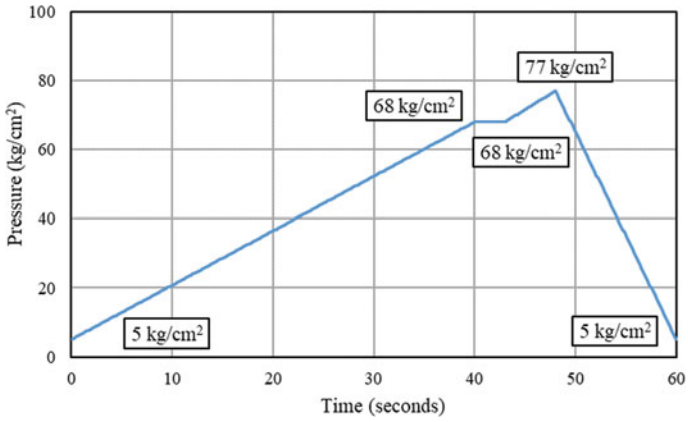
Fig. 3 Typical pressure cycle

4   Numerical Studies

Numerical studies have also been carried out on pipe containing longitudinal seam crack under cyclic internal pressure and stress intensity factor values are evaluated. Pipe dimensions and crack details are same as the one that is used in experimental investigations. Both the ends of the pipe are considered to be fixed and the defect is modeled as internal elliptical crack. Centre of the crack is located at 1780 mm from one end of the pipe. Young's modulus and Poisson's ratio are taken as 200 GPa and 0.3 respectively. The pipe was subjected to cyclic pressure of 5–77 kg/cm^2 and then back to 5 kg/cm^2. 3-D FEA is carried out to investigate the fracture behaviour of the pipe based on LEFM principles using eight noded solid elements with reduced integration (C3D8R). FE model is constructed with 54,400 elements and 98,646 nodes. Extended Finite Element Method (XFEM) is employed to carry out crack growth analysis. Stress intensity factor (SIF) was evaluated by varying crack length and depth using domain integral technique. SIF was evaluated at both the crack tips and also at the deepest point of the crack in the depth direction to understand the crack growth behaviour of the pipe.

5   Analytical Studies

Analytical prediction of remaining life of API 5L X 46 Grade steel pipes with different crack profiles subjected to internal pressure was carried out. Expressions available in API 579/ASME FFS-1 [17] and ASME B&PV Code Section XI Division I [18] were used to evaluate SIF corresponding to different values of crack depth, both at surface and deepest points.

5.1   API 579-1/ASME FFS-1

As per API 579-1/ASME FFS-1, the Mode I stress intensity factor for a cylinder subjected to internal pressure with longitudinally oriented semi-elliptical surface crack (as shown in Fig. 4) can be computed by the following equations:

$$
\begin{aligned}
KI = pRo2Ro2 - Ri2[2G0 - 2G1(aRi)2 + 3G2(aRi)3 \\
- 4G3(aRi)4 + 5G4(aRi)5]\sqrt{\pi a Q}
\end{aligned}
\tag{1}
$$

where p is internal pressure, Ro is the external radius of the pipe, Ri is the internal radius of the pipe, a is the depth of crack and $G0$, $G1$, $G2$, $G3$, $G4$ are the influence coefficients respectively. This equation is valid for $0.0 \leq a/t \leq 0.8$ and $0.0 \leq t/Ri \leq 1.0$. The influence coefficients $G0$ and $G1$ for inside and outside surface cracks can

Fig. 4 Mode I stress intensity factor for a cylinder subjected to internal pressure with longitudinally oriented semi-elliptical surface crack
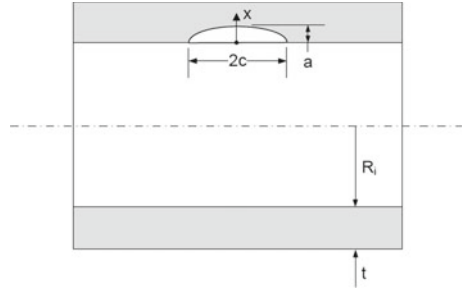
be determined using the following equations:

$$G0 = A0.0 + A1.0\beta + A2.0\beta2 + A3.0\beta3 + A4.0\beta4 + A5.0\beta5 + A6.0\beta6 \quad (2)$$

$$G1 = A0.1 + A1.1\beta + A2.1\beta2 + A3.1\beta3 + A4.1\beta4 + A5.1\beta5 + A6.1\beta6 \quad (3)$$

where $\beta = 2\phi\Pi$ and the parameters Aij (i.e., the values from the row corresponding to Gi and the column Aj) are for inside surface cracks and for outside surface cracks. The influence coefficients $G2$, $G3$, $G4$ for inside and outside surface cracks at surface and deepest point of a semi-elliptical crack are derived as follows:

At deepest point ($\phi = \pi/2$):

$$G2 = \sqrt{2Q\pi}(1615 + 13M1 + 16, 105M2 + 112M3) \quad (4)$$

$$G3 = \sqrt{2Q\pi}(3235 + 14M1 + 32, 315M2 + 120M3) \quad (5)$$

$$G4 = \sqrt{2Q\pi}(256, 315 + 15M1 + 2, 563, 465M2 + 130M3) \quad (6)$$

where the weight function coefficients $M1$, $M2$, $M3$ are calculated from the below equations:

$$M1 = 2\pi\sqrt{2}(3G1 - G0) - 245 \quad (7)$$

$$M2 = 3 \quad (8)$$

$$M3 = 6\pi\sqrt{2}(G0 - 2G1) - 85 \quad (9)$$

$$\text{At surface point}(\phi = 0), \ G2 = \sqrt{Q\pi}(45 + 23N1 + 47N2 + 12N3) \quad (10)$$

$$G3 = \sqrt{Q\pi}(47 + 12N1 + 49N2 + 25N3) \quad (11)$$

$$G4 = \sqrt{Q}\pi(49 + 25N1 + 411N2 + 13N3) \tag{12}$$

where the weight function coefficients $N1$, $N2$, $N3$ are calculated from the below equations:

$$N1 = 3\pi\sqrt{(2G0 - 5G1)} - 8 \tag{13}$$

$$N2 = 15\pi\sqrt{(3G1 - G0)} + 15 \tag{14}$$

$$N3 = 3\pi\sqrt{(3G0 - 10G1)} - 8 \tag{15}$$

The elliptical shape factor Q is determined using $Q = 1.0 + 1.464(ac)1.65$ for $a/c \leq 1.0$ and $Q = 1.0 + 1.464(ca)1.65$ for $a/c > 1.0$

5.2   ASME Section XI

From paragraph H-4221.2 under Article H-4000 Screening criteria in ASME Boiler and Pressure Vessel Code (Section XI), Mode I stress intensity factor for a pressure vessel with semi-elliptical axial flaw (as shown in Fig. 5) at the internal surface is given by the following equation:

$$K = (PRt)(\pi aQ)0.5F \tag{16}$$

where P is pressure inside the cylinder, R is the distance from the centre of the pipe to the deepest point of the semi-elliptical flaw, t is the thickness of the pipe, a and l are the depth and length of the crack respectively. The boundary correction factor F and the flaw shape parameter Q are determined by:

$$F = 1.12 + 0.053\alpha + 0.005\alpha2 + (1.0 + 0.02\alpha + 0.0191\alpha2)(20 - Rt)21,400 \tag{17}$$

Fig. 5 Mode I stress intensity factor for a pressure vessel with semi-elliptical surface crack
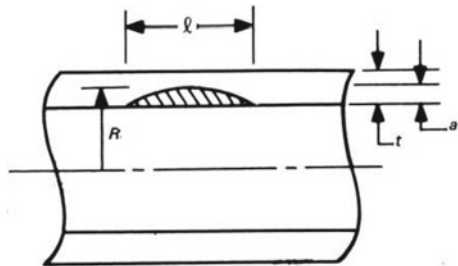
$$Q = 1 + 4.593(al)1.65 \qquad (18)$$

where $\alpha = (a/t)/(a/l)$.

SIF values were obtained using the both the approaches for the pipe specimen with longitudinal seam crack in surface and as well as deepest point of crack. Crack growth analysis was carried out using the SIF values obtained employing Paris' crack growth equation. The analysis was carried out for every 0.5 mm crack depth till the value reached 5.5 mm, which is approximately 0.8 times the thickness of the pipe specimen. Crack length was assumed to increase by 2.5 mm for every 0.5 mm crack depth. Crack length corresponding to 5.5 mm crack depth was 49.5 mm.

6   Results and Discussion

Figure 6 shows typical strain versus time curves and Fig. 7 shows typical strain versus pressure curves for pipe specimen with longitudinal seam crack. Figure 8 shows typical strain versus time curves and Fig. 9 shows typical strain versus pressure curves for pipe specimen with lamination defects. It is observed that strain in the circumferential direction was higher compared to the longitudinal direction at a given location. The strain values are observed to be almost constant till the initiation of through-wall crack. It can be observed that the strain values close to the crack location increased rapidly just before the appearance of through-wall crack. In the case of pipe specimens with longitudinal seam crack, the existing crack had become through-wall and the specimen failed after completion of 1412 cycles indicating 3.87 years of remaining service life. Figure 10 shows close-up view of failure of pipe specimen with longitudinal seam crack. The pipe specimen with lamination defects has developed a through-wall crack and failed after completion of 2010 cycles indicating 5.51 years of remaining service life. Figure 11 shows close-up view of failure of pipe specimen with lamination defect.

Figure 12 shows stress distribution of ahead of crack tip. It was observed that the SIF is higher for the crack tip located nearer to the support than for the crack tip located away from the support due to the geometrical constraint effect of the crack position. Figure 13 shows SIF versus crack depth. As expected, SIF increased with increase in crack depth. Both the axial and von-Mises distributions are exhibited the fracture behaviour based on the material yield zone. It was observed that the crack tip located nearer to the support reached the yield first than the crack tip located away from the support, which could be due to the geometrical constraints and the boundary conditions.

Figure 14a shows SIF for different values of crack length and Fig. 14b shows SIF for different values of crack depth obtained using API 579/ASME FFS-1 for the pipe specimen with longitudinal seam crack. Figure 15 shows comparison of SIF obtained using API 579/ASME FFS-1 and ASME B&PV Code Section XI Division I. SIF value obtained at deepest point of crack was always higher compared to surface point

(a) cycles 31 - 50

(b) cycles 1372 - 1392
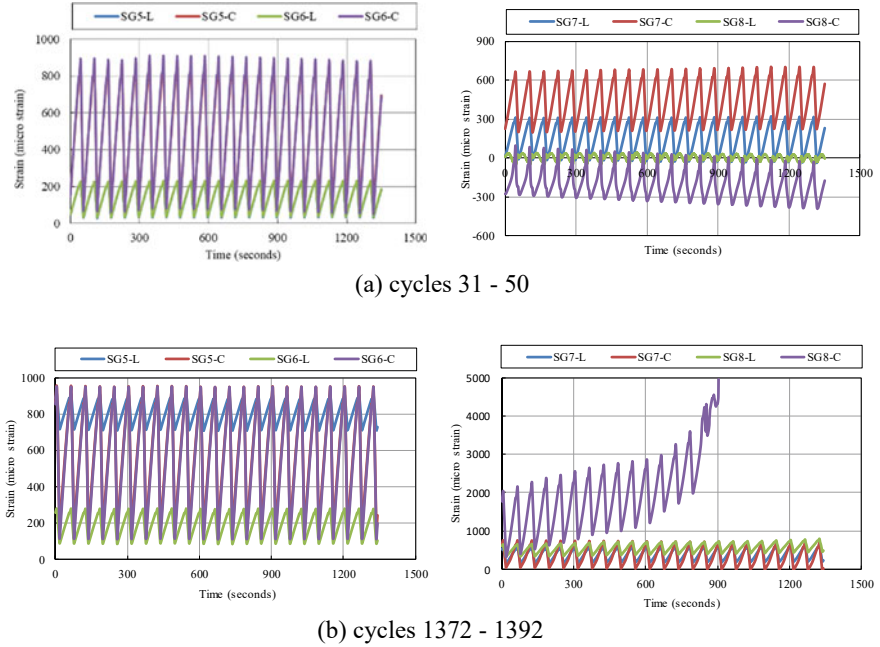
Fig. 6 Strain versus time curves for pipe specimen with longitudinal seam crack

of crack. SIF values predicted using ASME B&PV Code were slightly higher than
the values predicted using API 579/ASME FFS-1 both at the deepest and surface
points of crack. Employing Paris' crack growth model and crack growth constants
available in the literature, number of cycles to failure was predicted. The values of
Paris's crack growth constants C and m used in the present studies were 3×10^{-8}
and 2.615 respectively. The number of cycles predicted using API 579/ASME FFS-1
and ASME B&PV Code Section XI were 5264 and 1691 respectively. The number
of cycles predicted with the SIF values obtained from both the approaches were
un-conservative. Tiku et al. [7] compared fatigue crack growth rates obtained from
full-scale tests with the existing BS 7910 and API 579 formulations. The comparison
confirmed that the BS 7910 approach results in very conservative estimates of fatigue
crack growth rates for axial flaws. The BS 7910 stress intensity factor formulation
overestimated the bulging correction for axially oriented flaws.

7 Summary and Conclusions

Fatigue life studies on API 5L X46 grade steel in-service pipes of 350 mm diameter
and 7.14 mm thickness subjected to cyclic internal pressure was carried out experi-
mentally. One pipe had a longitudinal seam crack of 32 mm length and 2 mm depth
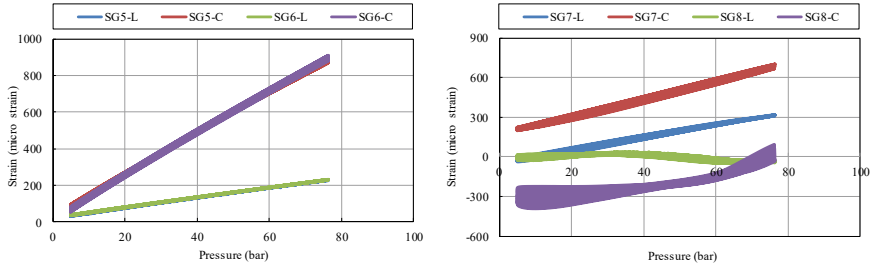
(a) cycles 31 - 50
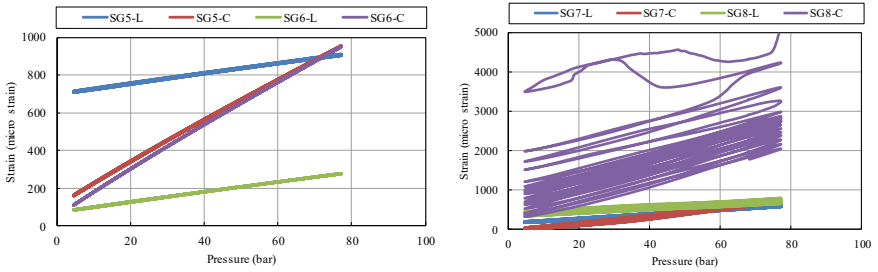
(b) cycles 1372 - 1392

Fig. 7 Strain versus pressure curves for pipe specimen with longitudinal seam crack
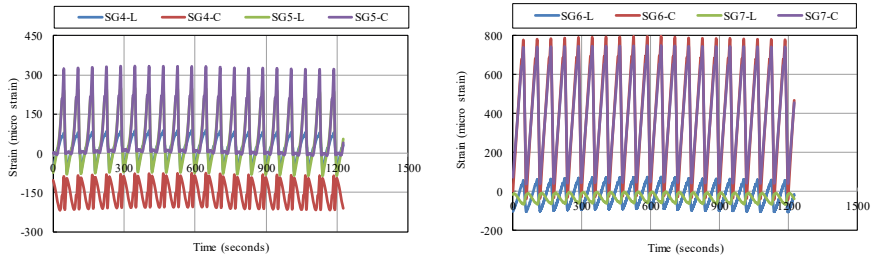
(a) cycles 1501 - 1520
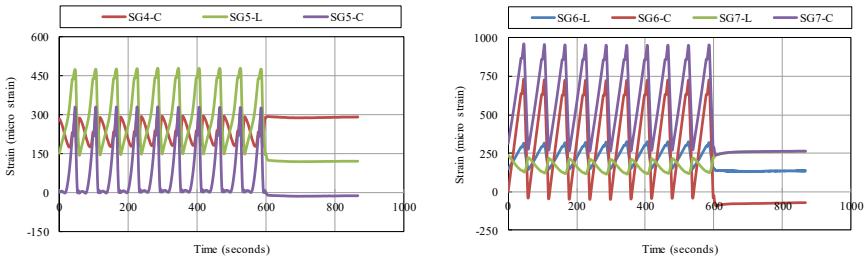
(b) cycles 2001 - 2010

Fig. 8 Strain versus time curves for pipe specimen with lamination defects
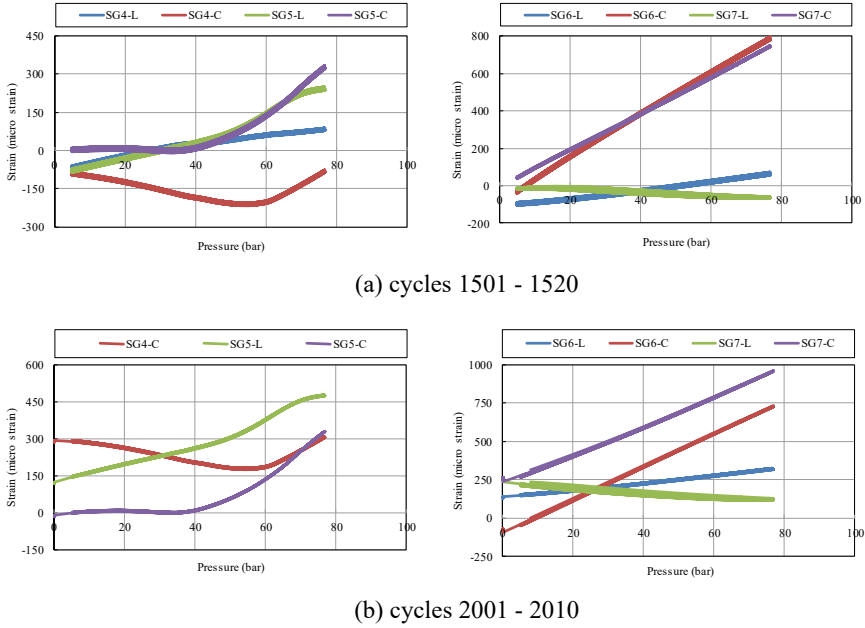
(a) cycles 1501 - 1520

(b) cycles 2001 - 2010

Fig. 9 Strain versus pressure curves for pipe specimen with lamination defects

Appearance of through-wall crack

Through-wall crack

(a)   (b)
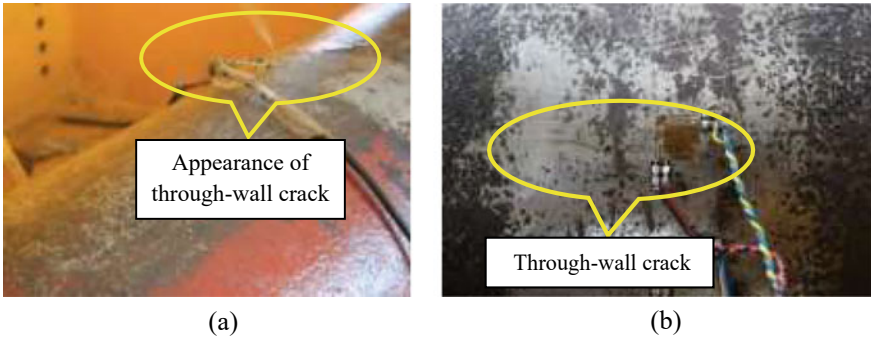
Fig. 10 Close-up views of failure of pipe specimen with longitudinal seam crack

and the other pipe had two lamination defects of different sizes. The pipe specimens were subjected to a cyclic pressure of 5–77 kg/cm^2 and then back to 5 kg/cm^2, typically being followed in oil pipeline industry in India. The existing defects became through-wall crack and the specimens failed at 1412 and 2010 cycles, indicating 3.87 years and 5.51 years of remaining service life. Numerical studies were carried out on the pipes under cyclic internal pressure and stress intensity factor was evaluated by varying crack length and depth using domain integral technique. It was observed that the SIF is higher for the crack tip located nearer to the support than for
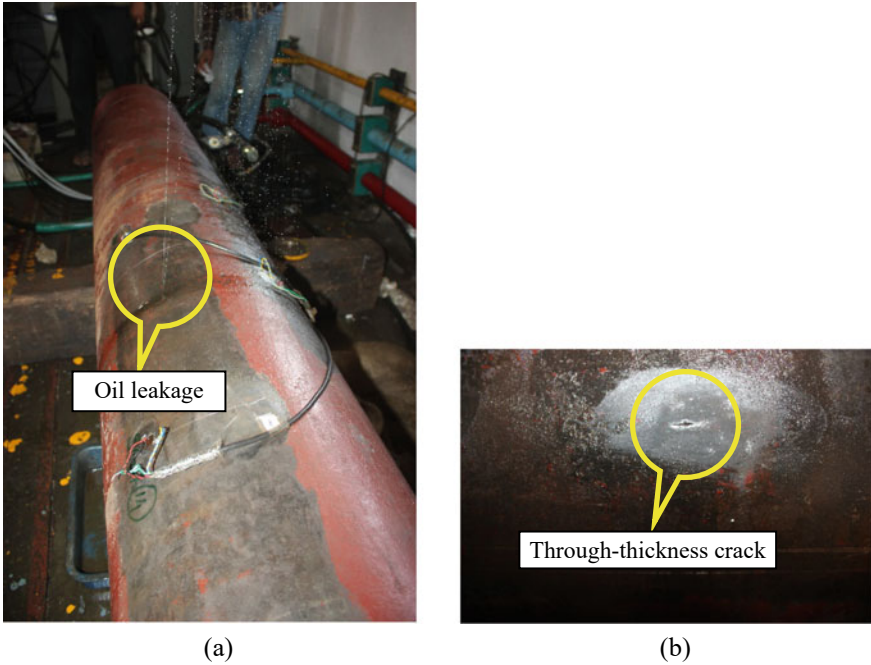
Fig. 11 Close-up views of failure of pipe specimen with lamination defects

Fig. 12 Stress distribution ahead of crack tip

the crack tip located away from the support due to the geometrical constraint effect of the crack position. SIF for different crack depths was also evaluated analytically using the expressions available in API 579/ASME FFS-1 and ASME B&PV Code Section XI Division I. SIF values predicted using ASME B&PV Code were slightly higher than the values predicted using API 579/ASME FFS-1 both at the deepest and surface points of crack. Employing Paris' crack growth model and crack growth constants reported in the literature for API 5L X46 grade steel, number of cycles to failure was predicted and the results are compared.

Fig. 13 Stress intensity
factor versus crack depth
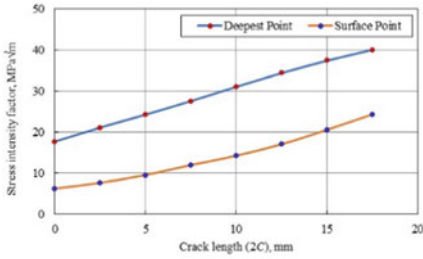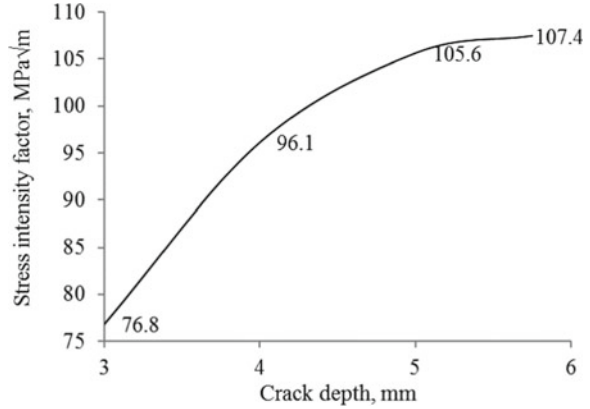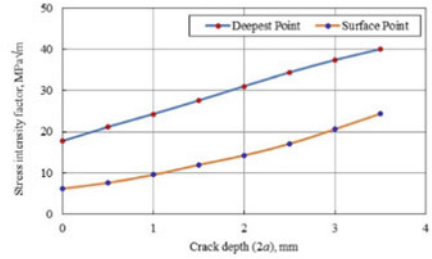

Fig. 14 SIF prediction using API 579/ASME FFS-1
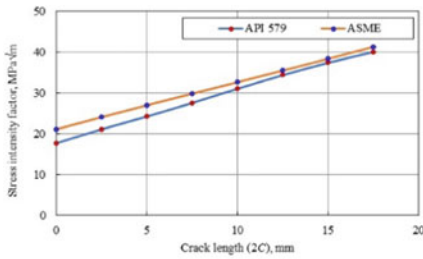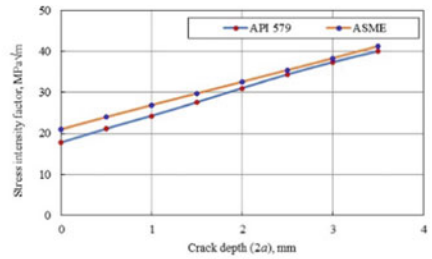
Fig. 15 Comparison of SIF obtained from API 579/ASME FFS-1 and ASME B&PV Code Section
XI Division I

References

1. Mogila M, Davis P, Burn S (2008) Strong exploration of a cast iron pipe failure model. Reliab
   Eng Syst Saf 93:863–874

2. Purbolaksono J, Hong YW, Nor SSM, Othman H, Ahmad B (2009) Evaluation on reheater tube failure. Eng Fail Anal 16(1):533–537
3. Palmer-Jones R, Paisley D (2000) Repairing internal corrosion defects in pipelines—a case study. In: 4th International pipeline rehabilitation and maintenance conference, pp 1–25, Prague
4. Popoola LT, Grema AS, Latinwo GK, Gutti B, Balogun AS (2013) Corrosion problems during oil and gas production and its mitigation. Int J Industr Chem 135(4):1–15
5. Zheng M, Luo JH, Zhao XW, Bai ZQ, Wang R (2005) Effect of pre-deformation on the fatigue crack initiation life of X60 pipeline steel. Int J Press Vessels Pip 82:546–552
6. Azevedo CRF (2007) Failure analysis of a crude oil pipeline. Eng Failure Anal 14:978–994
7. Liu PF, Zheng JY, Sun GY (2010) Fatigue lifetime evaluation of buried pipeline under internal pressure and vibrating loads. J Mech Strength 1:125–129
8. Liu PF, Zheng JY, Zhang BJ, Shi P (2010) "Fatigue analysis of natural gas buried X65 steel pipeline under deflection load using finite element method. Mater Des 31:1384–1391
9. Hasan F, Iqbal J, Ahmed F (2007) Stress corrosion failure of high-pressure gas pipeline. Eng Fail Anal 14:801–809
10. Hajibagheri HR, Heidari A, Amini R (2018) An experimental investigation of the nature of longitudinal cracks in oil and gas transmission pipelines. J Alloys Compd 741:1121–1129
11. Nguyen TT, Heo HM, Park J, Nahm SH, Beak UB (2021) Fracture properties and fatigue life assessment of API X70 pipeline steel under the effect of an environment containing hydrogen. J Mech Sci Technol 35:1445–1455
12. Jiao Z, Shuai J (2014) A cyclic internal pressure characteristics analysis of long distance transmission pipelines. Pet Sci Technol 32(1):61–67
13. Ghaednia H, Das S, Zohrehheydariha J, Wang R, Kania R (2016) Effect of crack depth on burst strength of X70 pipeline with dent-crack defect. In: 11th International pipeline conference (IPC2016), Calgary (2016)
14. Tiku S, Ghovanlou M, Dinovitzer A, Piazza M, Jones TA (2020) Full scale test validation of fatigue crack growth rate of flaws in ERW pipe. In: 13th International pipeline conference, Calgary (2020)
15. Tewari AK, Agarwal D (2018) A case study: failure analysis of crude oil pipeline rupture. Int Res J Eng Technol 5(7):2415–2422
16. API 5L (2018) Specification for line pipe. American Petroleum Institute, 46th ed
17. API 579-1/ASME FFS-1 (2016) Fitness-for-service. API Publishing Services, Washington DC, USA
18. Rules for inservice inspection of nuclear power plant components, Section XI, Division 1, ASME Boiler and Pressure Vessel Code, 2010, New York.

Health Care Management: Cancer Prediction and Diagnosis Using Artificial Intelligence (AI)

S. Parvathi, P. Vaishnavi, and S. Ananthi

1 Introduction

Big data is collection of data that varies in size and further expands dynamically. It deals with all the 3 varieties of data viz., structured, unstructured and semi-structured data. On recent scenario, big data is majorly used in healthcare for diseases' prediction. Multiple research organizations have unveiled an innovative big data analytics solution that has the potential to revolutionize various aspects of healthcare, including improving clinician and research productivity while also benefiting patient care. The uncontrolled growth and spread of abnormal cells is normally defined as cancer and it is become very common now a days. The uncontrolled cancer will have serious impacts and sometimes great threaten to life [1]. The major root causes of cancer are not defined properly whereas the innumerable reasons are known to surge the occurrence of disease, with numerous that are mutable (example, smoking and surplus body weight) and others that might not the reason (e.g., inherited genetic mutations). Accurate and comprehensive information plays a crucial role in medical research, clinical care, resource allocation, and operational efficiency. Consequently, there is extensive research focused on achieving precise diagnosis of cancer and effectively classifying patients into malignant or benign groups [2, 3]. Machine learning is a well-defined methodology for cancer pattern classification and also to forecast the affected person. Because of its advantages it is easy to detect the critical features from complex Cancer datasets. The focus of the paper revolves around an approach aimed at predicting survival time primarily based on a comprehensive clinical feature integrated within the tumor. The approach that utilizes an integrated clinical feature

S. Parvathi · S. Ananthi
Anna University, Chennai, India

P. Vaishnavi (✉)
Department of Computer Application, Anna University, BIT Campus, Tiruchirappalli, India
e-mail: vaishmk@gmail.com

comprising various tumor parameters to predict survival time. This comprehensive clinical feature incorporates significant factors such as genetic markers, histological grade, and lymph node involvement, which collectively contribute to the prediction of survival time in patients. Few cancer datasets are used in this paper. The major factors of risk may occur continuously or in a proper sequence to initiate and/or promote cancer growth.

2 Literature Review

In men, oral cancer, lung cancer, stomach cancer, colorectal cancer, and oesophageal cancer are observed as important types of cancer [4]. In women, breast cancer, colorectal cancer, lung cancer, and cervical cancer are commonly encountered [4]. It is noted that cancer accounts for 9.6 million deaths in 2018 and is considered a major cause of death worldwide [5]. Africa, Central and South America collectively represent over 60% of the worldwide cumulative annual cancer incidences [5]. Additionally, Asia exhibits a high frequency of cancer cases [6]. During the period from 2010 to 2020, there has been an increase of around 20% in new cancer occurrences among men, accounting for approximately one million cases per year, while women have experienced an approximately 18% rise, resulting in over 900,000 cases annually [7].

There are several common types of cancer that affect both men and women. Melanoma is a prevalent form of skin cancer that can occur in individuals of all genders. In men, prostate, kidney, liver, and bladder cancers are commonly diagnosed. Women and men, on the other hand, commonly experience lung, breast, uterine, and thyroid cancers.

When it comes to cancer-related deaths, there are various statistics to consider. Prostate cancer accounts for 26.4% of cancer-related deaths, making it a significant contributor. Colorectal cancer follows closely behind at 23.4%. Lung cancer is responsible for 21.3% of cancer-related deaths, and female breast cancer contributes to 19.6%. Cervical cancer and melanoma are also significant factors, resulting in 12.5% and 7.4% of cancer-related deaths, respectively.

The medical field has applied various methodologies to screen for early-stage cancer and identify cancer types before they become life-threatening. Additionally, novel strategies have been developed to predict the outcomes of cancer treatment at an early stage [8]. In the present era, a substantial amount of cancer-related datasets are available for medical research. However, disease prediction remains a formidable challenge for physicians. Consequently, Machine Learning methods have emerged as an effective tool for medical researchers. Currently, computer-aided diagnosis (CAD) is extensively used in diverse medical domains, such as the early detection of breast cancer [9], diagnosis of lung cancer [8], detection of arrhythmia [10], and diagnosis of dental and maxillofacial lesions [11]. Numerous studies have been conducted, focusing on the application of Machine Learning in cancer diagnosis and prognosis [12, 13]. Cancer, characterized by the abnormal spread of cells to other parts of the

body, encompasses various diseases [14]. Among women, the most prevalent types of cancer include breast, colorectal, lung, and cervical cancer [15].

A multitude of methods are employed to explore, identify patterns, establish relationships, and effectively predict future outcomes of specific cancer types using complex datasets. Considering the importance of personalized medicine and the increasing utilization of Machine Learning techniques, this research endeavor provides a comprehensive review of studies that utilize these methods in the context of cancer prediction and prognosis.

These statistics highlight the disproportionate burden of cancer in certain regions. Africa, Central and South America together account for more than 60% of the total annual cancer cases reported globally [5]. This disparity underscores the urgent need for targeted interventions and resources to address the growing cancer epidemic in these areas.

Furthermore, Asia experiences a high incidence of cancer [6]. The diverse population, lifestyle factors, and varying healthcare systems across different Asian countries contribute to the complex landscape of cancer prevalence in the region. Efforts aimed at prevention, early detection, and access to quality treatment are crucial to mitigate the impact of cancer in Asian populations.

The rise in cancer cases over the past decade is a cause for concern. From 2010 to 2020, there has been an alarming increase of approximately 20% in new cancer cases among men, translating to an estimated one million cases per year [7]. Similarly, women have experienced an approximately 18% rise, resulting in over 900,000 cases annually [7]. These escalating numbers necessitate comprehensive strategies for cancer prevention, timely diagnosis, and effective treatment to alleviate the burden on individuals, healthcare systems, and societies as a whole.

Addressing the global cancer burden requires a multifaceted approach, including public health initiatives, research advancements, and international collaborations. By focusing on prevention, early detection, and equitable access to quality care, we can strive towards reducing the impact of cancer and improving outcomes for affected individuals worldwide.

3 Problem Statement

The accurate forecast of early stage and the years of survival time of cancer patients with the growing complication of this disease, treatment etiquettes, and different patient population models is deemed the most important challenge. Patient care and treatment could be improved, and control over cancer development could be enhanced, with the provision of consistent and well-validated predictions.

An upsurge in the usage of machine learning methods in modern-day medical diagnosis is observed. Current bioinformatics, statistics, and machine learning techniques are extensively employed in cancer studies for more efficient and rapid diagnostics. Given the increasing importance of predictive measures to provide personalized medicine, there is a surging need to provide machine learning patterns for making

predictions and early detection of cancer [16], reflecting the growing demand in this area.

Heterogeneous medical datasets are utilized by classification-based approaches to enhance the quality of diagnostics. Recent advancements in computer science and engineering, data analytics, and machine learning contribute to accurate diagnosis in the medical field. Utilizing artificial intelligence practices for cancer analysis enables the provision of a knowledge extraction for more meticulous and rapid testing of cancer prediction and prognosis [17].

The study revealed that a significant portion (40%) of machine learning methodologies adopted helps doctors to diagnose the patient's early survivability. Diverse datasets were utilized, employing a range of machine-learning techniques to identify the precise state of cancer conditions among the patients. Major studies primarily relied on artificial neural networks (ANN) and support vector machines (SVM) were taken into consideration with the clinical studies, while statistical methods were employed for validation purposes. The need to amplify the influence of machine learning in predicting survival time for cancer patients is evident, emphasizing the importance of generalization, enhanced accuracy, and robust validation. Our research directly tackles these hurdles [18].

4   Algorithms

Deep Neural Networks (DNNs) Classifier in Machine Learning applies probabilistic principles. While DNNs can use a kernel estimator, it is not suitable for discretization. Instead, this process relies on conditional probabilities. Deep Neural Networks (DNNs) employ the network theorem, which incorporates probability considerations by analyzing the frequency of values and the combinations of historical data values. The probability equations derived from the network theorem are as follows:

$$P(A|B) = P(A \cap B)/P(B) \tag{1}$$

$$P(A \cup B) = P(A) + P(B) - P(A \cap B) \tag{2}$$

where

P(A|B) represents the conditional probability of event A given event B.
$P(A \cap B)$ denotes the joint probability of events A and B.
P(B) and P(A) represent the probabilities of events B and A, respectively.
$P(A \cup B)$ represents the probability of the union of events A and B.

These equations allow Deep Neural Networks (DNNs) to incorporate probabilistic reasoning, leveraging historical data combinations and frequency of values to enhance their predictive capabilities.

The instance-based classifier C* is a simple algorithm that is similar to the convolutional neural networks. Instances of new data or information, denoted as Xi where i = 2, 3, 4, …, m, are assigned to the class that is most frequently observed among the KNN data instances or items, represented as Yj where j = 2, 3, 4, …, m. The entropic separation metric is employed to determine this assignment, providing numerous benefits such as handling missing values and real-valued features or attributes. Equation 3 represents the analysis of the K* function:

$$C^*(1, x) = -\ln P^*(yi, x) \tag{3}$$

The probability transformational path, denoted as P, describes the probability of a random walk from data point or instance x to instance y. Equation 3 is utilized to comprehend the probability that instance x will reach the destination y through this random walk.

Within Eq. 3, the function K* (1, x) is defined as the negative natural logarithm of P* (yi, x). This formulation allows us to calculate the probability associated with the random walk between instances x and y. By applying the negative logarithm, we can obtain a measure that captures the likelihood or degree of success in reaching the destination.

The utilization of Eq. 3 enables the analysis and estimation of the probability transformational path, providing insights into the likelihood of a particular instance successfully navigating from one point to another within the dataset. This probability-based approach enhances our understanding of the dynamics and relationships within the data, aiding in various tasks such as classification, prediction, or decision-making processes.

5 Methodology

The National Cancer Registration and Analysis Service (NCRAS) plays a crucial role in understanding the information necessary for providing effective cancer services. They are involved in various activities aimed at improving the quality and timeliness of data related to cancer. Additionally, NCRAS focuses on linking different datasets together to enhance data analysis and make valuable information more accessible.

Predicting the outcomes of cancer diseases has become increasingly challenging yet fascinating with the advent of Machine Learning techniques. Analyzing medical data to identify diseased individuals is a complex task due to the presence of numerous variables, each with its own hidden values. However, Machine Learning methods have emerged as powerful tools for medical analysts. These methods allow them to recognize patterns and establish relationships among a vast number of variables, leveraging historical datasets to predict disease outcomes accurately.

In a cancer dataset, there are certain attribute information that aids in understanding the patients' condition. It includes an ID number for identification purposes and a diagnosis label indicating whether the patient is classified as harmful (H) or

Fig. 1 Dataset and X set after importing the dataset

normal (N). By utilizing this dataset, one can plot a standard deviation curve, which helps visualize the variations in the data. By analyzing this curve, it is possible to determine the number of normal and abnormal patients. The dataset also provides real-valued features computed for each cell nucleus, such as radius, texture, perimeter, area, and smoothness, which contribute to a comprehensive understanding of the patients' condition and aid in further analysis (Fig. 1).

The cleansing of the data has been carried out to remove irrelevant information (e.g., ID), ensuring that highly-correlated features, if not properly removed, do not adversely affect the results of the classification. It should be observed that the dataset itself, consisting of approximately 600 records, would likely derive benefits from a larger dataset for training purposes.

Table 1 provides an overview of key information related to the data processing and dataset in question. It includes specific details about the data processing steps that have been undertaken, such as the removal of irrelevant features and the handling of highly-correlated features. The status column indicates the current progress or completion of each data processing task.

Additionally, the table highlights the impact of these data processing steps on the results of the classification. It mentions that steps have been taken to mitigate any adverse effects on the classification results.

The table also provides information about the size of the dataset, indicating that it is relatively small, with approximately 600 records. Lastly, it acknowledges that a larger dataset would likely bring benefits in terms of training and improving the accuracy of the results.

Table 1 Data processing and dataset overview

Data processing information	Status
Irrelevant features removal	Completed
Handling highly-correlated features	Completed
Impact on classification results	Mitigated
Dataset size	Small (~600)
Potential benefits from larger dataset	Noted

The dataset preparation involves the utilization of the following techniques. The process of normalization is performed to rescale the pixel values, ensuring they fall within the range of 0–255. The use of large integer values for neural network processing can potentially disrupt or hinder the learning process. Therefore, small weight values are employed for the inputs.

Various transformations, including horizontal and vertical flipping, rotation, shear, brightness adjustment, and zoom range, are applied to an input image. These transformations result in slight movements or alterations in the image (Fig. 2).

The method employed for this research work is Classification Accuracy. It quantifies the ratio of correct predictions to the total number of input samples. Table 2 presents the results obtained from the dataset. Now, let's define the following terms (Fig. 3; Table 3):

1. True positive (TRP),
2. True negative (TRN),
3. False positive (FLP),
4. False Negative (FLN).
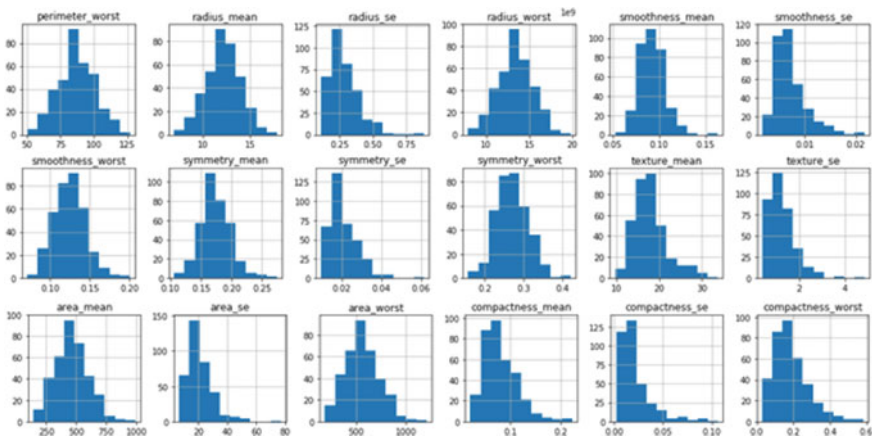
Fig. 2 Dataset visualization

Table 2 Top data of our dataset

Id-Radius mean	Mean	Fractal_dimenstion	Diagnosis
0-842,304	19.99	0.11892	H
1-842,519	22.57	0.008904	H
2-84,302,905	21.69	0.08760	H
3-84,388,503	13.42	0.017302	H
4-8,437,804	22.29	0.07680	H

Fig. 3 Shows the training and validation accuracy

Training and validation accuracy
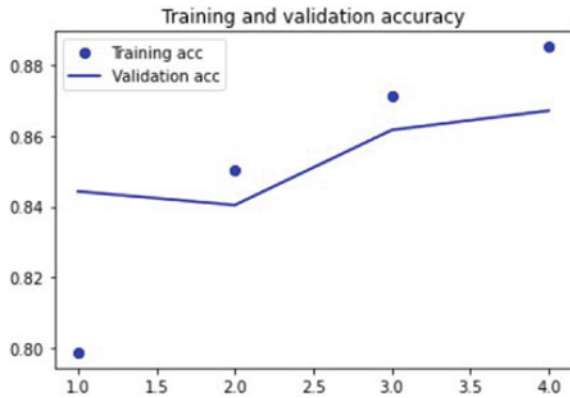
Table 3 Different parameter results

Sl. No.	Description	Parameters
1	Accuracy	0.965
2	Precision	1.0
3	Sensitivity	0.975
4	Specificity	1.0

$$\text{Accuracy} = \frac{\text{Number of correct assessments}}{\text{Number of all assessments}} = \frac{\text{TRN} + \text{TRP}}{\text{TRN} + \text{TRP} + \text{FLN} + \text{FLP}} \tag{4}$$

$$\text{Sensitivity} = \frac{\text{No. of TRP evaluation}}{\text{No. of all positive evaluation}} = \frac{\text{TRP}}{\text{TRP} + \text{FLN}} \tag{5}$$

$$\text{Specificity} = \frac{\text{No. of true negative evaluation}}{\text{No. of all negative evaluation}} = \frac{\text{TRN}}{\text{TRN} + \text{FLP}} \tag{6}$$

$$\text{Precision} = \frac{\text{Number of true positive assessment}}{\text{Number of all positive evaluation and negative evaluation}}$$
$$= \frac{\text{TRP}}{\text{TRP} + \text{FLP}} \tag{7}$$

The Validation Split technique is utilized to partition a portion of the training data and create a separate validation dataset. This validation dataset is used to assess the performance and effectiveness of the model. For this project, we have chosen to allocate 0.2 to 0.5 of the training data as the validation dataset.

As reflected in Table 4 our proposed algorithm provides better results than other existing algorithms in terms of Accuracy, Sensitivity, and Specificity.

Table 4 Result of the different classifier

S. No.	Classifier	Accuracy (%)	Precision	Sensitivity	Specificity
1	Naive Bayes	94.76	0.95	0.96	0.94
2	Bayes network	96.19	0.96	0.97	0.95
3	J-48 decision	93.8	0.94	0.94	0.90
4	SMO	95.71	0.96	0.96	0.94
5	Proposed implementation	96.5	1.0	0.975	1.0

6 Result and Discussion

The Deep neural networks (DNNs) technique depends on the famous approach following a simple, clear and fast classifier. A deep neural networks (DNNs) classifier is a simple probabilistic classifier based on applying network theorem with strong independence assumptions. An alternative term to describe the underlying probability model would be the "feature independence model." Within a deep neural networks (DNNs) classifier, this model assumes that the occurrence or non-occurrence of a particular feature within a class is unrelated to the presence or absence of any other feature, given the class variable.

Accuracy refers to the proportion of accurate predictions made by a model. Precision, on the other hand, gauges the accuracy of predictions within a particular class. Sensitivity quantifies the model's capability to accurately identify instances of a specific class from a dataset. Specificity, commonly employed in two-class problems, aligns with the true negative rate. These metrics, namely accuracy, precision, sensitivity, and specificity, can be calculated utilizing the aforementioned equations.

7 Conclusion and Future Work

This proposed algorithm is implemented using machine learning technique which is useful in diagnosing cancer type and it will assist oncologist to take decision for cancer patient. For this purpose we have used different algorithms and they are compared with the projected algorithm. The experimental results show that our approach performs better and provides better accuracy in predicting the cancer. We have used data cleaning algorithm to clean the data and to include the records with missing data which is obtained by the nearby attribute. In future endeavors, the research will encompass the exploration of alternative machine learning algorithms, including the utilization of hybrid algorithms. These hybrid algorithms involve combining two or more existing algorithms to construct a predictive model capable of achieving higher accuracy in predictions.

References

1. Torre LA, Bray F, Siegel RL, Ferlay J, Lortet-Tieulent J, Jemal A (2015) Global cancer statistics, 2012. CA Cancer J Clin 65:87–108. https://doi.org/10.3322/caac.21262
2. Weston AD, Hood L (2004) Systems biology: proteomics and the future of health care: toward predictive, preventative, and personalized medicine. J Proteome Res 3:179–196
3. Ning Z et al (2019) Pattern classification for gastrointestinal stromal tumors by integration of radiomics and deep convolutional features. IEEE J Biomed Health Inform 23(3):1181–1191
4. Al-Masni MA, Kim T (2018) Review of false positive reduction techniques for mammographic screening in computer-aided detection and diagnosis systems. J Digit Imaging 31(6):815–828
5. Cruz JA, Wishart DS (2006) Applications of machine learning in cancer prediction and prognosis. Cancer Inform 2
6. e Boer RH, Arrieta Ó, Yang CH et al (2011) Vandetanib plus pemetrexed for the second-line treatment of advanced non-small-cell lung cancer: a randomized, double-blind phase III trial. J Clin Oncol 29:1067–1074
7. Futschik ME, Sullivan M, Reeve A, Kasabov N (2003) Prediction of clinical behaviour and treatment for cancers. Appl Bioinform 2:53–58
8. https://www.cancer.gov/about-cancer/causes-prevention/risk
9. Herbst RS, Baas P, Kim DW et al (2016) Pembrolizumab versus docetaxel for previously treated, PD-L1-positive, advanced non-small-cell lung cancer (KEYNOTE-010): a randomised controlled trial. Lancet 387:1540–1550
10. Katsumata A, Fujita H (2014) Progress of computer-aided detection/diagnosis (CAD) in dentistry CAD in dentistry. Jpn Dent Sci Rev 50:63–68
11. Kim ES, Neubauer M, Cohn A et al (2013) Docetaxel or pemetrexed with or without cetuximab in recurrent or progressive non-small-cell lung cancer after platinum-based therapy: a phase 3, open-label, randomised trial. Lancet Oncol 14:1326–1336
12. Kim JH (2004) Computer-aided diagnosis for lung cancer. J Lung Cancer 3:67–70
13. Kourou K, Exarchos TP, Exarchos KP, Karamouzis MV, Fotiadis DI (2015) Machine learning applications in cancer prognosis and prediction. Comput Struct Biotechnol J(13):8–17
14. Mok TS, Wu Y-L, Ahn M-J et al (2017) Osimertinib or platinum-pemetrexed in EGFR T790M-positive lung cancer. N Engl J Med 376:629–640
15. Oweis R, Hijazi L (2006) A computer-aided ECG diagnostic tool. Comput Methods Programs Biomed 81:279–284
16. Ridolfi L, Bertetto O, Santo A et al (2011) Chemotherapy with or without low-dose interleukin-2 in advanced non-small cell lung cancer: results from a phase III randomized multicentric trial. Int J Oncol 39:1011–1017
17. Shandilya S, Chandankhede C (2017) Survey on recent cancer classification systems for cancer diagnosis. In: International conference on wireless communications, signal processing and networking (WiSPNET), Chennai, India, pp 2590–2594
18. Hagerty RG, Butow PN, Ellis PM et al (2005) Communicating prognosis in cancer care: a systematic review of the literature. Ann Oncol 16:1005–1053

Bayesian Network Framework for Human Reliability Analysis in Occupational Health and Safety

Vipul Garg, Vyom Saxena, Gopika Vinod, J. Chattopadhyay, and Vivek Kant

1 Introduction

Human operators are inseparable elements of complex systems and play a crucial role in safe operations of such systems. The performance of the operators is deeply influenced by the physical and psychological environment they work under. Human Factors and Ergonomics (HFE) plays a vital role in ensuring that there is harmony between the physical/psychological environment and the human operators (in relation to their ability and limitations) while discharging their duties [1–3]. Thus, in order to evaluate and enhance the human operator performance for safe operations, it is necessary to identify the essential Human Factors (HF) and how they affect the operator performance [4, 5]. In order to do so, data pertaining to operator performance under the influence of the identified HF is required. In addition to this, a mathematical approach is required to incorporate the HF information in a logical manner and evaluate the performance of the human operator. Currently, there is no state of the art available to evaluate the human operator performance for Occupational Health and Safety (OHS).

Accordingly, the objective of this work was identification of crucial Human Factors pertaining to OHS in a typical research organization and development of a suitable model to quantify the human operator performance. Based on the outcome,

V. Garg (✉) · G. Vinod · J. Chattopadhyay
Reactor Safety Division, Bhabha Atomic Research Centre, Mumbai 400 085, India
e-mail: vipulgarg@barc.gov.in

V. Garg · G. Vinod
Homi Bhabha National Institute, Anushaktinagar, Mumbai 400 094, India

V. Saxena
Industrial Hygiene and Safety Section, Bhabha Atomic Research Centre, Mumbai 400 085, India

V. Kant
IDC School of Design, Indian Institute of Technology Bombay, Mumbai, India

proactive measures to enhance the human operator performance through revision of practices related to OHS management, would be taken thereby minimizing the frequency of occurrences of undesired events.

2   Methodology Adopted for Study

The events generally modeled in risk analysis are rare events with high potential for losses. As a result, the simulations of the situations that require human operator intervention to handle such events are infrequent too [6]. This is the reason why Human Reliability Assessment (HRA) domain experts struggle to get abundant objective data to quantify the Human Error Probabilities (HEP) [6]. However, the HEPs produced by the currently practiced HRA methods generally contain lot of uncertainty owing to the expert judgments. Therefore, the empirical data, although miniscule, would facilitate better estimation of HEPs with reduced uncertainties in the results. Bayesian Inference is a suitable mathematical technique for this purpose. Bayesian inference assumes a prior distribution for the unknown random variable and based on the evidence/observations, the prior distribution is updated to arrive at the posterior distribution [6, 7]. The approach adopted for this work is depicted in Fig. 1.
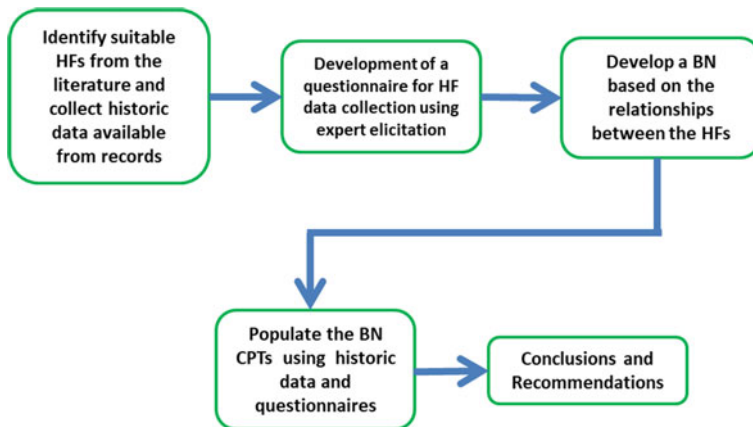
Fig. 1   Roadmap followed for this study

2.1 Identification of Suitable HFs from the Literature and Collection of Historic Data Available Form Records

A literature survey [4, 5, 8, 9] was done to identify the HFs pertaining to the OHS. The factors are shown in Table 1. All the factors were assumed to be binary in this study for the sake of demonstration. The respective states of all the HF are mentioned in Table 1.

2.2 Development of a Bayesian Network Based on the Relationship Between the HFs

Bayesian Network represents a set of random variables and their conditional dependencies via a directed acyclic graph (DAG) [7].

Nodes in Bayesian Networks (BN) represent random variables. Nodes can be further categorized as parent nodes and child nodes. A BN node can be a parent node or a child node or both.

Edges represent conditional dependencies among the nodes. The nodes that are not connected represent variables that are conditionally independent of each other [10]. Each node is associated with a probability function that takes, as input, a particular set of values for the node's parent variables, and gives (as output) the probability of the variable represented by the node. For example, consider a BN shown in Fig. 2 in which there is just one child node and multiple parent nodes. P1–Pk are the parents of C, and P1–Pk are orphans as they have no parents. Formally, the parents of Ci are those variables judged to have a direct influence on Ci. The degree of influence is quantified via conditional probability tables (CPTs) embedded in the networks. The number of probabilities required for the child node is given as [7, 10]:

$$NP = (m - 1)\Pi_{i=1}^{k}n_i \tag{1}$$

where

NP = Number of probabilities of the child node,
m = Number of states of child node i = 1, …, k.
n = number of states of parent node i = 1, …, k.

If a node has no parents, the product term drops from the equation and only the prior $(m - 1)$ probabilities are needed. For all the binary parent nodes:

$$NP = 2^k \tag{2}$$

Many types of information can be leveraged to build the BN model, including expert opinion, system dependency information, data, literature or any combination of sources. The BN exploits the chain rule to calculate the joint distribution from

Table 1 Human factors considered in this study as nodes in BN along with their respective states

Human factors		State S_1	State S_2
A. Organisational			
1	Resource management: man, material, machine, process	Good	Bad
2	Climate: safety beliefs, reward system, attitude towards blame	Favourable	Unfavourable
3	Process: reporting and feedback system, management communication and feedback, level of participation, (line management), error anticipation	Swift	Sluggish
4	Policies for: third party (intervention), procedures and training, systems of work (permits etc.), emergency resources	Robust	Nominal
5	Others		
B. Supervision/Overseeing			
1	Planning and preparations: manpower requirement/work allocation—manpower suitability/operations/Process/machine management	Good	Bad
2	Supervision violations (bypassing procedures), inadequate monitoring,	Acceptable	Unacceptable
3	Decisions: timely diagnosis and correction of problem, emergency measures, consideration of environmental factors	Adequate	Inadequate
4	Communication: (insufficient/wrong)	Acceptable	Unacceptable
5	Others		
C. Individual			
1	State of mind: mental/psychological/ attention/stress/lack of motivation/attitude	Normal	Abnormal
2	Skill: insufficient task knowledge/ intelligence deficit/training—experience deficit	Perfect	Imperfect
3	Decisional abilities: situation based errors/ perception based errors/confidence	Reliable	Unreliable
4	Physical: state of fitness (temporary or permanent handicaps)/health/strength/ physiological deficiency/hyper-stressed/ overworked	Suitable	Unsuitable
5	Others		
D. External factors			
1	Infrastructure—inadequate workspace and layout/design/material (quantitative/ qualitative)/job aids	Adequate	Inadequate

(continued)

Table 1 (continued)

Human factors		State S_1	State S_2
2	Inappropriate environment: social/health (pandemic)/economic/natural (weather/ climate etc.)	Appropriate	Inappropriate
3	Constraints: deadline urgency, security related	Acceptable	Unacceptable
4	State/national/global factors: sanctions/ environmental prohibitions/labour laws/ protocols/certifications	Favourable	Unfavourable
5	Others		
E. Job and task characteristics			
1	Procedures: SOPs/periodic maintenance/ rescheduling	Adequate	Inadequate
2	Flexibility: substitutes in machines, tools, and process	Sufficient	Insufficient
3	Degree of safety automation/scope of recovery	Present	Absent
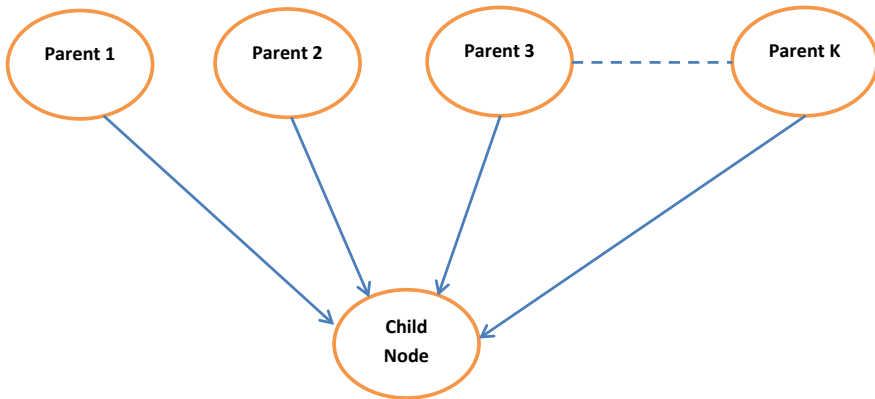
Fig. 2 A Bayesian network

the conditional distributions. According to the chain rule, the distribution of a set of variables can be calculated as the product of conditional distributions [7]:

$$P(N_1, N_2, \ldots, N_k) = P(N_1) * P(N_2/N_1) \cdots * P(N_k/N_1, N_2, \ldots, N_{k-1}) \quad (3)$$

In the BN, each node is conditionally independent of all of its non-descendants, given its parents, pa. This simplifies the joint distribution as:
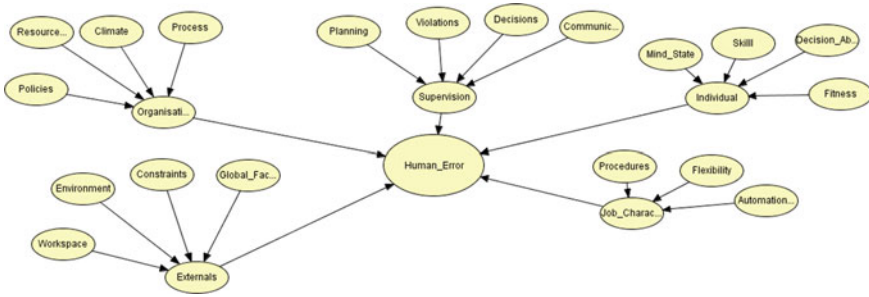
Fig. 3 BN depicting the relationship among the factors

$$P(N_1, N_2, \ldots, N_k) = P(N_1/pa(N_1)) * P(N_2/pa(N_2)) \cdots * P(N_k/pa(N_k)) \tag{4}$$

Bayes Theorem states that:

$$P(A/B) = \frac{P(B/A) \times P(A)}{P(B)}. \tag{5}$$

i.e. Bayes Theorem allows the user to compute the conditional probability of A/ B from the conditional probability of B/A and vice versa. The implication is that analysts can conduct reasoning forward from A to B (causal reasoning), but also backward from B to A (evidential reasoning).

Based on the identified HFs for this study as shown in the tables in the above section, their inter-relationship is modelled using BN [11] as shown in Fig. 3.

The prior distribution of the parent nodes was obtained through historic records and the CPT was populated with expert elicitation.

3 Results

After having fed the prior probabilities and CPTs, the network was compiled as shown in Fig. 4.

In Fig. 4, evidence is provided in form of observations of some of the nodes in particular states, e.g. 'Climate' node in 'Favorable' state, 'Policies' node in 'Robust' state and so on. Based on these evidences, the distribution of the node of our interest i.e. 'Human_Error' changes accordingly and the HEP i.e. 'Human_Error = True' is evaluated to be 0.2434.
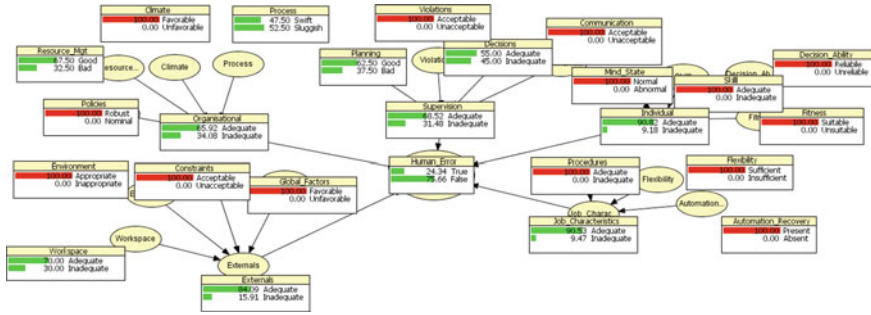
Fig. 4 Compiled Bayesian network

4 Conclusion

BN model for the evaluation of HEP is developed for OHS. The key highlights of the BN model developed are as follows:

(1) The model is generic in nature and can be utilized for evaluation/quantification of HEPs for various contexts pertaining to OHS and also supports qualitative analysis.

(2) However, the exquisiteness of BN is that once the framework is developed, the relationship among the nodes i.e. the BN model does not change and the data can be modified as and when available over the period of time to take care of the uncertainty in the prior data and CPTs.

(3) The BN models reduce a lot of subjectivity pertaining to the unobserved states of the nodes through its prior information.

References

1. Bridger RS (2018) Introduction to human factors and ergonomics, 4th ed. CRC Press
2. Dekker S (2019) Foundations of safety science: a century of understanding accidents and disasters
3. https://www.hfes.org/About-HFES/What-is-Human-Factors-and-Ergonomics
4. Methods for assessing and strengthening the safety culture of the regulatory body. OECD-NEA (2021)
5. Assessing behavioural competencies of employees in nuclear facilities. IAEA-TECDOC-1917 (2020)
6. Halbert B, Kolaczkowski A (2007) The employment of empirical data and Bayesian methods in human reliability analysis: a feasibility study. NUREG/CR-6949. US Nuclear Regulatory Commission, Washington DC
7. Mahadevan S, Zhang R, Smith N (2001) Bayesian networks for system reliability reassessment. Struct Saf 23(3):231–251
8. Guidance on investigating and analysing human and organisational factors aspects of incidents and accidents. Energy Institute, London, May 2008

9. Reducing error and influencing behaviour, HSG48 (Second edition, published 1999)
10. Langseth H, Portinale L (2007) Bayesian networks in reliability. Reliab Eng Syst Saf 92(1):92–108
11. Madsen A, Lang M, Kjærulff U, Jensen F (2003) The Hugin tool for learning Bayesian networks. Lecture notes in artificial intelligence (Subseries of lecture notes in Computer Science), 2711, pp 594–605. https://doi.org/10.1007/978-3-540-45062-7_49

Estimation of System Resilience Through Independent Parameter Transient Profile

Mahendra Prasad and V. Gopika

1 Introduction

In order to mitigate the consequences of an accident, the management techniques have envisaged the design of engineering systems to avoid the events or capable enough to absorb undesired events from occurring. Resilience is usually referred to an ability of an object (system/entity) to get back to the normal state after it was disturbed by an internal or external event in a continuous and unpredictable manner. This definition of resilience can be used for different fields of work. According to Allenby and Fink [1], resilience is the system's ability to keep its functions and configuration intact when a change is applied to it. In [2], Haimes defines resilience as a characteristic of a system to counter a disruption with parameters changing in a limited range (acceptable) and then recover to nominal condition in a suitable time without unreasonable load on cost. Disaster resilience is referred to, by Infrastructure Security Partnership [3], as the strength to protect against multiple hazards. The system should be able to get back to normalcy with minimal undesired affect to public. Vugrin et al. [4] mentions that resilience is the quality of a system to efficiently decrease change in the normal operating level of a system due an event. Both the quantity (difference between normal operating level and system performance level during disruption) and the time duration of change should be efficiently handled. Transient recovery path length can be a measure for resilience [5]. Hosseini et al. [6] have presented a detailed review of the qualitative and quantitative methods for resilience estimation in various types of applications.

The resilience metrics in literature has been proposed based on time of fault, repair and recovery process. However, the various proposals available in literature pertain to single parameter while there could be more than one parameter defining

M. Prasad (✉) · V. Gopika
Bhabha Atomic Research Centre, Mumbai, India
e-mail: mprasad@barc.gov.in

a system normal operability. The present have limitation in applying the concepts and mathematical formulation for multi dimensional parameters. In this work, first resilience estimation is carried out for a power system with three parameters assuming them to be independent.

2 Case Study: Resilience of Power Sub-station Failure

2.1 *Resilience Estimation from Literature Review*

The resilience analysis was performed using the data on voltage (V), active power (P) and reactive power (Q) following a voltage sag transient at a power sub-station (Tomiyama et al. [7]). Figure 1 shows the voltage sag event causing changes in P and Q with time. The 'pu' refers to 'per unit' which is normalization of parameter with respect to the rated value (prior to the transient, the 'pu' value for all three parameters is 1). The voltage decreases to 0.87 pu, due to a fault in the power system. P and Q, decrease to values lower than V in terms of 'pu'. The transient profile is different for each of the parameters.

The digitization of the parameters V, P and Q were as carried out from the use of Fig. 1. These values for V, P and Q were used to curve fit using regression analysis. In the analysis, normalization of time is not carried out for the curve fit since the methods from the literature do not require it. The continuous time dependent curve for V, P and Q are shown in Figs. 2, 3 and 4 respectively. As can be seen from the figures, the equations defining the fit are different for the parameters and the R^2 (coefficient of determination indicating goodness of fit for the regression analysis) are high (> 0.9) for all.

The resilience of the power system transient was determined considering independence among the parameters (Eq. 1).
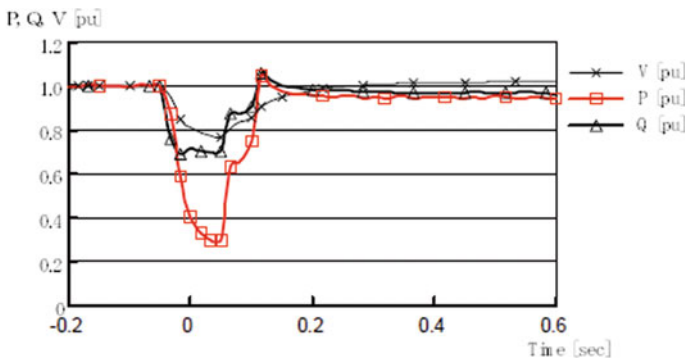
Fig. 1 Transient profile of voltage, active power and reactive power (Tomiyama et al. [7])

Fig. 2 Voltage versus time curve fit

$$y = 729.1x^4 - 840.9x^3 + 347.9x^2 - 59.74x + 4.397$$
$$R^2 = 0.979$$

Fig. 3 Active power versus time curve fit

$$y = -21628x^4 + 14686x^3 - 3477.x^2 + 333.0x - 9.886$$
$$R^2 = 0.922$$
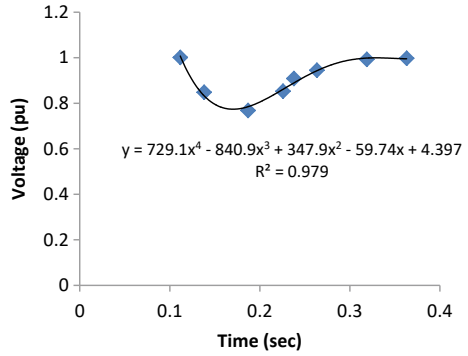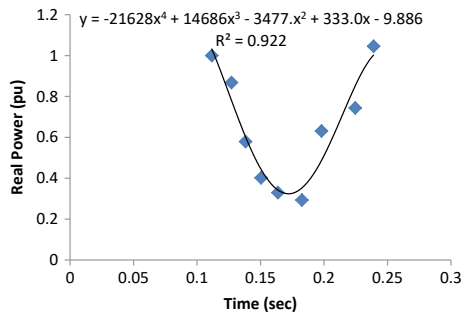
Fig. 4 Reactive power versus time curve fit

$$y = 17227x^4 - 12858x^3 + 3592.x^2 - 441.7x + 20.74$$
$$R^2 = 0.946$$
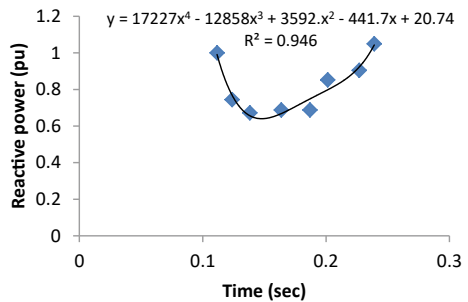
$$Я = Я_V Я_P Я_Q \tag{1}$$

The results of system resilience using various methods in literature presented in Table 1. Some methods were not found applicable in this case (Francis and Bekera [8]; Cimellaro et al. [9]; Youn et al. [10]; Chang and Shinozuka [11]).

It is observed from the Table 1 that the estimated resilience measure for the power system has vastly varying values from different methods that could be applied in this case.

Table 1 Power system resilience from different methods

Sr. No.	Author	Resilience model	Я (Resilience)
1	Zobel [12]	$$Я(X, T) = \frac{T^* - XT/2}{T^*}$$ T*: Long time interval XT/2: Area loss (X is dimensionless)	0.4063
2	Rose [13]	$$Я = \frac{\%\Delta Y_{max} - \%\Delta Y}{\%\Delta Y_{max}}$$ $\%\Delta Y_{max}$: Max degradation possible $\%\Delta Y$: Expected degradation	0.1465
3	Henry and Ramiez-Marquez [14]	$$Я = \frac{\varphi(t/e^j) - \varphi(t_d/e^j)}{\varphi(t_0) - \varphi(t_d/e^j)}$$ $\varphi(t/e^j)$: Parameter value at time 't' $\varphi(t_d/e^j)$: Parameter value at disruptive state (in current analysis it is point of minimum for V, P, Q from the graphs) $\varphi(t_0)$: Parameter value at start	8.6E−06 to 0.6755
4	Ayub [15]	$$Я = \frac{T_i + F\Delta T_f + R\,\Delta T_r}{T_i + \Delta T_f + \Delta T_r}$$ T_ii: Time to incident ΔT_f: $T_f - T_i$ T_f: Time to failure T_r: Time to recovery ΔT_r: $T_r - T_f$ F: Failure profile R: Measure of recoverability	0.3573

3   Resilience Using Parameter Transient Path

This concept of path length from failure to recovery was applied to the power supply failure case. The curve fit was carried out for the data which was normalized. The parameter values V, P and Q are in p.u. (per unit basis) hence are normalized between 0 and 1. The time was normalized by the time interval covering initiation of event to its recovery. The best fit curve for normalized voltage, normalized power and normalized reactive power are shown in Figs. 5, 6 and 7 respectively.

Fig. 5 Normalized data fit
for voltage

$y = 2.913x^4 - 8.191x^3 + 7.64x^2 - 2.374x + 1.007$
$R^2 = 0.979$
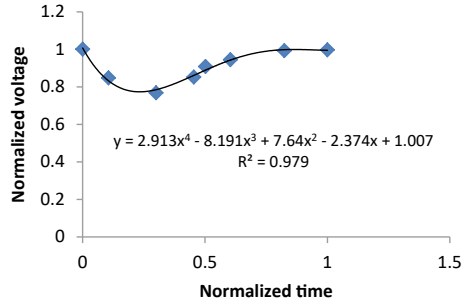
Fig. 6 Normalized data fit
for power

$y = -5.705x^4 + 10.40x^3 - 2.867x^2 - 1.865x + 1.032$
$R^2 = 0.922$
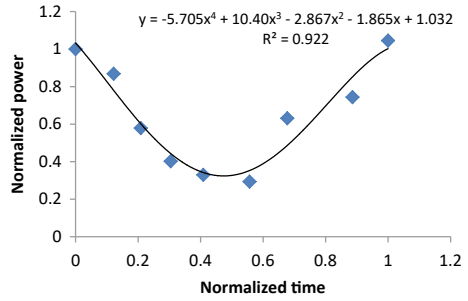
Fig. 7 Normalized data fit
for reactive power

$y = 4.544x^4 - 10.69x^3 + 9.326x^2 - 3.125x + 0.991$
$R^2 = 0.946$
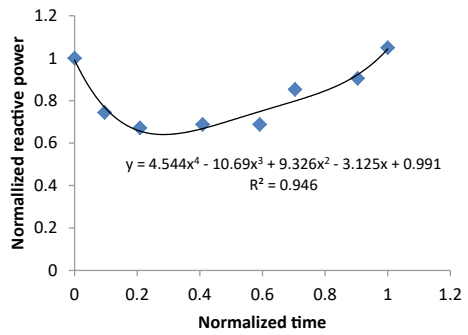
Munoz and Dunbar [5] mention that recovery curve length can be a measure of resilience. The curve length, a dimensionless value, is given by Eq. (2).

$$L = \int_a^b \sqrt{1 + \left(\frac{dy}{dx}\right)^2}\, dx. \tag{2}$$

$\frac{dy}{dx}$ is the slope of the curve at any x.

The curve length for the three transient paths were determined by numerical integration were in time steps of 0.001 was considered.

The curve length for each of the curve fits for V, P and Q were calculated as $L_V = 1.1656$, $L_P = 1.7541$ and $L_Q = 1.3257$ respectively.

The resilience for each parameter was calculated as follows:

$$Я_V = \frac{1}{L_V} = \frac{1}{1.1656} = 0.8579$$

$$Я_P = \frac{1}{L_P} = \frac{1}{1.7541} = 0.5700$$

$$Я_Q = \frac{1}{L_Q} = \frac{1}{1.3257} = 0.7543$$

The overall resilience for the system was calculated as,

$$Я = Я_V\, Я_P\, Я_Q = 0.3688$$

4   Discussion and Conclusions

The methods on resilience, from literature, implemented on a power system transient shows that these are applicable to single parameter defining the system. The power system transient involved multiple parameters that were required to be recovered to their nominal value after a fault. The path length method was proposed as a generally implementable concept for resilience estimation for a system. Using this method, resilience of the power system considering the parameters as independent was around 0.369, relatively low representation of system resilience. There are no standards to measure the resilience of engineering systems. Hence, the derived results cannot be compared against a standard value.

References

1. Allenby B, Fink J (2000) Social and ecological resilience: toward inherently secure and resilient societies. Science 24(3):347–364
2. Haimes YY (2009) On the definition of resilience in systems. Risk Anal 29(4):498–501
3. The Infrastructure Security Partnership (TISP) (2006) Regional disaster resilience: a guide for developing on action plan. American Society of Civil Engineers, Reston, VA
4. Vugrin ED, Warren DE, Ehlen MA, Camphouse RC (2010) A framework for assessing the resilience of infrastructure and economic systems. In: Gopalakrishnan K, Peeta S (eds) Sustainable infrastructure systems: simulation, modeling, and intelligent engineering. Springer-Verlag, Inc., Berlin

5. Munoz A, Dunbar M (2015) On the quantification of operational supply chain resilience. Int J Prod Res 53(22):6736–6751. https://doi.org/10.1080/00207543.2015.1057296
6. Hosseini S, Barker K, Ramirez-Marque JE (2016) A review of definitions and measures of system resilience. Reliab Eng Syst Saf 145:47–61
7. Tomiyama K, Ueoka S, Takano T, Iyoda I, Matsuno K, Temma K, Paserba JJ (2003) Modeling of load during and after system faults based on actual field data. In: 2003 IEEE power engineering society general meeting (IEEE Cat. No. 03CH37491), 2003, vol 3, pp 1385–1391. https://doi.org/10.1109/PES.2003.1267354
8. Francis R, Bekera B (2014) A metric and frameworks for resilience analysis of engineered and infrastructure systems. Reliab Eng Syst Saf 12:90–103
9. Cimellaro GP, Reinhorn AM, Bruneau M (2010) Seismic resilience of a hospital system. Struct Infrastruct Eng 6(1–2):127–144
10. Youn BD, Hu C, Wang P (2011) Resilience-driven system design of complex engineered systems. J Mech Des 133:10
11. Chang SE, Shinozuka M (2004) Measuring improvements in the disaster resilience of communities. Earthq Spectra 20(3):739–755
12. Zobel CW (2011) Representing perceived trade offs in defining disaster resilience. Decis Support Syst 50(2):394–403
13. Rose A (2007) Economic resilience to natural and man-made disasters: multidisciplinary origins and contextual dimensions. Environ Hazard 7(4):383–398
14. Henry D, Ramirez-Marquez JE (2012) Generic metrics and quantitative approaches for system resilience as a function of time. Reliab Eng Syst Saf 99:114–122
15. Ayyub BM (2014) System resilience for multi hazard environment: definition, metrics and valuation for decision making. Risk Anal 34(2):340–355

An Investigation on Data Sharing Security Risk Issues in Cloud System

S. Jayanthi and A. Valarmathi

1 Introduction

Sharing of information is essential service in cloud storage. For instance, bloggers can give their companions a chance to see a subset of their private pictures; an undertaking may give her workers access to a bit of delicate information [1]. Data sharing turns into an uncommonly appealing administration provided by cloud computing stages as a result of its suitability and economy [2–4]. With the approach of cloud computing, an ever-increasing number of information is outsourced to cloud servers from single user and enterprise [3]. The important concern is to know the manner to share encoded information effectively. Clients can download that particular information from the storage, decode them, at that point send to others for sharing, yet it loses the worth of the storage of cloud [5].

As a rule, the cloud service can be separated into three kinds, that is, people in general cloud, private cloud in addition to hybrid cloud, where normally untrusted cloud is a public cloud but the private cloud is thought to be semi-trusted or completely trusted, and hybrid cloud is the mix of public cloud as well as private cloud [6]. In this manner, when the clients need to offer their delicate information to the public cloud, including their documents, messages, etc., they requisite to execute control of access on the data except protecting security and data deduplication [7].

There is presently a thrust for IT association to enlarge their information sharing attempts [8]. In big business settings, there is the rise sought after for data outsourcing, which aids the vital administration of corporate data. It is likewise employed as a core innovation behind numerous online administrations for personal applications.

S. Jayanthi (✉)
Deparment of CSE, BIT Campus, Anna University, Trichy, Tamilnadu, India
e-mail: jayanthi@aubit.edu.in

A. Valarmathi
Deparment of MCA, BIT Campus, Anna University, Trichy, Tamilnadu, India

Fig. 1 Encryption and decryption process

With current technology, a client can get to the documents or messages by cell phone or PC from any side of the world. The user does not trust the servers of cloud coped by cloud providers the user though the data records placed away in a cloud may be subtle as well as private, for instance, strategies of business [9]. For data security protection, the process of encryption of information records, and then transmitting the encoded data into a cloud will take place. The design allows a content supplier to share her information in a secret and specific path, with a stable and little ciphertext extension, by circulating to each approved client a single, smaller, aggregate key [10].

A cryptographic elucidation, with confirmed security, depended on number-theoretic suppositions is more alluring Data sharing is imperative usefulness in the cloud storage. For instance, bloggers can give their companions a chance to see private information or an undertaking may give their representative access to essential information. The issue is the how to competently share the prearranged information competently. Clients can copy the encrypted information from the storage, unscramble them and afterward send them to other persons for distribution, yet it loses the cloud storage significance. So the client should possess the capacity to give get to privileges of sharing information to others with the goal that they can get to these data from server specifically (Fig. 1).

The systems create utilization of as a part of cryptography is encoding as well as decoding of information. These are additionally called encrypting and decrypting, or enciphering and translating. Encryption, encode or encipher is a strategy by which the original content, frequently termed as plaintext, is changed, with the end goal that the prominence of the content is covered up, i.e., the plaintext is changed into an incomprehensible string of text, frequently named as ciphertext. The end objective to get a plaintext from ciphertext, it should be decoded, decrypted or deciphered.

This present paper reviewed various techniques for security frameworks for data sharing in cloud computing. As the information along with data will be communicated to a stranger, cloud computing users required to stay beyond an untrusted cloud provider. Securing private and important data, for example, bank details of interest or a patient's health records from assailants or pernicious insiders are of basic importance. In addition to this study linked to the security problems in single to single cloud users in cloud computing are examined.

2 Related Works

This section highlights current academic successes of the data sharing protections in clouds along with the methods of data sharing in the IT, financial and healthcare industry. The dissimilarities amongst the prior related works are surveyed and stated in this section by comparisons.

2.1 Key Aggregation Encryption

Kate and Potdukhe [11] offered a scheme for encrypting public key which is recognized as Key-Aggregate Cryptosystem (KAC). KAC generated consistent size ciphertexts with the goal that effective appointment of deciphering rights for any procedure of ciphertext was possible. Any arrangement of secret keys can be collected and made them a single key, which incorporated energy of all the keys being aggregated. This key can be dispatched to other users for decryption of ciphertext set and remaining encrypted records external to the set stay.

Chu et al. [10] portrayed new public key cryptosystems which deliver steady size ciphertexts with the end objective that proficient appointment of decoding privileges for whichever arrangement of figure writings are possible. The curiosity was that one could aggregate any arrangement of secret keys and make them as smaller as a single key, however including the energy of all the keys being collected. As it looks, the owner of the secret key could issue a consistent total size of the key for flexible verdicts of ciphertext set in the storage of cloud, yet the additional encoded records which are external to the set stay secluded. This conservative aggregate key can be advantageously sent to others or be put away in a smart card with extremely restricted secure storage. This study gave formal security inspection of these plans in the standard model and furthermore portrayed other utilization of this plans.

Guo et al. [12] proposed a key-aggregate confirmation cryptosystem that can create a regular size key that supports the adaptable selection of decryption privileges for whichever ciphertexts arrangement. The extent of the key was autonomous of the quantity of greatest ciphertexts, implying that the cost of the plan is steady regardless of how as often as possible clients transfer documents to a cloud server. Astoundingly, this investigation demonstrated that the authentication key couldn't be fashioned, and the message in this key can't be denied. The technique that is utilized to accomplish proficient and secure data sharing in powerful cloud storage must be steady in cost and leakage versatile. Our plan at the similar time fulfills both of these necessities.

Gan et al. [13] proposed KAC understand proficient assignment of decoding privileges of whichever ciphertext subset. Be that as it may, the end-gadgets of IoT might not have the unique confided in equipment, and the put away keys can be spilled by side-channel assaults. This investigation planned two spillage strong KAC plans, which was demonstrated to secure with assistant information and furthermore

executed these plans more than two stages to verify their relevance for the asset obliged devices.

The current appearance of cloud computing and the IoT has made it basic to have proficient and secure cryptographic strategies for online sharing of information. Data proprietors would in a perfect world want to collect their data/documents online in an encrypted way, and delegate decryption rights for particular of these to clients with suitable qualifications [14, 15].

Patranabis et al. [16] proposed a safe and dynamic key total encryption conspire for online data sharing that works on elliptic bend subgroups while permitting dynamic renouncement of client get to rights. What's more, expanded this major development to a two-level progressive structure that accomplishes ideal space and time complexities, and furthermore proficiently outfit growth of information classes. At last, this exploration proposed an expansion to the general scheme that permits utilization of proficiently process able bilinear pairings for encryption and decryption activities. Each plan is formally turned out to be semantically secure. Pragmatic analyses have been led to approve all cases made in this examination.

Kumar and Dhanasekar [17] deliberated about the mode of compressing secret keys in cryptosystems of a public key. This key supported an allocation of secret keys for different ciphertexts in the storage of cloud. This method is moreover supple as associated with a hierarchical key assignment. The compressed key could only store spaces if every key-holder shares a similar set of rights.

Pawar et al. [18] recommended a cryptographic procedure having secret keys that could be combined with a single compact key by including the power of all keys. This permitted the secret key proprietor to provide a fixed size aggregate key for choosing ciphertext set in a cloud. Lee et al. [19] proposed a scheme of time-bound key-aggregate encryption for cloud storage, along with the outcomes of appropriate evaluations in addition to accuracy and security studies. Then the superiority of novel scheme over related works was proved. Not only the novel structure took the burden of keeping the attribute-based keys off the user, but it too offered satisfactory privacy and safety for cloud data in a well-organized manner.

Shanthi et al. [20] defined random key generation algorithm using random sized public/master-secret key pair was formed by the data owner. The innovation is that data owner converts the data using feistal structure network along with the public key and the data index into an image and this was achieved by utilizing steganography, and formerly the information was uploaded in a Cloud Server. Aggregate Decryption Key (ADK) was primarily utilized to produce the Master-secret key where it was used for distributing the information to further users by transferring its ADK to those who were interested in retrieving the contents through E-mail by the data owner. Original Data was moved only after Authentication of ADK and the verification that was done by a 3D scan of fingerprint authentication.

Li et al. [21] suggested the idea of "multi-owner key-aggregate searchable encryption" system and its execution, in which a consumer can only refer to the entry for examining the documents shared by multiple owners who only required distributing

an aggregate key for distributing enormous information. Therefore, the system maintained effective data sharing for both multiple owners and users by decreasing needless trapdoors which are tough for generating by mobile devices in the phase of querying. In conclusion, security study and concert assessment was conducted which presented that the suggested system was practical and secure.

2.2 Attribute-Based Encryption (ABE)

Data sharing turns into an astoundingly alluring administration provided by cloud computing stages as a result of its accommodation and economy. As a potential procedure for acknowledging fine-grained data sharing, ABE has drawn wide considerations. In any case, a large portion of the current ABE solutions experiences from the ill effects of the impediments of high calculation overhead and frail data security, which has seriously hindered asset, compelled cell phones to alter the service. At the equivalent time the problem for realizing fine-graininess, high-productivity on the data proprietor's side, and standard data secrecy of cloud information sharing in reality still stays uncertain [22].

Li et al. [21] tended to the above testing issue by proposing another attribute-based data sharing plan appropriate for asset constrained mobile users in cloud computing. The proposed plan dispenses with a larger part of the calculation undertaking by including framework public parameters other than moving halfway encryption calculation disconnected. Furthermore, an open ciphertext test stage is performed before the decryption stage, which dispenses with the greater part of calculation overhead because of ill-conceived ciphertexts. For data security, a Chameleon hash work is utilized to produce a quick ciphertext, which will be blinded by the offline ciphertexts to acquire the last online ciphertexts.

Wang et al. [23] explained that Ciphertext-policy ABE (CP-ABE) was an exceptionally motivating encoding practice for safe distribution of information regarding cloud computing. Data proprietor is permitted to completely control the entrance approach related with his information which to share. Moreover, CP-ABE is restricted to a potential security chance that is recognized as key escrow problem whereby a trusted key expert must deliver the secret keys of users. Additionally, the massive preponderance of the present CP-ABE strategies can't boost attribute with a self-assertive state. In this study, the researcher return to attribute-based data sharing plan with a specific end goal to illuminate the key escrow issue yet, in addition, enhance the expressiveness of characteristic, so the succeeding strategy is all the more inviting to cloud computing applications.

Zhang et al. [24] formalized the thought of ciphertext-strategy ABE supporting adaptable and direct disavowal (FDR-CP-ABE), and introduced a concrete development. The suggested method provided direct attribute and client renouncement. To accomplish this objective, this investigation acquaints a helper work with deciding the ciphertexts associated with denial occasions, and afterward refresh these included figure messages by receiving the strategy of communicating encryption. Besides, this

development is demonstrated secure in the standard model. Hypothetical investigation and trial come about to demonstrate that FDR-CP-ABE beats the past disavowal related techniques.

Balu and Kuppusamy [25] proposed a CP-ABE, which depends on a current secret sharing strategy named Linear Integer Secret Sharing Scheme. In this plan, the encryption can indicate the entrance approach as far as LISS network M, over the attribute in the framework. The strategy is specifically secure under Decisional Bilinear Diffie Hellman (DBDH) presumption.

Zhang et al. [26] proposed a CP-ABE structure which highlighted steady calculation cost and reliable size ciphertexts. The suggested CP-ABE system is established specific secure in the irregular oracle model under the choice n-BDHE suspicion, where n signifies the total quantity of features in the universe. It can effectively support AND-gate access to strategies with different attribute esteems and trump cards. Hypothetical examination and test come about to demonstrate that the proposed system is to a great degree reasonable for data sharing in mobile clouds.

Huang et al. [6] proposed a safe and proficient data collaboration scheme, in which fine-grained access to control of ciphertext and secure information composing task can be managed in light of ABE in addition to signature based on attribute respectively. Keeping in mind the end goal to diminish the attribute authority from substantial key administration load, our plan utilizes a full delegation mechanism based in Hierarchical ABE (HABE). Further, this investigation proposed a halfway decoding and marking development by assigning the greater part of the computation overhead on a client to cloud service provider.

Lai et al. [27] considered a novel requirement of ABE by way of outsourced decoding and its verifiability. Casually, verifiability assured that a consumer could capably test if the conversion were done appropriately. In this study, the correct ABE model was assumed with demonstrable outsourced decryption then suggested a concrete arrangement. The verification of novel scheme was safe as well as verifiable, without trusting on random oracles. In conclusion, the implementation of the proposed scheme was showed an outcome of performance measurements, which specified a substantial decrease in computing resources imposed on users.

Wang et al. [28] constructed a searchable ABE system by attribute revocation in cloud storage. The keyword search in this scheme was attributing based with access control, when the search prospers, the cloud server returns the equivalent ciphertext to a user, and the user could unconditionally decrypt the ciphertext. Also, this scheme supported multiple keywords search, which created the scheme more useful.

Sajitha and Catherine [29] made a scheme, which has numerous qualities like extraordinary performance, fine-grained access control, scalability and full delegation. HABE structure was also collusion resistant was verified to be safeguarding against adaptively selected plaintext attacks beneath the Bilinear Diffie-Hellman (BDH) assumption and the model of a random oracle.

Green et al. [30] suggested an outsourcing decryption ABE scheme. In their structure, the traditional private keys were separated into user and transformation keys. Therefore, complex decryption computations were out sourced to the cloud server, and users only want one exponentiation process to recuperate the plaintext. But,

the scheme cannot apply to multi-authority systems. Based on this technique, Yang and Jia [31] put advancing two multi-authority CP-ABE schemes which maintained outsourced decryption.

Li et al. [32] also recommended an outsourced ABE structure that maintained both outsourced key-issuing as well as decryption. Alternatively, the accuracy of outcomes was not deliberated from the cloud server. To explain this issue, Lai et al. [27] presented the verifiability of ABE and suggested a provable outsourced decryption ABE scheme. Nonetheless, in their scheme, both the ciphertext as well as the computation of encryption length were doubled.

Li et al. [7, 33] presented an outsourcing ABE structure with check ability which kept both outsourced key-issuing and decryption. But, the ciphertext size and the number of expensive pairing computations augmented with the number of attributes. To report this issue, two ABE structures [7, 33, 34] in which the ciphertext size is constant were put forward. However, their structures were not beneficial to ABE structures with Linear Secret Sharing Schemes (LSSS).

Mao et al. [35] recommended an overall notion of ABE in which CPA-secure construct has more compressed ciphertext and less computational budgets. Customers only require a constant quantity of simple calculations for the purpose of ciphertext decryption.

Aujla et al. [36] proposed Secure Storage, Verification, And Auditing (SecSVA) of big data in the background of a cloud. This scheme included the module known as a secure data deduplication framework which is based on an attribute in order to store the data storage in the cloud. It also included an identity authentication which is based on Kerberos and verification, then Merkle hash-tree-based trusted third-party checking on a cloud. From the study, it is obvious that SecSVA could offer secure third-party checking with integrity maintenance through multiple domains in the cloud background.

Almorsy et al. [37] presented a systematic study of security problem regarding the cloud. The issue was examined from the view of cloud design. The cloud offered features, the cloud investors, and the models of cloud-related to a provision of service. Based on this study the investigators developed a comprehensive description of the cloud security issue and important features that must be enclosed by any suggested solution for safety.

Puthal et al. [38] proposed a new load balancing method to validate the Edge Data centers (EDCs) and discovered less loaded EDC for allocation of a task. The suggested load balancing method is more effective compared to further surviving methods in discovering less loaded EDC for allocating the task. The recommended tactic not only enhanced the efficiency of balancing of load but also maintained the protection by validating the EDCs regarding the destination.

Manogaran et al. [39] suggested Meta Cloud Data Storage Design for guarding Big Data in the Environment of Cloud Computing. Map Reduce context was utilized to discover the number of customers who were registered into the data center of the cloud. Suggested framework guarded the planning of different data components to every supplier with a Meta Cloud Data Storage interface. However this suggested tactic needed heavy implementation effort, it offered valuable data for

cloud computing environment that can have great influence on the subsequent genera-
tion systems. The upcoming work is to prolong the recommended design for real-time
handling of streaming information.

Zhu et al. [40] designed Generic verifiable Searchable Symmetric Encryption
scheme (GSSE) which was a dynamically verifiable SSE scheme, which can be
applied to any SSE schemes with a three-party model and does not required modi-
fications on them. By building authenticators and a proof index, GSSE provided
efficient search result verification, while preventing data freshness attacks and data
integrity attacks in SSE. The experimental results demonstrated that GSSE introduced
acceptable overhead in authenticating search results.

Bonomi et al. [41] suggested Attribute-Based Access Control (ABAC) founded on
attributes to define access instructions and trusts on them to make approval verdicts.
The current ABAC systems have two drawbacks: low efficiency in rule execution and
high difficulty in rule writing. A lightweight ABAC scheme was suggested which
used Python logical expression to define access rule and utilizes the eval function to
implement the rule. Considered some techniques to simplify rule writing and verified
out comes presented that suggested rule could overcome the beyond two deficiencies.

Tiwari and Gangadharan [42] intended an active fine-grained revocation appa-
ratus, which permitted not only effective attribute-level revocation but also effi-
cient policy-level revocation to attain backward and forward secrecy. Furthermore,
they utilized a multiauthority key attribute center in the stage of key generation
to overcome the single-point performance bottleneck problem and the key escrow
issue. By formal security study, they exemplified that there commended scheme
attained privacy, secure key distribution, multiple collusions resistance, and policy-
or attribute-revocation security. By complete performance and implementation study,
the suggested scheme enhanced the practical efficiency of storing, computation price,
and communication price associated with the additionally related schemes.

Kamakshaiah et al. [43] suggested and technologically advanced Transmitted
Team Key Management (TTKM). A secret trust key proprietor was assigned to
every operator in the group. At this time, operator desired only transmission message
amongst information distribution in a cloud. Also examined the confidentiality of
proposed TTKM plan and associated with current SABE security plans in distributed
information distribution. The investigational outcomes presented efficient access
control of information via authorized security concerns.

2.3 *Identity-Based Encryption (IBE)*

Cloud computing gives a versatile and accommodating way for information sharing,
which brings diverse favorable circumstances for both people in public as well as
an individual. In any case, there exists trademark security for customers to clearly
outsource the necessary data to the cloud server since the information consistently
contains vital info. Moreover, it is vital to put cryptographically updated access
to control on the regular data. IBE is an accomplished crypto graphical unique to

develop a rational information sharing system. Regardless, get the opportunity to control isn't static. That is, the time when some customer's endorsement is passed, there should be a part that can empty him/her from the system. Accordingly, the repudiated customer can't access both the when shared information [44].

Wei et al. [45] recommended a notion named Revocable-Capacity IBE (RS-IBE). It can offer the forward/in reverse safety of ciphertext by way of given that the operations of client rejection and ciphertext recover at the similar time. Also, displayed a compacted growth of RS-IBE, and proved its safety in the considered safety model. The execution correlations demonstrate that the proposed RS-IBE system has focal points as far as usefulness and effectiveness, and accordingly is attainable for a pragmatic and cost-effective data sharing framework. At long last, we give usage after effects of the proposed plan to exhibit its practicability.

Liang et al. [46] gave an agreed answer for tackle the efficiency issue acquired by repudiation and proposed the primary cloud-based revocable identity-based proxy re-encryption (CR-IB-PRE) system that backings client disavowal yet in addition appointment of decoding rights. Regardless of a client is renounced or not, towards the finish of a given day and age the cloud going about as an intermediary will re-encrypt all ciphertexts of the client under the present era to whenever period. In the event that the client is repudiated in the pending era, he can't decode the ciphertexts by utilizing the lapsed private key any longer.

Liang et al. [46] has genuine security traps, for example, re-encryption key imitation and conspiracy assault, which leads to disavowed clients can decrypt any ciphertext in regards to their personalities whenever period and after that re-imagined the language syntax and security model of CR-IB-PRE system and proposed an enhanced CR-IB-PRE scheme from bilinear pairings. The enhanced plan accomplishes collusion protection, as well as takes bring down decryption computation and accomplishes consistent size re-encoded ciphertext. At long last, this investigation demonstrated the enhanced CR-IB-PRE system is adaptively secure in the standard model under DBDH suspicion.

Wang et al. [47] proposed another versatile RIBE conspire with decryption key contact flexibility by consolidating Lewko and Waters' IBE scheme and finish subtree method, and ended up being semantically secure utilizing double framework encryption method. As associated with surviving flexible as well as semantically secure RIBE plans, this recommended RIBE strategy is further useful in terms of ciphertext size, open parameters size and decryption budget at price of a little looser security failure. This is the primary development of versatile and semantically secure RIBE plot with constant size open framework parameters. Repudiation usefulness is vital and critical to character-based cryptosystems. Revocable personality based encryption (RIBE) has pulled in a considerable measure of concern as of late, various RIBE plans have been proposed in writing yet seemed to be either shaky or useless.

Pathare and Chouragade [48] discussed about the promising access control for information sharing in a cloud which is character-based encryption and present the proficient disavowal conspire for the framework which is revocable-capacity personality based encryption plot. It gives both forward as well as the reverse safety of ciphertext. At that point, this exploration examine had a look at the design and

steps associated with character-based encryption. Lastly, the proposed frameworks suggested that give secure record sharing framework utilizing personality based encryption conspire.

New construction of CCA-secure IBE scheme tolerating continuous-leakage attacks in the standard model was proposed by Zhou et al. [49] and its security was showed in the selective-ID security design founded on the hardness of decisional bilinear Diffie–Hellman theory, which was a classical static assumption. In this structure, the competitor unable to obtain any revelation on the private key from the corresponding ciphertext, since every element in the ciphertext was random in the opponent's view. The outstanding benefit of the structures was the key leakage ratio, which was considered as best one among the preceding leakage-resilient IBE constructions.

Gai et al. [50] proposed a Security-Aware Efficient Data Sharing and Transferring model, which was intended for safeguarding cloud-based Intelligent Transportation Systems (ITS) implementations. In relating this method, secure real-time multimedia data sharing and transferring was aimed and obtained. The investigational assessment has exposed that the suggested model offered an actual performance in safeguarding communications for ITS.

Kavuri et al. [51] suggested an innovative integrity procedure with ABE model to safeguard privacy for high dimensional information protection on cloud storage. The focal aim of this model was to store, communicate and save the high dimensional cloud information with low computational time and protection. Investigational outcomes presented that the suggested model has extraordinary data scalability, less computational time and low memory usage related to outdated models regarding confidentiality protection which was based on the cloud.

Sookhak et al. [52] provided a complete study on access control systems which were based on attributes and associated every scheme's functionality and feature. Also offered a thematic classification of attribute-based approaches built on significant parameters, like access control mode, design, revocation mode, etc. Studied dissimilar ABE techniques to determine the benefits in addition to drawbacks, the importance, and necessities, and recognized the gaps in the studies. Lastly, the study presented vulnerable difficulties and encounters for additional investigations.

Nepal et al. [53] presented an innovative scheme and analogous protocols to offer secure sharing and deletion of documents on public cloud facilities. This system utilizes AES for encryption of information to attain scalability. It also supported access control rules which are based on identity with public–private key pairs for flexibility. The proposed design utilized independent services regarding key management for supporting secure removal, in which the data is irretrievable once the keys were destroyed.

Imran et al. [54] addressed the issue regarding the verification of data integrity in the environment of cloud computing by way of suggesting a design. By using this design, users could be capable of scrutinizing the integrity of their information which was presented in clouds. Furthermore, the operators can track the degradation of data integrity if arisen. For this necessity, an innovative idea was used in the Cloud computing called "Data Provenance". The recommended system was capable of lessening the requirement of any third party services, extra hardware support and the duplication of data items on the client side for checking the integrity (Table 1).

3 Conclusion

In spite of the information that the utilization of cloud computing has rapidly prolonged, and its safety is however considered the actual concern. Clients would select not to lose their private data because of malignant insiders in the cloud. What's more, the loss of service accessibility has caused numerous issues for a countless number of clients recently. Moreover, data interruption prompts numerous issues for the clients of data computing. In this review paper, we thought about the distinctive cryptographic methodologies for secure information partaking in distributed computing. We additionally surveyed the principle interruption, identification, and counteractive prevention systems and investigated their viability regarding the working system, segments, and adaptability. At that point, we talk about the limitations and security difficulties of the key aggregate cryptosystem, ABE, and IBE of information in data computing. Next, we exhibited recent related works alongside security solutions and compressed the solutions in table format with the goal that the per users in this field can compare, examine and coordinate further research exercises. Finally concluded that the survey with some open issue and challenges need to be further investigated such as security and efficiency improvements which is required in the cryptographic techniques. Further, the data loss is also needed to focus for data sharing in cloud applications.

Table 1 Comparative study of various security schemes for data sharing in cloud computing

Schemes	Encryption type	Advantages	Limitations
Key aggregate cryptosystem (KAC)	Asymmetric	Decryption rights for any set of ciphertext are probable	Insufficient ciphertext classes for the future extension
KAC for scalable data sharing in cloud storage	Asymmetric	More flexible than hierarchical key assignment which can only save spaces if all key-holders share a related set of privileges	In cloud storage, the number of ciphertexts generally develops quickly. Thus we have to reserve sufficient ciphertext classes for the future extension
Key-aggregate authentication cryptosystem (KAAC)	Asymmetric	It supports safe, effective, and flexible sharing of information through cloud storage	The size of public system consideration had a linear association with the number of classes of ciphertext
Revocable key-aggregate cryptosystem (RKAC)	Asymmetric	The suggested scheme decreases the budget of storage in addition to broadcast and understands the user access control efficiently	Hard to build a CPA security structure
New attribute-based data sharing scheme	Asymmetric	The recommended scheme excludes a majority of the computation task by adding public system parameters besides moving partial encryption computation offline	Low fine grained access control, average efficiency
Ciphertext-policy attribute-based encryption (CP-ABE)	Symmetric	The storage budget of cipher text and time cost in encryption can be avoided	Average realization of complex access control Not efficient for modern enterprise environments
CP-ABE based on linear integer secret sharing scheme (LISS)	Asymmetric	Very expressive and provably safe under the decisional bilinear Diffie–Hellman assumption	High computational time and hard to build the security scheme
Generic attribute-based data sharing system based on CP-ABE	Symmetric	Small and constant cost required for computation	Excessive ciphertext size and price of computation
RS-IBE	Asymmetric	Profits in terms of efficacy as well as operation and thus more possible for applications related to real-world	Communication costs are higher and is un-scalable

Table 1 (continued)

Schemes	Encryption type	Advantages	Limitations
RIBE	Symmetric	More efficient regarding a size of ciphertext, public parameters in addition to decryption price	Does not provide the correctness property
KAS for safe distribution of cloud information	Asymmetric	This innovation can combine any set of secret keys and create them as a single compact key	The compressed aggregate key can be aptly referred to other users or be saved in a smart card with very limited secure storage
KP-ABE	Asymmetric	The suggested system offers a fine-grained system for access control to improve safety and confidentiality of big data shared over the cloud computing	There is no suppleness in controlling attribute
Role-based access control (RBAC) scheme	Role-based	RBE structure accomplishes effective revocation of user	The cloud provider (who stores the data) will not be able to see the content of the data if the provider is not given the appropriate role
Generic verifiable searchable symmetric encryption scheme (GSSE)	Symmetric	GSSE introduces acceptable overhead in verifying search results	It is not suitable for the large scale databases. Data integrity attacks
Attribute-based access control (ABAC)	Asymmetric	The system is not only safe but also easy to use	Complexity Scalability
CPAB proxy re-encryption	Symmetric	Develops the practical efficiency of storing, computation in addition to communication price compared to the additional associated structures	Prone to collusion attack

References

1. Yuen TH, Chow SS, Zhang Y, Yiu SM (2012) Identity-based encryption resilient to continual auxiliary leakage. In: Annual international conference on the theory and applications of cryptographic techniques. Springer, Berlin, pp 117–134
2. Li J, Yan H, Liu Z, Chen X, Huang X, Wong DS (2017) Location-sharing systems with enhanced privacy in mobile online social networks. IEEE Syst J 11(2):439–448
3. Li P, Li J, Huang Z, Li T, Gao CZ, Yiu SM, Chen K (2017) Multi-key privacy-preserving deep learning in cloud computing. Futur Gener Comput Syst 74:76–85

4. Li X, Tang S, Xu L, Wang H, Chen J (2017) Two-factor data access control with efficient revocation for multi-authority cloud storage systems. IEEE Access 5:393–405

5. Liang X, Cao Z, Lin H, Xing D (2009) Provably secure and efficient bounded ciphertext policy attribute based encryption. In: Proceedings of the 4th international symposium on information, computer, and communications security. ACM, pp 343–352

6. Huang Q, Yang Y, Shen M (2017) Secure and efficient data collaboration with hierarchical attribute-based encryption in cloud computing. Futur Gener Comput Syst 72:239–249

7. Li J, Chen X, Li M, Li J, Lee PP, Lou W (2014) Secure deduplication with efficient and reliable convergent key management. IEEE Trans Parallel Distrib Syst 25(6):1615–1625

8. Thilakanathan D, Chen S, Nepal S, Calvo RA (2014) Secure data sharing in the cloud. In: Security, privacy and trust in cloud systems. Springer, Berlin, pp 45–72

9. Kore BM, Jadhav A, Pottigar VV (2016) A literature survey on secure data sharing in cloud storage with key aggregate cryptosystem

10. Chu CK, Chow SS, Tzeng WG, Zhou J, Deng RH (2014) Key-aggregate cryptosystem for scalable data sharing in cloud storage. IEEE Trans Parallel Distrib Syst 25(2):468–477

11. Kate MK, Potdukhe SD (2014) Data sharing in cloud storage with key-aggregate cryptosystem. Int J Eng Res Gen Sci 2(6):882–886

12. Guo C, Luo N, Bhuiyan MZA, Jie Y, Chen Y, Feng B, Alam M (2017) Key-aggregate authentication cryptosystem for data sharing in dynamic cloud storage. Future Gener Comput Syst

13. Gan Q, Wang X, Wu D (2017) Revocable key-aggregate cryptosystem for data sharing in cloud. Secur Commun Netw

14. Chow SS, Chu CK, Huang X, Zhou J, Deng RH (2012) Dynamic secure cloud storage with provenance. In: Cryptography and security: from theory to applications. Springer, Berlin, pp 442–464

15. Chow SS, He YJ, Hui LC, Yiu SM (2012) Spice–simple privacy-preserving identity-management for cloud environment. In: International conference on applied cryptography and network security. Springer, Berlin, pp 526–543

16. Patranabis S, Shrivastava Y, Mukhopadhyay D (2015) Dynamic key-aggregate cryptosystem on elliptic curves for online data sharing. In: International conference in cryptology in India. Springer, Cham, pp 25–44

17. Kumar A, Dhanasekar S (2015) A literature survey on key aggregation system for secure sharing of cloud data

18. Pawar N, Ali SM, Jaid S, Sengar P (2016) Review on: multiple data sharing using key aggregate cryptosystem in cloud storage

19. Lee CC, Li CT, Chiu ST, Chen SD (2016) Time-bound key-aggregate encryption for cloud storage. Secur Commun Netw 9(13):2059–2069

20. Shanthi S, Kannan RJ, Santhi S (2018) Efficient secure system of data in cloud using steganography based cryptosystem with FSN. Mater Today Proc 5(1):1967–1973

21. Li T, Liu Z, Jia C, Fu Z, Li J (2018) Key-aggregate searchable encryption under multi-owner setting for group data sharing in the cloud. Int J Web Grid Serv 14(1):21–43

22. Bethencourt J, Sahai A, Waters B (2007) Ciphertext-policy attribute-based encryption. In: IEEE symposium on security and privacy, 2007, SP'07. IEEE, pp 321–334

23. Wang S, Liang K, Liu JK, Chen J, Yu J, Xie W (2016) Attribute-based data sharing scheme revisited in cloud computing. IEEE Trans Inf Forensics Secur 11(8):1661–1673

24. Zhang Y, Chen X, Li J, Li H, Li F (2014) Attribute-based data sharing with flexible and direct revocation in cloud computing. KSII Trans Internet Inf Syst 8(11):4028–4049

25. Balu A, Kuppusamy K (2014) An expressive and provably secure ciphertext-policy attribute-based. Inf Sci 276:354–362

26. Zhang Y, Zheng D, Chen X, Li J, Li H (2016) Efficient attribute-based data sharing in mobile clouds. Pervasive Mob Comput 28:135–149

27. Lai J, Deng RH, Guan C, Weng J (2013) Attribute-based encryption with verifiable outsourced decryption. IEEE Trans Inf Forensics Secur 8(8):1343–1354

28. Wang S, Zhao D, Zhang Y (2017) Searchable attribute-based encryption scheme with attribute revocation in cloud storage. PLoS ONE 12(8):e0183459
29. Sajitha VS, Catherine VR (2017) Hierarchical attribute-based encryption: a survey
30. Green M, Hohenberger S, Waters B (2011) Outsourcing the decryption of abe ciphertexts. In: USENIX security symposium, vol 2011, No 3
31. Yang K, Jia X (2012) Attributed-based access control for multi-authority systems in cloud storage. In: 2012 IEEE 32nd international conference on distributed computing systems (ICDCS). IEEE, pp 536–545
32. Li J, Chen X, Li J, Jia C, Ma J, Lou W (2013) Fine-grained access control system based on outsourced attribute-based encryption. In: European symposium on research in computer security. Springer, Berlin, pp 592–609
33. Li J, Huang X, Li J, Chen X, Xiang Y (2014) Securely outsourcing attribute-based encryption with checkability. IEEE Trans Parallel Distrib Syst 25(8):2201–2210
34. Chen Y, Song L, Yang G (2016) Attribute-based access control for multi-authority systems with constant size ciphertext in cloud computing. China Commun 13(2):146–162
35. Mao X, Lai J, Mei Q, Chen K, Weng J (2016) Generic and efficient constructions of attribute-based encryption with verifiable outsourced decryption. IEEE Trans Dependable Secure Comput 13(5):533–546
36. Aujla GS, Chaudhary R, Kumar N, Das AK, Rodrigues JJ (2018) SecSVA: secure storage, verification, and auditing of big data in the cloud environment. IEEE Commun Mag 56(1):78–85
37. Almorsy M, Grundy J, Müller I (2016) An analysis of the cloud computing security problem. arXiv preprint arXiv:1609.01107
38. Puthal D, Obaidat MS, Nanda P, Prasad M, Mohanty SP, Zomaya AY (2018) Secure and sustainable load balancing of edge data centers in fog computing. IEEE Commun Mag 56(5):60–65
39. Manogaran G, Thota C, Kumar MV (2016) Meta cloud data storage architecture for big data security in cloud computing. Proc Comput Sci 87:128–133
40. Zhu J, Li Q, Wang C, Yuan X, Wang Q, Ren K (2018) Enabling generic, verifiable, and secure data search in cloud services. IEEE Trans Parallel Distrib Syst
41. Bonomi F, Bhagra P, Chinnakannan P, Bhagavatula R, Kaliannan S (2018) U.S. patent application no. 15/785,290
42. Tiwari D, Gangadharan GR (2018) Sec cloud sharing: secure data sharing in public cloud using ciphertext-policy attribute-based proxy re-encryption with revocation. Int J Commun Syst 31(5):e3494
43. Kamakshaiah K, Rao KV, Subrahmanyam M (2018) SABE: efficient and scalable-filtered access control in distributed cloud data storage. In: Smart computing and informatics. Springer, Singapore, pp 31–42
44. Anthes G (2010) Security in the cloud. Commun ACM 53(11):16–18
45. Wei J, Liu W, Hu X (2016) Secure data sharing in cloud computing using revocable-storage identity-based encryption. IEEE Trans Cloud Comput
46. Liang K, Liu JK, Wong DS, Susilo W (2014) An efficient cloud-based revocable identity-based proxy re-encryption scheme for public clouds data sharing. In: European symposium on research in computer security. Springer, Cham, pp 257–272
47. Wang C, Li Y, Xia X, Zheng K (2014) An efficient and provable secure revocable identity-based encryption scheme. PLoS ONE 9(9):e106925
48. Pathare KG, Chouragade PM (2017) Reliable data sharing using revocable-storage identity-based encryption in cloud storage. In: 2017 International conference on recent trends in electrical, electronics and computing technologies (ICRTEECT). IEEE, pp 173–176
49. Zhou Y, Yang B, Mu Y (2018) Continuous leakage-resilient identity-based encryption without random Oracles. Comput J 61(4):586–600
50. Gai K, Qiu L, Chen M, Zhao H, Qiu M (2017) SA-EAST: security-aware efficient data transmission for ITS in mobile heterogeneous cloud computing. ACM Trans Embedded Comput Syst (TECS) 16(2):60

51. Kavuri SK, Kancherla GR, Bobba B (2017) An improved integrated hash and attributed based encryption model on high dimensional data in cloud environment. Int J Electr Comput Eng (IJECE) 7(2):950–960
52. Sookhak M, Yu FR, Khan MK, Xiang Y, Buyya R (2017) Attribute-based data access control in mobile cloud computing: taxonomy and open issues. Futur Gener Comput Syst 72:273–287
53. Nepal S, Friedrich C, Wise C, Sinnott RO, Jang-Jaccard J, Chen S (2016) Key management service: enabling secure sharing and deleting of documents on public clouds. Serv Trans Cloud Comput (STCC) 4(2):2016
54. Imran M, Hlavacs H, Haq IU, Jan B, Khan FA, Ahmad A (2017) Provenance based data integrity checking and verification in cloud environments. PLoS ONE 12(5):e0177576

Sensitivity Studies on the Behaviour of Bistable Cross-Ply Laminates Using Monte Carlo Simulation

K. S. Suraj, P. M. Anilkumar, C. G. Krishnanunni, and B. N. Rao

1 Introduction

Shape changing ability of bistable unsymmetrical laminate in response to different operating conditions have received growing interest in various field, including aerospace structures, wind turbines, solar tracking device, and robotics [1]. Unsymmetrical bistable laminates exhibit two stable shapes at the end of the curing process, where switching from one stable shape to another stable shape can be achieved by appropriate external energy actuation. Research on the analysis and design of bistable laminates for morphing applications is of considerable interest and well documented in the literature [2].

Energy-based semi-analytical models are widely used to predict bistable configurations and the corresponding snap-through requirements [3]. Due to the easiness of the formulation and lower computational requirements, semi-analytical models can be used for extensive parametric and optimization studies. Several semi-analytical models have been developed based on the Rayleigh–Ritz technique, where the geometrical non-linearity has been taken into account. To accurately evaluate the energy components and to predict the bistable configurations, semi-analytical formulations require higher-order polynomial approximations for the displacement fields, which lead to an increase in the computational cost. Recently, Wu et al. [4] developed an efficient analytical model to predict the behaviour of bistable laminates

K. S. Suraj (✉) · P. M. Anilkumar · B. N. Rao
Structural Engineering Division, Department of Civil Engineering, Indian Institute of Technology Madras, Chennai 600036, India
e-mail: surajksingh201@gmail.com

C. G. Krishnanunni
Department of Aerospace Engineering and Engineering Mechanics, University of Texas at Austin, Austin, TX 78712, USA

accounting for the difficulties mentioned above. The model has shown higher accuracy in comparison to the experimental and finite element observations. Further, this model has been extended to study the behaviour of bistable unsymmetrical laminates under different working conditions and has shown reasonably good accuracy in predicting the results [5, 6].

Although extensive literature has been reported to study the behaviour of bistable unsymmetrical laminates, the effect of small uncertainties in the design variables on the bistable nature and snap-through behaviour is still not much addressed in the literature. These uncertainties significantly influence the structural performance of adaptive structural components designed with bistable laminates. Che et al. [7] investigated the effect of variations in thickness and length on the stable configuration using analytical, finite element, and experimental studies. Brampton et al. [8] considered $\pm 5\%$ uncertainties in each design parameter to study the sensitivity of the curved shape using total potential energy and the Rayleigh–Ritz method. Recently, Emam et al. [9] performed a parametric study to investigate the curvature variation with the number of plies, aspect ratio of laminate, width-to-thickness ratio, moduli of elasticity ratio, and the ratio of the thermal coefficient. In continuation, Suraj et al. [10] considered $\pm 30\%$ perturbation in material parameters to study the sensitivity of the snap-through-force and out-of-plane displacement using the finite element model. The results show that the transverse modulus of elasticity and the thermal coefficient significantly affect both snap-through force and out-of-plane displacement.

Most of the reported studies related to the effect of uncertainties in the design parameters on the bistable behaviour are found to be deterministic. Few researchers explored the applicability of reliability and probability concepts in examining the same. Saberi et al. [11, 12] studied the bistability probability assuming design parameters as random variables and investigated the reliability by combining minimum potential energy formulation with the Monte Carlo approach. Although sensitivity analysis has been performed considering the individual perturbation in design variables, sensitivity analysis considering uncertainty in all design variables has not been done. The present study aims to perform sensitivity analysis on the deformation of unsymmetrical bistable laminates to uncertainty in design variables through an established semi-analytical formulation. Subsequently, Monte Carlo simulation has been used to predict the first and second-moment characteristics of bistable composite laminate responses by assuming an underlying probabilistic distribution of the input design variables.

2 Theoretical Formulation

2.1 Semi-Analytical Model

A semi-analytical model has been taken from Kumar et al. [5], which was extended from the works of Wu et al. [4] for the analysis of unsymmetrical bistable laminate. A curing temperature of 180 °C is imposed on the unsymmetrical bistable laminate and bought down to room temperature of 20 °C to obtain one of the cured shapes. Point load at the corners of the laminate is applied to trigger the snap-through process.

After the cool-down step the constitutive behaviour of bistable unsymmetrical laminate is represented as:

$$N(\varepsilon, \kappa) = A\varepsilon^0 + B\kappa - N^{th}, \quad M(\varepsilon, \kappa) = B\varepsilon^0 + D\kappa - M^{th} \tag{1}$$

where N represents the in-plane force resultant and M represents the bending moment resultant. ε^0 and κ represents the mid-plane strains and the bending curvatures. A, B, and D represents the membrane stiffness, the membrane bending-coupling matrix, and the bending stiffness matrix, respectively.

From Eq. 1, strain component can be derived as:

$$\varepsilon^0 = A^{-1}N + A^{-1}N^{th} - A^{-1}B\kappa = \varepsilon^m + A^{-1}N^{th} - A^{-1}B\kappa \tag{2}$$

where membrane strain field can be written as: $\varepsilon^m = A^{-1}N$.

The out-of-plane displacement function $w(x, y)$ is assumed as a quadratically varying curvature polynomial that satisfies the boundary condition of the laminate, fixed at the centre:

$$w(x, y) = c_{11}x^2 + c_{12}y^2 + c_{13}x^4 + c_{14}y^4 + c_{15}x^2y^2 \tag{3}$$

The assumed membrane strains are as follows:

$$\varepsilon_{xx}^m = c_1 + c_2 y^2 + c_3 y^4 + c_4 y^6 + c_5 x^2 y^2$$
$$\varepsilon_{yy}^m = c_6 + c_7 y^2 + c_8 y^4 + c_9 y^6 + c_{10} x^2 y^2 \tag{4}$$

The curvature field derived from the displacement (Eq. 3) field is represented as:

$$\kappa = \begin{bmatrix} \kappa_{xx} & \kappa_{xy} \\ \kappa_{yx} & \kappa_{yy} \end{bmatrix} = \begin{bmatrix} 2c_{11} + 12c_{13}x^2 + 2c_{15}y^2 & 4c_{15}xy \\ 4c_{15}xy & 2c_{12} + 12c_{14}y^2 + 2c_{15}x^2 \end{bmatrix} \tag{5}$$

The in-plane displacement can be computed using the expression for strain (Eq. 4):

$$u_0(x, y, z) = \int_L \left(\varepsilon_{xx}^0 - \frac{1}{2}\left(\frac{\partial w}{\partial x}\right)^2 \right) dx$$

$$v_0(x, y, z) = \int_L \left(\varepsilon_{yy}^0 - \frac{1}{2} \left(\frac{\partial w}{\partial y} \right)^2 \right) dy \tag{6}$$

The shear strain can be calculated from the equation below:

$$\gamma(x, y, z) = \frac{\partial u_0}{\partial y} + \frac{\partial v_0}{\partial x} + \frac{\partial w}{\partial x} \frac{\partial w}{\partial y} \tag{7}$$

Thus, the total potential energy of unsymmetrical bistable laminate during cool-down stage is given by:

$$\Pi = \iint_L \left(\frac{1}{2} \begin{bmatrix} \varepsilon_0 \\ \kappa \end{bmatrix}^T \begin{bmatrix} A & B \\ B & D \end{bmatrix} \begin{bmatrix} \varepsilon_0 \\ \kappa \end{bmatrix} - \begin{bmatrix} N^{th} \\ M^{th} \end{bmatrix}^T \begin{bmatrix} \varepsilon_0 \\ \kappa \end{bmatrix} \right) dx\, dy \tag{8}$$

The force and the moment represented by the N and M respectively are expressed as:

$$\left\{ N^{th} \right\} = \sum_{k=1}^n \Delta T \{Q\}_k \{\alpha\}_k (z_k - z_{k-1})$$

$$\left\{ M^{th} \right\} = \frac{1}{2} \sum_{k=1}^n \Delta T \{Q\}_k \{\alpha\}_k \left(z_k^2 - z_{k-1}^2 \right) \tag{9}$$

The potential energy (Eq. 8) can be expressed in the terms of unknown coefficients used in the displacement equations. The Rayleigh–Ritz method is used to minimize the potential energy ($\delta \Pi = 0$), and the deformed shapes of the unsymmetrical bistable laminate are obtained.

$$\frac{\partial \Pi_N(c)}{\partial c_i} = 0 \tag{10}$$

The set of non-linear equations obtained from Eq. 10 is solved using the Newton–Raphson technique to find the unknown coefficient. Further, the stability check has been performed by evaluating the Jacobian matrix (Eq. 11). For stable configurations, the corresponding Jacobian matrix is positive definite.

$$J = \frac{\partial^2 \Pi_N}{\partial c_i \partial c_j}, \quad i, j = 1, 2, 3, \ldots, n \tag{11}$$

2.2   Monte Carlo Simulation

The Monte Carlo simulation method is a very attractive numerical method to solve practical and complex problems and is used to predict the system behaviour assuming the pre-described probability distribution of design variables. It is an approximate method and the accuracy of results increases with the number of the generated samples. The set of values of design variables is sampled from a Gaussian distribution and the output responses are computed using the semi-analytical model. Statistical analysis has been performed on the set of output response variables to obtain their first and second-moment characteristics. Convergence studies of first and second-moment characteristics have been done to compute the numbers of samples required to predict the curvatures and the out-of-plane displacement with the desired accuracy.

Taylor's series approximation for curvatures and out-of-plane displacement about the standard design parameters can be written as:

$$f(x_0 + h) = f(x_0) + \frac{h}{1!}\nabla f + \frac{h^2}{2!}\nabla^2 f + \cdots \tag{12}$$

∇f and $\nabla^2 f$ are computed at $x = x_0$, where x_0 is the standard values of design variables, and h is small perturbation in x.

Linear approximation of function about $x = x_0$ is given as,

$$f(x_0 + h) \approx f(x_0) + h\nabla f \tag{13}$$

Expected value on both sides of the above equation gives

$$E[f(x_0 + h)] = E[f(x_0)] + E[h\nabla f], \text{ or}$$
$$E[f(x_0 + h)] = f(x_0) \tag{14}$$

where the following is used,

$$E[f(x_0)] = f(x_0) \text{ and}$$
$$E[h\nabla f] = \nabla f E[h] = 0 \tag{15}$$

simillarly, variance on both side of Eq. 13 results

$$\sigma[f(x_0 + h)] = \sqrt{(\nabla f)^2 \sigma_x^2} \tag{16}$$

where σ_x represents standard deviation assumed in the design variables.

The first order moment obtained from the Monte Carlo simulation is compared with standard values of the outputs variables and that will apprise the nonlinearity (second-order effects) present in the system near the design point.

3   Results and Discussions

A square CYCOM 977-2 lamina with a thickness of 0.210 mm is considered for the
present investigation (Fig. 1). A cross-ply stacking sequence [0/90] laminate with a
dimension of 135 mm × 135 mm is considered, and material properties are given in
Table 1.

3.1   Stable Configuration

Figure 2 depicts the two cylindrical stable shapes of the unsymmetrical cross-ply
laminate obtained from the semi-analytical model. These shapes are identical, with
principle curvatures orthogonal to each other.

To check the accuracy of the obtained results, the unsymmetrical bistable laminate
considering the geometrical non-linearity has also been modelled in the finite element
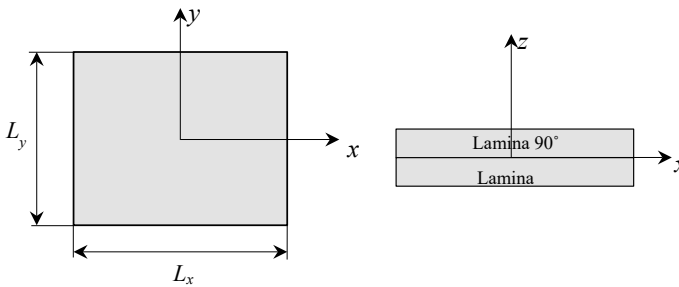
Fig. 1 Schematic representation of laminate selected for the analysis

Table 1 Material properties of the lamina used

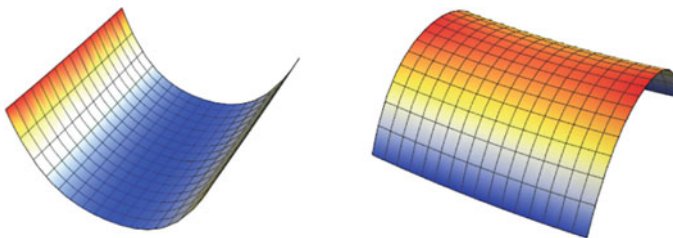| Property	E_{11} (GPa)	E_{22} (GPa)	G_{12} (GPa)	v_{12}	α_{11} (/°C)	α_{22} (/°C)
Value	156	8.35	4.2	0.33	$- 0.29 \times 10^{-6}$	24×10^{-6}

Fig. 2 Schematic representation of the bistable configurations after the curing process

Table 2 Out-of-plane displacement at corner for the first stable configuration

Lamina	Semi-analytical	FE	% error
0/90	14.248	13.675	4.19

package ABAQUS. Details of the finite element model can be seen at Anilkumar et al. [13]. The out-of-plane displacement of the first bistable shape contained after the curing process is given in Table 2, where the result from the semi-analytical model is in reasonably good agreement with the finite element result.

3.2 Effect on Curvature Due to Perturbation in Design Variables

A parametric perturbation study on the material parameters has been performed by Suraj et al. [10], where they showed that the perturbation in $E_{11}, E_{22}, \alpha_{22}$, and all their possible combinations have a significant effect on the out-of-plane displacement. A similar study has been performed to observe the sensitivity of curvature due to $\pm$ 10% perturbation in the design variables and the noticeable result has been shown in Fig. 3. Apart from E_{11}, E_{22}, and α_{22}, perturbation in L and t also have a significant influence on the curvature. A $\pm$ 10% perturbation in the L leads $-$ 28.6% and $+$ 43.5% change in the curvature K_{yy}, $\pm$ 10% perturbation in the t leads $-$ 10.5% and $+$ 12.7% change in the curvature K_{xx} and $+$ 26.2% and $-$ 23.5% change in the curvature K_{yy}.

Perturbation in some of the design variables significantly affects the out-of-plane displacement [10] and the curvature, as shown in Fig. 3. But practically, uncertainty can be possible in all design variables, so sensitivity analysis has been performed using Monte Carlo simulation assuming that the uncertain material and geometric parameters are random variables following Gaussian distribution based on the goodness-of-fit test result [14]. The statistical properties [mean and coefficient of variation (COV)] of the design variables are listed in Table 3.

Based on the convergence study of first and second-moment characteristics, 600 samples have been taken for the Monte Carlo simulation, and tailoring of samples has been done to avoid the negative samples. The first moment and COV of the output variables obtained from the set of outputs are presented in Table 4. The COV of the output variables suggests the dispersion of the probabilistic distribution. Among the out-of-plane displacement, curvature K_{xx} and K_{yy}, the dispersion present in the curvature K_{yy} is the most and least for the curvature K_{xx}.

The out-of-plane displacement and curvature K_{xx} and K_{yy} converge to a higher value than the standard. The relative contribution of the nonlinear term (second-order effect) for out-of-plane displacement, curvature K_{xx}, and K_{yy} are 0.01343, 0.01085, and 0.06495, respectively. Results obtained from the given semi-analytical model show that the contribution of the nonlinear term in *Taylor series* expansion
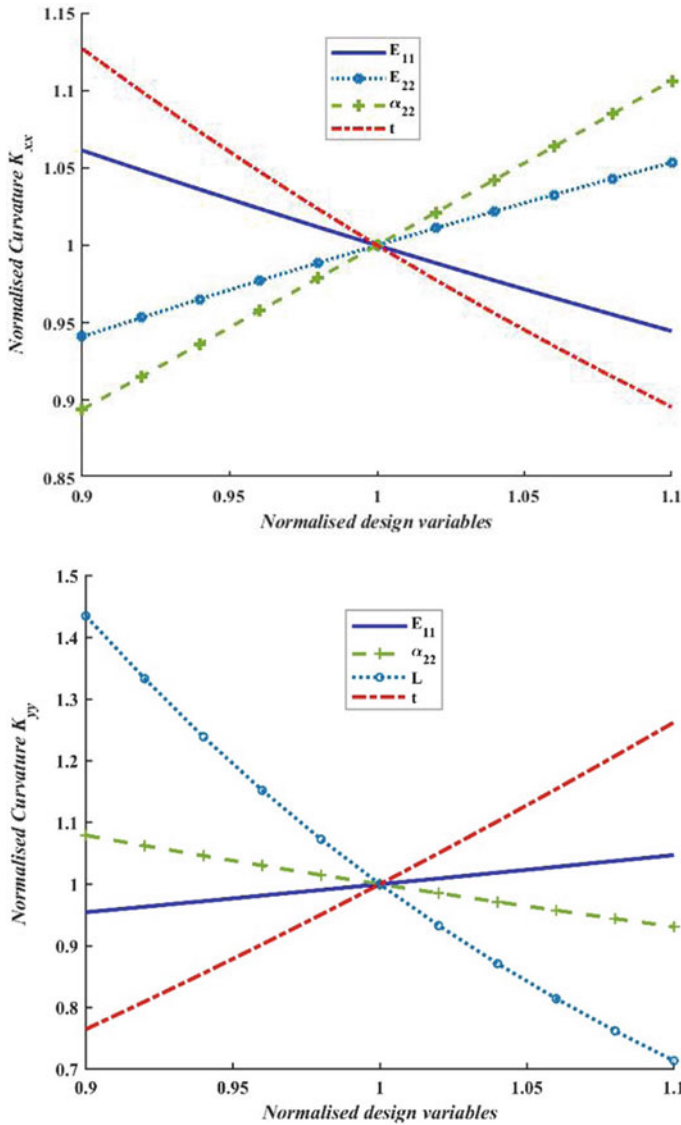
Fig. 3 Change in curvature K_{xx} and K_{yy} with the change in the design parameters

is significant for curvature K_{yy} and insignificant for out-of-plane displacement and curvature K_{xx}.

Further, the covariance of the distribution is given in Table 5, where 1, 2, and 3 represent out-of-plane displacement, curvature K_{xx}, and K_{yy}, respectively. The correlation coefficient gives an idea about the relationship between the output variables.

Table 3 Statistical properties of design parameters of the lamina used

Index	Property	Mean	COV	Distribution
1	E_{11}	156 GPa	0.1	Gaussian
2	E_{22}	8.35 GPa	0.1	Gaussian
3	ϑ_{12}	0.33	0.1	Gaussian
4	G_{12}	4.2 GPa	0.1	Gaussian
5	α_{11}	$- \ 0.29 \times 10^{-6}$ (/°C)	0.1	Gaussian
6	α_{22}	24×10^{-6} (/°C)	0.1	Gaussian
7	L_x	135 mm	0.1	Gaussian
8	L_y	135 mm	0.1	Gaussian
9	t	0.21 mm	0.1	Gaussian

Table 4 Mean and COV of outputs from Monte Carlo simulation

Output	Mean	COV
Out-of-plane displacement	14.442 mm	0.246
Curvature K_{xx}	6.268 mm^{-1}	0.159
Curvature K_{yy}	0.662 mm^{-1}	0.369

A positive correlation signifies that both variables are moving in the opposite direction. A negative correlation indicates that both variables are moving in the opposite direction, where correlation magnitude 1 signifies a perfectly positive or negative relation. The result depicts that the out-of-plane displacement is positively related to curvature K_{xx} and negatively associated with K_{yy}, whereas both curvatures correlated negatively.

It is to be noted that, in this study, the Gaussian random variables are transformed through a highly nonlinear map. Therefore, it is difficult to ascertain the output variables' distribution analytically. To understand the distribution of the output variables, a scatter plot of all the samples of out-of-plane displacement and curvatures considering 0.1 COV in design variables is shown in Fig. 4. It is seen that we have a skewed-right distribution for the output variable in this case. However, this may change if one assumes different probabilistic distribution of input variables.

Table 5 Correlation coefficient of the output variables

Index	Property	Numerical value
1	σ_{11}	3.551
2	σ_{22}	0.995
3	σ_{33}	0.244
4	σ_{12}	0.716
5	σ_{23}	$- \ 0.660$
6	σ_{13}	$- \ 0.563$
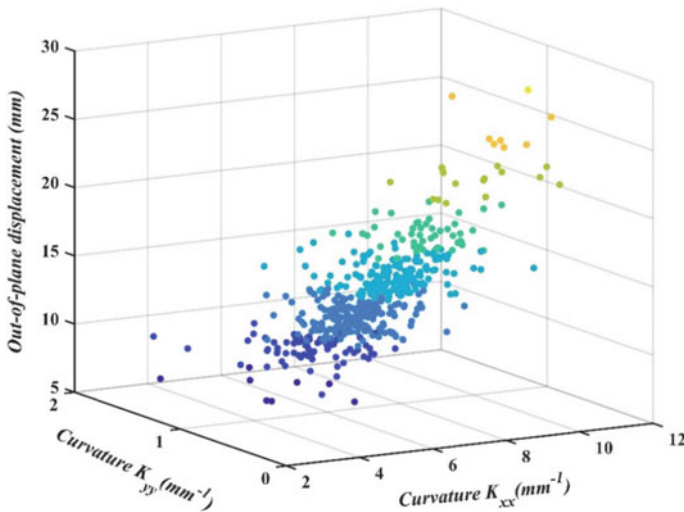
Fig. 4 Scatter plot of possible combinations of curvatures and out-of-plane displacement

4 Results and Discussions

An increase in the use of bistable composite structures in engineering applications demands studies of uncertainty in design variables. A parametric perturbation study on the design variables has been performed to study the sensitivity of the curvatures. Monte Carlo simulation has been performed assuming a Gaussian distribution of design variables to study the sensitivity of out-of-plane displacement and the curvatures considering perturbation in all design variables simultaneously. The studies have been performed on the semi-analytical method based on the Rayleigh–Ritz approach. The result obtained from the analysis reveals that the design variables E_{11}, E_{22}, α_{22}, L, and t significantly influence the curvatures. The mean obtained from the set of outputs from the Monte Carlo simulation reveals the nonlinearity present in the system. The contribution of nonlinear term present in curvature K_{yy} is significant. The first and second-moment characteristics obtained from Monte Carlo simulation give an idea about the range of the output variable (99.7% of data should be in the range of mean $\pm\, 3 \times$ standard deviation) and also about the probabilistic dispersion present in the output dataset. Note that the output data's dispersion depends upon the design variables' distribution. The correlation coefficient obtained reveals that out-of-plane displacement is positively and negatively correlated with the curvature K_{xx} and K_{yy}, respectively.

References

1. Zhang Z, Li Y, Yu X, Li X, Wu H, Wu H, Jiang S, Chai G (2019) Bistable morphing composite structures. A review. Thin-Walled Struct 142:74–79
2. Emam SA, Inman DJ (2015) A review on bistable composite laminates for morphing and energy harvesting. Appl Mech Rev 67.6
3. Haldar A, Groh RMJ, Jansen E, Weaver PM, Rolfe R (2020) An efficient semi-analytical framework to tailor snap-through loads in bistable variable stiffness laminates. Int J Solids Struct 195:91–107
4. Wu Z, Li H, Friswell MI (2018) Advance nonlinear dynamics modelling of bi-stable composite plates. Compos Struct 201:582–596
5. Kumar AP, Anilkumar PM, Haldar A, Scheffler S, Jansen EL, Rao BN, Rofles R (2021) Tailoring bistability in unsymmetrical laminates using an additional composite strip. Thin-Walled Struct 168:108212
6. Wu Z, Li H, Chen Y (2020) An improved model for unsymmetric plates. Compos Struct 252:112622
7. Che L, Fang G, Wu Z, Ma Y, Zhang J, Zhou Z (2020) Investigation of curing deformation behavior of curved fiber metal laminates. Compos Struct 232:111570
8. Brampton CJ, Betts DN, Bowen CR, Kim HA (2013) Sensitivity of bistable laminates to uncertainties in material properties, geometry and environmental conditions. Compos Struct 102:276–286
9. Emam S, Pherwani T, Anil A, Muhammed A (2021) Parametric study on the influence of material properties and geometry on the thermally induced bistability of composite laminates. J Mech Eng Sci 1–25
10. Suraj KS, Anilkumar PM, Rao BN, Krishnanunni CG (2022) Parametric perturbation studies on the behaviour of bistable unsymmetrical laminates. Aerospace and Associated Technology, Routledge, 2022, 414–419.
11. Saberi S, Abdollahi A, Friswell MI (2021) Probability analysis of bistable composite laminates using the subset simulation method. Compos Struct 271:114120
12. Saeid S, Abdollahi A, Inam F (2020) Reliability analysis of bistable composite laminates. AIMS Mater Sci 8(1):29–41
13. Anilkumar PM, Rao BN (2021) Impact of hygrothermal environment on the bistability of variable stiffness laminates with curvilinear fibre paths. Int J Adv Eng Sci Appl Math 13:33–48
14. Li X, Lv Z, Qiu Z (2018) A novel univariate method for mixed reliability evaluation of composite laminate with random and interval parameters. Compos Struct 203:153–163

Quantified Rams Based Infrastructure Asset Management

Somnath Pal

1 Introduction

Asset management policy helps in high quality services by tracking the inventory status, estimating lifecycle costs and planning financial investments. Asset maintenance covers a combination of all technical, administrative, and managerial actions during the system life cycle, from requirement specification preparation to realistic and time-bound evidence-based procurements, installation and maintenance policy decision making procedures and decommission. The key factors to be considered are the physical deterioration, obsolescence, operation, and system maintenance. Asset Management must be specific, measurable, actionable, realistic and time-bound. A Failure Reporting, Analysis and Corrective Action System (FRACAS) provides important information from failure analysis and corrective actions, based on management data reviews, for reliability data reports. Quantified Fault Tree Analysis (FTA) from an efficient FRACAS helps to identify fault prone modules in subsystems.

Main asset management tasks are preparing rigid unambiguous requirement specification, sub-system reliability and maintainability allocation according to their influences on the system function, system availability calculation, choosing interchangeable system architecture with redundancy as required, fixing sample size and acceptance based on lifecycle cost, choice of preventive and predictive maintenance policy, maintenance based on repair or replacement, location of spare parts and documented failure reporting analysis and corrective action systems. Supply contracts must include incentive on improved documented reliability data. Safety critical system asset management uses risk influencing factor, vulnerability and managerial oversight risk analyses. Acceptance testing should comply with reliability targets and stress testing targets.

S. Pal (✉)
Indian Railways, Secunderabad, India
e-mail: sompal8@gmail.com

Maintenance combines all administrative, technical and managerial actions during the life cycle and covers fault localization and restoration, enhanced Mean Time Between Failures (MTBF) for repairable and Mean Time To Failure (MTTF) for non-repairable components, reduced Mean Time To Repair (MTTR), resource management with least capital investment and human skill and aptitude management. It also reduces the duration of unplanned and planned outages. Asset management must identify the failure cause, probability and consequence, estimate the life-cycle cost, prioritize various renewal plans, award extensive performance-based maintenance contract registers.

System failures can be due to faults in design, manufacturing, installation and commissioning, operation, maintenance and decommissioning processes. Asset management policy can be based on following international standards like ISO 55001 [1] and EN 16646 [2].

All the calculations in this paper, are based on Reliability Engineering textbooks like Introduction to Reliability and Maintainability Engineering by Ebeling [3] and Practical Reliability Engineering by O'Connor [4]. The following flowchart explains the various activities in QRAMS based asset management.
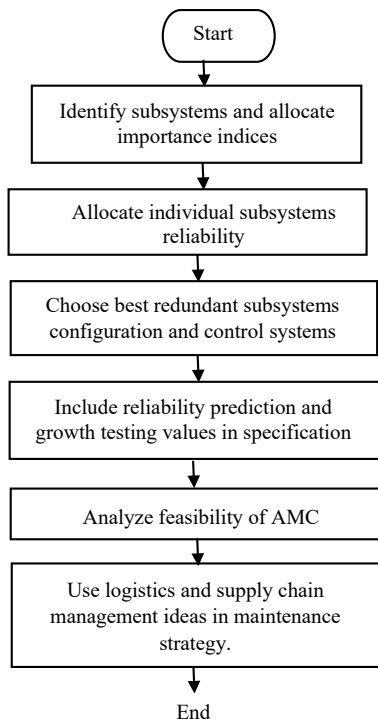
2 Quantified RAMS Based Asset Management

2.1 Benefits of Quantified RAMS Management

This technique uses mathematical calculations to reduce the likelihood of frequent failures, downtime duration and capital investment, maintaining proper alignment of maintenance resources. Lifecycle cost calculations help in choosing best asset procurement, maintenance policy with renewal plan, logistics and supply chain management, audit and review of activities. Quantified analysis helps to identify the key performance indicators and mathematically decides whether requirement specifications or design and installation processes are to be modified.

2.2 Quantified Asset Management Plan Attributes

The planning must have actual data based compliance with regulatory standards and must be fully traceable to RAMS specification goals. Calculations assist to compare performance of best spare parts procurement and storage policy. It also picks up the best offer and judge maintenance contracts. Renewal process for a system restoration to a condition like new, means replacing a failed component with one from same population. However, it might not result in keeping MTTF constant and guarantee services equal to the existing replaced component. All assumptions during replacement must be thoroughly analyzed and validated.

Treating all system hours as equivalent and all failures as equal ignores potential and likely real age effects. A better and less assuming approach to measure reliability is to analyze the data versus system age, i.e., apply time dependent reliability analysis.

Reliability Issues for a system of multiple systems are.

- The mean number of repairs, by time t
- The mean repair rate for all systems
- The expected variation in the mean number of repairs at a given time
- The distribution of failures across the identical systems.
- The expected time to 1st repair and kth repair
- The mean repair cost and whether the trend is changing
- The adequacy of spare parts
- Serviceability of the system for repairs.

2.3 Goals of Maintenance Management

Maintenance must be treated as an investment rather than a cost. Sustainable strategic plans in economic, environmental and social dimensions, set the management goals and activities. The maintenance team must strictly fulfill their allotted

responsibilities. Maintenance management goals can be classified as primary and secondary:

- Primary goals cover reliability, fault localization, accessibility, and diagnostics. It decides the repair level, chooses between repair and replacement, with the best repair option.
- Secondary goals cover repair resources with spare parts levels, human factors with competency level, ergonomics.

2.4 Tasks Associated with RAMS Management Plan

- A sustainable quantified RAMS plan, covers preparation of a rigid and unambiguous requirement specification, reliability and maintainability allocation to subsystems and availability calculation.
- Choosing interchangeability oriented best system architecture. Procurement policy including fixing sample size and acceptance test duration and acceptance of the best offer from suppliers.
- Choosing optimum life-cycle cost and adherence to specifications.
- Adapting the best maintenance practice with adequate spare parts provision
- Evaluating maintenance cost contract with suppliers, allowing incentive on improved reliability with documented data.
- Checking for compliance with reliability and maintainability specifications.

3 Quantified Life-Cycle RAMS Activities

3.1 Preparation of Specification

The various requirements included in the specification are related to system functions, operational procedures, subsystem interfaces, installation and commissioning, maintenance with on-site testing, RAM targets, power supply (if needed), system performance metrics, lifetime sustainability design modifications, physical constructions, environmental conditions, diagnostics and documentation.

System requirement Specifications must be cohesive, consistent, feasible, relevant, unique, unambiguous, verifiable and must be validated. Requirement specification for an equipment covers many aspects, each of which influences the performance of the system. The following requirements must be complied:

- Functional requirements
- System requirements
- System operation requirements
- Procedural requirements
- Interface requirements, if any

- RAM requirements
- Safety requirements, if the system is safety oriented
- Environmental condition requirements
- Maintenance requirements
- Power supply requirements, if any
- Installation, commissioning and on-site testing requirements
- Lifetime sustainability requirements
- Modification requirements
- Performance requirements
- Physical construction requirements
- Diagnostic requirements
- Documentation requirements.

RAM Specification should cover target system reliability, availability and maintainability, subsystem redundancy configuration, target maximum MTBF or MTTF and minimum MTTR, inspection intervals with durations and system integration RAM Qualification test criteria. It must also include reliability and maintainability demonstration clauses as per MIL HBKs 781 [5] and 471 [6] respectively. We are to consider that reliability reduces with time. If, a system has a constant failure rate of 3 per 10^7 h, and initial reliability of 0.99737, after 5 years, the reliability would come down to 0.98694.

Requirements written in natural language, could be interpreted differently by different professionals, engaged in development of a subsystem. Application of formal mathematical models like Markov Model and Petri Nets can reduce this problem. While specifications are prepared, care must be taken to avoid over-specification, which might increase the complexity of the system.

3.2 RAMS Allocation

During concept phase of the life-cycle of a complex system, allocations of RAM targets should be specified. When the system reliability is decided, all the sub-systems must be allocated their individual reliabilities in a least cost manner.

Reliability values between the subsystems are based on complexity, criticality, achievable reliability, or other factors that are deemed appropriate. Reliability is allocated usually to system, subsystem, module and component levels. The calculations depend on the system reliability block diagram. Each sub-system should be allotted its importance index to show its influence on the system reliability. The importance index wi for a particular subsystem, is allotted after studying failure history of similar systems installed and maintained earlier and in consultation with expert systems, if any. All the constituent systems or subsystems are treated to be independent and connected serially from reliability point of view. Subsystems having more failure effect probability, should have more reliability allocated.

Using Advisory Group on Reliability of Electronics Equipment (AGREE) method, which allows component operating time to be less than system operating time, individual sub-system failure rate λi is found for electronic subsystems using the following formula,

$$\lambda_i = -(1/t_i) \ln \left[1 - \left\{ (1 - (R^*)^{n/N} \right\}/wi_i \right] \tag{1}$$

where,

t_i operation time,
R^* System Reliability,
N total number of components,
n No. of similar components in sub-system.
wi_i Importance Index.

Example:

Find the individual subsystem (with Importance Index w_i) reliabilities for a Train Control System, that must have a reliability R^* of 0.99 after system operation time (t_i) of 10,000 h. There are 9 axle counters (wi = 0.95), 80 track circuits (wi = 0.0.85), 140 signals (wi = 0.95), 86 points (wi = 0.95) and 10 power supplies (wi = 1).

Answer:

Total number of units (N) = 325.

Results are calculated as per Eq. (1) from individual failure rate λi. We find failure rates and reliability after 10,000 h operation to be, as showed in Table 1.

However, the following flaws remain unattended. AGREE method, assumes exponential failure rate distribution, does not provide insight into the failure intensity function of the systems, ignores the systems/subsystem life characteristics and can't be used for mechanical or electro mechanical systems. Moreover, it works suitably only if wi is 1 or very near to 1. For the mechanical systems, Weibull distribution is more suited. The failure behaviour of mechanical components over continuous/cumulative operating time β factor is considered when Weibull distribution used.

Availability versus Failure period per year can be related to the downtime duration as showed in Table 2.

Availability depends on MTBF, MTTR and inspection interval. For a system with exponential distribution, it can be calculated if test time and repair time are negligible, as per the equation:

Table 1 Subsystem failure rates and availability after 10,000 h

Subsystem	Failure rate	Reliability
Axle counter	0.03×10^{-6}	0.9997
Track circuits	0.299×10^{-6}	0.99707
Signals	0.4557×10^{-6}	0.995453
Points	0.03×10^{-6}	0.9972
Power supply	0.299×10^{-6}	0.9997

Table 2 Availability versus Failure period per year

S. No.	Availability (%)	Failure period /year
1	99	~ 3, 5 days
2	999	~ 9 h
3	9999	~ 1 h
4	99,999	~ 5 min
5	999,999	~ 32 s
6	9,999,999	~ 3 s

$$A(T) = \left(1 - e^{-\lambda T}\right)/\lambda\left[T + t1 + t2\left(1 - e^{\lambda T}\right)\right] \tag{2}$$

where, T = Inspection interval, in Hrs. t1 = Inspection duration in Hrs. and t2 = MTTR in Hrs.

Availability after a specific time period can be calculated by the equation below

$$A(t) = \frac{MTTR}{MTTR + \lambda} + \frac{\lambda}{MTTR + \lambda}e^{(MTTR+\lambda)t}. \tag{3}$$

Maintainability depends on MTTR, which must comply with 95% confidence that repairs are performed within defined duration. MTTR can be calculated by the equation,

$$MTTR_i \leq \{(1 - A_i)/A_i\} \times MTBF_i \tag{4}$$

where, A_i = Individual availability.

Example:

A Four Component system with constant failure rate, has individual MTBF of 2100, 3200, 5000 and 1700 h. and the availability is specified to be 0.99 find the Individual MTTR.

Answer:

Individual Availability A_i, where i = 1, 2, 3, 4, is $(0.99)^{1/4}$ or 0.9975.

So, $MTTR_1 \leq 5.26$ h, $MTTR_2 \leq 8.02$ h, $MTTR_3 \leq 12.53$ h and $MTTR_4 \leq 4.26$ h.

3.3 Procurement Policy

3.3.1 Type Approval

The procurement policy includes type approval for newly designed systems covering manufacturing, maintenance needs with spares, test plan and quality control and cross acceptance for imported systems and suppliers' assurance. Cross this covers type approval for a newly designed system, cross acceptance for imported systems

and suppliers' assurance. The approval process covers manufacturing, maintenance requirements with spares, test plan and quality control. Type approval remains valid until the equipment is obsolete, design is changed or the performance is unsatisfactory. Reliability and supply of specific reliability data for the system must be implied in supply contract, considering other performance aspects.

The RAM points to be considered before type approval are:

- Documented compliance to installation, maintenance and RAM guidelines of the organisation,
- Interfacing with risk analysis to existing subsystems for a safety–critical system,
- System integrity with interchangeability between subsystems procured from different suppliers,
- Equipment manufacture must be done under an accredited documented quality control system,
- Supply of extensive hardware Failure Mode Effect and Criticality Analysis (FMECA) and Independent Software Verification and Validation reports must be done for computer based subsystems or system,
- If software development was partly done by third party, a domain expert must be the part of the development team.

Suppliers must inform the regulator regarding documented evidence of past or present product approval.

3.3.2 Acceptance Testing

Acceptance policy must be complied to ensure proper functioning in local environments. Acceptance testing comply with reliability targets. Highly Accelerated Life Test (HALT), Highly Accelerated Stress Screening (HASS) and Burn-in Tests are part of acceptance testing for electronic components. If there is any software involved, third party independent verification and validation of the software also become part of procurement policy. Failure rate calculations at thermal and electrical stress conditions, is very important.

For systems having electronic components reducing the room temperature reduces failure rate and increases reliability. We can use MIL HDBK 217F [7] to calculate failure rates of components depending on temperature and component quality. For example, temperature of 30 °C instead of 45 °C, reduces failure rate of Amplifier-Rectifier card of an Axle Counter, used in Train control, for example, from 8.13884 to 5.7342 per 10^6 h., i.e. an improvement of 29.5%. If we use components with better quality (naturally costlier option), failure rate further reduces to 1.62183 or by 80%. Whether these options would be chosen, depends on the criticality of the function of the card.

Burn-in does not reduce the failure rate of an electronic subsystem, but increases the lifetime. Components lost during burn-in test must be discarded and replaced by a new one. For example, a component for an electronic system has a decreasing failure rate of $0.0005(T/1000)^{-0.5}$/Year and Reliability R(t) 0.9.

Now, $e^{-(T/1000)-0.5} = 0.9$.
From this,

$$T = 1000\{-\ln(0.9)\}^2 = 1000 \times (0.10536)^2$$
$$= 1000 \times 0.0111 = 11.1 \text{ years}$$

When a burn-In period of 6 months (0.5 year) is introduced, reliability still being 0.9.
So, $e^{[-(t+0.5/1000)-0.5]}/e^{[-(0.5/1000)-0.5]} = 0.9$.
From this,

$$T = 1000\{0.10536 + 0.02236\}^2 - 0.5$$
$$= 1000\{0.12772\}^2 - 0.5 = (1000 \times 0.1631) - 0.5$$
$$= 16.31 - 0.5 = 15.81 \text{ Years}.$$

Thus, the Designed Life of the Component is increased by $(15.81 - 11.1)$ or 4.71 Yrs.

For software oriented systems, both static and dynamic testing are to be implemented during verification and validation task. Verification ensures that the output of a system life-cycle phase correctly reflects the inputs of that phase. It is performed for requirements, functional design, internal design, and coding phases. Validation checks whether the system matches user requirements. It covers software requirement review, software integration testing and system acceptance testing.

Maximum likelihood estimation for failure is calculated before asset acceptance. It is performed on a randomly selected and specified sample size. Suppose, N number of samples are tested and X failures are observed at time T. If X is much less than the specified number of failures that can be allowed, the material is accepted. Duration for acceptance testing are fixed by the asset managers.

Suppliers must inform the regulator regarding documented evidence of planned or current acceptance status in other similar organizations and report any non-compliance and any change in conditions of use. They must state that their offers meet the required RAM specifications, defined by the asset managers.

3.3.3 Sample Size

Asset managers fix sample size depending on margin of error, confidence level (Z score), and standard deviation. And is calculated as per the equation

$$\text{Sample Size} = (Z\text{-score})^2 * \text{StdDev} * (1 - \text{StdDev})/(\text{margin of error})^2 \qquad (5)$$

Z-scores for the most common confidence levels:

90%: Z Score $= 1.645$,

95%: Z Score $= 1.96$, and

99%: Z Score $= 2.576$.

Example:

Find the sample size for 95% confidence level, 0.5 standard deviation, and a margin of error of $\pm 5\%$,

Answer:

The sample size would be calculated as per Eq. (5) and is

$$\begin{aligned}
&\big((1.96)^2 \times 0.5(0.5)\big)/(0.05)^2 \\
&= (3.8416 \times 0.25)/0.0025 \\
&= 0.9604/0.0025 \\
&= 384.16
\end{aligned}$$

So, 385 samples are needed.

Since subsystems may be procured from different suppliers in future, interchangeability must be there for replacement. Interchangeability means that system components can be procured from any supplier and replace any legacy component without any substantial change in functionality or performance. It also allows the system to adapt to technology evolutions without significant modifications to its architecture.

3.3.4   Total Life-Cycle Cost

Before acceptance of an offer from suppliers, the total life-cycle cost of each offer, as stated by the suppliers, must be calculated and compared to find the best option. Annuity factors must be taken into consideration. Acquisition cost is the visible part of the submerged portion of life-cycle cost, which is calculated using the equation

$$\text{Life cycle cost} = (\text{Acquisition cost} \times \text{No. of Units}) + (\text{Annuity} \times \text{Units})$$
$$[\text{op.cost} + (\text{op.time} \times \text{failure cost})/\text{MTBF}] + \text{fixed repair labour cost} \qquad (6)$$

Example:

Choose the better option from two offered Designs for supplying 10 units of a subsystem having a lifetime of 15 years and an annuity of 9.125. Offer A has acquisition cost ₹2.70 lakh, failure rate 0.00833/h, MTTR 8 h, availability 0.9285, repair cost ₹2.0 lakh/yr, operating cost ₹65,000/yr and Offer B has acquisition cost ₹3.15 lakh, failure rate 0.00677/h, MTTR 6 h, availability 0.993, repair cost ₹27,650/h, operating cost ₹65,000/yr. Choose the better offer from lifecycle cost angle.

Answer:

Applying Eq. (6), we get lifecycle cost for system A is ₹14,896,333 and system B is ₹19,108,344. So, though the acquisition cost is higher in system B, it would be having less lifecycle cost.

The supplier must also provide documented support for life cycle maintenance cost after the warranty period and ensure critical spare part supply. The deliverables from system assurance are supplier's requirement specification compliance report, system assurance capability proof, design approval documents, system assurance report and system assurance audit report. Finally, asset management audits must be performed to check whether the specified strategies are being followed.

3.4 System Architecture for Electronic Systems

Computer based system architecture is divided into hardware, software, and power supply. In addition, for systems connected in a network depends on data transmission system as well.

Redundancy is used to increase availability. To avoid common mode failures, redundant elements must work independent from each other. Redundancy can be achieved by hardware, software as well as time. In the latter case, inputs are fed to all the processors but with time lag from each other, to avoid any glitch or spike in inputs. Redundant elements appear in parallel in the reliability block diagram. Redundancy can be in different configurations. For having high MTBF and improved availability, 2 out of 3 mode of redundancy is chosen, where inputs are fed to three processors connected in parallel and outputs are passed through a voter circuit with facility for reading back the output to check whether the intended output is actually available. Even if one processor fails, the system still remains available, as other two processor give the same output. Chosen redundancy configuration must be mentioned in specification for tender documents to avoid offers with different configurations.

Though the system reliability reduces due to redundant components, the quality of service increases due to better availability.

3.5 Maintenance Policy

3.5.1 Managing the Maintenance Process

Reliability and availability depend on managing the maintenance process. All maintainability criteria including logistics and EMC related hazards must be considered. Inter-department interfacing guidelines must be strictly followed. MTTR comprises preparation time, verification time, fault localization time, parts procurement time, logistics time, final testing time and over all administrative time. MTTR must comply with 95% Confidence that repairs are performed within defined duration.

Maintenance can be basically classified as corrective, preventive and predictive. Corrective or proactive maintenance means action is taken after a failure is reported.

Preventive maintenance takes action before the failure happens. This type of maintenance interval can be decided based on time based, volume of work based or condition based. Inspection interval and duration play vital roles in preventive maintenance. It needs properly trained personnel, regular inspection and service and has to maintain regular records.

Since preventive maintenance also keeps the system down during maintenance, a degraded condition based predictive maintenance is the best option. Maintenance resources should be stored in three levels—depot, supervisor level and on-site maintenance persons.

3.5.2 Optimum Inspection Interval

Optimum inspection interval must be calculated from failure rates, inspection duration and repair time. For example, an Axle Counter equipment has constant failure rate of $0.0000971/10^6$ h. Any defective component would be restored, if found faulty during the periodic inspection of 1 h. time. The repair/replacement time is 8 h. in the worst case. The availability after specific inspection intervals can be calculated by the equation,

$$A(T) = (1 - e^{-\lambda T})/\lambda[T + t1 + t2(1 - e^{\lambda T})] \qquad (7)$$

where, t1 = inspection duration, t2 = MTTR, and T = Inspection Periodicity.

Example:

A system has a constant failure rate $0.0000971/10^6$ h. Any failure identified during inspection would be rectified. Inspection duration is 1 h and repair or replacement takes 8 h, in worst case. What should be the optimum inspection interval?

Answer:

Let us calculate the system availability at different inspection intervals of 96, 168, 240, 336, 504, and 672 h. Using the Eq. (6), we find from Table 3 that the optimum gap between Periodic Inspections is found to be 168 h.

Inspection intervals (h)	Availability
96	0.98384
168	0.98526
240	0.983582
336	0.980197
504	0.973256
672	0.9662714

Table 3 Inspection interval versus availability

The optimum gap between Periodic Inspections is found to be 168 h.

3.5.3 Adequacy of Spare Parts

Adequacy of spare parts and location of stores, whether centralized or distributed, are to be specified after calculations to provide maximum availability. For example, 6 systems with $\lambda = 1 \times 10^{-5}$/h, and cumulative operating time of 50,000 h and reliability ≥ 0.99, the number of spare parts with centralized store will be 11. For decentralized 6 stores, each would need 10 spare parts. Thus, centralized stores needs less number of spare parts, but availability depends on supply chain and logistics.

Adequacy of spare parts available is to be checked by the equation.

Example:

Suppose an electronic component has a failure rate of 0.000003/h repair shop has procured two spare components. If the designed life of the component is 20 years, what is the probability that the spares would be adequate for 10 such components?

Answer:

Expected number of failures during lifetime for 10 components, is $0.00003 \times 10 \times 20 \times 8760$ or 5.256.

Probability of ≤ 2 failures in 20 years is

$$R_{(20)} = \sum_0^2 \left\{ e^{-5.256}(5.256)^n/n! \right\}, \quad \text{where n is 2.}$$
$$= e^{-5.256}(5.256)^0/0! + (5.256)1/1! + (5.256)^2/2!$$
$$= 0.005216(1 + 5.256 + 13.812768)$$
$$= 0.005216 \times 20.068768 = 0.1046787$$

It shows that the spares in stock will have only 10.46% probability of adequacy.

3.5.4 Repair and Renewal of Spare Parts

Maintenance using diagnostics and prognostics should be used and maximum availability is to be chosen after comparing repair and renewal of spare parts.

Replacement with a new unit enhances maintainability by reducing restoration time, maintenance skill requirement, document and test equipment. For a fixed number of failures and increasing unit cost, repair is preferable. For a fixed unit cost and reduced failures, replacement is advantageous.

Replacement is cheaper when,

$$ad + (c + bd)f \leq ar + (br + ck)f, \tag{8}$$

where,

ad Fixed cost of discarding,
ar Fixed cost of repair logistics,
bd Variable cost to remove and replace a discarded unit,
br Variable cost to repair a failure,
c   Unit cost,
f   Number of failure during unit life,
k   % of failures, that cannot be repaired.

3.5.5   Sustainability and Resilience Policy

A stringent asset sustainability and resilience policy against climate change causing disruption, must be strictly followed in construction and asset renewal activities in the most cost-effective manner. To avoid any on-site maintenance activity lapse, specific checklists, maintenance tools and drawings must be available. Though human errors causing system failures, are difficult to analyze quantitatively, proper.

Reliability growth testing must be done to verify stipulated MTBF or MTTF. This test improves the reliability of the design through root cause analysis of the observed failures to determine specific design modifications, verifying that failure modes have been removed or mitigated without introducing new failure modes. Updated training is mandatory for the concerned men-at-site.

Cost models on maintenance optimization can be based on Markov model with inspection and replacement policy. To avoid any on-site maintenance activity lapse, specific checklists, maintenance manuals and proper tools, measuring instruments and drawings must be available. Audit of employee competency must be properly planned and followed at scheduled intervals. While performing scheduled maintenance of the system, compliance to routine tests must be documented. Care is to be taken to avoid insertion of any new hazard during maintenance tasks and if any, whether they could be mitigated. Any process changes, modification or replacement/ repair action must be approved by competent authority.

3.5.6   Reliability Growth Testing

Reliability growth testing must be done to verify stipulated MTBF or MTTF. Checking for Compliance with Reliability and Maintainability Specifications calculated by using Fischer Distribution table, provided the confidence level is defined, must be performed to verify that the suppliers' documented claims are fulfilled.

For example, specifications for a part needs 0.95 reliability at 1000 operating hours. 1 failure in 50 parts failed. Is the Specification being met?

Answer:

Reliability at 1000 h, $R_{(1000)} = 1 - (r/n)$, where r is the number of Failures and n Is the Sample Size for Test.

$$R_{(1000)} = 1 - (1/50) = 1 - 0.02 = 0.98,$$

For a 95% Lower-Bound Interval, from Fischer Distribution Table,

$$F2 = F(0.05, 4, 98) = 2.48 \text{ and}$$

$$RL = \frac{1}{1 + (2/49) \times 2.4} = 0.908$$

We are Confident that the Reliability is at least 0.908.

So, we cannot certainly say that the Specification is being met.

Once the system is installed and worked for a reasonable time period, it is to be checked whether maintenance goal is achieved.

Example:

From a sample of 85 corrective maintenance repairs of a subsystem, 78 were completed within 5 h suppliers contract assured that 90% of repairs would be done within 5 h is the maintenance goal achieved?

Answer:

Sample proportion $p^* = 78/85 = 0.9176$

Lower bound confidence interval is 95%

$$p_L = p^* - z_\alpha \sqrt{\{p^* \times (1 - p^*)\}/n}$$

From Table, for 95% confidence, $z_\alpha = 1.66$

$$p_L = 0.9176 - 1.66\sqrt{(0.9176 \times 0.0824)/85}$$
$$= 0.8681$$

We are now 95% confident that 86.81% repairs are performed in < 5 h. So, the goal is not met.

3.5.7 Annual Maintenance Contract

When annual maintenance contract is awarded to the suppliers, RAMS engineers must check whether the AMC cost is justifiable.

Example:

An item is procured in a bunch of 50. Four items fail in the 1st year and 22 need repair within 5 years. The average cost of repair is ₹1000. If Weibull failures are assumed, what is the actual cost of repair for the manufacturer?

Answer:

If β is the shape parameter and θ is the scale parameter,

$$1 - e^{-(1/\theta)^\beta} = 4/50 = 0.08 \text{ and}$$
$$1 - e^{-(5/\theta)^\beta} = 22/50 = 0.44$$

Or, $(1/\theta) = [-\ln 0.92]^{1/\beta}$ and $(5/\theta) = [-\ln 0.56]^{1/\beta}$
From the two Equations,

$$5[-\ln 0.92]^{1/\beta}$$
$$= [-\ln 0.56]^{1/\beta}$$

So,

$$\beta = \log 6.199/\log 5 = 0.84/0.69897 = 1.2018 \text{ and}$$
$$(1/\theta) = [-\ln 0.92]^{1/\beta} = [0.0838]^{0.786} = 0.141893$$
$$\theta = 1/0.141893 = 7.04756$$

Assuming that a failure occurring during the 1st year is covered by warranty, the expected Cost of a failure in the 2nd year is

$$1000[e^{-(1/7.0476)^{1.2018}} - e^{-(2/7.0476)^{1.2018}}] = \text{Rs. } 100.63$$

Thus, the cost claimed by the supplier is too high.

3.6   RAM Metrics and Documentation

RAMS managers must have metrics to identify needs for improvement. Metrics are also extremely important to validate whether the maintenance team activities. There are dozens of reliability metrics. It is best to choose a few important KPIs.

Important Maintenance metrics are:

- Number of time directed task schedules are to be performed
- Number of preventive maintenance tasks identified
- Number of failure finding tasks identified
- Number of run to failure tasks identified
- Total number of preventive maintenance tasks identified
- Preventive maintenance tasks complied
- Preventive maintenance labour cost
- Predictive maintenance labour cost
- Emergency measure maintenance labour cost
- Corrective maintenance labour cost
- Total consumable cost
- Total maintenance cost
- Hours of scheduled and unscheduled downtime.

4   Future Strategies

Reliability influencing factors identification depends on expert judgment of actual data collection and analysis. So, cloud-based intelligent asset management implement expert systems, where views from several domain experts regarding failure removal can be collected and the best one can be adopted. Video conferencing with experts during emergency can help the on-site maintenance staff. Video surveillance of construction sites can supervise installation process and sensor-based degraded condition monitoring would help predictive maintenance. Artificial Intelligence with Machine-learning can help in decision making. A computerized maintenance management system keeps a computer database of information about all the maintenance operations and can produce status reports and detailed summaries of maintenance activities, allowing an efficient asset management. This management process can be local or cloud based. Local server based systems introduce higher costs, complex implementation and constant management system maintenance.

5   Conclusion

This paper describes the benefits, associated tasks plans and future strategies in quantified RAM based management of Train control assets. Some points are explained with mathematical equations and examples.

References

1. ISO 55001:2014 International standard for asset management
2. EN 16646:2014 Maintenance within physical asset management
3. Ebeling CE (2000) Introduction to reliability and maintainability engineering, TMH Edition 2000, seventh Reprint
4. O'Connor PDT, Practical reliability engineering, 4th edn. Wiley Student Edition
5. MIL HDBK 781 (1987) Reliability test methods plan engineering, 14 July 1987
6. MIL HDBK 471 (1997) Maintainability verification demonstration, 4 Aug 1997
7. Reliability prediction of Electronic components, 2 Dec 1991

Radiation Resistant Camera Testing in India—An Imperative Initiative Towards Sustainable Practice and Proactive Waste Management

A. K. Ahirwar, P. K. Ramteke, V. Gopika, P. K. Gupta, and K. Joe Peter

1 Introduction

Radiation resistant camera is need for nuclear industry, due to the requirement of remote handling for daily operation. Currently available solutions are Black and White tube cameras (normally highly resistant, but not colour) requires frequent tube replacement, which is not only adds frequent pressure on environment but also is plagued with inconsistent supply. It is an obsolete technology. This standard camera has a very short life and suffers from 'browning effect' very quickly. Colour cameras, which can resist shield upto 100 Mrad is the necessary option. Generating the evidence through testing is mandatory for equipment qualification, through independent laboratories, following rigorous test protocol. Recent development in CMOS hardened camera claims as a feasible technology for nuclear industry [2]. Though CMOS is at an early stage of technology life-cycle development but is proving positive results globally. It was indeed a promising technological shift, demanded by the industry operators and CMOS hardened camera technology displayed merit for inclusion in Indian nuclear industry.

A. K. Ahirwar (✉) · P. K. Ramteke · V. Gopika
Reactor Safety Division, Reactor Design and Development Group, Bhabha Atomic Research Centre, Trombay, Mumbai 400085, India
e-mail: babulk@barc.gov.in

P. K. Gupta · K. Joe Peter
Control and Instrumentation Procurement, Nuclear Power Corporation of India Ltd (NPCIL), Anuskatinagar, Mumbai 400094, India

2 Equipment Qualification for CMOS Cameras and Test Protocol

CMOS hardened camera technology based on CMOS sensors the cameras have the following advantages:

Extended radiation resistance via proven technique and combined with electronic hardened circuits ready to be placed into irradiated zones. The images are in color. CMOS cameras usually have smaller dimensions and weight for equal performance.

In order to qualify the above equipment, rigorous test protocol is applied:

  (i)   The test must be done in an independent laboratory.
 (ii)   The test laboratory must have independently calibrated radiation dosimeters.
(iii)   The radiation exposure must be continuous during the whole tests, possibly with short stops that must be tracked in the report.
(iv)   The devices must be switched on and totally operational during the exposure. If the camera is not powered, the test is not an evidence.
 (v)   Possible shielding material used to protect the device must be known.
(vi)   The evidence of the radiation resistance at the end of the test must be brought when the device is still exposed to radiation.

The test protocol is an extended Radiation Resistant Camera for assessing the long-term performance test in a radiation environment. This camera shall perform its designed function under normal operating conditions and continue to function during Design Basis Event and in Post Design Basis Event conditions for remote viewing system requirements in high radiation areas.

3 Specification of Radiation Resistant Camera

In order to obtain the cumulative dose of 100 Mrad, the equipment is irradiated under continuous dose rate of at least 0.1 Mrad. Typical Specifications of a Radiation Resistant Camera (Fig. 1) are:

- SD colour sensor 640×480 pixels, PAL signal
- Motorized Zoom $\times$ 10 (focal length 6.5–65 mm), Non-Browning lens, F/1.8, remote zoom, focus, iris control.
- Motorized Pan $\pm$ 170°, Tilt—38/240°
- LED lighting 5000 lm
- Gamma dosimeter (RADO): 1 MGy
- IP68—Water and Dust resistant
- Humidity—95% RH for complete camera system
- Maximum operating temperature 90 °C; camera system tested for temperature rise to 118 °C
- Control box power supply 230 V AC/110 V AC

Fig. 1 Radiation resistant
camera
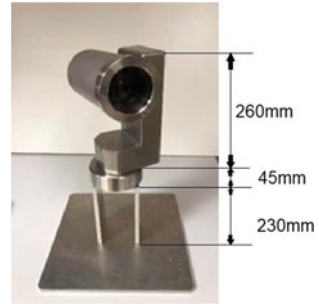
- Camera cable PMUC, C1, Waterproof.

The camera must be powered ON during the entire test period to maintain the actual field condition. The test must be proceeded in the same conditions like in the industrial situation where the camera is continuously ON. In fact, electronics systems under radiation have significantly different behavior following their power ON or OFF mode. The control box should be kept in cold zone, outside the radiation chamber. Since there is a provision for cable connecting the camera and control unit to cross the wall of the approved test facility, the control system can be easily be kept outside the radioactive zone. It is also recommended that the camera to be oriented towards the radiation source, but some movement will be necessary as we shall be using the pan and tilt function to check its operation at regular intervals for test record.

4 Performance Evaluation of Radiation Resistant Camera

To reach 100 Mrad cumulative dose at an exposure of 0.1 Mrad/h dose rate the test needs 1000 h of exposure which is approximately 42 days from start of test.

The test is considered to be successful if the camera is still operating after 100 Mrad cumulated dose, camera being ON during the test (apart from refresh periods managed autonomously by the control box). The last image, BEFORE removing the source, must be satisfactory and acceptable by the user in comparison with the recorded image at initiation of the test. The Pan, Tilt, Zoom movements must be operational to comment on the functionality of the RR camera system [3].

The test should also demonstrate the quality of captured images from the device under test during streaming video, captured at various resolutions, which has the quantifiable image clarity features. Resolution Video Test Chart (RVTC) provides the quantifiable value to measure the TVL (Television Lines)—TV Lines Resolution. Similarly the number of colour should be observed in the Video Colour Test Chart (VCTC) at different milestone that has to be counted and recorded.

The visual quality analysis is the prime basis for performance evaluation. The resolution (TVL—TV Lines Count for both—Horizontal and Vertical lines) has to

be recorded at different milestones. Similarly, the number of colour identified at the beginning and end of test has to be recorded against each test milestone.

The image BEFORE and AFTER the launch of 'Refresh' has to be recorded to check the efficiency of the process and camera's ability to resist gamma radiation.

5 Test Setup and Performance Analysis

The camera was placed in the radiation chamber facing the source where the camera received a continuous dose rate of at least 100 Krad/h. The performance of the radiation-resistant camera against gamma irradiation up to a cumulative dose of 100 Mrad has been tested. Figure 2 shows the placement of the camera and test setup for performance evaluation.

5.1 Functional Performance (PAN/TILT/ZOOM)

During each milestone, Pan, Tilt, and Zoom functional performance was checked in accordance with the defined specification criteria and has been recorded in Table 1.

Fig. 2 Placement of camera and test setup for performance evaluation

Table 1 Functional performance test parameters

Cumulative radiation (Mrad)	Performance test parameters					
Milestone	Time	Dosime-try record	PAN ± 170°	TILT 38° + / 240°	ZOOM 10 X	Record of VCTC and RVTC image
Initial	18-09-2020 09:07 h	0.0 Mrad	OK	OK	OK	Recorded
01 Mrad	18-09-2020 17:43 h	0.98 Mrad	OK	OK	OK	Recorded
10 Mrad	22-09-2020 20:08 h	9.96 Mrad	OK	OK	OK	Recorded
20 Mrad	27-09-2020 13:14 h	20.97 Mrad	OK	OK	OK	Recorded
50 Mrad	30-10-2020 10:15 h	51.82 Mrad	OK	OK	OK	Recorded
75 Mrad	10-11-2020 16:45 h	72.80 Mrad	OK	OK	OK	Recorded
100 Mrad (short closure)	15-11-2020 09:36 h	88.12 Mrad	OK	OK	OK	Recorded

5.2 Image Resolution

The test result needs to demonstrate the quality of captured images from the device under test during streaming video, captured at various resolutions. Images of a specified poster, RVTC—Resolution Video Test Chart has been recorded at suggested milestones. Additionally, the composite TVL Chart—'Initial versus the Milestone' (Fig. 3), has also been presented for better comparison of the result. The RVTC image has been used to record the TVL for both Horizontal and Vertical lines for the purpose of analysis in the performance test report.

The quantifiable resolution of TVL has been counted and recorded in Table 2 at each milestone. Both the horizontal and vertical TVL has been within the proposed acceptance criteria and demonstrates the picture clarity quantitatively.

5.3 Number of Colour Bar

Similarly, the number of colors observed at the initiation of the test and subsequently at different milestones has been counted and recorded in Table 3. Images of a specified poster VCTC—Video Colour Test Chart have been recorded to check against the
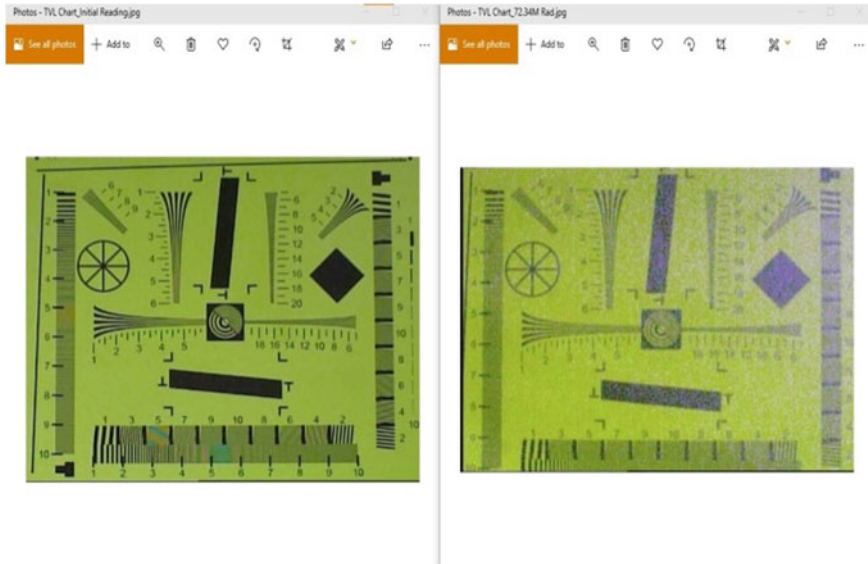
Fig. 3 Composite TVL chart-initial versus 72.80 Mrad

Table 2 TVL parameters for radiation dose milestones

Milestone	Horizontal TVL suggested (focus in the center)	Horizontal TVL actual (focus in the center)	Vertical TVL suggested (focus in the center)	Vertical TVL actual (focus in the center)
Initial	500	500	500	500
01 Mrad	ERMES proposed acceptance criteria: 5%	480	ERMES proposed acceptance criteria: 5%	480
10 Mrad	ERMES proposed acceptance criteria: 10%	480	ERMES proposed acceptance criteria: 10%	480
20 Mrad	ERMES proposed acceptance criteria: 15%	480	ERMES proposed acceptance criteria: 15%	480
50 Mrad	ERMES proposed acceptance criteria: 20%	400	ERMES proposed acceptance criteria: 20%	400
75 Mrad	ERMES proposed acceptance criteria: 25%	380 (72.80 Mrad)	ERMES proposed acceptance criteria: 25%	380 (72.80 Mrad)
100 Mrad (short closure)	ERMES proposed acceptance criteria: 25%	–	ERMES proposed acceptance criteria: 25%	–

actual number of color bars observed. Additionally, the composite VCTC—Initial versus the suggested Milestone, has also been presented for a better comparison of the result (Fig. 4).

Table 3 Number of colour bars for radiation dose milestones

Milestone	Number colour bar observed—suggested (horizontal colour bar)	Number colour bar observed actual (horizontal colour bar)
Initial	6	6
01 Mrad	6	6
10 Mrad	6	6
20 Mrad	5	5
50 Mrad	5	5
75 Mrad	4	4
100 Mrad (short closure)	4	–

Note - Contrast **Colour Bars** - Right to Left (**6 colour**)

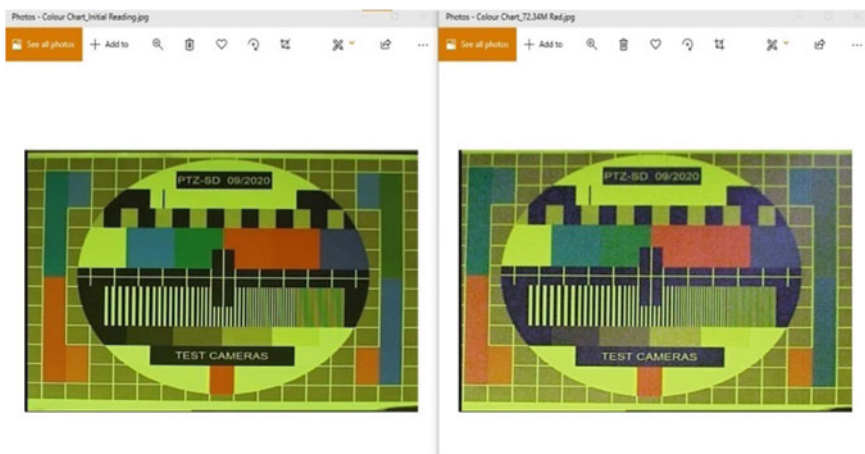| Yellow	Cyan	Green	Magenta	Red	Blue

Fig. 4 Composite colour chart—initial versus 72.80 Mrad

5.4 Refresh Process Image Record

During the exposed condition, the 'refresh process' is auto-programmed to reboot itself every fixed interval of time. The refresh process took 24 min every time it was initiated [4]. During the refresh process, the image is not available. The refresh data has been recorded. The 'refresh process' has demonstrated the efficiency of the process and the CMOS camera's ability to resist gamma radiation. The image BEFORE the launch of 'Refresh' and AFTER the launch of 'Refresh' has been recorded.

6 Conclusion

The camera was tested upto a cumulative dose upto 88.12 Mrad which was achieved in 678 h of exposure at dose rate of 100–144 Krad/h. There was no significant degradation in camera image quality upto 30 Mrads. Marginal degradation in image resolution and color quality was observed at 50 Mrads. The camera was observed to have failed at 88.12 Mrads. There was no noticeable change in its operation of Pan, tilt, Zoom. The overall test performance of the Radiation Resistant Camera was found satisfactory up to 50 Mrad of radiation ageing test.

References

1. Takeuchi T, Otsuka N, Tsuchiya K, Tanaka S, Ozawa O, Komanome H, Watanabe T, Ueno S (2016) Gamma irradiation effects of image sensor for radiation-resistant camera
2. Goiffon V et al (2016) Radiation hardening of digital color CMOS camera-on-a-chip building blocks for multi-MGy total ionizing dose environments. IEEE Trans Nucl Sci 64.1:45–53
3. Takeuchi T et al (2017) Development of radiation resistant monitoring camera system. In: 2017 IEEE nuclear science symposium and medical imaging conference (NSS/MIC). IEEE
4. Centurelli JL et al (2018) Europa imaging system wide angle camera: the effect of gamma radiation on the refractive index and transmission of radiation resistant glasses. In: Space telescopes and instrumentation 2018: optical, infrared, and millimeter wave, vol 10698. SPIE

Use of Simulator Experience and Insights in the Design of Control Room for New Nuclear Plants

Archana Yadav, Alpana Goel, and P. V. Varde

1 Introduction

Nuclear Reactors have evolved from the early prototype power reactors in the 1950s to evolutionary generation IV+ reactors, with advanced safety features and minimal waste generation. The commercial power reactors began operations in the 1960s with an expected lifetime of 40 years. With the advancements in technology and more emphasis on passive safety systems, the lifetime of generation III reactors could be extended to 60 years [1]. With more than seven decades of safe reactor operations, nations are still struggling to expand their fleet of nuclear reactors either due to lack of public acceptance or due to political hindrances. A nuclear incident and accident anywhere in the world make a significant impact on the fate of these sociotechnical complex systems. Probabilistic risk assessment (PRA) has, to some extent succeeded in imbibing faith in the technology. An important aspect of maintaining and assuring reliability on the technology is by utilization of reliable systems, structures, and manpower. Humans are an integral part of system operation. In almost all the nuclear accidents namely Three Mile Island (TMI), Chernobyl, or Fukushima: Humans and their erroneous interpretation of the situation have emerged as a potential error causing factor [2]. Taking this fact into consideration better understanding of the human factor is essential. Human reliability (HR) and human error rate prediction are of immense importance to ensure the smooth functioning of facilities and avoid incidents that might collate and grow into big accidents. Although the need for human factor study and reliability has been under consideration since the earliest

A. Yadav (✉) · A. Goel
Amity Institute of Nuclear Science and Technology, Amity University Uttar Pradesh, Noida Sector 125, Noida, India
e-mail: ayadav3@amity.edu

P. V. Varde
Bhabha Atomic Research Centre, Mumbai, India

PRA documents were in place, with evolving technologies, the approach must be reviewed and must consider effects due to digitalization [3] and include cultural and organizational factors.

For the past many years HR analysis has gained immense importance due to the increasing contributions of humans in the progression of accidents specifically in nuclear accidents. The creation of HRA software and its validation requires data. The data available is either not enough or the models rely completely on expert judgments. Another prominent way of generating data is with the aid of training simulators. The full scope simulators appear as an option for getting data for the development of human reliability software. Power plant and research simulators are a way of closely looking at some of the features like plant functionality, parameter evolution, and crew behavior analysis, human factor analysis etc. They are being used for training, authorization, licensing, and development purpose and have proved their efficacy [4].

Catering to the evolving control rooms in complex systems, human–computer interactions have been studied in dynamic scenarios and evolving technologies with the aid of video recordings, operator action evaluations, and activity tracking [5]. This paper gives brief insights into the control rooms, simulators, and their role in the determination of human reliability.

2   Control Room

The control rooms in complex systems are one such important locations wherein there is strong human–machine interaction. Through the control room, the plant can be operated either automatically or manually in almost all operational states. Plant activities are controlled and managed from the control room. The plant is spread out into different areas and zones. The status of equipment, as well as various processes and safety parameters, are brought to the control room for improved surveillance and monitoring of the plant to perform an action, coordination, and communication with various plant agencies that support reactor operation. These are manned by a highly trained and experienced crew.

The control room depicts the plant state with help of alarms, signals, indicators, and display units. The trip and alarm windows are lined up on top for operator attention and prompt action. The console offers operations like power maneuvering, startup, shutdown, safety system actuation etc.

With technological advances, a significant change has been witnessed in the way new reactors are designed and developed. So has been with control rooms, from big, bulky analog systems to compact and more user-friendly digital control rooms is what we can see in the advanced reactors. Supervisory control and data acquisition systems (SCADA) provide relevant information to control room operators [6]. The present technology focuses on building systems taking humans/operators at the center and then building systems around them, rather than a no participatory older approach. The newer control rooms come with a higher degree of automation and offer a better

understanding of dynamic plant states to the operator giving more time to think and respond particularly in emergency or non-routine tasks. The operators are now managers rather than operators.

The operator performance factors both physiological and psychological affect their performance along with the ergonomics. The human factors are dynamic and evolving in such evolving atmospheres of digitalized control rooms. Guiding documents and guidelines from IAEA, IEEE, and IEC, like IEC60964 along with ISO documents (ISO 11064, ISO 92415, EEMUA 991, EEMUA 201) are in place to help design control rooms and focus on the functional aspects right from the design stages. Detailed guidelines are available regarding both software and hardware reliability requirements. The focus is to ensure safe and secure plant operations along with a better equipped and informed operator [7].

2.1 Control Room Evolution

There has been significant technological development that has taken place in control rooms since the early reactor operations. The first-generation control rooms had fixed components and analog operations. Mostly hard panels, physical switches, and knobs to carry out operations. The second generation moved to visual display units and operations were carried out with help of keyboards. Through the improvement in ergonomics and anthropometric standards, human factor incorporation is also made possible, while designing control systems having strong human–machine interactions. With advancements in computers, communication methods, and digital systems, the third-generation control rooms emerged with better and improved performance parameters, which are augmented with operator support systems. The control rooms have been designed with high-density visual display units, larger displays, color-coded indicators, and with operator support systems [8, 9] to help operators make decisions in less time and have better utilization of their cognitive features (Fig. 1).

This is of importance in stressful situations like accidents or unanticipated operations. While this can also induce additional stress due to complex digital environments as embedded screens and panels can be difficult to trace. Studies reveal that humans fall short of cognition in stressful and non-routine situations [11]. Another challenging factor here is to create an interface between safety and non-safety systems. Complete overhauling of systems may be cost-intensive, better would be to digitize, and automate systems required during design basis accidents wherein response expected is quick and accurate. The areas requiring attention deal with the incorporation of attention and alertness aspects along with situation management and plant state assessment [12]. It has been observed that more automation is also increasing the possibility of human errors [13]. Humans are becoming more reluctant and completely relying on systems for guidance and actions to be taken.

Fig. 1 Control room of Dhruva [10]

3   Simulator

The control room evolution and up-gradation can be supported with simulator operations. The utility of simulators has been exploited across nations to both upgrade their existing control rooms and design modifications [2] suggested for newer ones. Simulators in an exact replica of control rooms and miniature versions are being utilized for various functionality evaluations. A Research reactor simulator is shown in Fig. 2. Personal computer-based versions of simulators are also available for majorly all reactor types [14].

Simulator exercises, drills, training, and procedure amendments can be suggested based on operator feedback, operating experience reports, and data collected during the operation of real-time systems. This can also be augmented with expert elicitation techniques and data collection from experienced operators and crew. Control room evaluations have been done with help of operator activity analysis (log of actions), questionnaire [15], and improvement in ergonomics with inputs from operators [16]. Further several quantitative analysis methods like analytical hierarchy processes and fuzzy logic can be used to arrive at subtle numbers to be utilized in PRA studies for risk calculation.

Fig. 2 Simulator of a research reactor [17]

3.1 Merits and Demerits of Simulator-Based Studies

Replica simulators, full-scope simulators are being utilized for a few decades for operator training and procedural developments. These have helped in training and development. Dynamic scenarios and design basis accidents can be simulated, and results will help improve the real systems. Significant work done [18–20] provide an insight into the development and application of operator support systems, particularly designed for maintenance of normal operation and if the need arises then for emergency scenario handling. Many beyond design accidents can also be simulated which do not lead to core damage [21].

Advantages of the technology are that the non-routine and emergency scenario training for example Loss of coolant accident and complete power failure scenarios can be simulated, and operator behavior recorded and analyzed. This will help in the development of training documents, procedures, and guiding documents for future reactors and emergency scenarios. This gives an opportunity to check for nonconformity to national and international standards which can be subsequently corrected. Through these exercises, the identification of safety–critical scenarios, components, and alarms can be established. Which will help in improved operator training and development of checklists, and guiding documents, not only for design basis accidents but for hypothetical and beyond design basis accidents.

Upgradation of simulators before actual control rooms gives a better understanding of system vulnerability and design amendments required. This also gives a better understanding of error-causing factors, aids human factor analysis and subsequent improvement in human reliability through the identification of appropriate performance shaping factors. Digital systems have testing and self-check features which is an added advantage.

The results of exercises done on simulator systems will aid the development and up-gradation of operator support systems, which is the need of the hour for newer and advanced control rooms as they might be completely digitalized [22].

With regards to licensing and regulatory aspects, these will support the identification of risk-significant scenarios and the identification of safety–critical systems. Since there is the feasibility of controlling experiment progression (speed and common mode failure induce) and with the possibility of tailoring of scenarios.

While the approach looks promising at the outset. There are some limitations and shortcomings as well, the economical liability is higher, and hence mostly full scope simulators are not preferred. While systems are being upgraded for real control rooms, up-gradation of the simulator before the actual control room increases the cost further.

Complete digitalization of control rooms can reduce human cognitive actions and has the potential to make operators error prone. Simulator bias (knowing that it's not a real system, propensity to hit and try with solutions) might be a potential challenge to develop data applicable for the real-time scenario. There is a need to eliminate the bias in data obtained due to environmental (different and unreal setup) and motivational (realization of no major consequences) effects introduced in the simulator experiments. Methods like the structural equation modeling approach quantitatively assess the motivational bias [23].

While identification and analysis of all potential error-prone conditions is a time-consuming task. Also, the possibility of simulating all possible combinations is quite improbable. A complete list of possible scenarios and analysis of all components can be a tedious task.

Simulator proficiency might also induce casual operator behaviors in routine situations due to prior positive simulator experiences. This may also induce faulty execution, omission, and deletion of crucial steps in procedures due to simulator exercises and end state prediction. An analysis with plant-specific data analyzed with help of the Technique for Human Error Rate Prediction (THERP) handbook shows the categorization of errors committed in the research reactor [24] (Fig. 3).

Fig. 3 Commission and omission error categorization for research reactor: THERP database
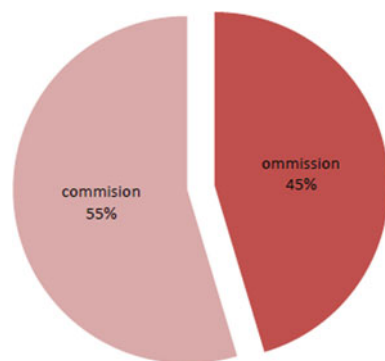
Lack of attention of operators due to over-reliance on technology can also be witnessed. With more and more digitalization and support systems for decision making error-prone conditions arise due to misinterpretation of the situation by computer or wrong logic interpretation. Further there would be significant difficulty encountered while modifications are taken up with control systems in both safety and operational aspects.

4 Human Reliability Assessment Tool Development

Probabilistic risk assessment has important contributors in terms of the human reliability factor. Humans being an important part of the system play a very crucial role. The need here is to remember that human error is a consequence rather than a cause; errors are shaped by workspace and organizational factors. There is a pressing need to change the conditions under which humans work and this would eventually improve the reliability of the entire complex facilities like nuclear power plants. While the first-generation methods (THERP, SPAR-H etc.) focus on humans being the sole contributors for creating errors the second-generation methods (ATHENA, CREAM) shift the focus on organizational and regulatory bodies (error producing conditions). Countries with sufficient data available from simulator exercises have also gone beyond the second-generation methods [25]. Human error behavior is determined by both environmental and human factors (physiological and psychological). Organizational factors play an important role in determining human error probability. Many well-developed methods are in place for the determination of Human reliability, but there is an increasing need to incorporate ergonomics, organizational and environmental factors like digital stress, safety culture, state/event-oriented procedures into the model. Owing to the lack of sufficient data and concerning guidelines there is a need for the development of methods that can provide satisfactory results within the available data either taken from operator logs, simulator exercises, and with the incorporation of expert opinions.

5 Analysis and Inference

Taking the reference and guidance of the THERP document (detailed handbook for HR analysis), Human error probability calculations were done and compared for plant-specific data from the research reactor. The pie chart at Fig. 4 shows the difference between the two. It is quite evident that there is a significant difference between the plant-specific values and that obtained from the standard document. This implies that for data under consideration THERP document might not be a suitable guiding document. The Human error probabilities might be very specific to the plant under consideration, the interface (HMI), safety culture, procedures, training, etc.
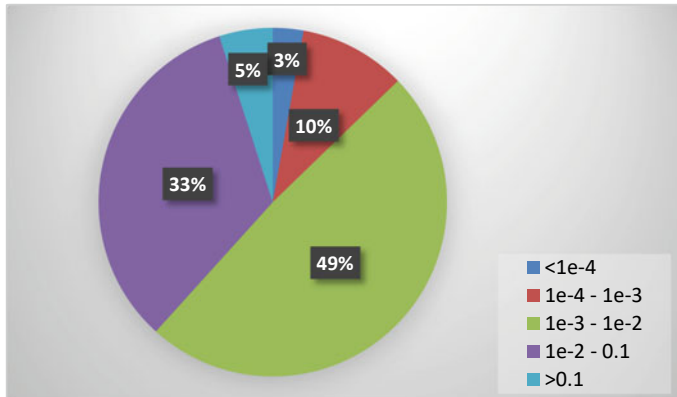
Fig. 4 Difference between THERP and plant specific values

Subsequently, the need for the identification of human factors arises. Factors like operator training, working environment, procedures, safety culture, human–machine interface, work timings, etc. require attention and quantification for the determination of human reliability.

6 Conclusions and Future Scope

For a better understanding of the Human–Machine Interface in a control room scenario, the advanced training simulators have proven their effectiveness and utility. This gains further importance when the control rooms are changing with the advancements in technology. There has been a significant reduction in the size of control rooms, which ensures major information about the state of the plant is available to the operator on large screens at the click of a button. This reduces the work stress of moving across panels and accessing controls that were conventionally done on hardwired panels. Further, the incorporation of simulators would help us understand the difficulties or shortcomings of digitalization. The simulators can be built with a reduced spaced requirement ranging from 10 to 30%, as compared to real control rooms. Artificial intelligence-based Techniques like operator support systems can be exploited to better equip operators in the control rooms to ensure the digital stresses are reduced [26]. Reducing the size of real control rooms with experience gained from simulators will bring down the cost of construction, improve communication between the team (reducing team errors), improve situation awareness of operators (better equipped with plant state), and have lesser space requirements. All these systems can be tested, validated, and improvised with aid of replica/non-replica simulators. Eventually, significant improvements can be seen in design, construction,

and user-friendly interfaces being utilized in future reactors. This may further reduce the manpower requirements in control rooms without compromising the safety and security of complex systems.

For analyzing operator behaviors and actions in a simulator environment for human reliability assessment, apart from video camera recordings and logbook data, information can be gathered from eye movements, brain waves, facial expressions, and language processing. Experiments can be executed for operator licensing, certifications, evaluations, and for these dynamic scenarios can be provided to assess the efficiency and efficacy of systems placed and humans operating them. This can be executed in full-scope or non-replica simulators. Experts like human factor analysts along with behavioral analysts can provide details about the state of an operator in stressful situations by evaluation of physiological and psychological parameters, giving insights about the decision-making capability in emergency and non-routine situations. This can be further verified with simple tests and diagnoses like blood pressure, pulse rate monitoring. The overall impact of a better understanding of HMI and human factors will strengthen the risk calculations with the incorporation of contributions from humans. Eventually, procedures, systems, culture at the workplace can be amended to have improved the reliability and availability of complex facilities like nuclear power plants [27, 28].

Methodological changes in terms of utilization of internet-based techniques, artificial Intelligence-based approaches, and mobile tracking devices are suggested for advanced systems like newer control rooms in advanced reactors to better equip the operators and prevent incidents and accidents.

References

1. International Atomic Energy Agency (1995) Control room systems design for nuclear power plants, TECDOC Series
2. Furet J (1985) New concepts in control-room design. IAEA BULLETIN, 25
3. Porthin M, Liinasuo M, Kling T (2020) Effects of digitalization of nuclear power plant control rooms on human reliability analysis—a review. Reliab Eng Syst Saf 194:106415
4. Theureau J (1998) Use of nuclear-reactor control room simulators in research and development. IFAC Proc Vol 31(26):365–370
5. Mentler T, Palanque P, Boll S, Johnson C, Van Laerhoven K (2021) Control rooms in safety-critical contexts: design, engineering, and evaluation issues. In: Ardito C et al (eds) Human-computer interaction—INTERACT 2021. Lecture notes in computer science, vol 12936. Springer, Cham
6. Joshi R, Daum B (2018) Human factors in design of control rooms for process industries
7. Kitamura M, Fujita Y, Yoshikawa H (2005) Review of international standards related to the design for control rooms on nuclear power plants. J Nucl Sci Technol 42(4):406–417. https://doi.org/10.1080/18811248.2005.9726408
8. Seminara JL, Seidenstein S, Eckert SK, Smith DL (1979) Human factors methods for nuclear control room design. Volume I. Human factors enhancement of existing nuclear control rooms. Final report, USA
9. Hsieh M-H, Hwang S-L, Liu K-H, C-F, Ling CS-FM (2012) A decision support system for identifying abnormal operating procedures in a nuclear power plant. Nucl Eng Design 249

10. Tikku AC (2006) Dhruva completes twenty years of service to the nation, nuclear India—A DAE publication, vol 39/No 7–8. http://www.dae.gov.in
11. Liu ZLP (2016) Comparison between conventional and digital nuclear power plant main control rooms: a task complexity perspective, part I: Overall results and analysis. Int J Ind Ergonomics 51
12. Rieger CG, Gertman DI, McQueen MA (2009) Resilient control systems: next generation design research. In: HSI 2009, Catania, Italy
13. Hickling EM, Bowie JE (2013) Applicability of human reliability assessment methods to human–computer interfaces. Cogn Tech Work 15:19–27. https://doi.org/10.1007/s10111-012-0215-x
14. International Atomic Energy Agency (2021) Development, use and maintenance of nuclear power plant simulators for the training and authorization of personnel, TECDOC series
15. dos Santos IJAL et al (2009) The use of questionnaire and virtual reality in the verification of the human factors issues in the design of nuclear control desk. Int J Ind Ergonomics 39.1:159–166
16. dos Santos IJAL et al (2013) Human factors applied to alarm panel modernization of nuclear control room. J Loss Prev Process Ind 26.6:1308–1320
17. Kumar J, Singh T, Joshi NS, Varde PV (2020) Dhruva simulator: core neutronics and thermal hydraulics modules. Life cycle reliability and safety engineering, vol 9, Issue 2. Springer
18. Wang C, Huang T, Gong A, Lu C, Yang R, Li X (2020) Human-machine interaction in future nuclear power plant control rooms—a review. IFAC-papers online, vol 53, issue 5, pp 851–856. ISSN 2405-8963. https://doi.org/10.1016/j.ifacol.2021.04.181
19. Joshi NS, Bhosale PY, Varde PVT, Nutan, (eds) (2019) Development of research reactor simulator. Indian Institute of Technology Madras, India
20. Joshi NS, Singh T, Varde PV (2020) Experience on development of research reactor simulator. In: Proceedings of ICRESH 2019, reliability, safety and hazard assessment for risk-based technologies. Springer
21. International Atomic Energy Agency (2004) Use of control room simulators for training of nuclear power plant personnel. TECDOC Series
22. Kovesdi CR, Le Blanc K (2020) A tool for performing link analysis, operational sequence analysis, and workload analysis to support nuclear power plant control room modernization. AHFE
23. Shirley RB, Smidts CS (2018) Bridging the simulator gap: Measuring motivational bias in digital nuclear power plant environments. Reliab Eng Syst Saf 177:191–209
24. Swain AD, Guttmann HE (1980) Handbook of human reliability analysis with emphasis on nuclear power plant applications. Draft, NUREG/CR-1278
25. Rangra S et al (2017) A graphical model based on performance shaping factors for assessing human reliability. IEEE Trans Reliab 66(4):1120–1143
26. Yoo KH, Back JH, Na MG, Hur S, Kim H (2018) Smart support system for diagnosing severe accidents in nuclear power plants. Nucl Eng Technol 50(4):562–569. ISSN 1738-5733. https://doi.org/10.1016/j.net.2018.03.007
27. Tambouratzis T, Giannatsis J, Kyriazis A, Siotropos P (2021) Applying the computational intelligence paradigm to nuclear power plant operation: a review (1990–2015). https://doi.org/10.4018/978-1-7998-7705-9.ch068
28. Park J, Boring RL, Ulrich TA, Lew R, Lee S, Park B, Kim J (2022) A framework to collect human reliability analysis data for nuclear power plants using a simplified simulator and student operators. Reliab Eng Syst Saf 221:108326. ISSN 0951-8320.https://doi.org/10.1016/j.ress.2022.108326

Enhanced Hybrid Optimal and Intelligent Technique for Data Storage in Cloud

R. Kavitha and A. Valarmathi

1 Introduction

The beginning of the twenty-first century witnessed a major change in the way healthcare is practiced globally. This is due to the emergence of digital technology that completely changed the way records are handled. The advantages of this technology include the ability to collect and share healthcare data among various healthcare providers. This process involves converting paper-based records into electronic ones that are used for various purposes. Some of these include electronic medical records, electronic health records, and personal health records [1]. Electronic health records or EHRs are the medical records of patients that are handled by healthcare professionals. Personal health records or PHRs are the records of patients that are regularly monitored by their relatives.

These records are commonly filled with a variety of data, such as a patient's medical history, demographic data, and laboratory test reports. EHD systems are more advantageous than traditional paper-based records in terms of their efficiency and cost-effectiveness. The various advantages of electronic health records include faster access to clinical data, better support for clinical decisions, and reduced medical costs [2]. E-Health has gained widespread acceptance in Australia's healthcare facilities. Through this system, hospitals can improve efficiency and minimize healthcare costs. Despite the advantages of E-Health, it still has various challenges that need to be addressed before it can be widely used. Some of these include security, privacy, and confidentiality [3].

Due to the various advantages of cloud-based environment, many healthcare organizations are shifting their patient data to the cloud. This is also beneficial for the healthcare industry as it allows them to store and manage their patient data anytime

R. Kavitha (✉) · A. Valarmathi
University College of Engineering, BIT-Campus, Anna University, Tiruchirappalli, India
e-mail: valar1030@yahoo.com

and anywhere. With cloud-based data, patients can access their medical records anytime, anywhere [4]. They can also get treatment and consult with their doctor from anywhere. The rise of digital data has allowed doctors to monitor their patients more effectively. The quality of healthcare services that are based on this technology is also improving [5].

Due to the nature of the attacks that can occur in cloud computing environment, it is important that the privacy and security of patient data are taken into account. If the patient's personal information is compromised, he or she may lose his or her reputation. Also, if the account information of a credit card was compromised, the patient may lose all of his money [6]. Due to the increasing number of cases of sensitive health information, the need for enhanced security and protection of this data has become more prevalent. This session will discuss various factors that affect the security and protection of this data [7].

The cloud has become the platform of choice for many healthcare organizations wanting to store and share their medical data. This paradigm has allowed them to collect, analyze, and share their data wherever they are. The cloud provides complete access to medical data, allowing patients to access their data from various devices such as mobile platforms and PCs. The ability to collaborate between healthcare organizations has made it possible to provide better healthcare services. The cloud also allows healthcare providers to easily implement and monitor emergency interventions that have a higher chance of success [8].

To take advantage of the cloud, healthcare organizations need to establish their infrastructure and storage in a third-party cloud platform. The cloud allows healthcare organizations to focus on their core activities, such as providing healthcare services. However, they should also consider the barriers to adopting the platform. One of the most critical factors that healthcare organizations should consider is the security of their patient's data. Since medical applications are sensitive, they can store and transmit sensitive information [9].

Imagine that your healthcare organization decides to outsource its data storage and access requirements to the cloud. Hybrid cloud is a strategy that combines the advantages of a private cloud with a public cloud. This allows the healthcare organization to store and manage sensitive data. This strategy involves separating the sensitive and non-sensitive parts of the data into separate and secure parts. This process involves carrying out sanitization operations to make the data secure. It allows authorized users to access the data collected by qualified individuals [10].

When sensitive data exceeds the non-sensitive data, it can create a side effect that can affect the correctness of the item sets. This issue usually affects the PPDM algorithm. Sometimes, inauthentic information may be presented or hidden. An extension algorithm can be used to prevent this issue. There are various extensions algorithms that can be used to find the best solution for this issue. Some of these include the Genetic Algorithm and the Particle Swarm Optimization [11].

This research introduces a privacy preservation model that customs AI techniques. It tackles the issues of preserving sensitive information in a cloud environment. For our study, we collected an (EMR) and applied it to a cloud environment. The cleansed data is then accessed by the user from the cloud. The work is organized into five

sections. The main ideas of the research are presented in the first section, while the related works are explained in the second and the proposed algorithms and system models are then analyzed in third sections followed by experimental analyses are carried out in Section fourth and the work is concluded in the fifth section.

The work is organized as follows: The first section describes the main ideas of the research, while the second section explains the related works. The third section deals with the proposed algorithms and system models are then analyzed and the experimental analyses are carried out in Sect. 4. The work is concluded in the fifth section.

2 Related Works

Prasser et al. [12] presented a method that involves analyzing and de-identification of collected health data. This procedure was highly adaptable and could be used for handling large amounts of collected data. The researchers focused on the de-identification method when the population characteristics were not known. In 2017 Wu et al. [13] Ant colony were created to hide sensitive item sets. Each ant would build a tour that would represent a deleted transaction. Their approach involves following steps: Ant routing map, termination condition, Heuristic function, and Delete transactions. Swathi and Sreedhar [14] presents an e-healthcare system based on particle swarm optimization (PSO) algorithm. The results of the study show that the PSO achieves the best fitness value for the small number of iterations. Ruthvik Reddy et al. [15] presents an algorithm for minimizing the number of iterations in an e-healthcare system using whale optimization. The proposed algorithm, known as Minmax WOA, achieves the best fitness value for minimizing the number of iterations. The novelty of this paper is that it presents a hybrid algorithm called Minmax WOA that is derived from the whale optimization principle. The proposed framework in Anand et al. [16] involves carrying out various operations designed to secure and preserve sensitive healthcare data. An optimal key is generated for a particular operation. This paper proposes a firebug-based algorithm for generating the optimal key. The experiments are performed using various healthcare datasets such as HPD, MHEALTH, and MIMIC-III.

3 Proposed Methodology

The data protection model proposed by the Health Information Technology (HIT) industry involves a series of steps that are designed to secure an organization's cloud-based applications. This model works by implementing a set of four entities: the data owner, the user, the smart agreement, and the transactional in cloud. The data owner (or institution that owns the files) is the client of the data protection model. The client is the entity that's authorized to view the files. Each entity has its own function related

to data protection and retrieval. The Department of Health has its own encryption model that's used to secure its EHR. Spider Monkey and Whale Optimization are two algorithms that were developed to protect the data collected by cloud applications.

The existing security mechanisms in e-health cloud are not enough to prevent unauthorized access to sensitive data. In most cases, this means that anyone who has access to sensitive data can easily launch attacks. This paper aims to provide a comprehensive review of the current security and privacy mechanisms that are used in e-health environments. E-health data contains various types of confidential and sensitive information that can be easily accessed by anyone. This includes patient data, credit card details, and social security number.

There are many factors that can affect the security of user information in hybrid cloud. Some of these include, unauthorized access to user data, disclosure of sensitive information, and inadequate encryption. The issue of keeping sensitive items in a database is one that can affect the support count of a given database.

3.1 System Model of Proposed Work

The architecture of our method consists of three main components: the data owner, the hybrid cloud, and the authorized user. Before the data is transferred to the cloud, the owner must protect it from unauthorized users. The other steps would be carried out in order to enable the authorized users to access the data (Fig. 1).

The concept of the SMO-WOA method is to find the optimal coefficient for privacy preservation. The second step involves converting the data into protected data. This procedure is done by extracting the data's input data and its optimal co-efficient. A search algorithm was then developed to find the optimal coefficient, which is necessary to secure the data in the cloud. The algorithm was then used to transfer the
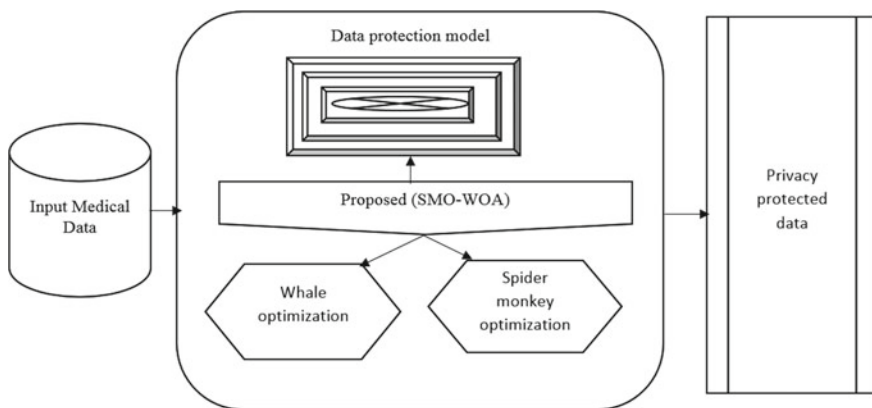

Fig. 1 Proposed architecture

two operators' data to the same product. The resulting data sets are then protected by the algorithm.

3.2 Patient's Data Description

In most clustering algorithms, the datasets are organized as vectors of $Y = y1; y2; y3$. The feature vectors are defined as the degrees of severity of the diseases indicated by the weights given to them. The severity of a disease depends on its severity, which is expressed as the value between 0 and 1–5.

3.3 Data Transmission Phase

This section transfers the protected data from the original healthcare records to a secure server. It uses the privacy and utility parameter to manage the data. The Tracy Singh product is an example of a secure cloud storage system that can store and transfer sensitive data. It works seamlessly while sharing the data in the network.

$$P_{c \times d} = \left(D_{c \times d} \oplus K_{1_{(1 \times 1)}}\right) \oplus K_{2_{(c \times d)}} \tag{1}$$

$$K = K_1 || K_2 \tag{2}$$

A key is a symbol that represents the data that is protected by a certain type of record. This key is usually used to obtain the exact key for preserving the data.

$$K_{1_{(1 \times 1)}} = \frac{1}{c \times d} \sum_{l=1}^{c} \sum_{m=1}^{d} G_{l,m} \tag{3}$$

3.4 Data Retrieval Phase

The Cloud Service Provider (CSP) stores the encrypted data that it collects on behalf of its customers. It uses the data retrieval mechanism to store the requested data. The retrieved data is stored in a protected format. This method retrieves the original data from the protected data.

$$D^*_{c \times d} = \left(P^*_{c \times d} \oplus K_{2_{(c \times d)}}\right) \oplus K_{1_{(1 \times 1)}} \tag{4}$$

The D* and P* represent the retrieved data of size c * d, while the K_1 and K_2 indicate the keys to retrieve the original data.

3.5 Proposed Privacy-Preserving Whale Optimization and Spider Monkey Optimization

A proposed algorithm proving the security and latency of web-based crowdsourcing platforms is presented. The latency refers to the total computational time taken to perform a given task, and the monetary value is calculated using the following formula taking into account numerous tuple values. The main challenge in implementing swarm based optimization algorithms is that they tend to fail to achieve the optimal solution and the improved convergence rate.

Whale Optimization Algorithm overview

This behavior is the reason why many people consider humpback whales as intelligent animals. They use bubble-net techniques to hunt and gather prey. When a whale approaches a certain point, it forms bubbles around it to keep its body from moving toward a standard point. The animals then attack this area to attract food.

Exploration in WOA

These creatures exploit the ocean's n-dimensional search space for prey without mimicking any leader whale.

$$L(t + 1 = L_R(t) - K.Y \tag{5}$$

$$Y = |Z.L_R(t) - L(t) \tag{6}$$

This function is modeled as a shrinking circle mechanism that gets deceased over the course of iterations.

The sum of the positions Ll and K is the sum of the positions k and b, which is a function of b.

$$K = 2.b.x - b \tag{7}$$

$$Z = 2.x \tag{8}$$

where

$$b = 2 - (2.\frac{current\ iteration(t)}{total\ no\ of\ iterations} \tag{9}$$

A whale's search for the best solution is made possible through the uniform random vector x.

Exploitation Phase

A bubble-net attack is a behavior utilized by a whale to locate and harass prey. This is a type of whale attack that involves herding other whales to a certain location.

$$L(t + 1 = L_l(t) - K.Y \tag{10}$$

$$Y = |Z.L_l(t) - L(t) \tag{11}$$

The goal of this behavior is to get killed in a linear fashion over the course of iterations. It's modeled as a shrinking circle mechanism.

$$L(t + 1) = Y.e^{ms} \cos(2\Pi s) + L(t) \tag{12}$$

The following strategy is used to find the next position. This strategy uses the random number s and m to find the next position.

$$L(t + 1) = \begin{cases} L_l(t) - K.Y & if \ F_j < 0.5 \\ Y.e^{ms} \cos(2\Pi s) \ if \ F_j \geq 0.5 \end{cases} \tag{13}$$

where v is a random integer with a uniform distribution in the range [0, 1].

Spider monkey optimization algorithm

The spider monkey's fission–fusion social structure is the central component of its foraging behavior that inspired the SMO algorithm. Due to the existence of only a few spider monkeys in a small group, the SMO algorithm is considered a swarm intelligence method. The goal of this paper is to represent spider monkeys in the SMO algorithm.

Initialization of population

The SMO distributes the first spider monkey in the swarm as M. *Smj* Eq. (14) initializes each *Smj*.

$$sm_{j,k} = sm_{\min k} + v(0, 1) \times (sm_{\max k} - sm_{\min k}) \tag{14}$$

The lower and upper limits of search space are known as $Sm_{\min k}$ and $Sm_{\max k}$, respectively.

Local leader stage

The positions are updated depending on the level of fitness of the individual spider monkeys. For each new position, the fitness value is calculated.

$$sm_{newj,k} = sm_{jk} + v(0, 1) \times (L_oL_e - sm_{jk} + v(-1, 1) \times (sm_{pk} - sm_{jk}) \quad (15)$$

The jth spider monkey has a kth dimension and a local leader dimension. The kth group's dimension is LocalL.

Global leader stage

The algorithm takes into account the selection probability and the fitness function of the selected solution. The concept of fuzzy rules can be used to estimate the fitness value of a given solution.

$$Fitness_j = \begin{cases} \frac{1}{1+F_j}, & if\ F_j \geq 0 \\ 1 + cdr(F_j)\ if\ F_j\ < 0 \end{cases} \quad (16)$$

The calculation of the probability of being selected as the global leader is performed according to the procedure.

$$prb_j = 0.1 + \left(\frac{Fitness_j}{Maximum\ Fitness} \right) \times 0.9 \quad (17)$$

The spider monkey knows the position of the global leader. It uses its knowledge to update its position.

$$sm_{newj,k} = sm_{jk} + v(0, 1) \times (G_oL_e - sm_{jk} + v(-1, 1) \times (sm_{pk} - sm_{jk}) \quad (18)$$

The concept of global leadership is linked to the characteristics of a parent spider monkey. This animal's behavior is similar to that of a global leader.

Global leader learning stage

The overall swarm best solution is determined in this stage.

Local leader learning stage

The local leader can now update its position by choosing members of a group. It can also do so by clicking on the group's selection is set as 1or 0.

Local leader decision stage

The global leader's experience is then updated according to the group's position. The local leaser limit is never changed. It stays the same as the global leader's experience.

$$sm_{newj,k} = sm_{jk} + v(0, 1) \times (G_oL_e - sm_{jk}) + v(0, 1) \times (sm_{pk} - L_0L_e) \quad (19)$$

The number of spider monkeys in a group is equal to the number of solutions that the global leader attracts. Set the local leader count as zero to determine if the local learning leader is more powerful than the global leader.

Global leader decision stage

The global leader's threshold is the limit of his or her ability to influence global decisions when the global leader never gets reoriented to a specific verge.

4 Result and Discussion

The purpose of this section is to discuss how to protect the sensitive health records of users in a cloud environment. This data is stored on a third-party server. When someone tries to access it, they are authenticated using multifactor. Contextual authentication and Biometric based verification help establish trust between the service provider and the user. The multifactor algorithm is used to prevent unauthorized access and minimize privacy and security risks. The system's performance is evaluated using encryption time and decryption time. A successful implementation of this strategy will involve the following steps: validating the user's identity, granting access, and securing the data. The PHR Sample Database was used to evaluate the system's performance. It was created using Python 3.6.5. Figure 2 shows the PHR upload and the encryption process. It is important that the user's sensitive health information is kept private. Privacy is an important aspect of ehealth records systems. It is achieved through a set of procedures and mechanisms that can be easily implemented. Security and privacy of e- health data are two of the most critical factors that concern organizations when it comes to implementing an e-health system. Cloud servers are considered semi-trusted because they can't actively collect and store sensitive information (Fig. 3).

Figure 4 shows the cloud and user decryption process of PHR. Instead of allowing the providers to store and share their patients' PHR data, PHR services should give them full control over how their data is used. By restricting the sharing of their PHR data, providers can ensure that only their own individuals have access to it. Each patient has her own decryption key. They can then distribute them to their authorized users. They should also be able to restrict the access to their PHR data to prevent unauthorized users from accessing it. Figure 5 shows the Performance analysis of our proposed model in terms of Security level, Privacy, accuracy, Reliability, Encryption and decryption time.

Figure 6 illustrates that WOA-SMO An algorithm known as WOA-SMO was developed to provide fast and secure encryption for large files. This feature can help prevent data loss. Due to the algorithm's minimum execution time, the system uses it while protecting data therefore, the graphical investigation of the overall system execution time is plotted in Figs. 6 and 7.

Figure 7 illustrates that WOA-SMO The goal of this study was to develop a method that would allow people to store and access health data without having to spend a long time on encryption. The system's implementation time is computed based on the minimum amount of time it takes to perform a successful encryption is plotted in Fig. 7.
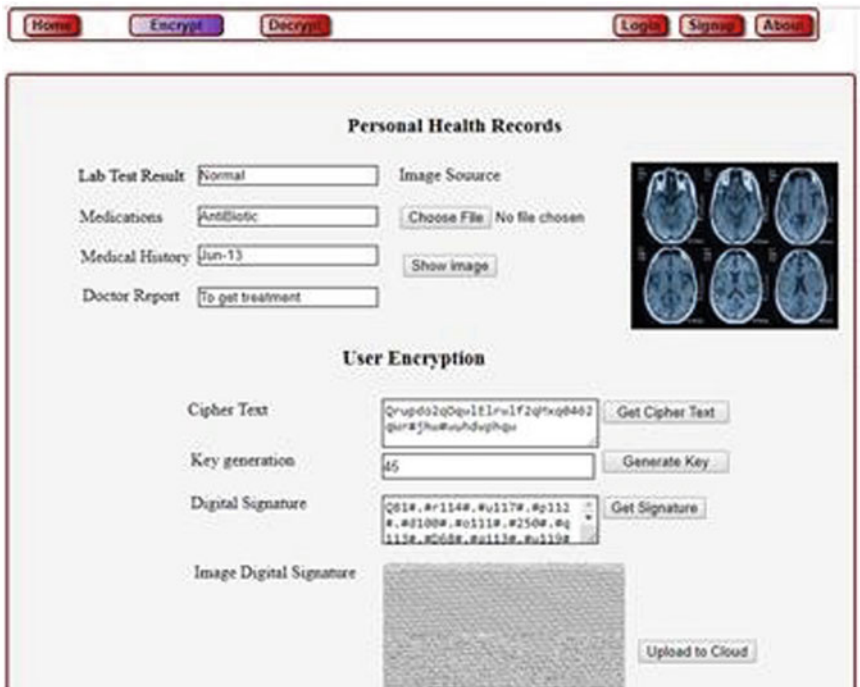
Fig. 2 PHR upload

5 Conclusion and Future Scope

Privacy and data protection are very challenging issues when it comes to storing and accessing the data of a healthcare facility. Various research is being conducted on how to improve the security of healthcare facilities' data. This article aims to provide an overview of the current research on this topic. An efficient method of storing and protecting healthcare facility's data is by implementing a security scheme that is designed to prevent attacks. This method can be commonly utilized in e-health cloud storage due to its level of security. However, this approach is not ideal for sensitive data such as patient records. Due to this, it is not considered as an acceptable security method. Also, this type of security scheme is not ideal for patient-centric data storage setups. As a result, it cannot be considered for use in healthcare facilities. Modern Access Control mechanisms are also needed to enable fine-grained access control. Privacy disclosure techniques are also needed to prevent unauthorized access to cloud-based EHRs.
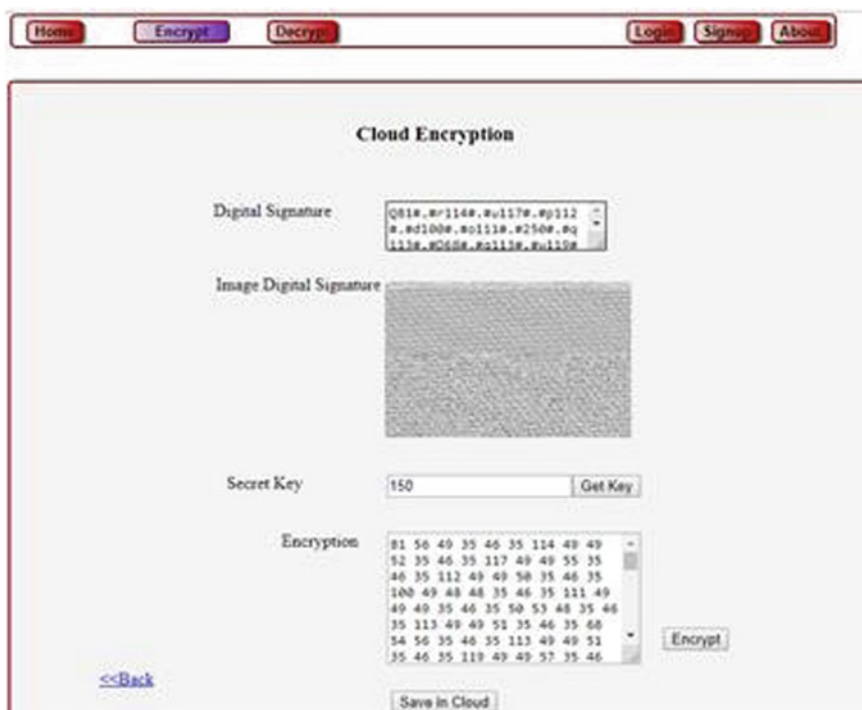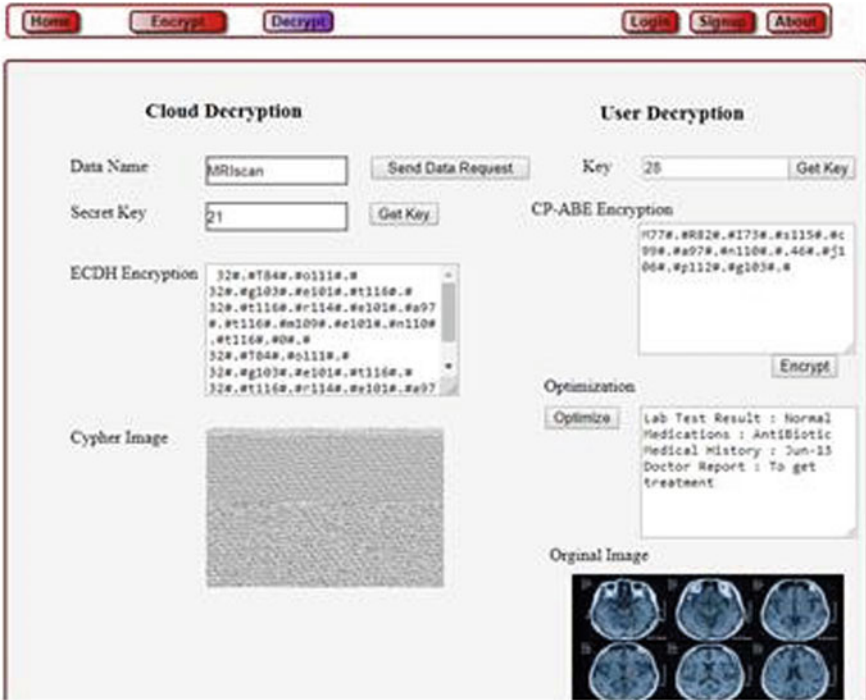
Fig. 3 PHR cloud encryption

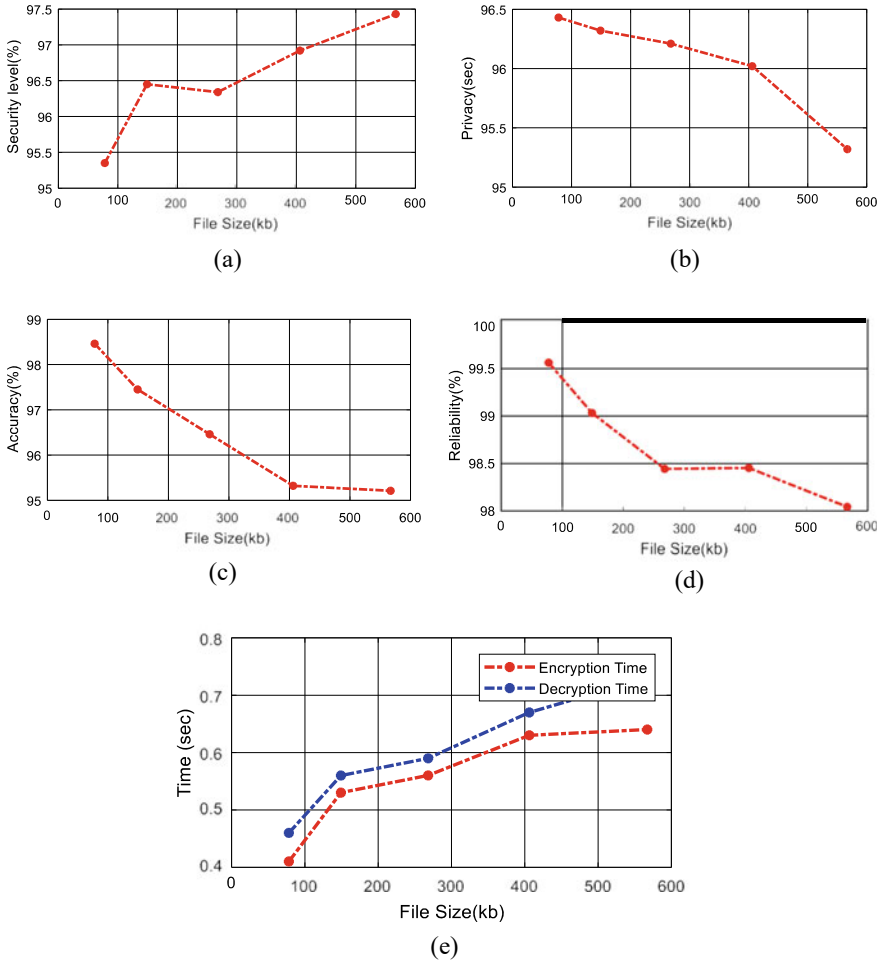**Fig. 4** Cloud and user decryption process of PHR

Fig. 5 Performance analysis of **a** security level, **b** privacy, **c** accuracy, **d** reliability and **e** encryption and decryption time
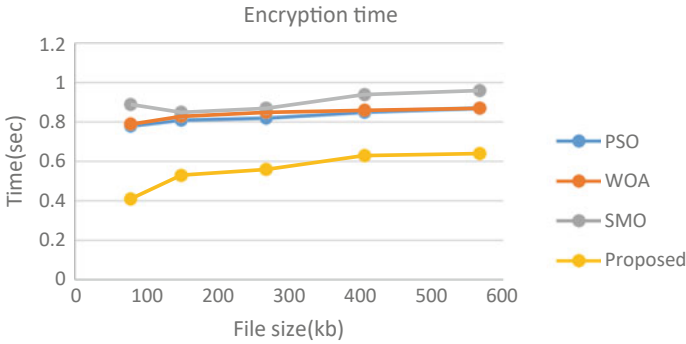
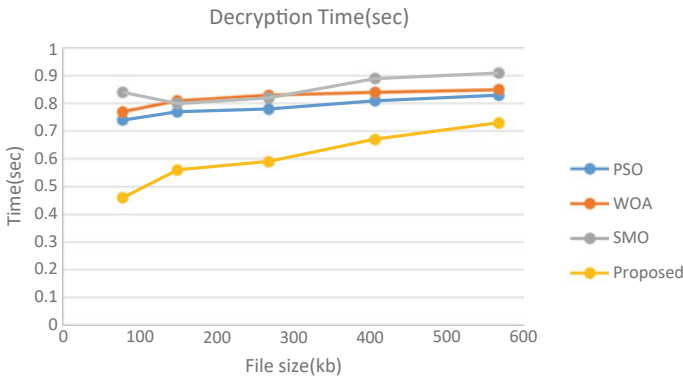**Fig. 6** Encryption time analysis for different file sizes

Fig. 7 Decryption time analysis for different file sizes

References

1. Elavarasan RM, Pugazhendhi R (2020) Restructured society and environment: a review on potential technological strategies to control the COVID-19 pandemic. Sci Total Environ 725:138858
2. Khoza-Shangase K (2021) Confronting realities to early hearing detection in South Africa. In: Early detection and intervention in audiology: an African perspective, pp 66–68
3. Zeadally S, Isaac JT, Baig Z (2016) Security attacks and solutions in electronic health (e-health) systems. J Med Syst 40(12):1–12
4. Kaur H, Alam MA, Jameel R, Mourya AK, Chang V (2018) A proposed solution and future direction for blockchain-based heterogeneous medicare data in cloud environment. J Med Syst 42(8):1–11
5. Gogia S (2020) Rationale, history, and basics of telehealth. In: Fundamentals of telemedicine and telehealth. Academic Press, pp 11–34
6. Ghorbel A, Ghorbel M, Jmaiel M (2017) Privacy in cloud computing environments: a survey and research challenges. J Supercomput 73(6):2763–2800
7. Frustaci M, Pace P, Aloi G, Fortino G (2017) Evaluating critical security issues of the IoT world: present and future challenges. IEEE Internet Things J 5(4):2483–2495

8. Nguyen DC, Pathirana PN, Ding M, Seneviratne A (2019) Blockchain for secure EHRs sharing of mobile cloud based e-health systems. IEEE Access 7:66792–66806
9. Liu Y, Zhang L, Yang Y, Zhou L, Ren L, Wang F, Liu R, Pang Z, Deen MJ (2019) A novel cloud-based framework for the elderly healthcare services using digital twin. IEEE Access 7:49088–49101
10. Kanwal T, Jabbar AA, Anjum A, Malik SU, Khan A, Ahmad N, Manzoor U, Shahzad MN, Balubaid MA (2019) Privacy-aware relationship semantics–based XACML access control model for electronic health records in hybrid cloud. Int J Distrib Sens Netw 15(6):1550147719846050
11. El Khalil F (2015) Sécurité de la base de données cadastrales (Doctoral dissertation, Université de la Polynésie Française; Université de la Polynésie française)
12. Prasser F, Kohlmayer F, Spengler H, Kuhn K (2018) A scalable and pragmatic method for the safe sharing of high-quality health data. IEEE J Biomed Health Inform 22(2):611–622
13. Wu J, Zhan J, Lin J (2017) Ant colony system sanitization approach to hiding sensitive item sets. IEEE Access 5:10024–10039
14. Swathi M, Sreedhar KC (2020) A cloud-based privacy-preserving e-healthcare system using particle swarm optimization. In: Proceedings of the third international conference on computational intelligence and informatics. Springer, Singapore, pp 133–143
15. Ruthvik Reddy P, Sri Sai Nikhil G, Sreedhar KC, Shaik M, Swathi M (2019) A cloud-based privacy preserving e-healthcare system using whale optimization. In: International conference on computational and bio engineering. Springer, Cham, pp 97–109
16. Anand K, Vijayaraj A, Vijay Anand M (2022) Privacy preserving framework using Gaussian mutation based firebug optimization in cloud computing. J Supercomput 1–24

Human Reliability Analysis of a High-Impact Aeronautical Situation Using a Second-Generation HRA Technique

Sharath. B. Boosnur

1 Introduction to Human Reliability

By 1950, it was clearly seen that the capability of machines had increased more than that of human beings. Instead of being the executioners of the whole job, humans were playing the role of operators. The capabilities of the hardware and software far outweigh that of humans. Most systems are so large in scale that humans cannot even monitor the whole of it without some assistance from the machines themselves.

It is seen that the extent of autonomy of the systems has increased over the years. Yet it has not been possible to eliminate the human in the loop to make systems truly autonomous. Some operators are invariably involved in the loop and required for some occasional interventions. Though the amount of required intervention has reduced, the significance of such interventions has increased.

This brings out the importance of Human Reliability. Very often, accidents and untoward incidents are attributed to "human error" due to lack of deeper analysis. However, on further analysis, many more causes can be found and their influences can be quantified, ranked and acted upon as per their priority.

1.1 HRA Standards

As of now, many standards are available for guidance in the field of human reliability [1]. Several of them are proprietary and not available for public use. HRA is a niche field. Hence, it is expectable that many standards are more suitable for the domain that they were developed for than for the others. The leading developers were the

Sharath. B. Boosnur (✉)
Indian Institute of Technology, Khaagpur, Kharagpur, West Bengal 721302, India
e-mail: sharathbb@hotmail.com

atomic energy agencies, especially from the USA. Several of the NRC standards are usable for non-nuclear scenarios also but further work needs to be done for such customization.

The HRA techniques which were developed initially had several disadvantages. It was felt that they were lacking in accuracy. Another prominent issue was the disagreement of the contemporary domain experts with the results produced.

CREAM method offers several advantages and is very practical compared to the older methods.

1.2 CREAM Method

The "Cognitive Reliability and Error Analysis Method", popularly referred to as CREAM was introduced by Hollnagel [2]. Right from the time of development, the developers took care to make it usable for both Event analysis and performance prediction. Event analysis is a retrospective method wherein the analysis begins from the incident under investigation and concludes with probable causes. Suggesting probable outcomes or calculating their probabilities constitutes performance predication. The method is detailed enough to cater for both Qualitative and Quantitative analysis.

The process in this standard is very methodical. More importantly, it has a good correlation with the psychology with which human reliability is deeply connected to. The scenarios where HRA is applied have human operators as a main stakeholder. Hence, the individual differences between operators have to be accounted for. A psychological model called "COCOM" is used for this purpose. The Common Performance Conditions are used to identify the differences between the operators.

1.3 Importance of Flight Safety

Safety cannot be emphasized enough in the field of Aircraft operations. Failure is too costly a consequence which has to be avoided at any cost. The loss of lives resulting from a single accident can bring forth a slew of lawsuits that can bankrupt the airline itself.

Lesser incidents than an outright crash also have their impact on the airline. The reputation is at stake. There are many other airlines and so, bad publicity will just drive the passengers away. That is a brief account of the importance of safety in flight.

Also, there are many challenges in airline operations. Aircraft have grown larger and more complex with time. Also, the cockpits have more instruments, displays and controls. So, flying an aircraft needs awareness of a large number of parameters. In parallel, the pilots have to communicate regularly with the ATC (Air Traffic Controller). Pilots have to make adjustments to account for natural variations in the

weather. They also have to deal with irregular work hours and the resultant stress and fatigue.

Air travel is far safer now than it has been in the past. According to the Civil Aviation Authority, the fatality rate per billion kilometres travelled by plane is 0.003 compared to 0.27 by rail and 2.57 by car [3]. But due to all the challenges mentioned above, airplane accidents do occur and are associated with huge costs to the passengers as well as to the airlines.

Importance of human reliability in flight operations: According to NTSB (National Transport Safety Board of USA), 75% of all airplane accidents are pilot-related. This safety record of general aviation offers an opportunity for advancing the practice of HRA. HRA methods can be used to analyze human errors and identify interventions that would increase flight safety.

2   Considered Task

HRA analysis of the situation involving the mid-air collision in Alaska on 13-5-2019 between plane-1 (de Havilland DHC-2, N952DB also known popularly as "Beaver") and plane-2 (de Havilland DHC-3, N959PA also known popularly as "Otter").

The details of the accident are taken from the reference document: Accident Report No: NTSB/AAR-21/04 *PB2021-100,915* by NTSB, USA [4].

2.1   Details of the Scenario Selected for Analysis

An accident took place on May 13, 2019 at about 1221 h Alaska time. It involved the two airplanes as mentioned before, which collided in midair about 8 miles northeast of Ketchikan, Alaska. The DHC-2 pilot and four passengers sustained fatal injuries. The DHC-3 pilot sustained minor injuries, nine passengers sustained serious injuries, and one passenger sustained fatal injuries. The DHC-2 was destroyed and the DHC-3 sustained substantial damage.

Both airplanes had been conducting sightseeing flights and were both converging on a scenic waterfall before returning to the Ketchikan Harbor Seaplane Base (5KE), Ketchikan, Alaska, when the accident occurred.

Automatic dependent surveillance-broadcast (ADS-B) tracking data for both airplanes revealed the following information: At 1217:15, the DHC-3 was about level at 4000 ft. mean sea level (msl) on a track of 225°, and the DHC-2 was 4.2 nautical miles (nm) south of the DHC-3, climbing through 2800 ft. msl, on a track of 255°. About 1219, the DHC-3 started a descent from 4000 ft., and the DHC-2 was at 3175 ft. and climbing. During the next 1 min 21 s, the DHC-3 continued to descend on a track between 224° and 237°, and the DHC-2 leveled out at 3350 ft. on a track of about 255°. The airplanes collided at 1221:14 at an altitude of 3350 ft., 7.4 nm northeast of 5KE.
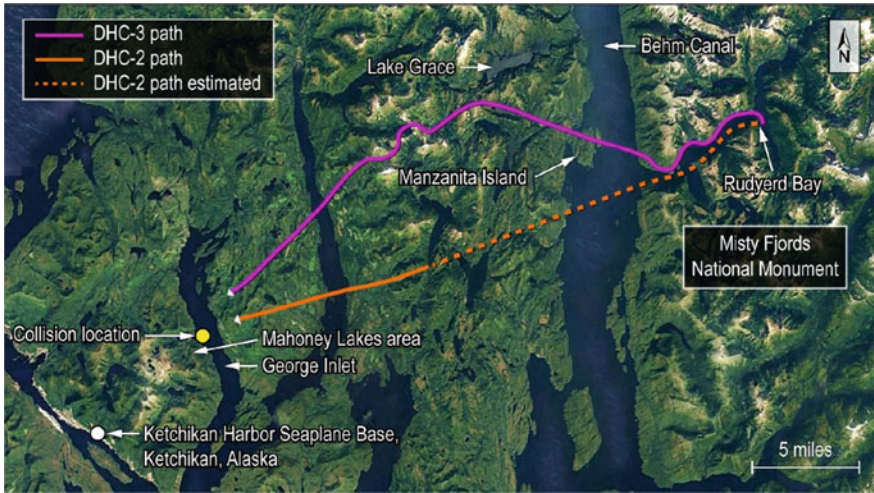
Fig. 1 Location of the accident

Figure 1 shows the location of the accident.

Figure 2 shows the bearing of the airplanes and their altitudes just before the accident.

2.2 Event Tree Analysis

The incident involved is one of very very low probability and hence not commonly observed. It is very difficult to pinpoint an event as the initiator. It is also difficult to enumerate the supporting events for the event tree. An attempt is carried out as follows:

Consider an initiating event as "two planes in courses leading to collision".

Some possible pivotal event are: Air Traffic Controller notices the possibility and alerts the pilots, Pilot(s) note the warning and take corrective action. (Even if one pilot takes effective corrective action, it is enough), Passenger(s) notice approaching plane and alert the pilot, Pilot(s) take action based on passenger(s) warning, Just before impact, one pilot notices that the other plane is dangerously close and Pilot makes a high-g maneuver after noticing the other plane (Fig. 3).

Some possible end outcomes are: No collision, Near miss leading to disturbance in aircraft attitudes, Low-impact collision (with possibility of an emergency landing and prevention of fatalities) and High-impact collision with fatalities.
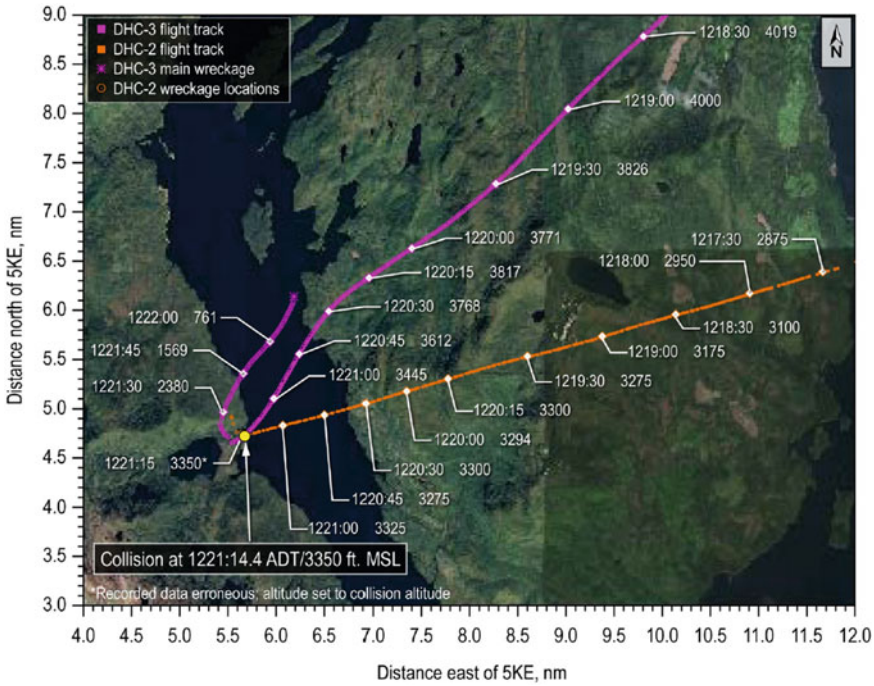
Fig. 2 Bearing and altitudes just before the accident

3 HRA Analysis of the Scenario Using CREAM Standard

Two methods are provided by CREAM standard—a basic method and an extended method. The procedure for both is as shown in Fig. 4:

3.1 Details of the Analysis Carried Out—Basic Method

A Human Reliability Analysis has been carried out for the above described situation. The situation involves aircraft which are in widespread usage and also involves operators. It also involves external influences like environmental conditions, regulatory influences, organizational influences and possible influences by passengers. Hence, it is a fit case for usage of the CREAM standard which addresses cognitive factors in depth.

The Common Performance Conditions are analyzed as follows for the most taxing situation: the one near the waterfalls where the accident took place (Table 1):

Initiating	Pivotal events				Outcome
event	PV-1	PV-2	PV-3	PV-4	
2 planes on courses leading to collision	Air Traffic Controller notices the possibility and alerts the pilot(s)	Passenger(s) notice approaching plane and alert the pilot.	Pilot(s) notices that the other plane is dangerously close	Pilot(s) take satisfactory corrective action	Collision or safe flight or other effect
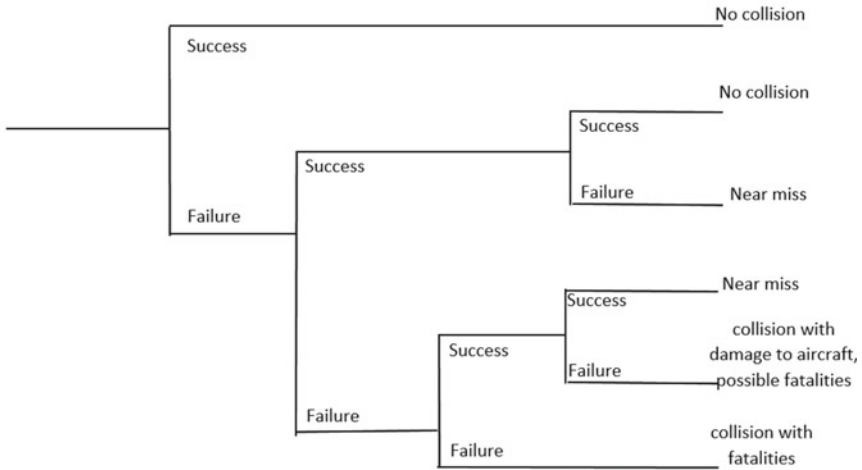
Fig. 3 Event tree of the scenario

As per the simple method of CREAM method, the analysis is carried out as follows:

No of reduced = 2, No of improved = 1. Not significant ones: 6.
Mode of operation determined from CREAM definition: Tactical.
Probability of action failure for this mode: 0.001–0.1 (i.e., 0.1–10%).
Predicted performance reliability: 0.9–0.999 (90–99.9%).

3.2 Details of the Analysis Carried Out—Extended Method

Next, the possible modes of error are analysed as follows [5] (Table 2):
A Hierarchical Task Analysis has been carried out as shown in Fig. 5:
In tabular form, the tasks involved are as shown in Table 3:
The sub-tasks for the scenario have been analysed as shown in Table 4:
The cognitive activities in our scenario have been analyzed and the cognitive functions associated have been identified as shown in Table 5:
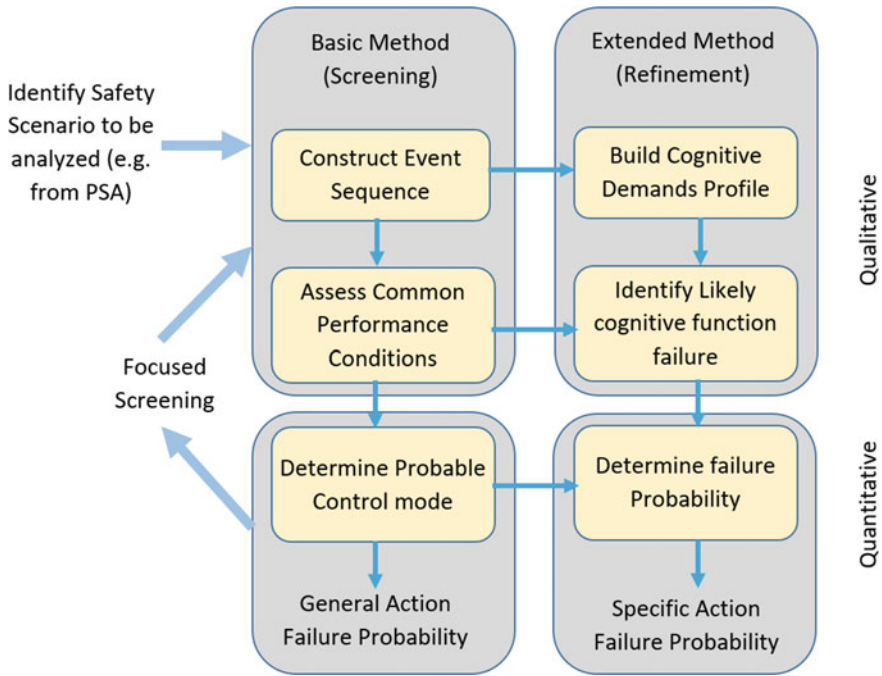
Fig. 4 Two methods of analysis in CREAM standard

Table 1 Analysis of common performance conditions

CPC name	Level determined for the situation
Adequacy of organization	Inefficient
Working conditions	Compatible
Adequacy of MMI and operational support	Adequate
Availability of procedures/plans	Acceptable
Number of simultaneous goals	More than capacity
Available time	Temporarily inadequate
Time of day (circadian rhythm)	Day-time (adjusted)
Adequacy of training and experience	Adequate, high experience
Crew collaboration quality	Inefficient

Table 2 Analysis of possible error modes

Error mode	Possibility 0: = impossible, 1: = possible, 2: = very likely
Timing	1
Duration	0
Force	0
Distance/magnitude	1
Speed	1
Direction	1
Wrong object	0
Sequence	0

Fig. 5 Hierarchical task analysis of the scenario

Considering the weighting factors, the CFP (Cognitive Failure Probability) values will get modified and the final calculated values are shown in Table 6:
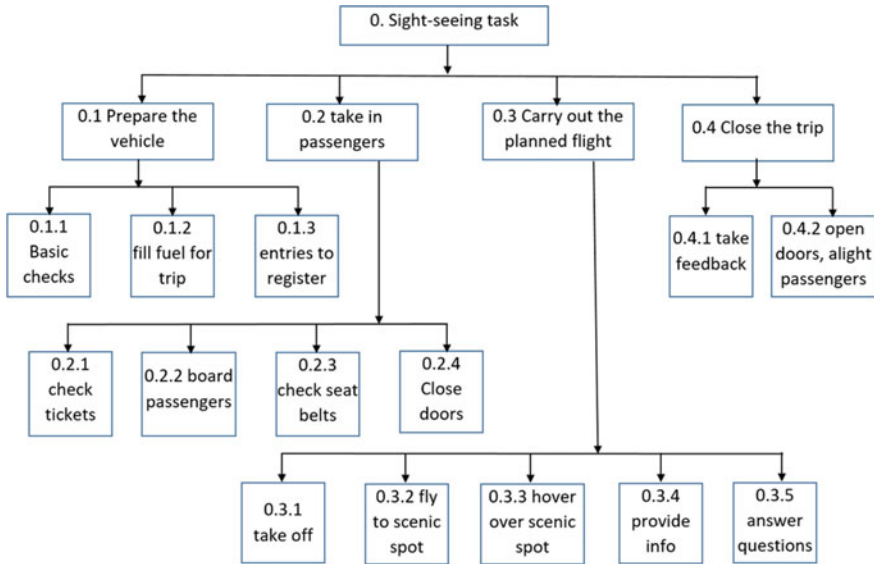
Now, these values can be used in an Event Tree to determine the real event probabilities.

Table 3 Steps in the sight-seeing flight task

#	Goal	Task step or activity
0.1.1	Prepare the vehicle	Basic check of plane operations
0.1.2		Fill fuel for trip
0.1.3		Make entries to register
0.2.1	Take in passengers	Check passengers tickets
0.2.2		Board passengers
0.2.3		Check seat belts of passengers
0.2.4		Close doors
0.3.1	Carry out planned flight	Take off
0.3.2		Fly to scenic spot
0.3.3		Hover over scenic spot
0.3.4		Provide notable information in any
0.3.5		Answer passengers' questions if any
0.3.6		Return to base and land
0.4.1	Close the trip	Take feedback from passengers
0.4.2		Open doors and alight passengers

Table 4 Cognitive activities in the flight trip task

#	Goal	Task step or activity	Cognitive activity
0.1.1	Prepare the vehicle	Basic check of plane operations	Verify
0.1.2		Fill fuel for trip	Execute
0.1.3		Make entries to register	Execute
0.2.1	Take in passengers	Check passengers tickets	Verify
0.2.2		Board passengers	Monitor
0.2.3		Check seat belts of passengers	Scan
0.2.4		Close doors	Execute
0.3.1	Carry out planned flight	Take off	Execute
0.3.2		Fly to scenic spot	Execute
0.3.3		Hover over scenic spot	Execute
0.3.4		Provide notable information in any	Communicate
0.3.5		Answer passengers' questions if any	Communicate
0.3.6		Return to base and land	Execute
0.4.1	Close the trip	Take feedback from passengers	Execute
0.4.2		Open doors and alight passengers	Execute

Table 5 Cognitive demands table for the flight task

#	Goal	Task step or activity	Cognitive activity	Observe	Interpret	Plan	Execute
0.1.1	Prepare the vehicle	Basic check of plane operations	Verify	*	*		
0.1.2		Fill fuel for trip	Execute				*
0.1.3		Make entries to register	Execute				*
0.2.1	Take in passengers	Check passengers tickets	Verify	*	*		
0.2.2		Board passengers	Monitor	*	*		
0.2.3		Check seat belts of passengers	Scan	*			
0.2.4		Close doors	Execute				*
0.3.1	Carry out planned flight	Take off	Execute				*
0.3.2		Fly to scenic spot	Execute				*
0.3.3		Hover over scenic spot	Execute				*
0.3.4		Provide notable information in any	Communicate				*
0.3.5		Answer passengers' questions if any	Communicate				*
0.3.6		Return to base and land	Execute				*
0.4.1	Close the trip	Take feedback from passengers	Execute				*
0.4.2		Open doors and alight passengers	Execute				*

4   Results

The Basic method of analysis provided an output for Probability of action failure in the range: 0.001–0.1 (i.e., 0.1–10%).

However, the detailed method of analysis provided an output for probability of action failure for all the individual actions as detailed in the previous section.

Table 6 Final CFPs

#	Goal	Task step or activity	Adjusted CFP
0.1.1	Prepare the vehicle	Basic check of plane operations	0.00160
0.1.2		Fill fuel for trip	0.00576
0.1.3		Make entries to register	0.00576
0.2.1	Take in passengers	Check passengers tickets	0.20000
0.2.2		Board passengers	0.20000
0.2.3		Check seat belts of passengers	0.00160
0.2.4		Close doors	0.00576
0.3.1	Carry out planned flight	Take off	0.00576
0.3.2		Fly to scenic spot	0.00576
0.3.3		Hover over scenic spot	0.00576
0.3.4		Provide notable information in any	0.00576
0.3.5		Answer passengers' questions if any	0.00576
0.3.6		Return to base and land	0.00576
0.4.1	Close the trip	Take feedback from passengers	0.00576
0.4.2		Open doors and alight passengers	0.00576

5 Conclusion

After analysis of the results, the following recommendations were provided for improvement of the human reliability.

(a) Pilot can be provided information on number of flights near hot spots so flights can be staggered in time.
(b) Some facilities for situational awareness can be incorporated.
(c) Procedures can be updated to cater for emergencies and unusual type of errors.
(d) The pilot can take another person as a guide for the tours—a local resident, not necessarily a trained guide.
(e) The tour operating company can keep track of similar flights in the area by sharing information with the others.

References

1. (2009) Review of human reliability assessment methods. Health Saf Executive
2. Hollnagel E (1998) CREAM-cognitive reliability and error analysis method. Elsevier Science Ltd
3. https://www.nsc.org/. Webpage of the National Safety Council of USA
4. https://www.ntsb.gov/. NTSB report No NTSB/AAR-21/04 adopted on 20 Apr 2021
5. Hollnagel E et al (2004) Failures without errors: quantification of context in HRA. Reliab Eng Syst Saf 83

Sensitivity of Angle Parameters in the Modelling of Bistable Variable Stiffness Laminates

B. Danish, K. S. Suraj, P. M. Anilkumar, and B. N. Rao

1 Introduction

Morphing structures capable of adapting their behavior in response to surrounding environmental stimuli are highly desirable in various engineering applications. In recent years, unsymmetrical bistable laminate has become an ideal candidate for morphing application due to its ability to exhibit two stable configurations in room temperature conditions. The shape change between stable equilibrium states can be made by applying sufficient energy to trigger the snap-through action [1]. Apart from the established aerospace applications, bistable laminates finds its position in other fields like wind and solar energy harvesting, robotics, and foldable structures [2]. The energy required for snap-through can be provided by either mechanical load [3, 4] or using smart materials like shape memory alloys and piezoelectric macro fiber composite (MFC) actuators [5–7].

The energy needed to trigger snap-through is crucial to the development of multi-stable structural components. If the snap-through energy requirements are high, the shape-transition becomes infeasible. Energy requirements for the snap-through transition can be reduced by spatially tailoring the stiffness of the individual bistable plate [8]. By changing the orientation of the fibres, it is possible to vary the spatial stiffness, producing laminates with variable stiffness (VS). Sousa et al. [8] proposed the idea of VS laminate in morphing applications. Later, Haldar et al. [9] explored the possibility of expanding the design space by tailoring VS angle parameters. Further, Anilkumar et al. [10] performed parametric studies on the snap-through and snap-back behaviors by varying the angle parameters of the VS laminate where the snap-through has been triggered using MFC actuators. In the studies mentioned, stable

B. Danish · K. S. Suraj (✉) · P. M. Anilkumar · B. N. Rao
Structural Engineering Division, Department of Civil Engineering, IIT Madras, Chennai 600036, India
e-mail: ce21d402@smail.iitm.ac.in

217

shapes and snap-through requirements were predicted using semi-analytical models based on the Rayleigh–Ritz minimization method. In addition, finite element (FE) frameworks have been widely adopted to study the behavior of bistable composites due to its improved accuracy in predicting the snap-through behavior in comparison with semi-analytical models. The variable stiffness laminates are getting paramount of attraction due to their ability to ensure the continuity of the smooth fiber between the two regions to avoid the stress concentrations along with the advantage of lower snap-through energy requirements, which is beneficial in morphing applications.

Although curvilinear path alignments to produce variable stiffness laminates can be accomplished through the Automated Fibres Placement technique, however manufacturing laminate layups with the precise VS parameters may not be easy. Uncertainties in the angle parameters due to the manufacturing constraints can lead to inaccurate evaluation of snap-through requirements. In order to access the tolerance limits of VS angle parameters, the sensitivity needs to be investigated. Studies on sensitivity analysis and uncertainty quantification due to uncertainties in design variables have been reported only on straight fibres laminates [11–14]. However, the VS laminates may or may not behave in the similar way as reported for straight fiber laminates. Additionally, there is still room for research into how variations in the VS angle factors affect the bistable behavior. Therefore, the goal of the current study is to comprehend the significance of minor perturbations of VS angle parameters on the bistability of VS unsymmetrical laminates, where sensitivity analysis on the deformation and snap-through load of bistable VS laminates due to uncertainty in angle parameters are investigated. Uncertainties in the snap-through loads and out-of-plane displacements due to the individual variations of ϕ, T_0, and T_1 has been investigated. The analysis has been performed on a commercially available finite element package, *ABAQUS*. Finally, design contour charts exploiting the change in characteristic parameters by altering the orientation angle for a family of VS laminate are prepared from the finite element analysis.

2   Variable Stiffness Laminate

The variable stiffness laminate defines by the three angle parameters ϕ, T_0, and T_1 as shown in Fig. 1. Modelled VS laminate fibres follow the curvilinear path suggested by Gürdal et al. [15]. The fiber orientation θ is defined as follows:

$$\theta\left(x'\right) = \phi + \frac{(T_1 - T_0)\left|x'\right|}{d} + T_0, \quad \text{where,} \quad x' = x\cos\phi + y\sin\phi$$
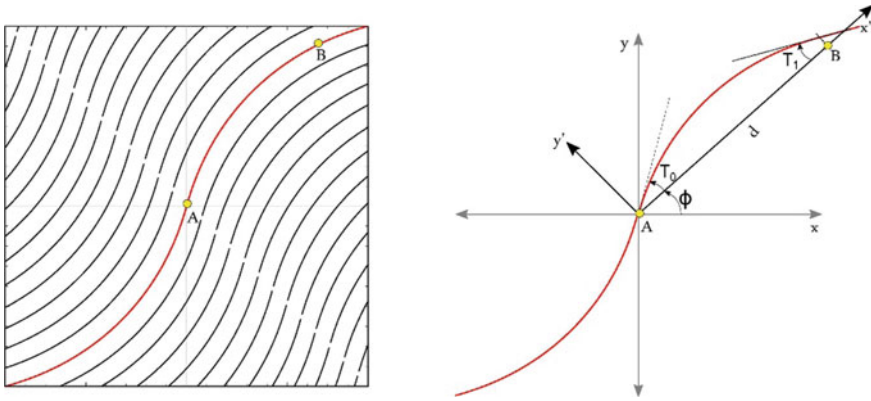
Fig. 1 Curvilinear path description of VS laminate

3 Finite Element Model

FE analyses of VS composite laminates considering geometric nonlinearities are performed in a commercially available FE package, *ABAQUS*. To take non-linear geometric behavior into consideration, the large deformation theory based on the NLGEOM option has been used. Four-node quadrilateral (S4R) shell elements with reduced integration have been used to model the laminates. A balance between computational speed and accuracy has been achieved by carefully studying mesh convergence and choosing the appropriate mesh sizes. The procedures that were used in the analysis are explained below.

3.1 Step 1: The Initial Step

In this initial step, thermal loading given as curing temperature of 180 °C is imposed on the laminate. The laminate has been clamped from its geometric centre by restraining the centre most node.

3.2 Step 2: The Cool-Down Step

The temperature of the laminate has been lowered to 20 °C in this step, where residual stresses are introduced into the laminate. The composite laminates deviate from their initial alignment in one of their potential stable shapes as a result of temperature differences. To prevent the appearance of unstable saddle shapes, imperfections are added to the proposed laminate model.

3.3   Step 3: The Snap-Through Step

In this stage, a static snap-through process has been simulated. At the four corners of the laminate, transverse point loads are applied to cause snap-through. In order to arrive at a converged equilibrium solution, automatic stabilization with a specific dissipated energy fraction has been imposed during the analysis. To deform the laminate into another stable shape, a load greater than the snap-through requirement must be applied.

3.4   Step 4: The Stability Check Step

After achieving the second stable state, the concentrated loads at the corners of the laminate are removed so that the laminate rests in one of its stable states (Fig. 2).
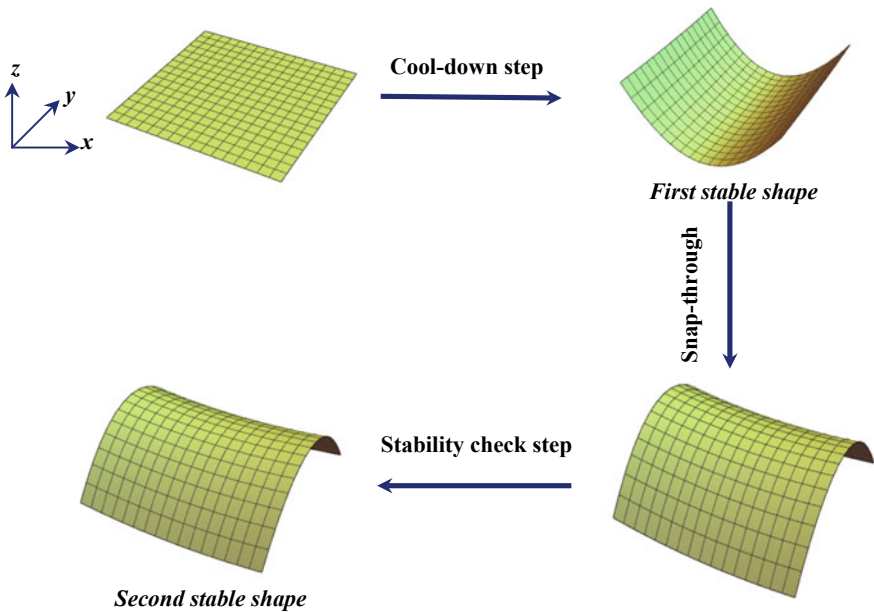

Fig. 2   Flowchart of steps followed in snap-through process

4 Result and Discussion

A square Cycom 977-2 VS lamina of 0.210 mm thickness is considered for the present investigation. A square laminate with a side length of 135 mm is considered, the material properties and the angle parameters are given in Table 1. Effects of individual perturbations on the angle parameters and all possible combinations of T_0 and T_1 are investigated.

4.1 Effect of Individual Perturbation in the Angle Parameters

The VS family following $\phi = 45°$, $T_0 + T_1 = 90°$ has been taken to investigate the sensitivity of ϕ, T_0, and T_1 parameters on the out-of-plane displacements and snap-through loads. The proposed finite element framework is used to perform a parametric study. Schematic representation of the individual perturbation of ϕ parameters is shown in Fig. 3. Similarly, the schematic representation of perturbation of T_0 and T_1 parameters are given in Fig. 4. In the perturbation studies, ϕ, T_0, and T_1 have been modified as $\phi + \delta\phi$, $T_0 + \delta T_0$, and $T_1 + \delta T_1$ respectively, where the range of $\delta\phi$, δT_0, and δT_1 limited to $\pm 5°$ in this study. In order to compare the results effectively, the output response of the model for the perturbed parameters has been normalised with the output response of the model with standard parameters. In the graphical illustrations, the x-axis denotes X_n/X_s where X_n is the changed property and X_s is the standard property. Similarly, the y-axis denotes Y_n/Y_s where Y_n is the output response for the changed property and Y_s is the output for the standard properties.

　　The result obtained from individual perturbation in the angle parameters is shown in Figs. 5 and 6. Among the VS parameters, the perturbation in ϕ is highly sensitive to the out-of-plane displacement profile, where $\pm 5°$ perturbation in ϕ leads to a change of -19 to $+19\%$ in the out-of-plane displacement. The individual perturbation of T_0 and T_1 parameters also has been studied and it is found that the perturbation in these parameters are less sensitive on the displacement profile variation. For $-5°$

Table 1 Material and angle properties of VS laminate used

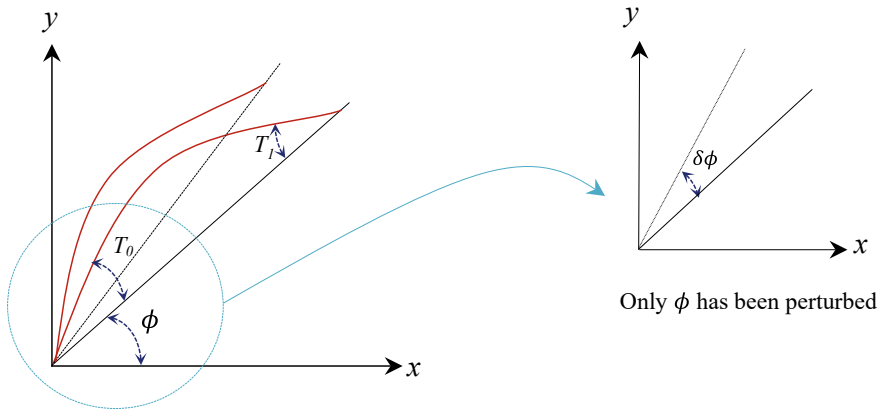| Property	Value
E_{11}	156 GPa
E_{22}	8.35 GPa
υ_{12}	0.33
G_{12}	4.2 GPa
α_{11}	-0.29×10^{-6} (°C)
α_{22}	24×10^{-6} (°C)
ϕ	45°
T_0	45°
T_1	45°

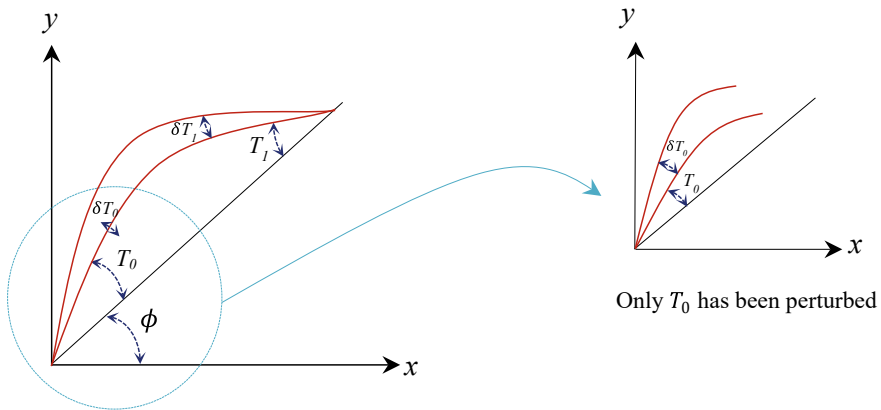**Fig. 3** Schematic representation of perturbation of ϕ

Fig. 4 Schematic representation of perturbation of T_0, and T_1

perturbation in T_0 and T_1 values, the maximum change in out-of-plane displacement is $+ 4.3\%$. Whereas, for 5° perturbations in T_0 and T_1 values, the maximum change in out-of-plane displacement is $- 7.3\%$. A similar study has been performed to check the sensitivity of the snap-through loads, and the result obtained has been depicted in Fig. 6.

Among the VS angle parameters, the perturbation in T_0 and T_1 parameters are highly sensitive to the snap-through load, where $\pm 5°$ perturbation in T_0 leads to a change of $+ 3.2$ to $- 10.6\%$, and $\pm 5°$ perturbation in T_1 leads to a change of in $- 6.5$ to 10% in the snap-through load. The perturbation in ϕ is less sensitive to the snap-through load requirements, however, the change in snap-through load is within $- 2.73\%$ due to $\pm 5°$ perturbation in ϕ. It can be concluded from the study that the perturbation in T_0 and T_1 has a significant effect on the snap-through
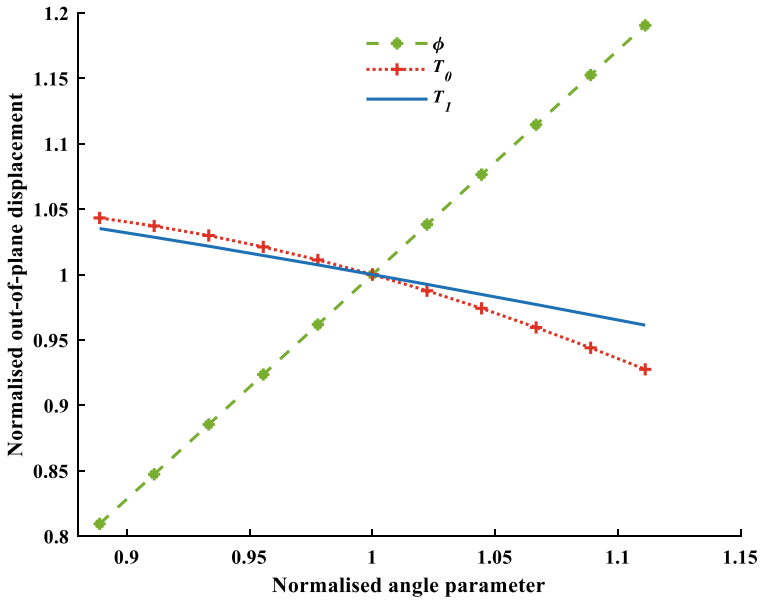
Fig. 5 Change in out-of-plane displacement with the change in ϕ, T_0 and T_1
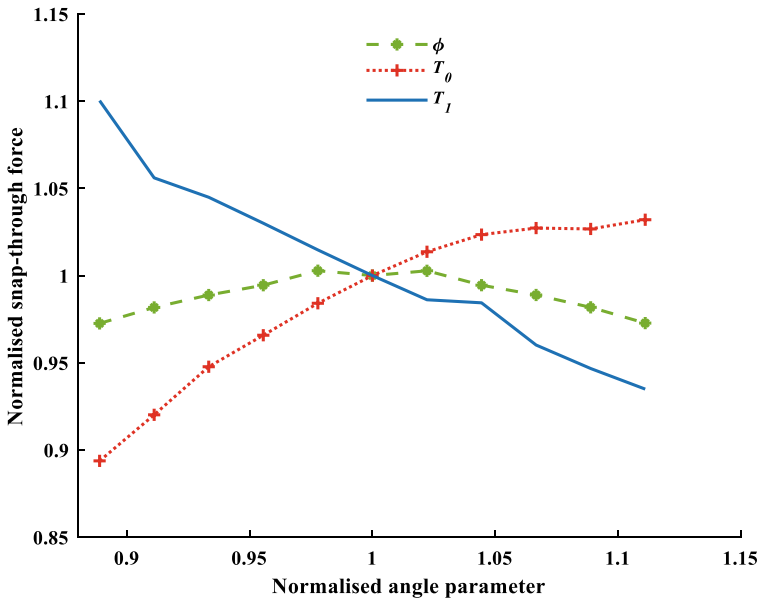

Fig. 6 Change in snap-through load with the change in ϕ, T_0 and T_1

load. Even though perturbation in these parameters does not have much effect on the out-of-plane displacement however perturbation in their combination may lead to a significant change in out-of-plane displacement and alter the deformation profile.

4.2 Effect of Combined Perturbation in the T_0 and T_1 Parameters

To investigate the combined perturbation effects in T_0 and T_1, a sampling plan has been suggested in Fig. 7. A $\pm 5°$ perturbation in δT_0 and δT_1 is selected for the present analysis. Lower limit and upper limit of T_0 and T_1 are 40° and 50° respectively. A set of points with all possible combination of T_0 and T_1 has been selected for the analysis. The contour plot on the sensitivity of out-of-plane displacement and snap-through load resulting from the combined perturbation in T_0 and T_1 is shown in Figs. 8 and 9. From the contour plot of out-of-plane displacement (Fig. 8), it is observed that the perturbation in the combination of T_0 and T_1 leads to a displacement change of $+$ 7.31% to $-$ 11.36%, where the maximum value of 14.67 mm occurs at $T_0 = T_1 =$ 40° and minimum value of 12.12 mm occurs at $T_0 = T_1 = 50°$. It is evident from this study that both angle parameters alter the deformation profile in the same way, positive change in both angle parameters leads to negative change in out-of-plane displacement and vice-versa.

Figure 9 represents the contour plot of the variation of snap-through load due to combined perturbation in T_0 and T_1 parameters. The combined perturbation in these parameters leads snap-through to varies from $-$ 15.32 to 13.73% with maximum values of 4.74 N occurring at $T_0 = 50°$, $T_1 = 40°$ and minimum value of 3.23 N occurs at $T_0 = 40°$ and $T_1 = 50°$.

Fig. 7 Sampling scheme of combined perturbation in T_0 and T_1 parameters
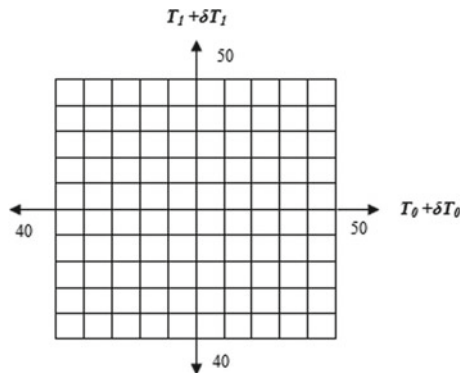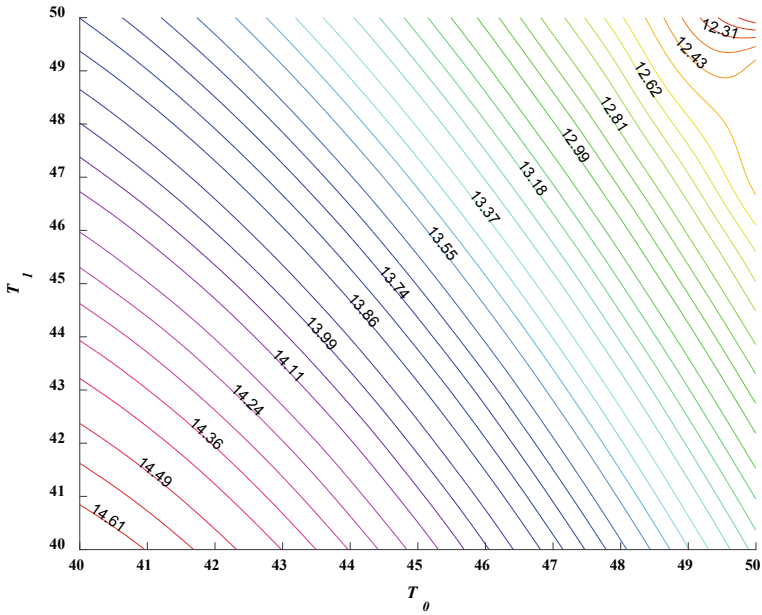
Fig. 8 Change in out-of-plane displacement with the change in combination of T_0 and T_1
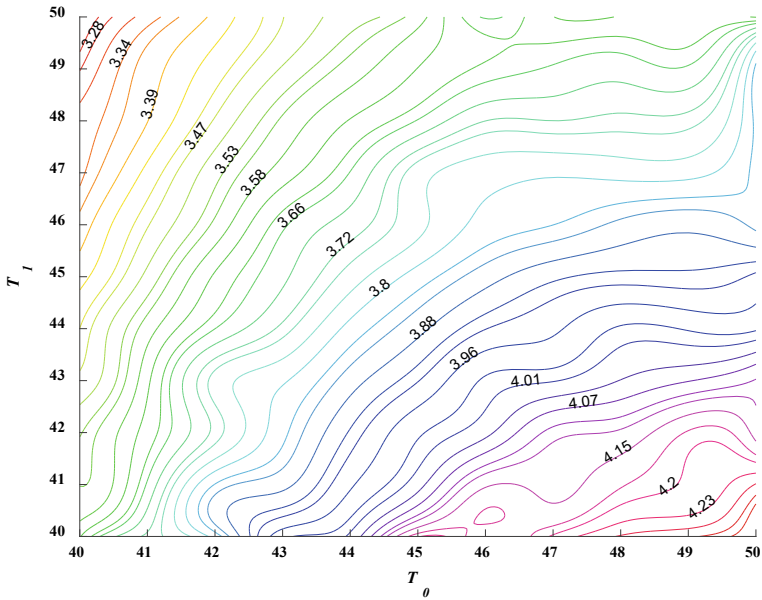

Fig. 9 Change in snap-through load with the change in combination of T_0 and T_1

5 Conclusion

The variable stiffness composites generated using curvilinear fiber alignments can be used as an alternative to conventional composites in bistable structures to tailor the deformations and snap-through requirements. However it could be challenging to create laminate layups with the precise designated VS angle specifications due to manufacturing constraints. A study on the impact of minor changes in design variables is needed to check for the tolerance limits of fibre angle alignments. In this paper, the effect of individual perturbation of ϕ, T_0, and T_1 and a set of combinations of perturbation in T_0, and T_1 are performed using a finite element-based model. The results reveal that angle parameter ϕ is highly sensitive while the parameters T_0, and T_1 are less sensitive to the deformation profile of the VS laminate. A $\pm 5°$ change in ϕ leads to a maximum change of 19% in the out-of-plane displacement. The individual perturbation in T_0 and T_1 significantly affects the snap-through requirements. A $\pm 5°$ individual perturbation in T_0 and T_1 leads to a maximum change of -10.6 and 10% in the snap-through load. The perturbation in the combination of T_0 and T_1 also has been studied and it is found that even though the deformation profile is less sensitive to individual perturbation in these parameters however perturbation in their combination leads to a maximum change of 11.36% in out-of-plane displacement. Further perturbation in these combinations leads to a maximum change of 15.32% in snap-through load. The results can be used as a design tool while taking the tolerance limits of T_0 and T_1 parameters into account.

References

1. Hyer MW (1981) Some observations on the curved shape of thin unsymmetric laminates. J Composite Mater 15(2):175–194
2. Zheng Z, Li Y, Yu X, Li X, Wu H, Wu H, Jiang S, Chai G (2019) Bistable morphing composite structures. A review. Thin-Walled Struct 142:74–79
3. Dano ML, Hyer MW (1996) The response of unsymmetric laminates to simple applied forces. Mech Compos Mater Struct 3(1):65–80
4. Cantera MA, Romera JM, Adarraga I, Mujika F (2015) Modelling and testing of the snap-through process of bi-stable cross-ply composites. Compos Struct 120:41–52
5. Portela P, Camanho P, Weaver P, Bond I (2008) Analysis of morphing, multi stable structures actuated by piezoelectric patches. Compos Struct 86(3–5):347–356
6. Schultz MR, Hyer MW (2003) Snap-through of unsymmetric cross-ply laminates using piezoelectric actuators. J Intell Mater Syst Struct 14(12):795–814
7. Anilkumar PM, Haldar A, Eelco J, Rao BN, Raimund R (2021) Snap-through of bistable variable stiffness laminates using MFC actuators. Compos Struct 266:113694
8. Sousa CS, Camanho PP, Suleman A (2013) Analysis of multistable variable stiffness composite plates. Compos Struct 98:34–46

9. Haldar A, Jose R, Eelco J, Raimund R (2018) Thermally induced multistable configurations of variable stiffness composite plates: semi-analytical and finite element investigation. Compos Struct 183:161–175
10. Anilkumar PM, Haldar A, Eelco J, Rao BN, Raimund R (2019) Design optimization of multistable variable-stiffness laminates. Mech Adv Mater Struct 26:48–55
11. Brampton CJ, Betts DN, Bowen CR, Kim HA (2013) Sensitivity of bistable laminates to uncertainties in material properties, geometry and environmental conditions. Compos Struct 102:276–286
12. Samir E, Tarun P, Arvindh A, Aneman M (2021) Parametric study on the influence of material properties and geometry on the thermally induced bistability of composite laminates. J Mech Eng Sci 1–25
13. Suraj KS, Anilkumar PM, Krishnanunni CG, Rao BN (2021) Parametric perturbation studies on the behaviour of bistable unsymmetrical laminates. In: International conference on theoretical applied computational and experimental mechanics, IIT Kharagpur, India
14. Saeid S, Azam A, Fawad I (2020) Reliability analysis of bistable composite laminates. AIMS Mater Sci 8(1):29–41
15. Gürdal Z, Tatting BF, Wu C (2008) Variable stiffness composite panels: effects of stiffness variation on the in-plane and buckling response. Compos Part A: Appl Sci Manuf 39(5):911–922

Probabilistic Global Seismic Damage Analysis Based on a Novel Factor Mapping Method

Bibhas Paul and C. S. Manohar

1   Introduction

Under the action of strong earthquakes, engineering structures are designed to display controlled inelastic behavior. Damage measures, such as the Park and Ang damage index and maximum inter-storey drift, are commonly used to characterize the global measures of damage [1, 2]. The framework of incremental dynamic analysis (IDA) offers a systematic tool to characterize the range of behavior a structure displays due to earthquake ground motions of varying severities [3, 4]. Apart from inelastic structural behavior, another equally important feature one needs to incorporate into analysis is the inherent uncertainties associated with the specification of earthquake loads and structural properties, including material constitutivity under cyclic loads in the inelastic regime [5–7]. In a recent study, the present authors have considered the problem of estimating global response sensitivity indices (GRSIs) in this class of problems [8] using Monte Carlos simulation methods. These indices are estimated in this study using the factor mapping method [9, 10]. The essence of this method lies in defining a behavioral set in terms of a chosen response variable and classifying the samples of input random variables into two distinct bins depending on whether a given sample realization of the input vector produces the response in the behavioral set or not. Subsequently, the datasets in the two bins are processed to estimate a measure of distance between samples of individual random variables lying in the two bins. The distances associated with each of the random variables are taken to be a measure of the importance of the corresponding input variable. Our earlier study [8] generalizes this method to determine the GRSIs with respect to groups of input

B. Paul · C. S. Manohar (✉)
Department of Civil Engineering, Indian Institute of Science, Bengaluru 560 012, India
e-mail: manohar@iisc.ac.in

B. Paul
e-mail: bibhaspaul@iisc.ac.in

random variables (in contrast to most studies in GRSA, which provide GRSIs with respect to a set of scalar random variables). A solution to this problem requires the estimation of the distance between two vectors of random variables, and the study has employed Bhattacharyya's distance for this purpose [11]. However, deducing a workable estimator for this distance has remained a challenge. The difficulty here is associated with the fact that one needs to find the distance between two vector random variables, each of which comprises dependent and non-Gaussian components. Whereas in our earlier study we deduced an estimator for the Bhattacharyya's distance based on the application for Nataf's transformation [12] to the data set, we focus, in the present study on exploring alternative methods to represent the non-Gaussian data set in the development of the estimator for the Bhattacharayy's distance. Specifically, we consider the application of independent component analysis [13] and copula-based methods to achieve this [14]. Illustrative examples include an exactly solvable problem involving correlated groups of random variables and a study on 4-storied and 3-bays inelastic steel frames.

2   Problem Statement

We consider an inelastic frame structure subject to a specified earthquake-induced ground motion. Let the response be characterized in terms of global damage measures such as the maximum inter-storey drift ratio and modified Park-Ang damage index given respectively by

$$DM_1 = \max_{1 \le i \le N_f} \max_{0 < t < \infty} \left| \frac{\Delta_i(t) - \Delta_{i-1}(t)}{h_i} \right|$$

$$DM_2 = \sum_{i=1}^{N_c} \lambda_i D_i; \quad D_i = \left(\frac{\varphi_{\max} - \varphi_y}{\varphi_u - \varphi_y} + \beta \frac{E_d}{M_y \varphi_u} \right)_i;$$

$$\varphi_{\max} = \max_{0 < t < \infty} \varphi(t); \quad E_d = \int_0^\infty M(t)\dot{\varphi}(t)\mathrm{d}t; \quad \lambda_i = \frac{(E_d)_i}{\sum_{j=1}^{N_c} (E_d)_j}$$

In these equations, $\Delta_i(t) =$ displacement of ith floor, $h_i =$ height of the ith storey, $N_f =$ number of floors, $N_c =$ number of plastic hinges, $\lambda_i =$ weight factor for ith hinge, $D_i =$ modified Park and Ang damage index for the ith hinge, $\varphi(t) =$ hinge rotation, $\varphi_y =$ hinge rotation at first yield, $\varphi_u =$ ultimate hinge rotation under monotonic loading, $\beta =$ calibration parameter, $E_d =$ energy dissipated through hysteresis, and $M(t) =$ hinge moment. The frame under the study is modeled on the OpenSees platform [15], and the analysis accounts for geometric and material nonlinearities. The inelastic behavior is represented through a set of discrete hinges characterized based on the modified IMK model [16] (shown in Fig. 1). The frame parameters pertaining to the hinge characteristics M_y, K_e, φ_p, $\varphi_{pc}, M_c, M_r, \varphi_u,$ and Λ (Fig. 2)

for every hinge are treated as a set of dependent and non-Gaussian random variables with specified properties. We denote by $\boldsymbol{\Theta}$ the $n \times 1$ vector of system property random variables and represent the response as $DM = \mathrm{f}(\boldsymbol{\Theta})$ where DM could be either DM_1 or DM_2. We define a behavioral set A such that $A = [\underline{D} \leq DM \leq \overline{D}]$ where $\underline{D}$ and $\overline{D}$ are specified bounds on DM. We take that the vector $\boldsymbol{\Theta}$ comprises of m disjoint groups such that

$$\boldsymbol{\Theta} = [\boldsymbol{\Theta}^{n_1} \ \boldsymbol{\Theta}^{n_2} \ \cdots \ \boldsymbol{\Theta}^{n_m}]; \quad n_1 + n_2 + \cdots + n_m = n$$

Next, we introduce two sets $\boldsymbol{\Theta}_A$ and $\boldsymbol{\Theta}_{A^c}$ such that, $\boldsymbol{\Theta}_A = \{\boldsymbol{\Theta} | \mathrm{f}(\boldsymbol{\Theta}) \in A\}$ and $\boldsymbol{\Theta}_{A^c} = \{\boldsymbol{\Theta} | \mathrm{f}(\boldsymbol{\Theta}) \in A^c\}$. A measure of the importance of the group of random variables Θ^k is given by $d_k = \mathrm{dist}(\Theta^k_A, \Theta^k_{A^c})$ which in this study is taken to be given by the Bhattacharyya's distance

$$d_k = -\ln \rho_k, \quad \text{where} \quad \rho_k = \int_\Omega \sqrt{p_{\boldsymbol{\Theta}^k_A}(\boldsymbol{u}) \, p_{\boldsymbol{\Theta}^k_{A^c}}(\boldsymbol{u})} \, \mathrm{d}\boldsymbol{u}.$$

Here $p_{\boldsymbol{\Theta}^k_A}(\boldsymbol{u})$ and $p_{\boldsymbol{\Theta}^k_{A^c}}(\boldsymbol{u})$ represent the n_k dimensional joint pdf of the random vectors $\boldsymbol{\Theta}^k_A$ and $\boldsymbol{\Theta}^k_{A^c}$, respectively. The problem on hand consists of developing estimators for the distances d_k; $k = 1, 2, \ldots, m$. We propose in this study to achieve

Fig. 1 Location and numbering scheme of plastic hinges. (Column hinges: 1–32, beam hinges: 33–56)
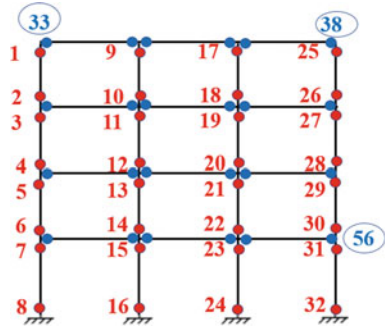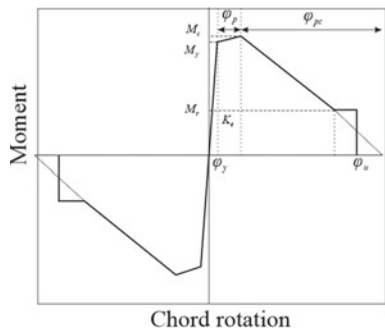

Fig. 2 Representative backbone curve of the modified IMK model

this by using two alternatives: the first based on the application of independent component analysis, and the second based on modeling non-Gaussian data using the theory of copulas. In both cases, the estimator for the Bhattacharyya distance is obtained as

$$\rho = \int_{\Omega} \sqrt{p_X(\boldsymbol{u}) p_Y(\boldsymbol{u})} \mathrm{d}\boldsymbol{u} = \int_{\Omega} \sqrt{\frac{p_X(\boldsymbol{u})}{p_Y(\boldsymbol{u})}} p_Y(\boldsymbol{u}) \mathrm{d}\boldsymbol{u}$$

$$= \mathrm{E}_{p_Y} \left[\sqrt{\frac{p_X(\boldsymbol{U})}{p_Y(\boldsymbol{U})}} \right] = \frac{1}{N_2} \sum_{i=1}^{N_2} \sqrt{\frac{p_X(\boldsymbol{u}^{(i)})}{p_Y(\boldsymbol{u}^{(i)})}} \tag{1}$$

The difference between the two approaches lies in the details of estimating the pdfs $p_X(\boldsymbol{u})$ and $p_Y(\boldsymbol{u})$.

3 Analysis

For the sake of simplicity of notations, we consider two $r \times 1$ vector random variables X and Y and consider the problem of estimating the Bhattacharyya distance between these two random vectors based on the simulated datasets $D_1 = \{\boldsymbol{x}^{(i)}\}_{i=1}^{N_1}$ and $D_2 = \{\boldsymbol{y}^{(j)}\}_{j=1}^{N_2}$, $N_1 + N_2 = N$.

3.1 Steps for Estimating dist(X, Y) Based on Independent Component Analysis

Here we seek to represent the vector X in the form $X = \boldsymbol{\mu}_X + \Phi \Lambda^{1/2} \mathbf{R} \boldsymbol{\Psi}$ where $\boldsymbol{\mu}_X$ = mean of X, Φ = matrix of eigenvectors of covariance of X, Λ = diagonal matrix of eigenvalues of covariance of X, $\mathbf{R}$ = mixing matrix and $\boldsymbol{\Psi}$ = vector of independent non-Gaussian random variables. The independent component analysis (ICA) algorithm aims to determine the matrix $\mathbf{R}$ and first-order pdf of components of $\boldsymbol{\Psi}$. This is achieved by maximizing a measure of non-Gaussianity of $\boldsymbol{\Psi}$. We use, in our work the *rica* [17] command on the MATLAB platform, which maximizes the differential entropy (or equivalently, the negentropy) associated with $\boldsymbol{\Psi}$. The steps involved here are as follows:

1. From the dataset $D_1 = \{\boldsymbol{x}^{(i)}\}_{i=1}^{N_1}$, estimate the mean and covariance

$$\boldsymbol{\mu}_X = \frac{1}{N_1} \sum_{i=1}^{N_i} \boldsymbol{x}^{(i)}; \quad \Sigma_X = \frac{1}{N_1} \sum_{i=1}^{N_1} (\boldsymbol{x}^{(i)} - \boldsymbol{\mu}_X)(\boldsymbol{x}^{(i)} - \boldsymbol{\mu}_X)^t$$

2. Center and whiten the data:

$$\tilde{x}^{(i)} = \Lambda^{-1/2}\Phi^t(x^{(i)} - \mu_X), \quad i = 1, 2, \ldots, N_1; \quad \text{where } \Sigma_X = \Phi\Lambda\Phi^t$$

Here Φ and Λ are the matrix of eigenvectors and eigenvalues of the covariance matrix Σ_X.

3. Perform ICA on whitened data $tilde X = \mathbf{R}\Psi$, using the *rica* command on the MATLAB platform. This leads to the mixing matrix $\mathbf{R}$ and samples of components of Ψ.

4. Considering the component-wise data, $\left\{\psi_k^{(i)}\right\}_{i=1}^{N_1}, k = 1, 2, \ldots, r.$, estimate the 1st order pdfs of each of the components of Ψ leading to $p_\Psi(\psi) = \prod_{k=1}^{n} p_{\Psi_k}(\psi_k)$ and the estimate

$$\hat{p}_X(x) = \left.\frac{\hat{p}_\Psi(\psi)}{|J_X|}\right|_{\psi = J_X^{-1}(x - \mu_X)} = \frac{1}{|J_X|}\prod_{k=1}^{r}\hat{p}_{\Psi_k}\left(\sum_{m=1}^{r}[J_X^{-1}]_{km}(x_m - [\mu_X]_m)\right) \tag{2}$$

where, $J_X = \nabla_\psi x = \Phi\Lambda^{1/2}\mathbf{R}, x = [x_1 \ x_2 \ \ldots \ x_r]^t$.

5. Following the similar procedure as mentioned in steps 1 through 4, one can find the independent components $\{\Xi_k\}_{k=1}^{n}$, associated with the dataset $D_2 = \left\{y^{(j)}\right\}_{j=1}^{N_2}$ under a linear mapping $y = \mu_Y + \Theta\Gamma^{1/2}\mathbf{S}\Xi$. Accordingly, we get

$$\mu_Y = \frac{1}{N_2}\sum_{i=1}^{N_2} y^{(i)}; \quad \Sigma_Y = \frac{1}{N_2}\sum_{i=1}^{N_2}(y^{(i)} - \mu_Y)(y^{(i)} - \mu_Y)^t; \quad \Sigma_Y = \Theta\Gamma\Theta^t,$$

$$\hat{p}_Y(y) = \left.\frac{\hat{p}_\Xi(\xi)}{|J_Y|}\right|_{\xi = J_Y^{-1}(y - \mu_Y)} = \frac{1}{|J_Y|}\prod_{k=1}^{r}\hat{p}_{\Xi_k}\left(\sum_{m=1}^{r}[J_Y^{-1}]_{km}(y_m - [\mu_Y]_m)\right) \tag{3}$$

$J_Y = \Theta\Gamma^{1/2}\mathbf{S}, y = [y_1 \ y_2 \ \ldots \ y_r]^t$

6. The Bhattacharyya's coefficient ρ is calculated using a Monte Carlo integration, given as,

$$\hat{\rho} = \frac{1}{N_2}\sum_{i=1}^{N_2}\sqrt{\frac{\hat{p}_X(u^{(i)})}{\hat{p}_Y(u^{(i)})}} = \frac{1}{N_2}\sum_{i=1}^{N_2}\sqrt{\frac{\frac{1}{|J_X|}\prod_{k=1}^{r}\hat{p}_{\Psi_k}\left(\sum_{m=1}^{r}[J_X^{-1}]_{km}\left(u_m^{(i)} - [\mu_X]_m\right)\right)}{\frac{1}{|J_Y|}\prod_{k=1}^{r}\hat{p}_{\Xi_k}\left(\sum_{m=1}^{r}[J_Y^{-1}]_{km}\left(u_m^{(i)} - [\mu_Y]_m\right)\right)}} \tag{4}$$

Note that, here $u^{(i)} \sim p_Y(\cdot), \quad i = 1, 2, \ldots, N_2$. Thus, while the values of $p_Y(u^{(i)})$ are readily available, the values of $p_X(u^{(i)})$, on the other hand, need to be determined using an interpolation scheme. If $u^{(i)}$ lies outside the domain of

X, we take that $p_X(u^{(i)}) = 0$. Finally, one gets the estimator for the distance, $\text{dist}(X, Y) = -\ln \hat{\rho}$.

3.2 Steps for Estimating dist(X, Y) Based on the Theory of Copulas

Here, we seek to represent the joint pdf of the vector random variable X, in the form

$$p_X(x) = c\left(\begin{bmatrix} u_1 \ u_2 \ \ldots \ u_r \end{bmatrix}^t\right) \prod_{k=1}^{r} p_{X_k}(x_k) \tag{5}$$

where $x = \begin{bmatrix} x_1 \ x_2 \ \ldots \ x_r \end{bmatrix}^t$, $u_k = F_{X_k}(x_k)$, $F_{X_k}(x_k) = 1$st order cumulative distribution function (CDF) of X_k, and $c(\cdot)$ is called copula density function. The function $c(\cdot)$ carries information about the dependence among the components of vector X several alternatives exist to formulate this function [14]. Thus, for the case of vine copula, a r-dimensional copula density function is decomposed into products of $\frac{1}{2}r(r-1)$ numbers of bivariate copula density functions leading to

$$\hat{p}_X(u) = \prod_{j=1}^{r-1} \prod_{i=1}^{r-j} c_{i,i+j|i+1:i+j-1} \prod_{k=1}^{r} \hat{p}_{X_k}(u_k), \tag{6}$$

here $c_{i,i+j|i+1:i+j-1}$ represents a bivariate copula density function. Thus, for example, for a 3-dimensional case, one gets

$$p_{123}(x_1, x_2, x_3) = c_{31|2}\big[F_{3|2}(x_3|x_2),\, F_{1|2}(x_1|x_2)\big]c_{32}[F_3(x_3),\, F_2(x_2)]$$
$$c_{12}[F_1(x_1),\, F_2(x_2)]p_1(x_1)p_2(x_2)p_3(x_3)$$

Here $c_{31|2}[\cdot]$, $c_{32}[\cdot]$, and $c_{12}[\cdot]$ are a set of bivariate copulas that can be represented, for example, by functions known as Gaussian copula, given respectively by

$c_{UV}(u, v) = \phi_2\big[\Phi^{-1}(u), \Phi^{-1}(u), \gamma\big]$, where $\phi_2[\cdot]$ is the joint pdf of 2-dimensional standard Gaussian distribution, $\Phi^{-1}(\cdot)$ is the inverse of the univariate standard Gaussian distribution function, and $\gamma \in [-1, 1]$ is the parameter, that needs to be estimated from the realizations of U, and V using maximum likelihood estimation. The expression given by Eq. (6) is fairly general and applicable for any other best fit copulas selected from a large class of copula functions available in the literature [14]. A vine copula toolbox, called MTVines [18], is available on the MATLAB platform, and the present study has employed this toolbox. The steps involved here are as follows:

1. From the dataset $D_1 = \{x^{(i)}\}_{i=1}^{N_1}$, the 1st order pdfs $\hat{p}_{X_k}(x_k)$; $k = 1, 2, \ldots, r$ are estimated using the normalized histogram approach.
2. Using the MTVines toolbox in MATLAB, estimate the bivariate copula densities associated with Eq. (6). Here we use Gaussian and t-copulas mentioned above.

3. Implement steps 1 and 2 for the data set $D_2 = \left\{ y^{(j)} \right\}_{j=1}^{N_2}$.
4. Obtain the joint pdfs

$$\hat{p}_X(\boldsymbol{u}) = \prod_{j=1}^{n-1} \prod_{i=1}^{n-j} c_{i,i+j|i+1:i+j-1} \prod_{k=1}^{n} \hat{p}_{X_k}(u_k);$$

$$\hat{p}_Y(\boldsymbol{u}) = \prod_{j=1}^{n-1} \prod_{i=1}^{n-j} \tilde{c}_{i,i+j|i+1:i+j-1} \prod_{k=1}^{n} \hat{p}_{Y_k}(u_k)$$

5. Estimate the Bhattacharyya coefficient using

$$\hat{\rho} = \frac{1}{N_2} \sum_{i=1}^{N_2} \sqrt{\frac{p_X\left(\boldsymbol{u}^{(i)}\right)}{p_Y\left(\boldsymbol{u}^{(i)}\right)}} = \frac{1}{N_2} \sum_{i=1}^{N_2} \sqrt{\frac{\prod_{j=1}^{r-1} \prod_{i=1}^{r-j} c_{i,i+j|i+1:i+j-1} \prod_{k=1}^{r} \hat{p}_{X_k}\left(u_k^{(i)}\right)}{\prod_{j=1}^{r-1} \prod_{i=1}^{r-j} \tilde{c}_{i,i+j|i+1:i+j-1} \prod_{k=1}^{r} \hat{p}_{Y_k}\left(u_k^{(i)}\right)}}$$

(7)

Again, note that, $p_{Y_k}\left(u_k^{(i)}\right)$ are readily available, while the values of $p_{X_k}\left(u_k^{(i)}\right)$ need to be determined using an interpolation scheme.

6. Estimate Bhattacharyya's distance using $\text{dist}(X, Y) = -\ln \hat{\rho}$.

4 Numerical Illustrations

4.1 Example-1: An Exactly Solvable Problem

We consider an example studied earlier by Jacques et al. [19], for which the exact Sobol's sensitivity indices, with respect to groups of random variables, are exactly determinable. The function here is given by $Y = a\Theta_1\Theta_2 + b\Theta_3\Theta_4 + c\Theta_5\Theta_6$, where $\Theta_i; i = 1, 2, \ldots, 6$ are a set of Gaussian random variables with zero mean and unit standard deviation. The correlation coefficient between Θ_3 and Θ_4 and Θ_5 and Θ_6 are taken to be $\rho_1 = \rho_2 = 0.8$, with all other correlation coefficients being zero. For illustration, we form four groups of random variables, viz., $\Theta_1, \Theta_2, \{\Theta_3, \Theta_4\}$ and $\{\Theta_5, \Theta_6\}$ and aim to estimate the GRSIs with respect to these four groups. The exact Sobol's indices for this case are given by

$$S_1^T = S_2^T = \frac{a^2}{a^2 + b^2\left(1 + \rho_1^2\right) + c^2\left(1 + \rho_2^2\right)}; \ S_{\{3,4\}}^T = \frac{b^2\left(1 + \rho_1^2\right)}{a^2 + b^2\left(1 + \rho_1^2\right) + c^2\left(1 + \rho_2^2\right)};$$

$$S_{\{5,6\}}^T = \frac{c^2\left(1 + \rho_2^2\right)}{a^2 + b^2\left(1 + \rho_1^2\right) + c^2\left(1 + \rho_2^2\right)}$$

(8)

Table 1 GRSIs with respect to groups of variables for Example-1; numbers in parenthesis indicate the rank of the associated group of variables

Variables	Exact total sensitivity indices	Estimated GRSIs				
		Nataf	Gaussian copula	t-copula	ICA	Closed form
Θ_1	0.0575 (3)	0.0880 (3)	0.0880 (3)	0.0880 (3)	0.0880 (3)	0.0379 (3)
Θ_2	0.0575 (3)	0.0872 (4)	0.0872 (4)	0.0872 (4)	0.0872 (4)	0.0369 (4)
$\{\Theta_3, \Theta_4\}$	0.0943 (2)	0.1266 (2)	0.1258 (2)	0.1275 (2)	0.1196 (2)	0.0871 (2)
$\{\Theta_5, \Theta_6\}$	0.8483 (1)	0.3276 (1)	0.3263 (1)	0.3228 (1)	0.3230 (1)	0.1163 (1)

These exact results, along with results from the methods discussed in this paper (with $N = 10^5, a = b = 1, c = 3, A = [-9.2475, -0.9325]$) are summarized in Table 1. It may be noted that Table 1 contains results based on Nataf's model to model the datasets, and also, the numbers in the parenthesis in columns 1–5 represent the relative rank of the corresponding groups. We observe that the four alternative estimators for Bhattacharyya's distance show good mutual agreement. The rank ordering of the groups of the random variables matches in all the cases with the corresponding results from the exact Sobol analysis.

4.2 Evaluation of GRSIs for an Inelastic Moment Frame Subjected to Earthquake Excitation

Here we consider a 4-storied and 3-bay inelastic moment frame with fixed supports subjecting to the recorded the Northridge Canyon Country-WLC station record earthquake ground motion [20] with the first mode spectral acceleration set to 0.5 g. The response quantities of interest are seismic damage measures in terms of (a) maximum inter-storey drift and (b) modified Park-Ang damage index [1, 2]. The details of the geometric dimensions, cross-sectional properties, material properties, gravity load, and considered ground motion can be found in our earlier study [8]. The frame has a total of 56 hinges (32 column hinges and 24 beam hinges), and each hinge is specified by a set of eight parameters, namely, $M_y, K_e, \varphi_p, \varphi_{pc}, M_c, M_r, \varphi_u,$ and Λ (Figs. 1 and 2). Each hinge parameter is treated as a random variable, resulting in a total of 448 random variables for the frame model. The details of the 1st order pdfs, and the correlation matrix considered in this study are available in Ref. [8]. Furthermore, the 448 random variables are grouped into a total of 224 subgroups by grouping the 8 parameters at every hinge into the following four subgroups: $\left[M_y \ K_e \right], \left[M_c/M_y \ \varphi_p \right], \left[M_r/M_y \ \varphi_{pc} \ \varphi_u \right],$ and $[\Lambda]$. Thus, groups 1 through 56 are the subgroups made by $\left[M_y \ K_e \right]_i, i = 1, 2, \ldots, 56$, groups 57 through 112 are the subgroups made by $\left[M_c/M_y \ \varphi_p \right]_i, i = 1, 2, \ldots, 56$, groups 113 through 168

are made by $\left[M_r/M_y \; \varphi_{pc} \; \varphi_u \right]_i$, $i = 1, 2, \ldots, 56$, and groups 169 through 224 are made by single-member subgroups $[\Lambda]_i$, $i = 1, 2, \ldots, 56$.

A Monte Carlo simulation of the inelastic frame is performed with 5000 samples for the hinge characterizing parameters. The average maximum inter-storey drift observed here is 2.39% of the storey height, and the mean Park and Ang overall damage index is found to be 0.33. The behavioral set, A, is chosen here to cover [mean $- 2 \times$ standard deviation, mean] of the simulated damage measures DM_1 and DM_2. The GRSIs obtained for each subgroup using Gaussian copula, t-copula, and ICA-based approximations are reported in Figs. 3 and 4. The GRSIs evaluated using Nataf's model are reported in [8], and these are used here for comparison purposes. Table 2 summarizes the top 20 groups of random variables for the two damage measures considered based on alternative estimators for the GRSIs.

Based on results in Figs. 3 and 4, and Table 2, it is noted that insofar as identifying the most important variables is concerned, all the five estimators of the Bhattacharyya distance lead by and large similar conclusions (see Fig. 4) while a similar feature is not observed with respect to the least important variables. Note that the methods based on ICA, Gaussian copula, t-copula, and Nataf's model, and method based on closed-form expression for Bhattacharyya's distance assuming Gaussianity of the datasets, are designated as Case I, II, III, IV, and V, respectively. The following observations are made:

1. From Fig. 3, it is observed that the seven groups are common in all the five lists of top 20 groups of random variables based on GRSI values obtained in cases I through V. These seven groups are [9, 16, 17, 24, 65, 121, 129]. These groups correspond to the variables $\left[M_y, K_e \right]$ for the hinge numbers 9, 16, 17, and 24, the group $\left[M_c/M_y \; \varphi_p \right]$ for hinge number 9, and the group $\left[M_r/M_y \; \varphi_{pc} \; \varphi_u \right]$ for hinge 9, 17, respectively. Here, hinges 16 and 24 are formed at the base of interior columns.

2. Furthermore, it can be noticed that the list of top 20 random variables in cases I and II share 13 common groups, cases I and III share 11 common groups, cases I and IV share 9 common groups, and cases I and V share 15 common groups. It is observed that The GRSIs obtained using the Nataf, Gaussian copula, and t-copula match appreciably well in terms of GRSI values and ranking.

3. Based on the results of cases II and III, it is noted that 18 groups are found to be common among the last 20 entries. Consistency in the ranking of the least important groups of random variables is also noticed. It is noticed that there is no common entries in the least important 20 groups when all the five cases are considered.

4. In terms of implementation, it is observed that the model based on the ICA is computationally the most efficient. For the sample size used (i.e., 5000), the computational times needed to estimate GRSIs with respect to 224 groups of random variables for cases I-IV are 6.5, 9.5, 11, and 8.5 min, respectively (on a processor of 11th Gen Intel(R) Core(TM) i7-11700 K @ 3.60 GHz).

5. The estimators for the GRSI based on ICA, copula, and Nataf's model account for the non-Gaussian features of the underlying datasets to varying degrees of

Fig. 3 GRSIs for maximum
inter-storey drift ratio
(DM_1); **a** Nataf model;
b Gaussian copula model;
c t-copula functions model;
d ICA model; **e** GRSIs based
on assumption of Gaussian
datasets and using the closed
form expression; the peak
GRSI values are 0.0569,
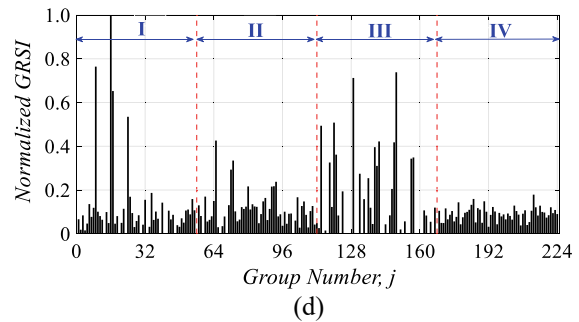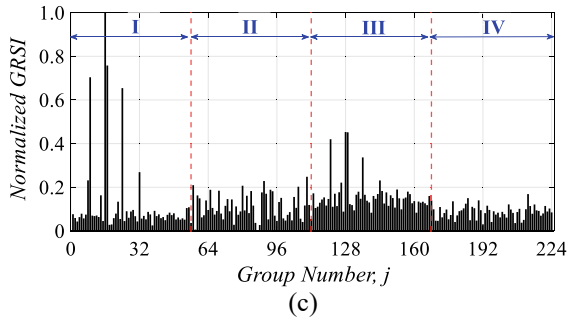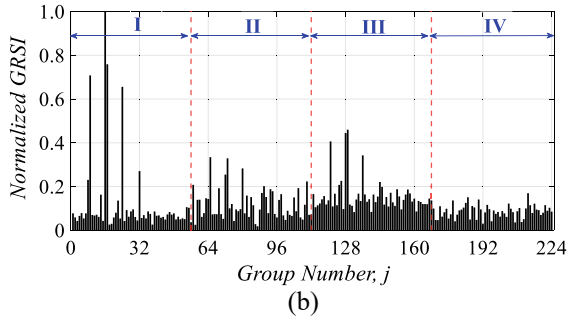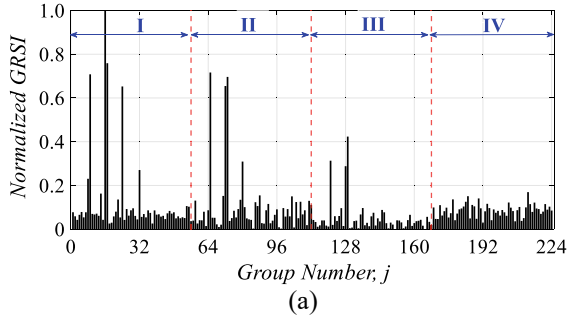0.0569, 0.0572, 0.0540,
0.0397, respectively

(a)
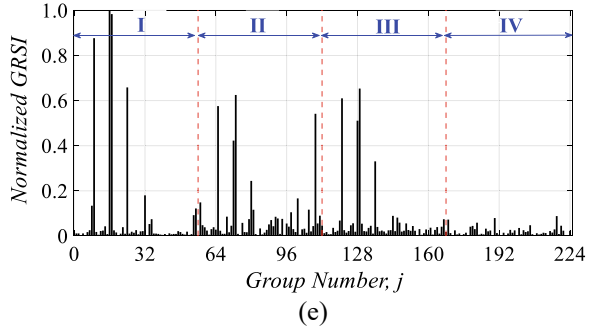
(b)

(c)

(d)

Fig. 3 (continued)

(e)

Fig. 4 Comparison of different estimators for DM_1; peaks seems to be robust irrespective of the estimators
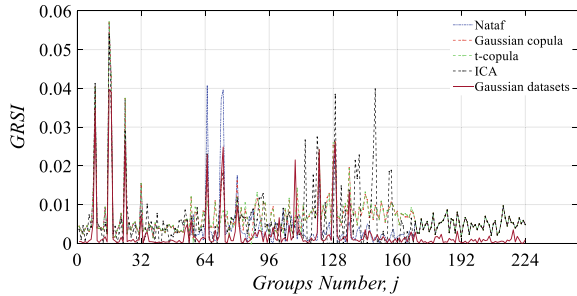

Table 2 List of top 20 groups of random variables corresponding to the two damage measures based on alternative estimators for the GRSIs

Measures	DM_1	DM_2
Nataf	16, 17, 65, 9, 73, 72, 24, 129, 121, 80, 128, 32, 8, 213, 14, 88, 71, 185, 103, 190	24, 8, 136, 128, 32, 80, 16, 72, 120, 9, 36, 144, 56, 69, 148, 154, 75, 167, 112, 64
t-copula	16, 17, 9, 24, 128, 129, 121, 136, 32, 110, 8, 144, 90, 126, 57, 80, 106, 152, 93, 65	24, 8, 64, 32, 88, 80, 16, 72, 136, 168, 36, 56, 93, 84, 99, 106, 128, 66, 109, 138
Gaussian-copula	16, 17, 9, 24, 129, 128, 121, 136, 65, 73, 80, 32, 72, 8, 126, 110, 144, 57, 125, 90	24, 8, 32, 80, 16, 64, 88, 72, 136, 168, 36, 56, 93, 99, 138, 76, 87, 84, 112, 106
ICA	16, 9, 149, 129, 17, 24, 120, 114, 65, 141, 148, 139, 121, 157, 156, 73, 118, 140, 72, 132	120, 167, 24, 32, 16, 161, 147, 166, 8, 72, 116, 80, 168, 142, 136, 141, 138, 130, 112, 64
Closed-form expression	16, 17, 9, 24, 129, 73, 121, 65, 109, 128, 72, 136, 80, 213, 185, 190, 178, 32, 184, 204	24, 109, 32, 90, 136, 8, 93, 80, 16, 72, 128, 144, 64, 120, 176, 92, 184, 36, 170, 88

completeness. Accordingly, it is expected that the distances estimated and, hence, the resulting rank ordering of random variables would differ depending upon the estimator used. The estimator based on the ICA is computationally the most advantageous, and, also, the ICA framework allows for greater details of non-Gaussianity to be included in the estimator and, therefore, seems to be the suitable choice.

5 Conclusions

The study considers the probabilistic analysis of seismic global damage indices in inelastic steel frames. We perform GRSA with respect to groups of random variables within the framework of the factor mapping method. The focus of this study has been on the treatment of non-Gaussian features of multi-variate datasets in characterizing the GRSIs. The proposed method employs the Bhattacharyya distance to characterize the GRSIs. Five alternative estimators for the GRSIs with respect to groups of random variables have been presented. The correctness of the deductions is first verified by applying the formulation on an exactly solvable problem that has been reported in the existing literature [19]. The method has been applied to perform GRSA of a randomly parametered multi-storied inelastic steel frame (with 448 input random variables), and the relative importance of 224 groups of random variables has been estimated. Further work aimed at assessing the implication of these importance measures and relative merits of alternative distance measures in the formulation of the GRSIs is currently being carried out by the present authors.

References

1. Park Y-J, Ang AH-S, Wen YK (1985) Seismic damage analysis of reinforced concrete buildings. J Struct Eng 111(4):740–757
2. Ghobarah A, Abou-Elfath H, Biddah A (1999) Response-based damage assessment of structures. Earthq Eng Struct Dyn 28(1):79–104
3. Vamvatsikos D, Allin CC (2002) Incremental dynamic analysis. Earthq Eng Struct Dyn 31(3):491–514
4. Vamvatsikos D, Fragiadakis M (2010) Incremental dynamic analysis for estimating seismic performance sensitivity and uncertainty. Earthq Eng Struct Dyn 39(2):141–163
5. Dolsek M (2009) Incremental dynamic analysis with consideration of modeling uncertainties. Earthq Eng Struct Dyn 38(6):805–825
6. Liel AB, Haselton CB, Deierlein GG, Baker JW (2009) Incorporating modeling uncertainties in the assessment of seismic collapse risk of buildings. Struct Saf 31(2):197–211
7. Gokkaya BU, Baker JW, Deierlein GG (2016) Quantifying the impacts of modeling uncertainties on the seismic drift demands and collapse risk of buildings with implications on seismic design checks. Earthq Eng Struct Dyn 45(10):1661–1683
8. Paul B, Manohar CS (2022) Factor mapping method for grouped input variables and its application to seismic damage analysis. Struct Saf
9. Saltelli A, Tarantola S, Campolongo F, Ratto M (2004) Sensitivity analysis in practice: a guide to assessing scientific models. Wiley Online Library, vol 1

10. Saltelli A, Ratto M, Andres T, Campolongo F, Cariboni J, Gatelli D et al (2008) Global sensitivity analysis: the primer. Wiley
11. Pardo L (2005) Statistical inference based on divergence measures. CRC Press
12. Der Kiureghian A, Liu P-L (1986) Structural reliability under incomplete probability information. J Eng Mech 112(1):85–104
13. Hyvärinen A, Oja E (2000) Independent component analysis: algorithms and applications. Neural Netw 13(4–5):411–430
14. Joe H (2014) Dependence modeling with copulas. CRC Press
15. McKenna FT, Fenves G, Scott M, Jeremic B (2000) Open system for earthquake engineering simulations (OpenSees). University of California, Berkley CA
16. Lignos DG, Krawinkler H (2011) Deterioration modeling of steel components in support of collapse prediction of steel moment frames under earthquake loading. J Struct Eng 137(11):1291–1302
17. Le Q, Karpenko A, Ngiam J, Ng A (2011) ICA with reconstruction cost for efficient overcomplete feature learning. Adv Neural Inf Process Syst 24:1017–1025
18. Coblenz M (2021) MATVines: a vine copula package for MATLAB. SoftwareX 14:100700
19. Jacques J, Lavergne C, Devictor N (2006) Sensitivity analysis in presence of model uncertainty and correlated inputs. Reliab Eng Syst Saf 91(10–11):1126–1134
20. https://peer.berkeley.edu/peer-strong-ground-motion-databases. Last accessed in Mar 2021

Sampling Variance Reduction in Structural Reliability Estimation via Sequential MCMC Sampling Strategies

Adwait Sharma and C. S. Manohar

1 Introduction

The problem of estimating the probability of failure of structures based on Monte Carlo simulation with variance reduction is considered. The focus of the study is on treating difficulties that arise when the underlying limit surface exhibits one or more of the following features: (a) possible presence of multiple regions that make comparable contributions to the failure probability, (b) possible presence of disconnected failure regions, and (c) the limit state function rapidly changing values in the neighborhood of regions of importance. One can tackle these problems either by simplified representation of the limit surface based on first/second-order Taylor's series expansions or by using simulation-based methods [1]. The first class of the methods leads to the notions of reliability index and design point, and their determination involves the solution to constrained nonlinear optimization problems. The second class of methods most often are augmented by variance reduction strategies so that the problem of estimating low probabilities of failure is tackled with reasonable computational effort. The above-mentioned difficulties make the application of both of these approaches challenging. In the first class of methods involving optimization, one ends up dealing with nonconvex constraints and attendant difficulties in identifying global minima. On the other hand, in implementing simulation-based methods, one faces challenges in devising effective variance reduction strategies. Moreover, the limit state functions in problems of practical interest are invariably defined implicitly through long-running computer codes and, therefore, detecting the possible presence of the geometric difficulties associated with limit surfaces mentioned above itself

A. Sharma (✉) · C. S. Manohar
Department of Civil Engineering, Indian Institute of Science, Bengaluru 560012, India
e-mail: adwaitsharma@iisc.ac.in

C. S. Manohar
e-mail: manohar@iisc.ac.in

243

remains a difficult task. The present study focuses on simulation-based approaches and compares the performance of four alternative variance reductions strategies in dealing with these challenges. These approaches are the subset simulation method [2], generalized splitting methods [3], sequential space conversion [4], and a new strategy being proposed in this study, which employs replica-exchange based Markov chain Monte Carlo (MCMC) sampling [5, 6]. A common feature of all these methods is that the domain of integration is sequentially partitioned so that the problem of estimating a probability of occurrence of a rare event is converted into a sequence of analyzing of events with larger probabilities of occurrences. We first outline the key steps in implementing these methods and then illustrate them by considering examples involving failure of simple structures due to elastic buckling or snap-through buckling. The superior efficacy of the newly developed scheme vis-à-vis the other three methods is demonstrated.

2 Problem Statement

Consider a structure with uncertainties modeled as an n_d-dimensional random vector X with joint probability density function $f_X(x)$ and let $g(X)$ be the performance function. The probability of failure of the structure is given by

$$P_f = \mathbb{P}[g(X) \leq 0] = \int_{x:g(x)\leq 0} f_X(x)\mathrm{d}x = \int_{-\infty}^{\infty} I[g(x) \leq 0]f_X(x)\mathrm{d}x \qquad (1)$$

It is assumed that $f_X(x)$ in general is non-Gaussian and components of X are dependent. We first transform X into a standard normal vector U and obtain

$$P_f = \mathbb{P}[G(U) \leq 0] = \int_{-\infty}^{\infty} I[G(u) \leq 0]\phi(u)\mathrm{d}u \qquad (2)$$

Here F $= [G(U) \leq 0]$ is the failure region, $G(u)$ is the transformed LSF and $\phi(u)$ is the n_d-dimensional standard normal pdf. The problem on hand consists of developing Monte Carlo simulation-based methods that incorporate variance reduction strategies for estimating P_f. We anticipate that the function $G(u)$ potentially exhibits the geometric complications mentioned above. However, the implementation of the simulation algorithms does not assume any prior knowledge of the nature of these difficulties.

3 Analysis

In this section, we briefly outline the steps involved in implementing the four variance reduction strategies which are being compared in this paper.

3.1 Subset Simulation Method [2]

SSM is a variance reduction technique where the failure probability P_f is expressed as a product of larger conditional probabilities. L "intermediate failure regions" are constructed, $F_1 \supseteq F_2 \supseteq ...F_L = F$, such that $F_i = \{u \in \mathbb{R}^{n_d} : G(u) \leq a_i\}$, where a_i are called "intermediate thresholds" and $a_L = 0$. Then the failure probability is written as,

$$P_f = \mathbb{P}[U \in F] = \mathbb{P}[U \in F_1]\mathbb{P}[U \in F_2 | U \in F_1]...\mathbb{P}[U \in F_L | U \in F_{L-1}] = \prod_{i=1}^{L} p_i. \tag{3}$$

MCMC methods can be used to sample from the conditional pdfs $\phi(u|F_i)$ to estimate these conditional probabilities. However, because it is not straightforward to define these intermediate failure regions beforehand, in SSM, the conditional probabilities are chosen by the user and the intermediate failure regions are determined adaptively during the simulation. The algorithmic steps are given as follows.

Given

- The performance function in the n_d-dimensional standard normal space $G(u)$.
- Number of samples in each intermediate level N.
- Intermediate failure probability ($p = 0.1$ used in this study).

Algorithm

1. Generate N iid samples $\{u^1, u^2, ..., u^N\}$ from $\phi(u)$.
2. Set $i = 1$, where i counts the intermediate failure regions.
3. Arrange $G(u^j)$, $j = \{1, 2, ...N\}$ in ascending order. Let $G(u^{(1)})$, $G(u^{(2)})$, … $G(u^{(N)})$ be the ordered LSF values.
4. The value $a_i = G(u^{(Np)})$ is the ith intermediate threshold. Let $S_i = \{u^{(1)}, u^{(2)}, ...u^{(Np)}\}$, be the seeds that lie in the ith intermediate failure region.
5. Using each element of S_i as seeds, run the modified Metropolis algorithm with target pdf $\phi(u|F_i)$ and generate $\frac{1}{p}$ samples from each seed, producing a total of N samples approximately distributed according to the pdf $\phi(u|F_i)$.
6. Arrange in ascending order the LSF values of this set of N samples. Let the ordered values be $G(u^{(1)})$, $G(u^{(2)})$, … $G(u^{(N)})$.

7. If $G\left(\boldsymbol{u}^{(Np)}\right) \leq 0$, set the final intermediate threshold $a_{i+1} = 0$, Set N_f as the number of samples that lie in the actual failure region, and output $\hat{P}_f = p^i \frac{N_f}{N}$. Otherwise, $i = i + 1$ and go to Step 4.

3.2   *Generalized Splitting Method (GSM)* [3]

Similar to SSM, GSM also decomposes the probability of failure into a product of larger conditional probabilities. The major difference here is that the intermediate failure regions and approximate values for the conditional probabilities need to be defined apriori. The values of conditional probabilities are used to determine "splitting factors" in the algorithm which govern the length of MCMC chains used for sampling. In [7], authors propose a FORM-based method to estimate the conditional probabilities and fix the intermediate failure regions. However, for LSFs with aforementioned difficulties, FORM may not provide acceptable approximations to the failure probability. Therefore, we adopt the strategy proposed in [8] where a subset simulation run is executed on a smaller scale and the intermediate failure regions along with approximate conditional probabilities are outputs of said run. The algorithmic steps are given as follows.

Given

- The performance function in the n_d-dimensional standard normal space $G(\boldsymbol{u})$.
- Number of samples in each intermediate level N.
- Intermediate thresholds a_i and conditional probabilities p_i, $i = 1, 2, ..., L$ from a pilot subset simulation run.

Algorithm

1. Generate N iid samples $\left\{\boldsymbol{u}^1, \boldsymbol{u}^2, ..., \boldsymbol{u}^N\right\}$ from $\phi(\boldsymbol{u})$.
2. Compute $G\left(\boldsymbol{u}^j\right)$, $j = \{1, 2, ...N\}$ and let $S_1 = \left\{\boldsymbol{u}^{(1)}, \boldsymbol{u}^{(2)}, ...\boldsymbol{u}^{(N_{(1)})}\right\}$, be the set of seeds that lie in the 1st intermediate failure region.
3. Set $i = 2$, where i counts the intermediate failure regions.
4. Define "splitting factors" for each $\boldsymbol{u}^{(j)} \in S_{i-1}$ as $s_j = \left\lfloor \frac{1}{p_i} \right\rfloor + E_j$ where $E_j \sim$ Bernoulli $\left(\frac{1}{p_i} - \left\lfloor \frac{1}{p_i} \right\rfloor\right)$ where $\lfloor . \rfloor$ is the floor function.
5. From each $\boldsymbol{u}^{(j)} \in S_{i-1}$, run the modified Metropolis algorithm for s_j steps with target pdf $\phi(\boldsymbol{u}|F_{i-1})$.
6. Compute the LSF value for these samples and say N_i of these samples lie in F_i. Let this set of samples be denoted by S_i.
7. If $i = L$, output $\hat{P}_f = \frac{N_L}{N} \prod_{i=2}^{L} p_i$. Otherwise, $i = i + 1$ and go to Step 4.

3.3 Sequential Space Conversion Method [4]

This method expresses failure probability P_f as, $P_f = \int_F \phi(\boldsymbol{u}) \mathrm{d}\boldsymbol{u} = \alpha \int_F \phi_a(\boldsymbol{u}) \mathrm{d}\boldsymbol{u} + \int_F \phi(\boldsymbol{u}) - \alpha \phi_a(\boldsymbol{u}) \mathrm{d}\boldsymbol{u}$, where $\phi_a(\boldsymbol{u})$ is the normal distribution with $\boldsymbol{0}$ mean and covariance matrix $a^2 \boldsymbol{I}$ (standard deviation increased by a factor of a, called the augmenting factor). Increasing standard deviation of the standard normal distribution by factor a is equivalent to scaling down the LSF by a factor of a in the standard normal space. Thus, if $\hat{G}_a(\boldsymbol{u}) = G(a\boldsymbol{u})$ is the scaled LSF, we write the previous equation as, $P_f = \alpha \int_{-\infty}^{\infty} \mathrm{I}\left[\hat{G}_a(\boldsymbol{u}) \leq 0\right] \phi(\boldsymbol{u}) \mathrm{d}\boldsymbol{u} + \int_{-\infty}^{\infty} \mathrm{I}[G(\boldsymbol{u}) \leq 0] \phi(\boldsymbol{u}) - \alpha \mathrm{I}\left[\hat{G}_a(\boldsymbol{u}) \leq 0\right] \phi(\boldsymbol{u}) \mathrm{d}\boldsymbol{u}$. The first integral is easy to evaluate (since the failure regions are closer to the origin). Then, the parameter α is determined so that the second integral reduces to 0. Thus, $\alpha = \frac{\int_{-\infty}^{\infty} \mathrm{I}[G(\boldsymbol{u}) \leq 0] \phi(\boldsymbol{u}) \mathrm{d}\boldsymbol{u}}{\int_{-\infty}^{\infty} \mathrm{I}\left[\hat{G}_a(\boldsymbol{u}) \leq 0\right] \phi(\boldsymbol{u}) \mathrm{d}\boldsymbol{u}}$

and therefore $P_f = \alpha p_a$ where $p_a = \int_{-\infty}^{\infty} \mathrm{I}\left[\hat{G}_a(\boldsymbol{u}) \leq 0\right] \phi(\boldsymbol{u}) \mathrm{d}\boldsymbol{u}$ is easier to evaluate.

Instead of defining a single augmenting factor a, SESC iterates this process over a decreasing sequence of augmenting factors decided beforehand, thus leading to computation of a sequence of correcting factors and finally multiplying all of them together. The algorithmic steps are given below.

Given

- The performance function in the n_d-dimensional standard normal space $G(\boldsymbol{u})$.
- Vector of augmenting factors $\boldsymbol{a} = [a(1), a(2), ..., 1]$ ([3, 2.9, 2.8, ..., 1] used in this study.)
- Number of failing samples N_f.

Algorithm

1. Generate iid samples from $\phi(\boldsymbol{u})$ until N_f of them satisfy $G(a(1)\boldsymbol{u}) \leq 0$. Let these samples be $S_1 = \{\boldsymbol{u}^1, \boldsymbol{u}^2, ..., \boldsymbol{u}^{N_f}\}$. Let N_1 be the total number of samples generated to achieve this.
2. Compute $\alpha_1 = \frac{N_f}{N_1}$.
3. Set $i = 2$, where i counts the position in the augmented vector.
4. Run modified Metropolis algorithm from each $\boldsymbol{u}_j \in S_{i-1}$ with target pdf $\phi(\boldsymbol{u}|G(a(i-1)\boldsymbol{u}) \leq 0)$ until there are at least N_f samples that satisfy $G(a(i)\boldsymbol{u}) \leq 0$.
5. Let this set of samples be $S_i = \{\boldsymbol{u}^1, \boldsymbol{u}^2, ..., \boldsymbol{u}^{N'_f}\}$. Let N_i be the total number of samples generated to achieve this. Compute $\alpha_i = \frac{N'_f}{N_i}$.
6. If $i = L$, output $\hat{P}_f = \prod_{i=1}^{L} \alpha_i$. Otherwise, $i = i + 1$, and repeat from Step 4.

3.4 Proposed Method Based on Replica Exchange MCMC Sampling [5]

The estimator of the proposed method is based on the Holmes-Diaconis-Ross method which is a variant of particle splitting methods. The novel element is the utilization of the replica exchange algorithm as the MCMC sampler at each intermediate failure region. The precise steps are outlined in [5]. Here we outline the basic strategy.

Consider an intermediate limit surface F_i along with n seeds lying in the intermediate failure region. We normalize the mean distance of seeds to the origin to 1 and scale the LSF accordingly. Then, we generate iid samples according to $\phi(\boldsymbol{u}|\{\|\boldsymbol{u}\| \geq 1\})$, which we call "explorers". We consider the explorers that lie in this failure region and run MCMC algorithm on them with target pdf $\phi(\boldsymbol{u}|F_i')$ where F_i' is the scaled version of F_i. Then, we record the orthants in which these MCMC samples lie. Let the union of these orthants be $\mathbb{O}$. Finally, the "explorer pdf" is defined as $\phi(\boldsymbol{u}|\{\|\boldsymbol{u}\| \geq R_m, \mathbb{O}\})$.

During the actual MCMC sampling, in addition to the n chains that draws samples from the desired $\phi(\boldsymbol{u}|F_i)$, corresponding to each of them, n secondary chains are also run which draws iid samples from the explorer pdf. For each pair of these chains at each time step, a sample from the secondary chain is accepted with a certain probability during the so-called "exchange step" of the RE algorithm. Then the chain that samples from $\phi(\boldsymbol{u}|F_i)$ continues propagating from the new accepted sample.

It is worth mentioning that the issue of burn-in in the proposed method has been partially resolved by constructing a quadratic response surface of the LSF at each intermediate failure region and stationarity is diagnosed using the well-known Gelman-Rubin diagnostic. Finally, the coefficient of variation (CoV) of the estimator along with a 95% confidence interval of the estimator is deduced through a bootstrap technique called circular block bootstrap. Further details are provided in [5].

4 Numerical Illustrations

First, we consider two benchmark examples that exist in the current literature, which display geometry complications of the kind described above. Next, we present two examples in structural mechanics whose LSFs display such difficulties. It is worth noting that the complications in the geometry of LSFs arise in structural engineering problems related to failure due to buckling. Indeed, the problems that we have considered are: (a) a stable-symmetric buckling problem and (b) a snap-through buckling problem of rigid bars. We compare the results obtained using SS, the GSM, the recently proposed SESC method, and the proposed method. In all the illustrations, the LSF is formulated in the standard normal space before conducting the simulation runs. All the algorithms are run 100 times independently, and the mean failure probability, along with the empirical value of the coefficient of variation (CoV) obtained from the 100 runs are reported. We verify the results using the direct Monte Carlo

(DMC) estimate with a relatively large number of samples. In the tables presented below, the value of CoV in the parentheses for the proposed method is the value estimated using the bootstrap method. 95% confidence interval for the estimator is also reported. In addition, in reporting the number of LSF calls for GSM and the proposed method, the summands correspond to the number of LSF calls during the true run and the pilot run, respectively.

4.1 Example 1

Consider in the standard normal space, the LSF [9],

$$G_1(\boldsymbol{u}) = \begin{cases} 4 - u_1 & \text{if } u_1 > 3.5 \\ 0.85 - 0.1u_1 & \text{if } u_1 \leq 3.5 \end{cases},$$

$$G_2(\boldsymbol{u}) = \begin{cases} 0.5 - 0.1u_2 & \text{if } u_2 > 2 \\ 2.3 - u_2 & \text{if } u_1 \leq 2 \end{cases},$$

$$G(\boldsymbol{u}) = \min(G_1, G_2). \tag{4}$$

It is noted that the difficulty in treating this LSF lies in the fact that it sharply changes its value near the important region. Figure 1 shows the details of samples generated and the sequence of integration subdomains for the four methods. The results on the estimated P_f, using the four methods, are summarized in Table 1. It is seen that SS and GSM algorithms perform poorly on this LSF since they often fail to detect the presence of the most important region. This is reflected as a large value of CoV of the estimator.

4.2 Example 2

Consider the following LSF in the standard normal space [9],

$$G(\boldsymbol{u}) = 15 - |u_1 u_2|. \tag{5}$$

The difficulty associated with this LSF is in the presence of more than one region, contributing notably to the failure probability. Figure 2 shows the samples generated in a sample run for each of the four methods. The numerical results are summarized in Table 2. As seen in Fig. 2, SSM, GSM and SESC have difficulty in adequately exploring all regions of comparable importance. This results in the estimates having high CoV. The proposed method shows less CoV since all failure regions here are explored effectively.
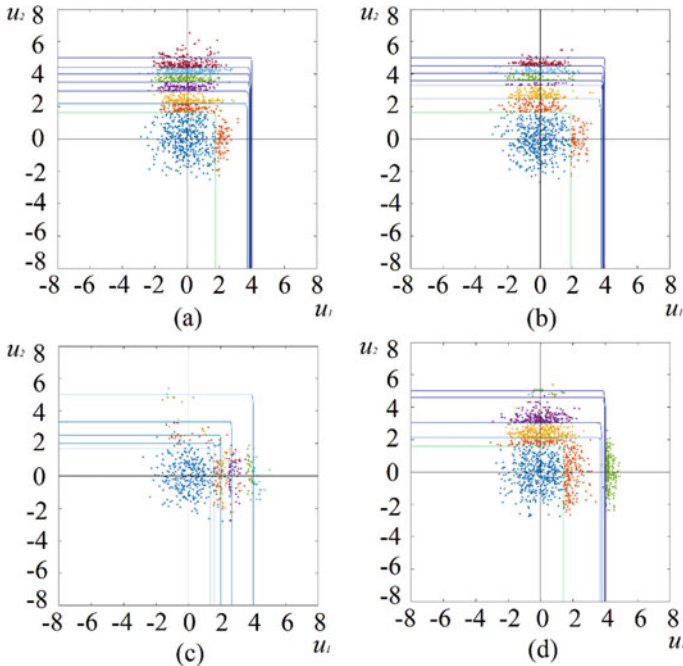
Fig. 1 Example 1. Typical propagation of samples towards failure region in **a** SSM, **b** GSM, **c** SESC, **d** proposed method

Table 1 Results for Example 1

	SS	GSM	SESC	Proposed
No. of samples per level	500	500	–	500
Mean failure probability	2.39×10^{-5}	3.04×10^{-5}	3.82×10^{-5}	3.82×10^{-5}
Coefficient of variation	3.67	3.16	0.87	0.71(0.64)
LSF calls	2684	$1983 + 2107$	4271	$2940 + 550$

95% bootstrap confidence interval from the proposed method is $\left(5.24 \times 10^{-6}, 7.57 \times 10^{-5}\right)$

Direct Monte Carlo estimate of $P_f = 3.29 \times 10^{-5}$ using 10^7 samples

4.3 Example 3 (Stable-Symmetric Buckling Problem)

Here we consider a one bar system shown in Fig. 3 [10]. We take length of the bar, $L = 1$ m and the load $P = 1.13 \times 10^9$ N. The random variables under considera-tion are eccentricity, $\varepsilon \sim U(-0.1\,\text{m}, 0.1\,\text{m})$ and stiffness of the torsional spring, $K_t \sim \text{Lognormal}\left(\mu = 1.75 \times 10^9 \text{ Nm/rad, CoV} = 0.05\right)$, which are statistically independent. The performance function is defined as, $g(\varepsilon, K_t) = 0.35 - |\theta|$, where θ is the angular displacement of the rigid bar. The problem is transformed to the
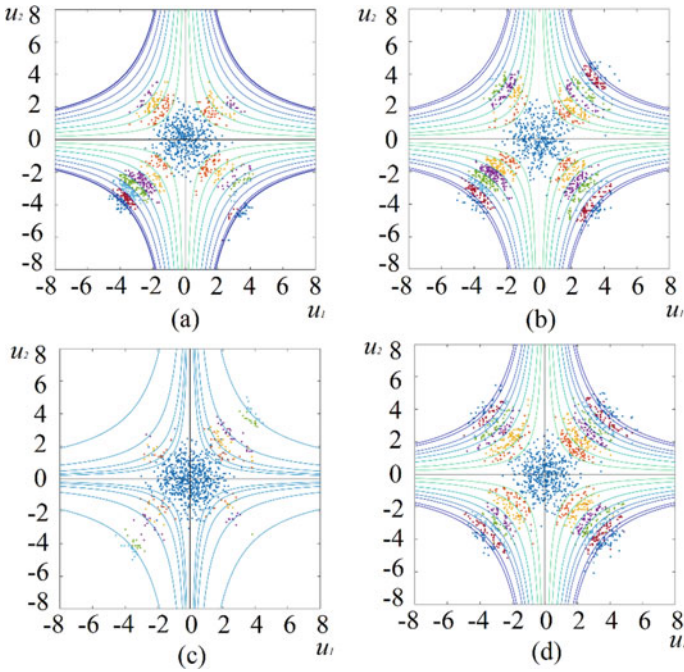
Fig. 2 Example 2. Typical propagation of samples towards failure region in **a** SSM, **b** GSM, **c** SESC, **d** proposed method

Table 2 Results for Example 2

	SS	GSM	SESC	Proposed
No. of samples per level	700	400	–	500
Mean failure probability	6.26×10^{-8}	6.37×10^{-8}	5.20×10^{-8}	6.32×10^{-8}
Coefficient of variation	0.97	0.87	1.45	0.72(0.63)
LSF calls	4503	$4831 + 640$	6992	$4189 + 823$

95% bootstrap confidence interval from the proposed method is $\left(4.74 \times 10^{-9}, 8.09 \times 10^{-8}\right)$

Direct Monte Carlo estimate of $P_f = 6.00 \times 10^{-8}$ using 10^8 samples

standard normal space. In this example also, the difficulty associated with the LSF lies in the presence of multiple important regions of failure.

Figure 4 shows the samples generated in a sample run of the four methods considered, and Table 3 provides the details of the numerical results obtained. Again, we see higher value of CoV for SSM, GSM, and SESC due to inadequate exploration of all failure regions in these methods compared to the proposed method.

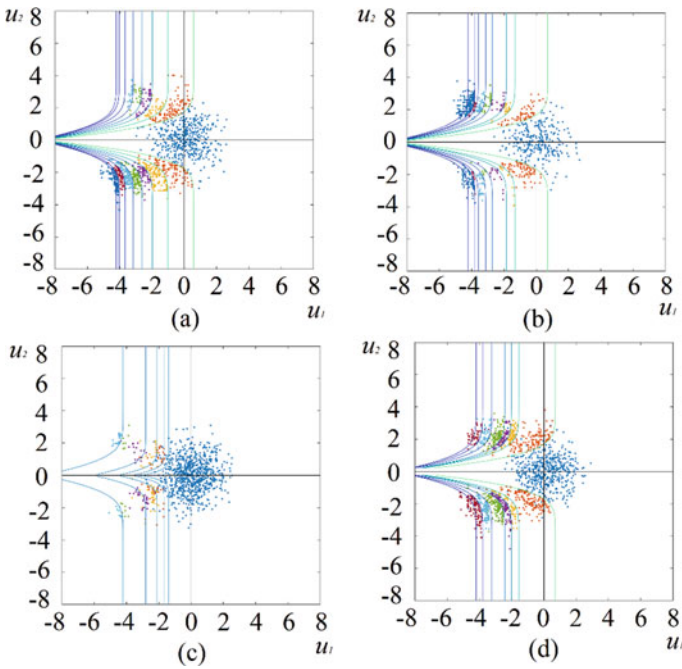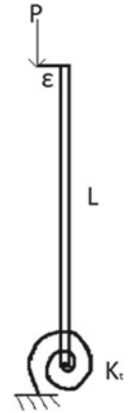**Fig. 3** Stable-symmetric
buckling setup

Fig. 4 Example 3. Typical propagation of samples towards failure region in **a** SSM, **b** GSM, **c** SESC, **d** proposed method

4.4 Example 4 (Snap-Through Buckling)

Figure 5 shows a truss with two rigid bars which is prone to loss of stability through snap-through bucking [10]. Here length of the rigid bar, $L = 1$ m, and stiffness of the spring, $K = 5 \times 10^9$ N/m and initial angle made by the bar with

Table 3 Results for Example 3

	SS	GSM	SESC	Proposed
No. of samples per level	750	300	–	500
Mean failure probability	7.70×10^{-7}	6.79×10^{-7}	6.10×10^{-7}	6.45×10^{-7}
Coefficient of variation	2.45	1.78	1.56	0.91(0.86)
LSF calls	4217	$4605 + 715$	5504	$3523 + 924$

95% bootstrap confidence interval for proposed method is $(3.01 \times 10^{-8}, 1.12 \times 10^{-6})$

Direct Monte Carlo estimate of $P_f = 6.00 \times 10^{-7}$ using 10^7 samples

Fig. 5 Snap-through buckling setup
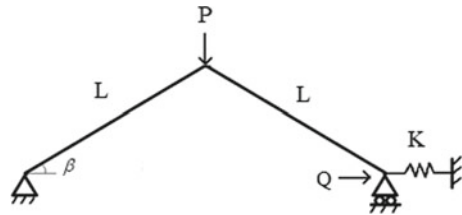
the horizontal $\beta = 63°$. The random variables under consideration are the forces $P \sim U(0 \text{ N}, 3.412 \times 10^9 \text{ N})$ and $Q \sim N(\mu = 1.533 \times 10^8 \text{ N}, \text{CoV} = 2)$, which are statistically independent. The performance function $g(P, Q)$ is defined as the following:

$$
\begin{aligned}
g_1(P, Q) &= \theta, \\
g_2(P, Q) &= \delta^* - 2L(\cos \beta - \cos \theta), \\
g(P, Q) &= \min(g_1, g_2).
\end{aligned} \tag{6}
$$

Here, $\delta^* = 0.35$ m is the permissible tensile deformation in the spring and θ is the angle made by the bars with the horizontal after deformation. The difficulty in the treatment of this LSF arises due to the fact that the LSF value rapidly changes near the most important failure region. Figure 6 shows the propagation of generated samples towards the failure region for each of the four methods. Table 4 shows the numerical results. Here, SS and GSM were unable to discover and sample from the most important failure region, which results in severe underestimation of failure probability. In the case of SESC, even with significant computational investment, it overestimates the failure probability. Here, only the proposed method could estimate the failure probability with a fair degree of accuracy.
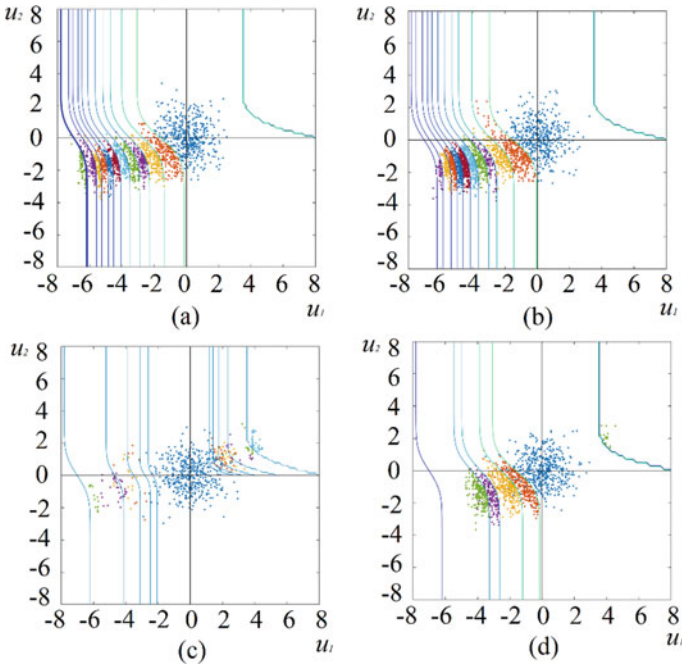
Fig. 6 Exampe 4. Typical propagation of samples towards failure region in **a** SSM, **b** GSM, **c** SESC, **d** proposed method

Table 4 Results for Example 4

	SS	GSM	SESC	Proposed
No. of samples per level	500	500	–	500
Mean failure probability	3.56×10^{-11}	4.25×10^{-11}	4.09×10^{-4}	7.40×10^{-6}
Coefficient of variation	3.02	1.48	0.69	0.91(0.72)
LSF calls	4714	$4291 + 2130$	17823	$3530 + 678$

95% bootstrap confidence interval for proposed method is $\left(8.30 \times 10^{-7}, 7.52 \times 10^{-6}\right)$

Direct Monte Carlo estimate of $P_f = 7.00 \times 10^{-6}$ using 10^6 samples

5 Conclusions

We have considered two examples arising in structural engineering applications where the LSF under consideration have complications in geometry such as multiple regions of comparable importance and/or LSFs with sharply changing values near regions of importance. We have solved these problems using four alternative variance reduction methods viz., SSM, GSM, SESC, and a proposed method. The effectiveness of these methods in addressing the mentioned difficulties has been compared.

Based on the obtained results, we see that SSM and GSM are ill-equipped to handle the complications of the kind mentioned above. In cases of LSFs which sharply change around important failure regions, these algorithms may entirely miss out on the important failure regions. In cases of multiple regions of comparable importance, they are not able to adequately explore all failure regions. The SESC method tackles these difficulties to an extent as shown by the results. However, as also seen, this method can sometimes overestimate failure probabilities. The results, therefore, show that the proposed method, with the replica-exchange MCMC scheme integrated into the PSM framework, deals with these LSFs more satisfactorily with a reasonable computational expense.

References

1. Melchers RE, Beck AT (2018) Structural reliability analysis and prediction. Wiley
2. Au SK, Beck JL (2001) Estimation of small failure probabilities in high dimensions by subset simulation. Probabilistic Eng Mech 16:263–277. https://doi.org/10.1016/S0266-8920(01)000 19-4
3. Botev ZI, Kroese DP (2012) Efficient Monte Carlo simulation via the generalized splitting method. Stat Comput 22:1–16. https://doi.org/10.1007/s11222-010-9201-4
4. Rashki M (2021) SESC: a new subset simulation method for rare-events estimation. Mech Syst Signal Process 150:107139. https://doi.org/10.1016/j.ymssp.2020.107139
5. Sharma A, Manohar CS. Improved particle splitting method for estimation of structural reliability involving limit state functions with complicated geometry, under preparation, to be submitted to Structural Safety
6. Swendsen RH, Wang JS (1986) Replica Monte Carlo simulation of spin-glasses. Phys Rev Lett 57:2607–2609. https://doi.org/10.1103/PhysRevLett.57.2607
7. Kanjilal O, Manohar CS (2015) Markov chain splitting methods in structural reliability integral estimation. Probabilistic Eng Mech 40:42–51. https://doi.org/10.1016/j.probengmech.2015. 02.004
8. Kroese DP, Taimre T, Botev ZI (2011) Handbook of Monte Carlo. Methods. https://doi.org/10. 1002/9781118014967
9. Breitung K (2019) The geometry of limit state function graphs and subset simulation: Counterexamples. Reliab Eng Syst Saf 182:98–106. https://doi.org/10.1016/j.ress.2018.10.008
10. Thompson JMT, Hunt GW (1973) A general theory of elastic stability. Wiley, London

Probabilistic Model Reduction in the Analysis of Building Frames Subject to Sudden Loss of Columns

Abira Rather and C. S. Manohar

1   Introduction

Engineering structures sometimes could be called upon to bear loads that are not envisaged at the time of their design. When such loads are spatially localized, as in the case of vehicle impacts or explosions, it is desirable that the resulting consequences are not disproportional to the cause and do not trigger extensive damage (or collapse) of the structure. This desirable property of the structure has been termed the robustness, and its study has remained challenging in structural engineering research [1–6]. Unlike other loads, such as those due to earthquakes and wind, the quantification of hazard associated with the above-mentioned loads is not easy. The resulting difficulty is side-stepped by artificially modeling the damage caused by the sudden removal of a load-bearing member like a column. This kind of approach, in which the initiating event is not modeled, but only the consequences caused by the event are modeled, is known as the threat-independent approach. This method is also known as the alternate path method (APM), and the philosophy behind this method is to check whether a structure can mitigate the effects of a localized damage by providing alternate load paths. Within the structural engineering community, the resistance of a structure to disproportionate collapse is known as the robustness, and one of the most used methods to analyze a structure for robustness is the APM.

One of the earliest studies on disproportionate collapse is due to Ellingwood [7], who analyzed the probability of failure of an unreinforced brick wall under a gas explosion. Lind [8] studied the effect of damage on the reduction in reliability. Starrosek and Faberland [9] gave a detailed classification of different types of

A. Rather (✉) · C. S. Manohar
Indian Institute of Science, Bengaluru, Karnataka 560012, India
e-mail: abirarather@iisc.ac.in

C. S. Manohar
e-mail: manohar@iisc.ac.in

progressive collapse based on the collapse mechanisms involved. The authors here found that the APM does not indicate how close the surviving structure might be to collapse. To overcome this limitation, they proposed a pushdown analysis method in which the existing gravity loads on the building were monotonically increased till collapse. Xu and Ellingwood [11] analyzed the pre-Northridge steel frames for disproportionate collapse under sudden loss of column and concluded that those structures were not safe under this scenario. Yu et al. [12] studied RC frame structures under the missing column scenario and investigated the sensitivity of various parameters on the pushdown curve. Brunesi et al. [13] compared the disproportionate collapse potential of RC structures designed for seismic loads versus those designed for gravity loads using fragility curves. These authors concluded that the seismically designed buildings were more robust towards progressive collapse. Felipe [14] gave a systematic reliability-based method to determine the key element, the removal of which can trigger progressive collapse. Feng et al. [15] used the probability density evolution method to compute the change in system reliability caused by the loss of a member. They, however, did not take the transient dynamic nature of the problem into consideration.

There have been attempts to quantify the robustness of a structure: thus, Frangopol [16] suggested an index of robustness based on the ratio of reliability of damaged and intact structures. A vulnerability index was suggested by Lind [8] as a ratio of the probability of failure of the damaged structure to the probability of failure of the corresponding intact structure. Baker [17] proposed a risk-based index of robustness as a ratio of direct risk and summation of direct and indirect risks caused by an abnormal event. Fascetti et al. [18] proposed two structural robustness indices, one based on the number of columns removed for collapse and another based on the axial load multiplier for the removed columns. A risk-based method to quantify robustness was proposed by Praxedes et al. [19] and further employed as a cost–benefit assessment tool for design against progressive collapse. Bhattacharyya [20] proposed an index of robustness based on concepts of system reliability. The index here is bounded between 0 and 1 and hence can be used to compare the robustness of two different structures.

In the present study, we employ Monte Carlo simulations to characterize the propagation of uncertainties onto the structural response upon the sudden removal of a column in a moment resisting steel frame structure. The response of the sample structure is analyzed on the OpenSEES platform based on a finite element model that incorporates both material and geometric nonlinearities. The ensemble of resulting response time histories is processed by using the factor mapping method [21], which leads to the rank ordering of the input random variables in terms of relative contributions to the variability in the response. This, in turn, leads to the formulation of a probabilistic reduced-order model for the structure. The study demonstrates the efficacy of the model reduction and, for the specific example considered, a reduction in the number of random variables by about 70% is witnessed.
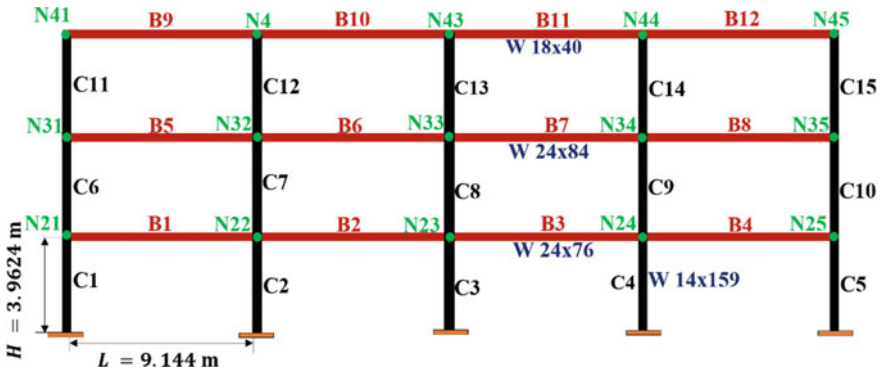
Fig. 1 Frame structure under study [11]

2 Problem Statement

The study considers steel moment-resisting frames carrying prescribed dead and live loads (e.g., the frame in Fig. 1). The properties of the frame and the applied loads are taken to be random in nature. If any of the columns is suddenly removed, the resulting dynamic response of the system constitutes a vector of random processes. Furthermore, this response needs to be determined, taking into account the material and geometric nonlinearities, and the transient dynamic nature of the response. Consequently, one can expect the response process vector to be nonstationary and non-Gaussian in nature. The problem on hand consists of (a) probabilistically characterizing the response, (b) identifying the most and least influential input random variables in terms of their contributions to the variability in a chosen response quantity, and (c) arriving at reduced-order models in which the variables which are deemed least influential are treated as being deterministic thereby leading to a model with fewer input variables treated as being random.

3 Analysis

The frame under consideration is modeled on the OpenSEES [22] platform allowing for geometric and material nonlinearities. The response of the structure following a sudden loss of columns is analyzed by using nonlinear transient dynamic response analysis procedures. The uncertain input variables (which include applied dead and live loads, parameters in material constitutive models, and inertial properties) are modeled as a vector of non-Gaussian and dependent random variables with a prescribed joint probability density function (pdf). An ensemble of the input variables is digitally simulated, and a Monte Carlo simulation-based approach is adopted to generate an ensemble of response time histories. This ensemble is further processed to study quantities such as response pdfs and the evolution of variability as time

progresses. The problem of GRSA is tackled in this study using the factor mapping-based method as outlined by Saltelli [21]. The study proposes a few novel improvisations in the selection of distance measures that underlie this method. The steps involved in this are as follows:

1. Let X be the $n \times 1$ vector of input random variables, $Y(t)$ be the random process representing a chosen response quantity of interest and let $Y \max_{0<t<\infty} |Y(t)|_m$ represent the absolute peak response.
2. Let N Monte Carlo runs be performed leading to a $N \times 1$ ensemble of time histories of $Y(t)$ and samples of Y_m.
3. Define the behavioral set B = $\{Y_m$ such that $a_m \leq Y_m \leq b_m\}$ with B^C being its complement.
4. Define $X_B = \{X$ such that $Y_m(X) \in B\}$ and $X_{B^C} = \{X$ such that $Y_m(X) \in B^C\}$. Let the sizes of X_B and X_{B^c} be $N_B \times n$ and $N_{B^C} \times n$ such that $N_B + N_{B^c} = N$.
5. Define $d_i = \mathrm{dist}\big(X_B^i, X_{B^c}^i\big); i = 1, 2, \ldots, n$ where the superscript i on X_B and X_{B^C} denote the ith column. In the framework of the factor mapping method d_i represents the measure of importance associated with the ith random variable X_i. The estimate for d_i depends on the definition chosen for characterizing $\mathrm{dist}\big(X_B^i, X_{B^c}^i\big)$. The work by Saltelli proposes the Kolmogorov-Smirnov statistic for this purpose leading to

$$d_I^i = \mathrm{dist}\big(X_B^i, X_{B^c}^i\big) = \max_{-\infty < x < \infty} \Big| F_{X_B^i}(x) - F_{X_{B^c}^i}(x) \Big|; \ i = 1, 2, \ldots, n \quad (1)$$

In the present study, we propose that dist $\big(X_B^i, X_{B^c}^i\big)$ also be estimated by using the following two alternative measures [22]

$$d_{II}^i = \mathrm{dist}\big(X_B^i, X_{B^c}^i\big) = \big| E\big(X_B^i\big) - E\big(X_{B^c}^i\big) \big|; i = 1, 2, \ldots, n \big[\text{Engineer's metric}\big] \quad (2)$$

$$d_{III}^i = \mathrm{dist}\big(X_B^i, X_{B^c}^i\big) = \int_{-\infty}^{\infty} \Big| F_{X_B^i}(x) - F_{X_{B^c}^i}(x) \Big| dx;$$

$$i = 1, 2, \cdots, n[\text{Kantrovich's metric}] \quad (3)$$

6. The first-order cumulative distribution functions (CDFs) in the preceding steps are estimated using the command *ecdf* on the MATLAB platform. While estimating $d_{III}^i; i = 1, 2, \ldots, n$ the integral on the right-hand side is evaluated numerically using the trapezoidal rule.
7. Rank order element of X based on the estimated distance measures $\mathrm{dist}\big(X_B^i, X_{B^c}^i\big); i = 1, 2, \ldots, n$. In the present study, the measures d_I^i, d_{II}^i, and $d_{III}^i; i = 1, 2, \ldots, n$ lead to three different ordering of the input variables. A family of reduced-order models can be obtained based on this ordering by treating the lower-ranked variables as being deterministic.

3.1 Remarks

a. The analysis in the present study is based on the assumptions that the frame can be adequately represented using a planar frame model, the joints can be treated as being rigid, the soil-structure interaction can be neglected, and the possible secondary effects caused due to fall of debris in the damaged structure are negligible. These assumptions can indeed be relaxed to achieve greater sophistication in modeling by using more elaborate FE models.

b. The distance measures used in this study obey all the four axioms[1] of a proper metric [23, 24].

c. The importance measures as defined above depend crucially on the definition of the behavioral set B, and this choice can be made to reflect not only the effects of local damage but also on the spatial distribution of the damage.

4 Numerical Illustrations

The study develops FE models (on OpenSEES platform in conjunction with MATLAB codes) for moment-resisting frame structures taking into account both material and geometric nonlinearities following the macro-modeling approach [25]. A corotational formulation with distributed plasticity elements (with fiber sections) has been used in modeling. The corotational formulation here allows for the formation of catenary action at large deformations.

4.1 Study on a Steel Frame Subassembly

We begin by considering the steel subassembly shown in Fig. 2, which has been investigated experimentally earlier by Sadek et al. [26]. The subassembly forms a portion of the structural framing system of a 10-storey steel frame building that has been designed by the National Institute of Standards and Technology research program to study the disproportionate collapse of structures. The sub-assembly comprises of two W24 $\times$ 94 beams connected to three W24 $\times$ 131 columns by reduced beam section (RBS) connections. Multilinear material available in OpenSEES was used to define the material constitutive law at fiber level. The mechanical properties of ASTM A992 steel used are $F_y = 345$ MPa, $F_u = 540$ MPa, $E = 200$ GPa, $\varepsilon_u = 0.18$ mm/mm. Panel zone was modeled using a combination of rigid and spring elements. Pure

---

[1] For a distance measure (d : X x X $\to$ R, x, y and $z \in X$) to be classified as a metric, it should follow following axioms:
  1. Non-negativity, d(x, y) $\geq$ 0
  2. Identity of indiscernible, d(x, x) $= 0$
  3. Symmetry, d(x, y) $=$ d(y, x)
  4. Triangle Inequality, d(x, z) $\leq$ d(x, y) + d(y, z).

shear deformation was ensured in the panel zone by providing pinned connection between the rigid elements. The RBS region was modeled by using distributed plasticity elements of reduced thickness in the flange. The nonlinear static analysis was carried out under displacement control using the Krylov-Newton algorithm. A monotonically increasing displacement was applied at the top of the central column up to a total displacement of 850 mm. This was the displacement at which failure took place in the experimental results. In Fig. 3, the prediction on the axial force in beam 1, as a function of the applied vertical displacement, has been compared with corresponding results experimental observations and predictions from computational models reported by other researchers. It is observed that the predictions from the present model show satisfactory agreement with these other results. This lends credence to the nonlinear FE modeling strategy adopted in the present study.
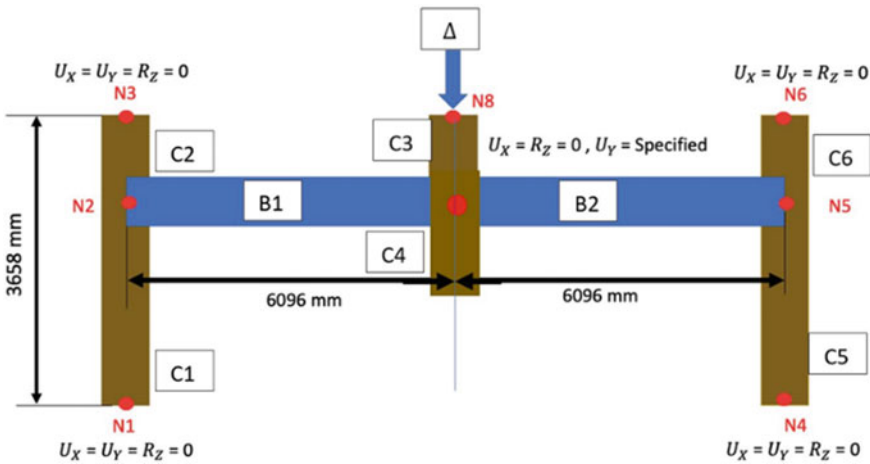
Fig. 2 Steel sub-assembly used for FE model validation

Fig. 3 Axial force in beam B1 as a function of applied vertical displacement at N8
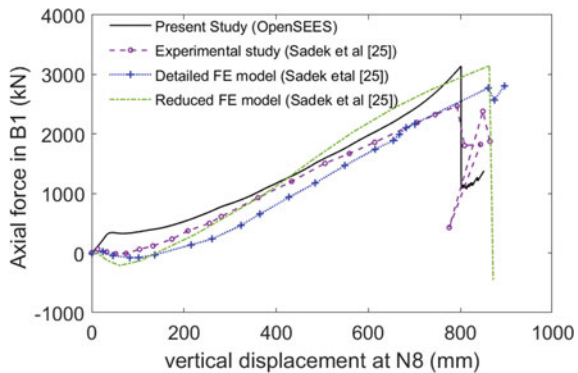
4.2 Study on a 3-Storied Steel Building Frame

Here we consider the frame shown in Fig. 1 (investigated earlier by Ellingwood [11]) and investigate the structural response upon sudden removal of C2. Table 1 provides details of applied dead and live loads. The OpenSEES model for the frame had 4 elements per beam, and each column is represented using one element with 5 integration points per element. The joints are taken to be rigid. The dimensions of the frame and the beam and column sections are considered as being deterministic. The loads acting on the frame and the material properties of the beam, and column sections are considered as a set of random variables, and their probabilistic model is shown in Table 1. The random variables considered are listed in Table 2. A total of 132 random variables are considered. Between any two distinct beams/columns, the associated random variables are treated as being independent. For any given element, the material parameters f_y, f_u, and ε_u are taken to be correlated with the correlation coefficients $\rho(f_y, f_u) = 0.75$, $\rho(f_y, \varepsilon_u) = -0.45$ and $\rho(f_u, \varepsilon_u) = -0.60$. All the dead loads and live loads are taken to be uncorrelated. The associated linear frame is taken to be viscously damped, and a stiffness proportional Rayleigh damping model with the proportionality constant $\beta = 2.803 \times 10^{-3}$ s. The first three natural frequencies of the linear frame are 34.59, 36.26 and 38.56 rad/s. Figure 3 shows the ensemble of vertical displacement at node 22. Figure 4 shows the moment–curvature response near the beam-column junction of beams B9 and B10. The differences in the loading and unloading paths provide an idea of the inelastic action triggered by the removal of the column. From Figs. 3 and 5 it can be deduced that the response is nonstationary and non-Gaussian in nature.

For the purpose of GRSA, we consider the vertical displacement at node 22 as the variable of interest and select the regions of interest to define the behavioral set as B1 = [117.6, 123.8] mm and B2 = [119.2, 145.4] mm. A Monte Carlo simulation with 5000 samples is employed in estimating the distances d_I^i, d_{II}^i, and d_{III}^i; $i = 1, 2, \ldots, n$ (Eqs. 1–3) and these results are shown in Fig. 6. Note that the distances here have been normalized with respect to the highest value, and the details of

Table 1 Distribution of random variables

Random variables	Probability distribution considered	Mean	COV
Dead loads (including self wt.) of the floors	Normal [11]	1.05DL DL = 21,031.2 N/m (floor) DL = 18,150.84 N/m (roof)	0.1
Live load on the floors	Extreme value Type 1 [11]	0.3LL LL = 4389.12 N/m	0.6
Young's modulus of steel, **E**	Lognormal JCSS	200 GPa	0.03
Yield strength of steel, **f_y**	Lognormal JCSS	345 MPa	0.07
Ultimate strength of steel, **f_u**	Lognormal JCSS	450 MPa	0.04
Failure strain of steel, **ε_u**	Lognormal JCSS	0.18 mm/mm	0.06

Table 2 List of random variables

Random variables	Denotation
$X_1, X_2, X_3, \ldots X_{12}$	Yield strength of B1, B2, B3..., B12
$X_{13}, X_{14}, X_{15}, \ldots X_{24}$	Ultimate strength of B1, B2, B3..., B12
$X_{25}, X_{26}, X_{27}, \ldots X_{36}$	Failure strain of B1, B2, B3..., B12
$X_{37}, X_{38}, X_{39}, \ldots X_{48}$	Young's modulus of B1, B2, B3..., B12
$X_{49}, X_{50}, X_{51}, \ldots X_{63}$	Yield strength of C1, C2, C3..., C15
$X_{64}, X_{65}, X_{66}, \ldots X_{78}$	Ultimate strength of C1, C2, C3..., C15
$X_{79}, X_{80}, X_{81}, \ldots X_{93}$	Failure strain of C1, C2, C3..., C15
$X_{94}, X_{95}, X_{96}, \ldots X_{108}$	Young's modulus of C1, C2, C3..., C15
$X_{109}, X_{110}, X_{111}, \ldots X_{120}$	Live loads on beams B1, B2, B3..., B12
$X_{121}, X_{122}, X_{123}, \ldots X_{132}$	Dead loads on beams B1, B2, B3..., B12

Fig. 4 Vertical displacement at node 22 due to the sudden removal of column C2
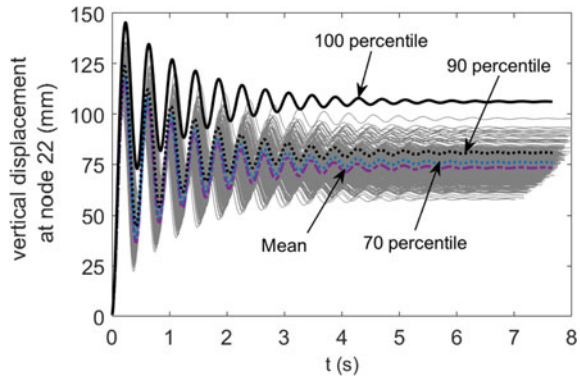
this highest value are indicated in the figure caption. Figure 7 shows the distance measures in descending order, with the x-axis showing the rank. It is observed that three distance measures show similar patterns, with the mutual agreement being good for the top 20 random variables. This can be more easily seen in Fig. 8, which shows the details of the rank order as per the three distance measures. The influence of the choice of behavioral set and the distance measure employed on the probabilistic model order reduction is studied in Fig. 9. The top 30 influential random variables, as per the three distance measures, for B1 and B2 are considered. It is seen that the

Fig. 5 Inelastic action in the beams is represented by $M-\kappa$ relation
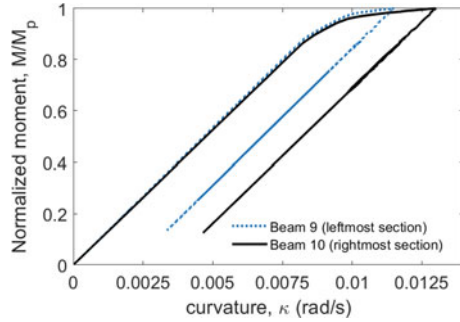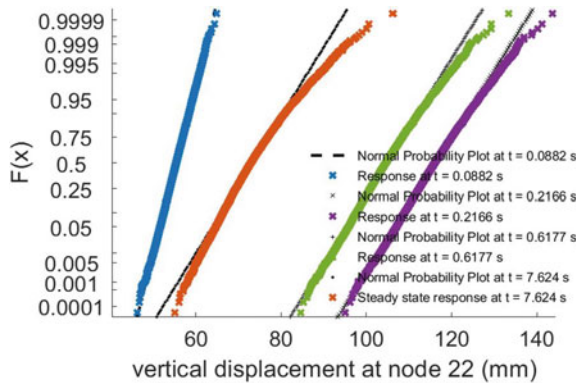

Fig. 6 Probability plot for vertical displacement at node 22 as a function of time


distance measures d_{II} and d_{III} computed for B2 give a more accurate estimate of the most influential random variables leading to efficient model reduction. The study reveals that the most influential random variables here are comprised of dead load, inelastic material properties of the beam, and the live loads associated with bays 1 and 2, which are directly affected by the sudden removal of the column. In contrast, the properties associated with the columns are found to be less influential, and so are the loads acting on members in bays 3 and 4.

5   Conclusions

The study combines nonlinear finite element modeling (using OpenSEES), Monte Carlo simulations, and factor mapping-based global response sensitivity analysis to investigate the response of a randomly parameterered building frame in which one of the columns is suddenly removed. The acceptability of the procedure used in the simulation is first ascertained by simulating the response of a steel frame subassembly which has been experimentally studied in the existing literature. Subsequently, a detailed study on a four-bay, three-storied steel frame building frame with

Fig. 7 **a** Comparison of results for different distance measures, **b** distance measures in descending order for B2
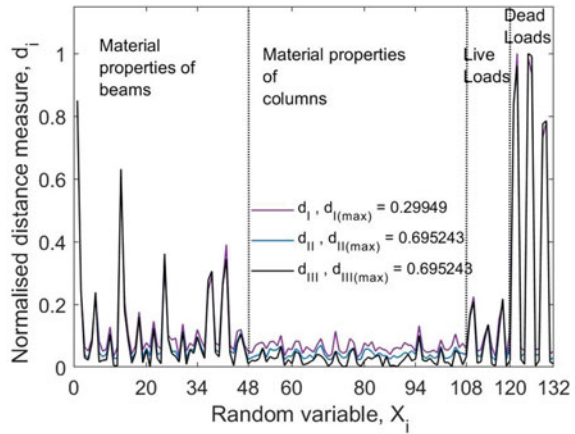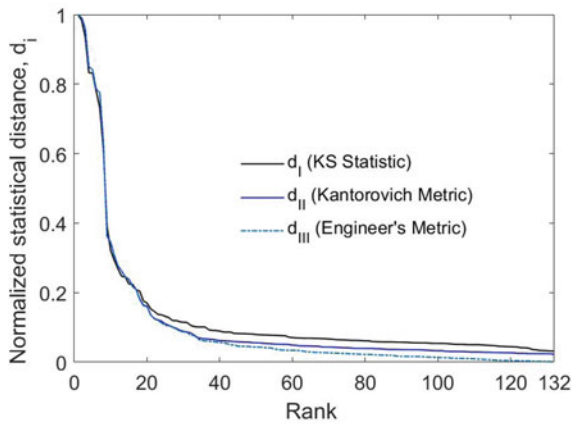
random parameters is carried out. The existing factor mapping method is improvised to incorporate two alternative distance measures (viz., Engineer's and Kantrovich metrics), and it is shown that the analysis with Kantrovich measure is most effective in achieving probabilistic model reduction. The present authors are currently investigating further applications of statistical distance measures within the broad context of characterizing structural robustness.

Fig. 8 Rank ordering of the first 15 most influential random variables for B2; **a** KS statistic-based distance measure; **b** Kantrovich distance; **c** Engineer's metric
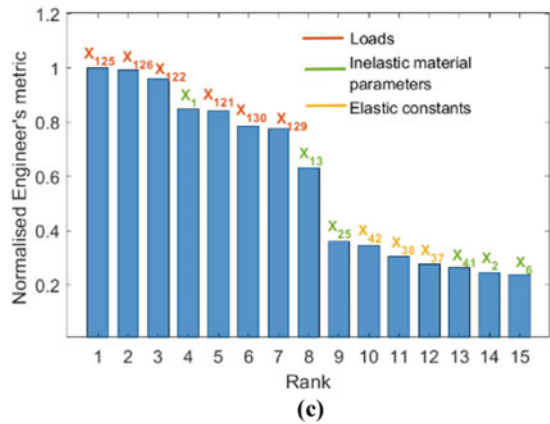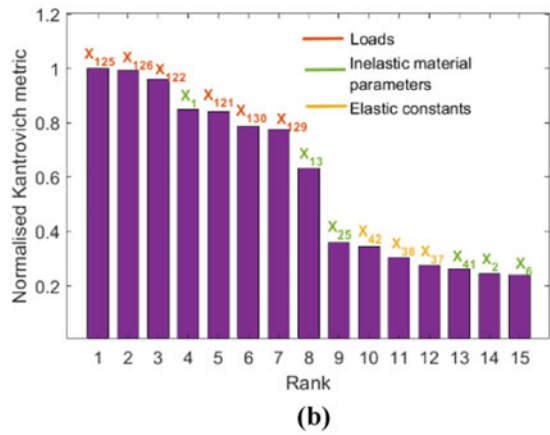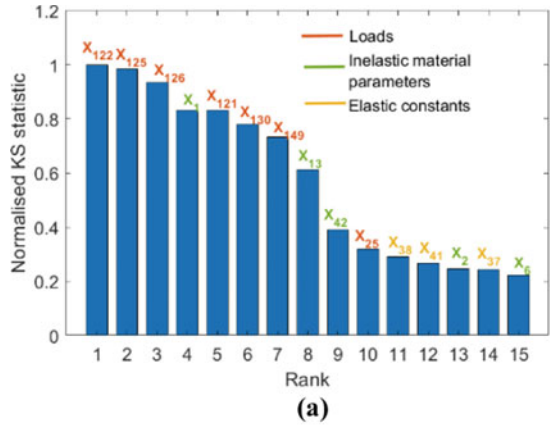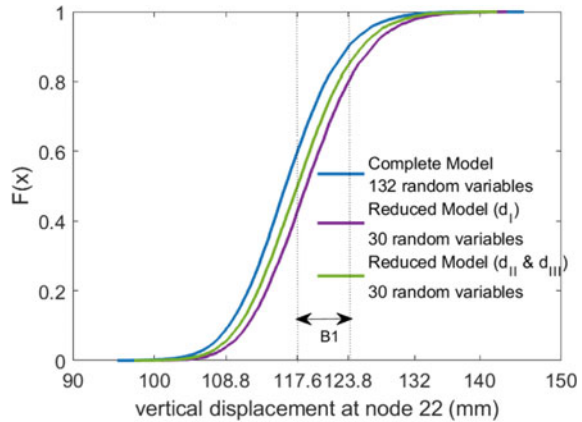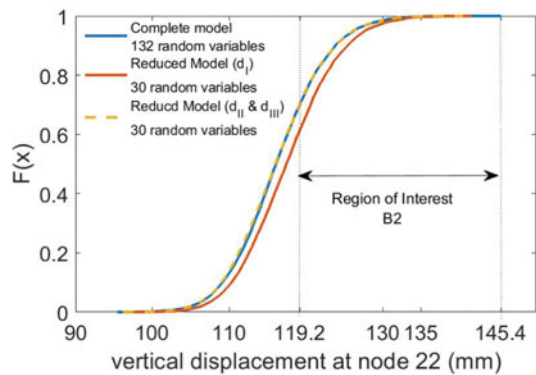
Fig. 9 Comparison of region of interest on model reduction, **a** region of interest B1, and **b** region of interest B2

(a)

(b)

References

1. Fu F (2016) Structural analysis and design to prevent disproportionate collapse. CRC Press
2. Starossek U (2009) Progressive collapse of structures, vol 153. Thomas Telford, London
3. Brett C, Yong L (2013) Assessment of robustness of structures: current state of research. Front Struct Civ Eng 7(4):356–368
4. Ellingwood BR, Smilowitz R, Dusenberry DO, Duthinh D, Lew HS, Carino NJ (2007) Best practices for reducing the potential for progressive collapse in buildings
5. Wang H, Zhang A, Li Y, Yan W (2014) A review on progressive collapse of building structures. Open Civil Eng J 8(1)
6. Bita HM, Huber JA, Voulpiotis K, Tannert T (2019) Survey of contemporary practices for disproportionate collapse prevention. Eng Struct 199:109578
7. Ellingwood B, Leyendecker EV, Yao JTP (1983) Probability of failure from abnormal load. J Struct Eng 109:875–890. https://doi.org/10.1061/(ASCE)0733-9445(1983)109:4(875)
8. Lind NC (1995) A measure of vulnerability and damage tolerance. Reliab Eng Syst Saf 48:1–6. https://doi.org/10.1016/0951-8320(95)00007-O
9. Starossek U, Haberland M (2010) Disproportionate collapse: terminology and procedures. J Perform Constr Facil 24:519–528. https://doi.org/10.1061/(ASCE)cf.1943-5509.0000138

10. Bao Y, Kunnath SK, El-Tawil S, Lew HS (2008) Macromodel-based simulation of progressive collapse: RC frame structures. J Struct Eng 134:1079–1091. https://doi.org/10.1061/(ASCE)0733-9445(2008)134:7(1079)
11. Xu G, Ellingwood BR (2011) Probabilistic robustness assessment of pre-Northridge steel moment resisting frames. J Struct Eng 137:925–934. https://doi.org/10.1061/(ASCE)st.1943-541x.0000403
12. Yu XH, Lu DG, Qian K, Li B (2017) Uncertainty and sensitivity analysis of reinforced concrete frame structures subjected to column loss. J Perform Constr Facil 31:04016069. https://doi.org/10.1061/(ASCE)cf.1943-5509.0000930
13. Brunesi E, Parisi F (2017) Progressive collapse fragility models of European reinforced concrete framed buildings based on pushdown analysis. Eng Struct 152:579–596. https://doi.org/10.1016/j.engstruct.2017.09.043
14. Felipe TRC, Haach VG, Beck AT (2018) Systematic reliability-based approach to progressive collapse. ASCE-ASME J Risk Uncertain Eng Syst Part A Civ Eng 4:04018039. https://doi.org/10.1061/ajrua6.0000990
15. Feng DC, Xie SC, Xu J, Qian K (2020) Robustness quantification of reinforced concrete structures subjected to progressive collapse via the probability density evolution method. Eng Struct 202:109877. https://doi.org/10.1016/j.engstruct.2019.109877
16. Frangopol D, Curley J (1986) Effects of damage and redundancy on structural reliability. J Struct Eng 113:1533–1549
17. Baker JW, Schubert M, Faber MH (2008) On the assessment of robustness. Struct Saf 30:253–267. https://doi.org/10.1016/j.strusafe.2006.11.004
18. Fascetti A, Kunnath SK, Nisticò N (2015) Robustness evaluation of RC frame buildings to progressive collapse. Eng Struct 86:242–249. https://doi.org/10.1016/j.engstruct.2015.01.008
19. Praxedes C, Yuan X-X (2021) Robustness assessment of reinforced concrete frames under progressive collapse hazards: novel risk-based framework. J Struct Eng 147:04021119. https://doi.org/10.1061/(ASCE)st.1943-541x.0003075
20. Bhattacharya B (2021) A reliability based measure of structural robustness for coherent systems. Struct Saf 89:102050. https://doi.org/10.1016/j.strusafe.2020.102050
21. Saltelli A, Ratto M, Andres T et al (2008) Global sensitivity analysis the primer
22. McKenna F, Fenves GL, Scott MH (2000) Open system for earthquake engineering simulation. University of California, Berkeley. http://opensees.berkeley.edu
23. Rachev ST (1991) Probability metrics and the stability of stochastic models
24. Clement P, Desch W (2008) An elementary proof of the triangle inequality for the Wasserstein metric. Proc Am Math Soc 136(1):333–339
25. El-Tawil S, Li H, Kunnath S (2014) Computational simulation of gravity-induced progressive collapse of steel-frame buildings: current trends and future research needs. J Struct Eng 140:1–12. https://doi.org/10.1061/(ASCE)st.1943-541x.0000897
26. Sadek F, Main JA, Lew HS, Bao Y (2011) Testing and analysis of steel and concrete beam-column assemblies under a column removal scenario. J Struct Eng 137:881–892. https://doi.org/10.1061/(ASCE)st.1943-541x.0000422

Probabilistic Modeling of Non-Gaussian Wind Induced Peak Pressures on a Model of Tall Building

M. Keerthana and **P. Harikrishna**

1 Introduction

Design of building envelopes/claddings of modern day tall buildings for wind loads warrants accurate estimate of the wind pressures, including the peak pressures. The fluctuating pressures in the zones of flow separation, vortex formation and wake of a tall building have been observed to be stationary and non-Gaussian [1, 2], for which the peak pressures associated with the physical phenomena will be significantly higher than that estimated based on Gaussian assumption. The non-Gaussianity owing to complex aerodynamic interactions around buildings and structures have posed challenges to the wind engineering fraternity. Estimation of peak factors towards evaluation of wind induced peak pressures on low-rise and high-rise buildings still continues to be an active research problem owing to its significance in engineering design [3–7]. Conventionally, the peak factor for Gaussian process have been evaluated based on Davenport's approach, which is based on the premise that the peaks of a Gaussian process follow Gumbel distribution. For non-Gaussian process, the process definition mandates accounting of higher moments or cumulants of the parent process, namely, skewness and kurtosis [8].

The pressures in the impinging and windward zone of the structures typically have kurtosis less than 3 and they fall under the category of hardening process. The pressures in the flow separated regions have kurtosis more than 3 and they fall under the category of hardening process. Davenport's approach results in conservative estimates of the peak factor for hardening process. The key concern in wind engineering is with estimating peak factor corresponding to softening process in

M. Keerthana (✉) · P. Harikrishna
Wind Engineering Laboratory, CSIR-Structural Engineering Research Centre, Chennai, India
e-mail: keerthana@serc.res.in

P. Harikrishna
e-mail: hari@serc.res.in

separated zones, where heavy tailed distributions of negative/suction pressures have been reported. These suction pressures cause failure of glass cladding/facade during gust wind events and cyclonic storms. Hence, the present study is centered on the method of evaluation of peak factor and peak pressures for softening process. For the experimentally measured wind induced pressures on the model of a rectangular tall building, variants of HPM have been applied to estimate the peak factor for three angles of wind incidence, namely, 0°, 45° and 90° under boundary layer flow.

2 Hermite Polynomial Model (HPM)

Among the methods for evaluating non-Gaussian distribution, Gram–Charlier series, Edgeworth series and Longuet-Higgins series distributions from Gaussian process have inherent limitations of exhibiting oscillatory tail behavior [9, 10]. Hermite Polynomial Model (HPM) and their improved variants provide an alternate approach and are being increasingly used for estimation of peak pressures on structures, owing to their advantages of alleviating the need for solving complex differential equations and applicability over a wide range of skewness and kurtosis values.

HPM adopts a non-linear polynomial transformation involving third-order Hermite polynomials to obtain a Gaussian process, which corresponds to the underlying non-Gaussian process. This univariate nonlinear translation expressed only in terms of first four moments of the non-Gaussian process is given by

$$y = \frac{x - \bar{x}}{\sigma_x} = P_Y^{-1}[\Phi(u)] = g(u) \tag{1}$$

where

y   is a standardized non-Gaussian random variable;
P_Y the distribution of non-Gaussian random variable y;
$\Phi(u)$ the distribution of standard normal variable u;
g(u)   a nonlinear function of u that is considered to increase monotonically;
u   a Gaussian random variable.

The non-linear function g(u) characterised by moment based Hermite polynomial model, facilitates the description of probability density function in an analytical form. For softening process, PDF of the process y, relating non-Gaussian and Gaussian process is given by

$$y = g(u) = u + h_3(u^2 - 1) + h_4(u^3 - 3u) \tag{2}$$

where $u(y) = \left[\sqrt{\xi^2(y) + c} + \xi(y)\right]^{1/3} - \left[\sqrt{\xi^2(y) + c} - \xi(y)\right]^{1/3} - a;$

$$\xi(y) = 1.5b\left(a + \frac{y}{\kappa}\right) - a^3; \quad a = \frac{h_3}{3h_4}; \quad b = \frac{1}{3h_4}; \quad c = (b - 1 - a^2)^3$$

$$h_3 = \frac{\gamma_3}{4 + 2\sqrt{1 + 1.5\gamma_4}}; \ h_4 = \frac{\sqrt{1 + 1.5\gamma_4} - 1}{18}; \ \kappa = \frac{1}{\sqrt{1 + 2h_3^2 + 6h_4^2}}$$

where γ_3 and γ_4 are the skewness and excess kurtosis (kurtosis-3) of the process y. u(y) is the solution of Eq. (2) for random variable u. h_3, h_4 and κ are the coefficients of moment based Hermite model. The shape of the distribution is governed by the coefficients of the Hermite polynomial h_3 and h_4.

Hence, the non-linear function g(u) and u(y) depends on higher-order statistical moments. Upon availability of data, the higher order moments can be obtained from standardized process y. The probability density function of a standardized non-Gaussian process is then given by

$$P_Y(y) = \frac{1}{\sqrt{2\pi}} \exp\left[-\frac{u^2(y)}{2}\right] \frac{du(y)}{dy} \tag{3}$$

HPM yielded conservatives values of peak factor in cases where process of strongly non-Gaussian. Hence, the improvements as mentioned in Table 1 have been evolved. These are the key milestones with regard to the research on peak factor using HPM. For the present study, two improved HPM, namely, Revised Hermite Polynomial Model (RHPM) and closed form solution based assessment of HPM coefficients approach by Yang et al. [12], referred as RHPM-Yang have been adopted owing to their inherent advantages and ease of implementation. The formulations and expressions for the models have been presented elsewhere [12, 17]. The PDF of extremes for all these models is given by

$$P_{Y,ext}(y) = \exp(-\psi)\frac{d\psi}{dy}; \quad \psi = v_0 T \ \exp\left(-\frac{u^2(y)}{2}\right) \tag{4}$$

From the PDF, the peak factor is evaluated as

$$g_{ng} = \kappa\left\{\left(\beta + \frac{\gamma}{\beta}\right) + h_3\left[\beta^2 + (2\gamma - 1) + \frac{1.98}{\beta^2}\right] \right.$$
$$\left. + h_4\left[\begin{array}{l} \beta^3 + 3\beta(2\gamma - 1) \\ + \frac{3}{\beta}\left(\frac{\pi^2}{6} - \gamma + \gamma^2\right) + \frac{5.44}{\beta^3} \end{array}\right]\right\} \tag{5}$$

The above equation is used to obtain positive extremes. The sign of negatively skewed time series needs to be reversed by multiplying with –1 to get negative extremes. Upon evaluation of peak factor, the positive and negative extremes of the process are obtained using the following expressions.

$$x_{ext} = \overline{x} + \sigma_x . g_{ng}$$
$$x_{ext} = \overline{x} - \sigma_x . g_{ng} \tag{6}$$

Table 1 Evolution of HPM models

Author	Key milestones in HPM
Winterstein [11]	Introduction of moment based HPM with method of moments for estimation of shape parameters
Kareem and Zhao [8]	Derivation of expressions for peak factors based on HPM
Huang et al. [6]	First order approximation of HPM coefficients
Yang et al. [12]	Evaluation of parameters of improved HPM through closed form solution proposed by Kwon and Kareem [13]
Ding and Chen [4]	Proposal of new moment based translation function for hardening process
Peng et al. [7]	Mapping procedure to alleviate the limitation of working range of HPM
Ma and Xu [14]	Bayesian estimation of shape parameters of HPM for improved fitting of non-Gaussian distribution in the entire range of PDF covering bulk and tail regions
Zhang et al. [15]	Proposed unified HPM for both hardening and softening process
Liu et al. [16]	Proposed a piecewise HPM with renewed definition of first four statistical moments of the process

3   Wind Tunnel Studies

Spatio-temporal variations of wind induced pressures have been measured on the surface of a rigid model of a rectangular tall building with full-scale dimensions of $30 \, m \times 60 \, m$ in plan and height of 270 m, which is geometrically scaled with a scale ratio of 1:300. The dimensions of the scaled model of the tall building are 10 cm $\times$ 20 cm in plan and 90 cm high. The model has been fabricated using plexiglass sheet of 3 mm thickness, and sufficiently stiffened to ensure rigidity of the model for the tested wind speeds. A thick base plate is provided for rigid connectivity at the base of the model.

The wind tunnel experiments have been carried out in the Boundary Layer Wind Tunnel (BLWT) facility of CSIR-SERC, which has test section dimensions of 2.5 m (width) $\times$ 1.8 m (height). The wind characteristics at the center of the test section, where the model has been mounted was measured using TFI Cobra probes. The boundary layer flow characteristics correspond to that of open terrain with a power law coefficient that characterizes the mean velocity variations along the height of 0.165.

The pressure taps were provided at five levels as shown in Fig. 1a. The normalized height (z/H) of the five levels considered are 0.1, 0.3, 0.5, 0.7 and 0.9. Each level is instrumented with 28 pressure taps, the layout of which at a level is shown in Fig. 1b. Wind incident on the shorter face (with width of 10 cm) and longer face (with width of 20 cm) of the rectangular building has been considered as 0° and 90° angle of

wind incidence (θ), respectively. Figure 1 also indicates wind incident direction for θ of 90°. The pressures have been collected for a time duration of 24 s at a sampling frequency of 650 Hz, using pressure scanners with digital temperature compensation (Fig. 2).

The pressure from the pressure taps have been expressed in the form of non-dimensional pressure coefficients given by
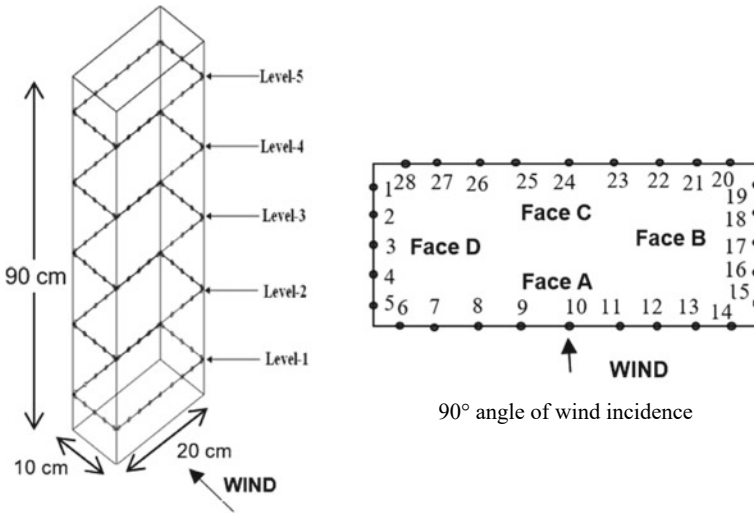

Fig. 1 a Instrumentation scheme along the height of the model and **b** layout of pressure taps at a level

Fig. 2 View of the model of tall building in wind tunnel for **a** $\theta = 0°$ and **b** $\theta = 90°$

$$C_p = \left(\frac{p_{total} - p_{static}}{\frac{1}{2}\rho \overline{U_z}^2} \right) \qquad (7)$$

where $(p_{total} - p_{static})$ is the mean pressure acting on the surface of the rectangular building model

ρ = mass density of air taken as 1.2 kg/m^3
$\overline{U_z}$ = velocity of the oncoming flow at height 'z' of the model.
(z = 9 cm, 27 cm, 45 cm, 63 cm and 81 cm, for five levels respectively).

Considering velocity scale of 1:1 and geometric scale of 1:300, the sampling duration corresponds to a full scale duration of 2 h. Nine trials of data have been acquired for every angle of wind incidence. Hence, total data available is 18 h in full-scale. The data has been divided into segments of 10-min duration in full-scale, consistent with the literature [18] and peaks have been picked from each 10-min segment for further processing to evaluate the peak factor. The experimentally measured/observed peak pressures can be estimated based on [5]

- A single peak value from the pressures sampled during a longer sampling period
- Mean value of various observed maximum values of pressures
- A fractile level corresponding to a level of probability of non-exceedance from cumulative distribution function (CDF) of the observed peak values.

For observed peak from experiments, maximum values of the above three approaches have been adopted for conservatism.

4 Results and Discussions

The time history of pressure coefficients from the pressure taps have been standardized, i.e., zero mean and unit normal, making it feasible towards application of Hermite based models. Higher order moments, viz, skewness and kurtosis have been evaluated in order to study the Gaussian/non-Gaussian characteristics of the pressure coefficients. These higher order moments are also immensely useful in determining the category of the process, i.e., softening or hardening type. The skewness and kurtosis contours for three considered angles of wind incidence of 0°, 45° and 90° have been presented in Fig. 3. For 0° and 90° angles of wind incidence, the faces D and A are directly exposed to incident wind, respectively. The skewness and kurtosis in these incident faces are close to the standard values of 3 and 0 for Gaussian process, in which variability in probability density function beyond second moment is not expected. Owing to flow separation at the corners of incident faces, it has been observed that the higher order moments are no longer constant and exhibit significant non-Gaussian features with values deviating from expected values of Gaussian process. The negative skewness for the pressure taps on the flow separated faces

of the rectangular building for all the studied angles of wind incidence are indicative of heavy tailed probability distribution in the suction side owing to separation region dynamics and vortex formation. Excess kurtosis is also observed to be positive in these three faces. The boundary layer wind characteristics causes rapid fluctuations in the form of increased suction and high overpressure events on lateral faces, leading to higher peak pressure values with an abnormally skewed distribution. It is such characteristics that cause failure of glass claddings of tall buildings, if they are not appropriately considered during design. Further, it also mandates non-Gaussian modeling of the extreme of pressure coefficients.

The representative probabilistic characteristics have been presented for a pressure tap at level 2 of the tall building model, immediately after flow separation for 0°, 45° and 90° angles of wind incidence. The histogram of standardised pressure coefficient from the measurements is shown in Fig. 4.

The probability density function evaluated based on the considered Hermite models and Gaussian distribution are included in the plots for comparison. The figures are indicative of the deviation of the probability distribution from Gaussian to non-Gaussian in the separated flow regions, as expected. The standardized pressure coefficient is the peak factor of the parent distribution. Among the non-parametric distributions, HPM model provides a higher magnitude of peak factor and is observed to be over conservative. RHPM and MHPM-Yang provide better description of the non-Gaussianity in the separated flow. These trends well corroborates with those reported in literature. Further, numerical integration of PDF of extremes have been carried out to obtain the CDF of extremes as shown in Fig. 4. The expression for peak factor in Eq. (6) corresponds to non-exceedance probability of 57%. Hence, consistently the same level of non-exceedance probability is considered from experimental data. It has been observed that MHPM-Yang provides an improved estimate of peak factor better than HPM and close to the experimentally derived magnitudes of peak pressures in the flow separated regions. However, the Poisson assumption considered in Hermite based models is manifested in the form of slightly higher values of peak factor in comparison with the observed value from experiments. The peak factors for all the pressure taps at Level-1 of the tall building for 90° angle of wind incidence has been presented in Fig. 5. It can be observed from Fig. 5 that MHPM-Yang provides a conservative estimate of the peak factor for the flow separated regions. Similar trend in variation of peak factors have been observed for all other levels. The implementation of the improved variants of the HPM model has been observed to be simple compared to the other models adopted in literature. Further, the PDF and CDF of the processes are in consistent/conformal with the first four moments of the parent aerodynamic process in structures.
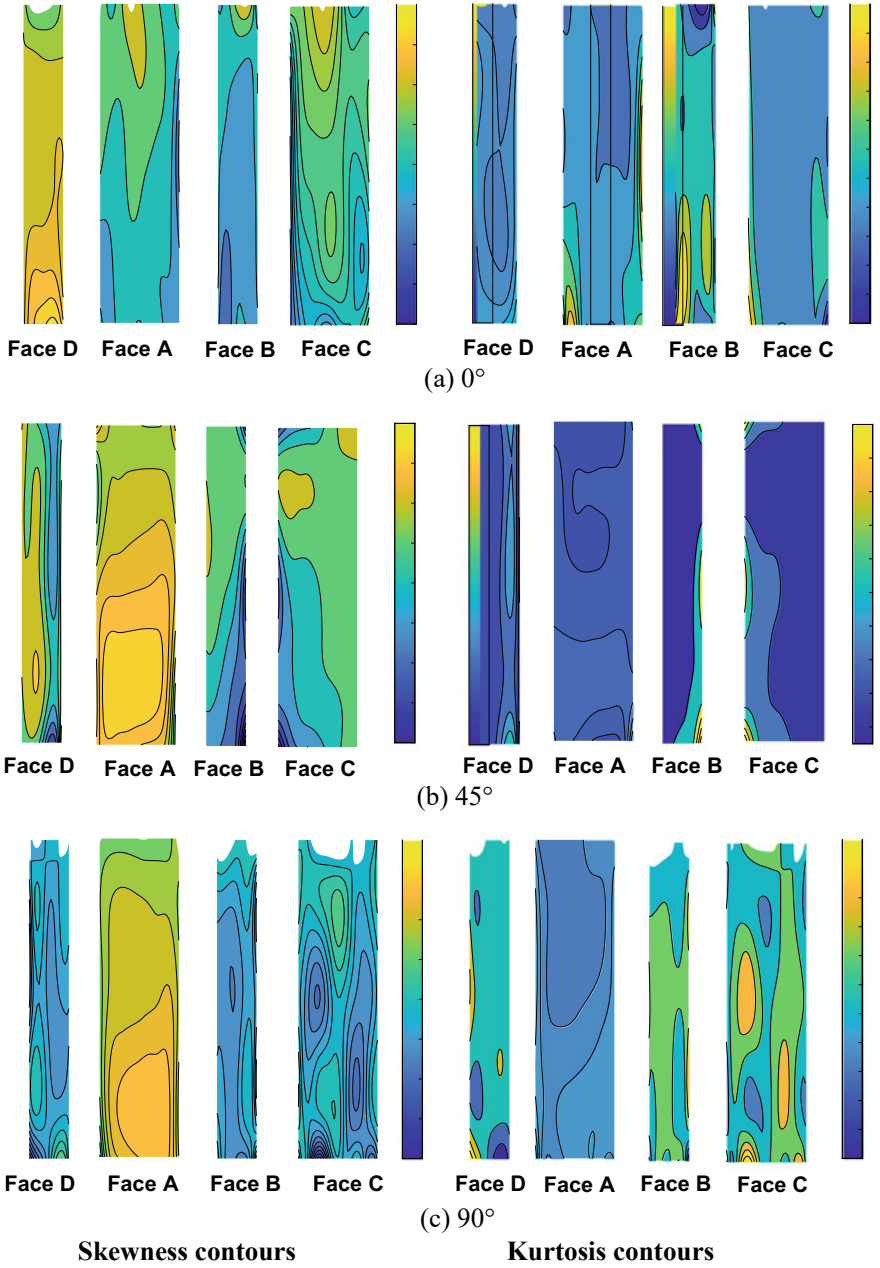
Face D   Face A   Face B   Face C   Face D   Face A   Face B   Face C

(a) 0°

Face D   Face A   Face B   Face C   Face D   Face A   Face B   Face C

(b) 45°

Face D   Face A   Face B   Face C   Face D   Face A   Face B   Face C

(c) 90°

Skewness contours   **Kurtosis contours**

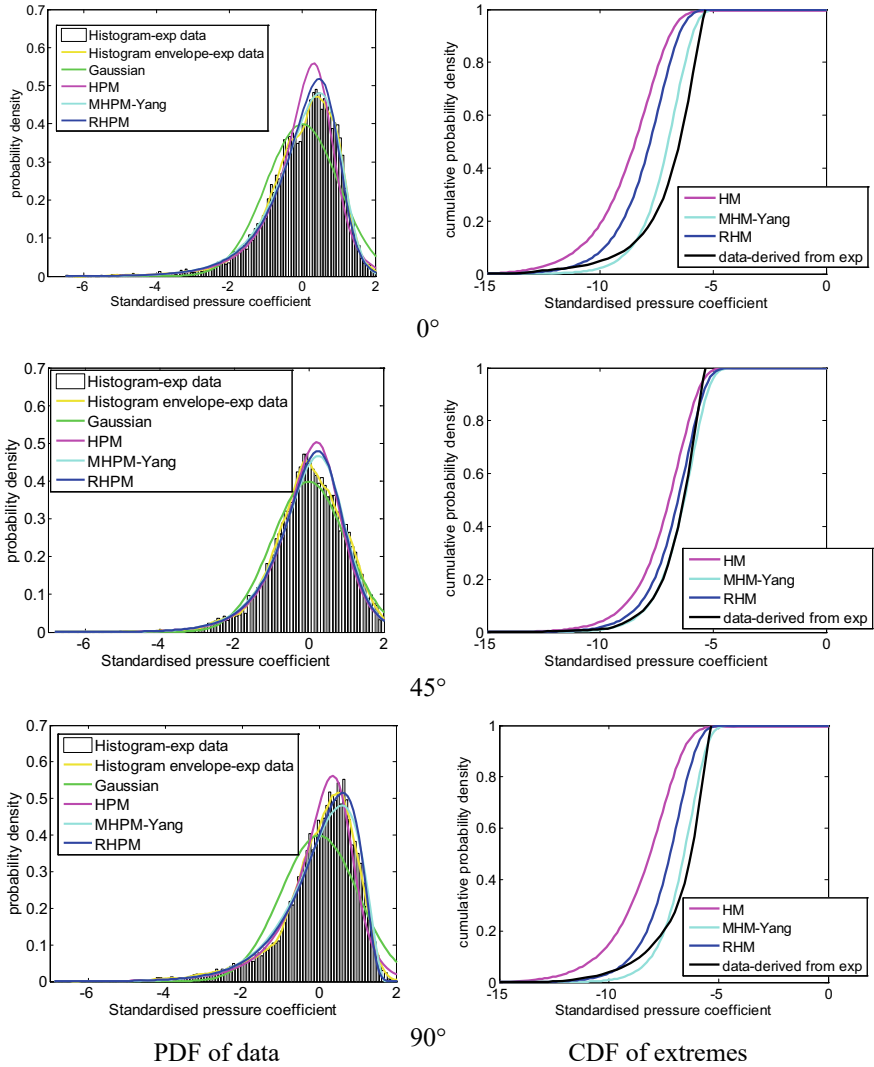**Fig. 3**   Skewness and Kurtosis contours for **a** 0° **b** 45° and **c** 90°

Fig. 4 PDF of data and CDF of extremes for the considered angles of wind incidence

5   Summary and Conclusions

Data-driven Hermite polynomial based models, viz, HPM, RHPM, and MHPM-Yang have been used to evaluate the peak factors required for estimating wind pressure extremes on a model of tall rectangular building in regions after flow separation. A comparison of peak factors estimated through aforementioned models has been made with the observed values from wind tunnel experiments to demonstrate the
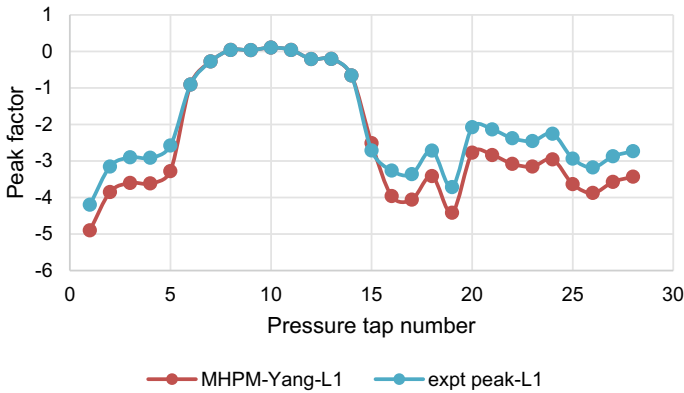
Fig. 5 Comparison of peak factor for pressure taps in Level-1 for 90° angle of wind incidence

efficacy of the models. The extreme fractiles of non-Gaussian process is evaluated by transforming it to underlying Gaussian process, with analytical formulations for PDF and CDF. The performance of MHPM and RHPM-Yang are comparable with each other and provide conservative estimate of peak factor for pressure taps on the faces of the building in the zones of flow separation and vortex formation/movement, which may not be appropriately modeled and estimated by conventional Gaussian framework. It has been observed that such data driven Hermite polynomial based models provide rational estimation of peak pressures, which will be useful towards reliability based design of building envelopes under stochastic wind loading.

References

1. Holmes JD (1981) Non-Gaussian characteristics of wind pressure fluctuations. J Wind Eng Ind Aerodyn 7:103–108
2. Kasperski M (2005) Specification of the design wind load based on a consistent probabilistic approach. Engineering 91(3):1161–1168
3. Balaji Rao K, Anoop MB, Harikrishna P, Selvi Rajan S, Iyer NR (2013) Alpha-stable distribution for prediction of negative peak wind pressures on roofs of low-rise building. In: Proceedings of 8th Asia-Pacific conference on wind engineering. APCWE 2013, vol 19, no 6, pp 958–967
4. Ding J, Chen X (2014) Assessment of methods for extreme value analysis of non-Gaussian wind effects with short-term time history samples. Eng Struct 80:75–88
5. Gavanski E, Cook NJ (2019) Evaluation of XIMIS for assessing extreme pressure coefficients. Front Built Environ 5
6. Huang MF, Lou W, Chan CM, Lin N, Pan X (2013) Peak Distributions and peak factors of wind-induced pressure processes on tall buildings. J Eng Mech 139(12):1744–1756
7. Peng X, Yang L, Gavanski E, Gurley K, Prevatt D (2014) A comparison of methods to estimate peak wind loads on buildings. J Wind Eng Ind Aerodyn 126:11–23

8. Kareem A, Zhao J (1994) Analysis of non-Gaussian surge response of tension leg platforms under wind loads. J Offshore Mech Arct Eng 116(3):137–144
9. Choi M, Sweetman B (2010) The hermite moment model for highly skewed response with application to tension leg platforms. J Offshore Mech Arct Eng 132(2):1–8
10. Ochi MK (1986) Non-Gaussian random processes in ocean engineering. Probabilistic Eng Mech 1(1):28–39
11. Winterstein SR (1989) Nonlinear vibration models for extremes and fatigue. J Eng Mech 114(10):1772–1790
12. Yang L, Gurley KR, Prevatt DO (2013) Probabilistic modeling of wind pressure on low-rise buildings. J Wind Eng Ind Aerodyn 114:18–26
13. Kwon DK, Kareem A (2009) Peak factor for non-Gaussian processes revisited. In: 7th Asia-Pacific conference on wind engineering. APCWE-VII (1988)
14. Ma X-L, Xu F-Y (2016) Extreme estimations of non-Gaussian wind pressures integrated with Hermite polynomial model and Bayesian method. Adv Civil Environ Mater Res
15. Zhang X-Y, Zhao Y-G, Lu Z-H (2019) Unified Hermite polynomial model and its application in estimating non-Gaussian processes. J Eng Mech 145(3):04019001
16. Liu M, Chen X, Yang Q (2017) Estimation of peak factor of non-Gaussian wind pressures by improved moment-based Hermite model. J Eng Mech 143(7):06017006
17. Kwon DK, Kareem A (2011) Peak factors for non-Gaussian load effects revisited. J Struct Eng 137(12):1611–1619
18. Ma X, Xu F, Kareem A, Chen T (2016) Estimation of surface pressure extremes: hybrid data and simulation-based approach. J Eng Mech 142(10):04016068

Role of Interfacial Transition Zone on Response of Concrete Under Tension: A Micromechanical Approach

Nikhil Gupta and J. M. Chandra Kishen

1 Introduction

Various studies have been performed on concrete's macro-scale properties, while micro-scale research is still seldom. The main challenge of analyzing the micro-mechanics of concrete is the complexity involved due to its heterogeneity. On a macro-scale, the concrete is viewed as a two-phase system consisting of aggregates and mortar, but micro-scale concrete is modeled as a three-phase system consisting of aggregates, mortar, and a layer of mortar near the vicinity of aggregates, which is termed as Interfacial Transition Zone (ITZ).

Each aggregate is surrounded by an ITZ layer that ranges from 0 to 20 μm [1]. The test performed in the literature [1, 2] suggests the ITZ layer's physical properties in concrete. The findings confirm that the ITZ is the material's weakest layer. Cracks arise in this zone as the loading progresses, resulting in pre-peak non-linear stress–strain behavior. ITZ has thus been highlighted as a viable study field.

All statements presented here confirm that to know insights into the behavior of concrete, continuum micromechanics is a perfect study. Continuum micromechanics helps us precisely understand the microstructure and underlying mechanism at that scale. A represented volume element of concrete [3] is considered to study the specimen at different scales. Thus, a proper homogenization scheme links these scales, i.e., macro and micro scales [4]. Further research has also studied crack propagation[5–7]. Also, various researchers have modeled the concrete specimen in finite element software (Abaqus) [8, 9] to study the response of the concrete and validate it with the experimental data [10–12].

N. Gupta (✉) · J. M. Chandra Kishen
Civil Engineering Department, Indian Institute of Science, Bangalore, India
e-mail: nikhilgupta1@iisc.ac.in

J. M. Chandra Kishen
e-mail: chandrak@iisc.ac.in

1.1 Contribution

To analytically model the ITZ layer, two approaches are suggested in the literature. The first one is where the ITZ layer is taken as a layer of vanishing thickness. This model does not assume a separate material property for the ITZ layer. Cracks initiating in the model are presented by displacement jump occurring at the aggregate and mortar matrix interface. The second approach realizes the ITZ as a finite small layer with separate material properties different from the matrix mortar. The boundaries are assumed to be perfectly bonded, and crack initiation starts at the ITZ layer. The cracks are then propagated within the layer and transferred to the mortar matrix. The model with the first approach is present in the literature [13]. Efforts are being made in this study to develop the analytical equations to capture the properties of concrete by the second approach. The results are also linked to the number and size of microcracks generated in the non-linear regime of stress–strain curve. The work also focuses on the effect of different parameters such as aggregate volume fraction, ITZ strength, aggregate diameter, ITZ thickness [14] on concrete response. Thus, parametric analysis is done to understand the sensitivity of each of these parameters on the response of concrete.

2 Modeling and Computation

2.1 Modeling of Interface Layer

A represented volume element (RVE) of concrete is considered to develop a 3D microscopic model. Figure 1 shows a sample of RVE. Within an RVE, concrete is shown as three-phase material: Mortar, Aggregate, and a small layer around the aggregate known as Interfacial Transition Zone (ITZ). The interface has a finite thickness of around 15–20 µm with different material properties. Usually, the material properties assigned to the interface layer are lower than the properties of the mortar.

2.2 Computation of Stress at the Microscopic Level

The model from the literature [3] is chosen to achieve the objective. The Eshelby solution and Mori Tanaka homogenization are utilized to compute the stresses at the ITZ layer. A code is written in MATLAB to compute stresses at the interface due to uniaxial loading in the Z-direction. The stresses are plotted along with three-volume fractions of aggregate, including 0.35, 0.45, and 0.7. The materials properties used are presented in Table 1.

   As the cracking event initiates from the local tensile stress peaks, it is essential to understand the behavior of maximum tensile stresses within the structure of RVE.
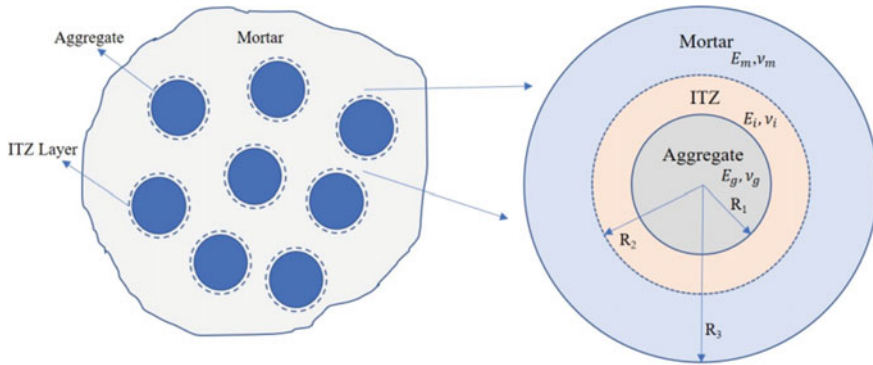
Fig. 1 Represented volume element of the concrete and 3 phases of concrete at the microscopic level

Table 1 Materials properties used [13]

Reference	Aggregate	Cement paste
Bulk modulus	$Kagg = 38.89$ GPa	$Kcp = 13.89$ GPa
Shear modulus	$Magg = 29.17$ GPa	$Mcp = 10.42$ GPa

The results obtained in Fig. 2a suggest that for volume fraction of aggregate of 0.45, the increase of applied stress is up to 21% at the ITZ layer. The failure always occurs at the zenith point ($\theta = 0$) for tensile uniaxial loading in the z-direction. For Fig. 2b, the stress amplifications are observed around $\theta = \pi/8$ for tensile uniaxial loading along the z-direction and $\theta = \pi/6$ for compressive uniaxial loading. The computed amplification values are observed up to 22% for the volume fraction of 0.45. The increase in volume fraction of aggregate shows a decrease in the amplification factor, i.e., the highest stress an ITZ layer achieves due to the applied macro stress reduces with an increase in the volume fraction. This can be attributed to the fact that the macroscopic stress is distributed on more aggregates for more volume fractions of aggregate, thus reducing the concentration on each of the aggregate interfaces. Hence, the failure in such a specimen is delayed, and more significant strains can be observed.

3 Micromechanical Model

A micromechanical model is proposed to study the role of the Interfacial Transition Zone in the concrete specimen. All three phases, aggregate, mortar, and Interface (ITZ) are attributed to different material properties, with ITZ properties being the lowest. The macroscopic stress applied to specimen is distributed according to the volume fraction of each phase present in the specimen.
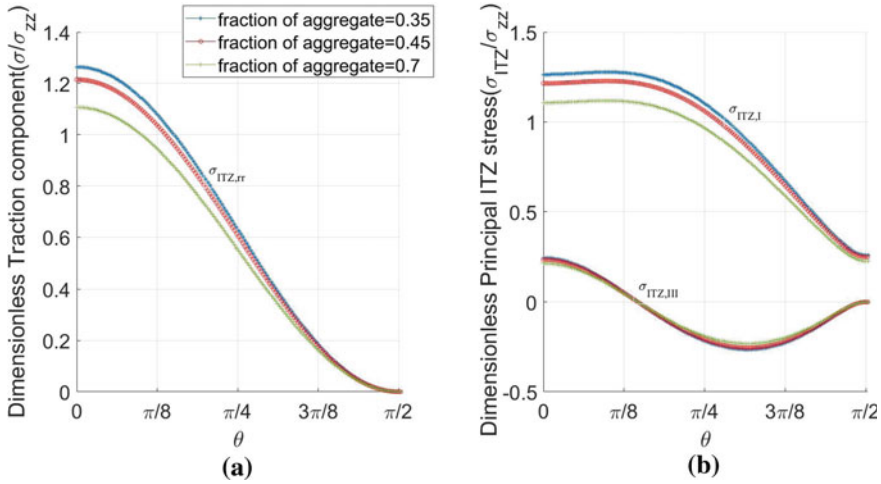
Fig. 2 **a** Variation of stress in ITZ zone for uniaxial tensile loading. **b** Variation of principle ITZ stress for uniaxial tensile loading

$$\Sigma = f_a \sigma^a + f_{ITZ} \sigma^{ITZ} + f_m \sigma^m \tag{1}$$

where Σ = Macro stress applied at RVE. σ^a = Average aggregate stress due to applied macro stress. σ^{ITZ} = Average stress in the ITZ zone due to applied macroscopic stress. σ^m = Average stress in the matrix due to applied macro stress. f_a, f_{ITZ}, f_m are the volume fraction of aggregate, ITZ layer, and matrix, respectively. Assuming all voids are filled with mortar matrix thus, no cavity is considered in the model. Hence,

$$f_a + f_{ITZ} + f_m = 1 \tag{2}$$

From Eq. 1:

$$\sigma^m = \frac{\Sigma - f_a \sigma^a - f_{ITZ} \sigma^{ITZ}}{1 - f_a - f_{ITZ}} \tag{3}$$

Thus, the average mortar stress can be computed by knowing the average stress in other phases.

3.1 Macroscopic Constitutive Relation

A represented volume of element (RVE) of concrete is considered with uniaxial tensile loading acting on it. Furthermore, stress control testing is implied for the

model. Thus, corresponding strains are computed using the constitutive relationship presented in Eq. 4 for each load step. The stress value at the micro-level calculated in the previous section is upscaled to the macro level to obtain the constitutive behavior of the material. Thus, the constitutive model for the model is presented as:

$$\varepsilon = S^m : (1 - f_a - f_{ITZ})\sigma^m + S^a : f_a\sigma^a + S^{ITZ} : f_{ITZ}\sigma^{ITZ} \tag{4}$$

Substituting the value of σ^m from Eq. 3:

$$\varepsilon = S^m : \Sigma + f_a(S^a - S^m) : \sigma^a + f_{ITZ}(S^a - S^{ITZ}) : \sigma^{ITZ} \tag{5}$$

where ε is the macroscopic strain S^m, S^a, S^{ITZ}, are the compliance matrix of each phase. Assuming RVE as isotropic linear material, the compliance matrix of each phase is stated as under:

$$S^x = \frac{1}{E_x} \begin{bmatrix} 1 & -v_x & -v_x & 0 & 0 & 0 \\ -v_x & 1 & -v_x & 0 & 0 & 0 \\ -v_x & -v_x & 1 & 0 & 0 & 0 \\ 0 & 0 & 0 & 1+v_x & 0 & 0 \\ 0 & 0 & 0 & 0 & 1+v_x & 0 \\ 0 & 0 & 0 & 0 & 0 & 1+v_x \end{bmatrix} \tag{6}$$

where x is m, a, ITZ respectively for each phase.

4 What Happens When Microcracks Occur?

When stresses in the ITZ layer reach their initial strength, microcracks start to initiate within the zone. The effect of the micro-cracks can be directly viewed in the response by the occurrence of non-linearity. Thus, pre-peak non-linearity in concrete response is due to the micro-cracks generated in the ITZ layer. The microcracking in the layer is attributed to two phenomenons:

(a) **First is the reduction of the elastic modulus of the ITZ layer**

The occurrence of microcracks tends to decrease the material's stiffness, thereby reducing the elastic modulus. As the load step is increased beyond the stress limit, the Elastic modulus decreases at each stage. The decrement in the value of Elastic modulus and Poisson's ratio is calculated by the following relations presented in the literature [15, 16]

$$E = E_0 \left[1 - \frac{16(10 - 3v_0)(1 - v_0^2)N\langle a \rangle^3}{45(2 - v_0)} \right]$$

Fig. 3 Microcracks
initiation in ITZ layer
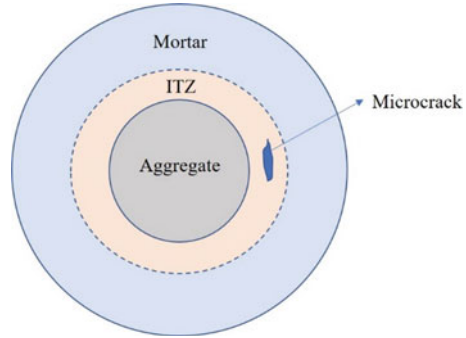
$$v = v_0 \left[1 - \frac{16(3 - v_0)\left(1 - v_0^2\right) N \langle a \rangle^3}{15(2 - v_0)} \right] \tag{7}$$

where C = Crack Parameter = N $\langle a \rangle^3$ N = Number of microcracks per unit volume
and a = mean radius of microcracks E_0 and v_0 are the Elastic modulus and Poisson's
ratio of the uncracked specimen. E and v are the Elastic modulus and Poisson's ratio
of the section after microcracks occur.

(b) **Increase in volume of the cavity of the specimen**

At each load step, the amount of microcracks increases, reducing the volume fraction
of other phases. Total volume after initiation of microcrack can be stated as (Fig. 3):

$$V_T' = V_m + V_{ITZ} + V_a + V_c \tag{8}$$

where V_T' = Total volume of the specimen after initiation of microcracks. V_m, V_{ITZ},
V_a, V_c are the volume of mortar, ITZ, Aggregate, cavity, respectively. The value of
volume fraction of cavity (f_c) is calibrated from the experimental data for the concrete
response, assuming the same increment for all other load steps until failure. Hence,
other phases' volume fraction will be decreased by $(1 + f_c)$ factor at initiation, and
the factor increases by f_c at each load step.

4.1 Failure Criteria

Two limits can define the strength of concrete specimen:

- **Initial strength**: It represents the value of stress at which the microcracking in
  material starts.

- **Final strength**: It represents the value at which the material fails.

  Failure of material can occur in two ways:

- **Mortar final strength is reached**: All microcracks have joined within the mortar matrix, and failure occurs due to macro crack in mortar material.
- **ITZ layer reaches its final strength**: At this stage, segregation of Aggregate and ITZ layer occurs, and material fails.

5 Numerical Algorithm

Stress control analysis is performed on the model equations proposed. The equations are computed for the uniaxial tensile load applied to the specimen. The analysis is performed in MATLAB following the algorithm presented below.

Step 1: Assume volume fraction of cavity to be a fraction of volume of ITZ, start with 2%.

Step 2: Calculate the volume fraction of the ITZ layer and crack parameter as shown in Appendix 2.

Step 3: For the known value of each phase's volume fractions, calculate the volumetric (Bvol) and deviatoric (Bdev) part of stress concentration tensor from Appendix 1.

Step 4: Initialize the value of uniaxial macroscopic stress to zero and increase its value to 0.1 MPa after each iteration. Also, initialize the value of mortar stress as zero in the first iteration.

Step 5: Calculate the average stresses in the ITZ layer occurring due to applied macro stress using Appendix 1.

Step 6: Compare the value of ITZ stress and mortar stress with the initial strength of both phases, respectively.

Step 7: If both stresses are lower than the initial strength, continue to calculate the macroscopic strain from the constitutive relations proposed in Eq. 5.

Step 8: Calculate the stress value in mortar material and update it for the next iteration in Step 4.

Step 9: At the iteration, when the stress in any phase reaches the initial strength, reduce the value of Elastic modulus, Poisson's ratio of corresponding material using Eq. 7 and also reduce the volume fractions of the corresponding phase as discussed in Sect. 4.

Step 10: Update the values of mortar stress, volume fraction of the cavity, and the crack parameter for the next iteration in Step 4.

Step 11: Repeat the iteration until either stress in the ITZ layer or mortar reaches the corresponding final stress.

Step 12: Compare the response from the experimental data. In case of deviation, go to step 1, increase the volume fraction of cavity and follow the steps until experimental results are matched.

6 Result and Discussions

6.1 Response of Concrete Under Uniaxial Tension

The analysis is done to obtain the stress–strain curve of the concrete specimen under uniaxial tensile loading along with change in crack parameter at each load step. The results are calibrated with the experimental results presented in the literature [12]. The value of crack parameter is assumed to increase constantly at each load steps. The calibrated results are presented in Fig. 4a, which corresponds to the 0.00013 increase in volume fraction of cavity for each load step after microcracking starts. The value is approx. 5.7% of the volume fraction of the ITZ layer. Thus, the corresponding value of crack parameter is observed as 0.0138 (Table 2).
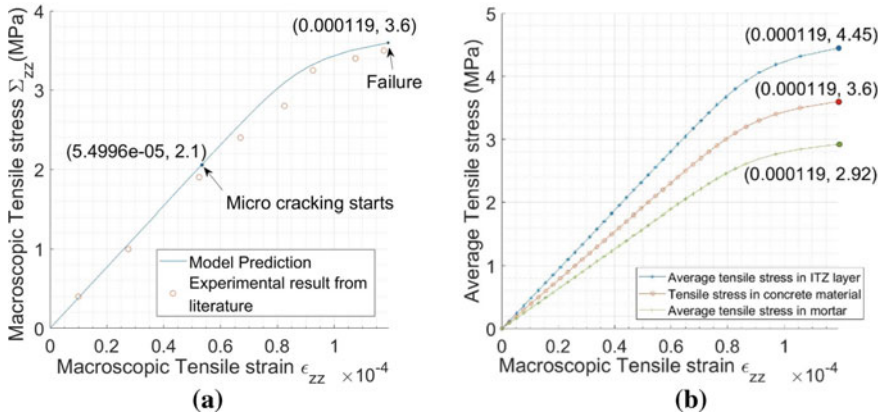

Fig. 4 **a** Stress–Strain curve of concrete from the proposed model ($f_c = 0.00013$) and experimental result [12]. **b** Average stress in mortar and ITZ layer along with concrete response obtained from model

Table 2 Data used in analysis [13]

Properties	Aggregate	Mortar	ITZ Layer
Elastic modulus	70 GPa	25 GPa	20 GPa
Poisson's ratio	0.2	0.2	0.2
Volume fraction	0.45	0.54775	0.00225
Initial strength	–	3 MPa	2.5 MPa
Final strength	–	5 MPa	4.5 MPa
Diameter	24 mm	–	–
Thickness	–	–	0.02 mm
Crack parameter	0.0138		

6.2 Analysis

The results obtained show good agreement with the experimental data [12], and the model can capture the pre-peak non-linearity of the material. The response is linear up to 2.1 MPa, i.e., 58% of the peak load, showing no microcracks generation in this region. Figure 4b shows the variation in stress observed in the individual phase along with the concrete material. The results suggest that the ITZ layer receives a higher amount of stress at each loading step, and initial cracking starts in this region. Moreover, material failure is observed when stress in the ITZ layer reaches its final strength. Figure 5a is the graph of the Elastic modulus of concrete versus macroscopic tensile stress applied. It can be concluded that the initial elastic modulus of concrete is observed as 38,542.85 MPa, which remains constant until the micro-cracks starts. The decrement in the value of elastic modulus is carried out further, and at the time of failure elastic modulus of concrete is observed to be 30,199.54 MPa. The decrement in the elastic modulus of concrete is 21.64%. The same decrement of elastic modulus is also plotted with respect to the crack parameter (Fig. 5b). A total decrement of 21.64% in the value of elastic modulus corresponds to the 0.224 value of the crack parameter. The decrement rate is observed as slow for the lower value of the crack parameter but increases rapidly as the crack parameter increases. This is because of the high number or size of cracks at a large value of crack parameter.

Figure 6 shows the variation of crack parameter ($C \in [0.0138, 0.224]$) with respect to variables mean radius ($a \in [0.02, 0.07]$) and number of cracks per unit volume ($N \in [500, 2000]$). Figure 7a shows the variation of mean crack radius (a) with respect to crack parameter (C) along with decreasing number of cracks per unit volume (N). Figure 7b shows the variation of the number of cracks per unit volume (N) with respect to crack parameter (C) along with an increase in crack mean radius (a).
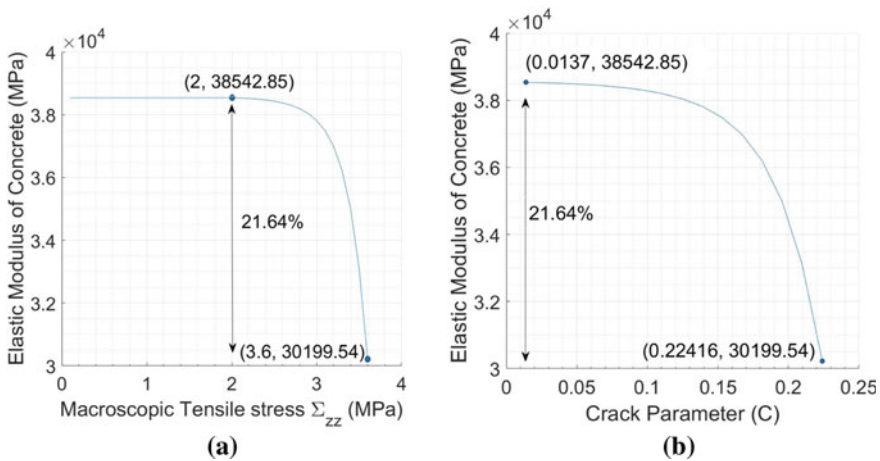

Fig. 5 a Decrease in elastic modulus of concrete at each load step. **b** Variation of elastic modulus and crack parameter (C)
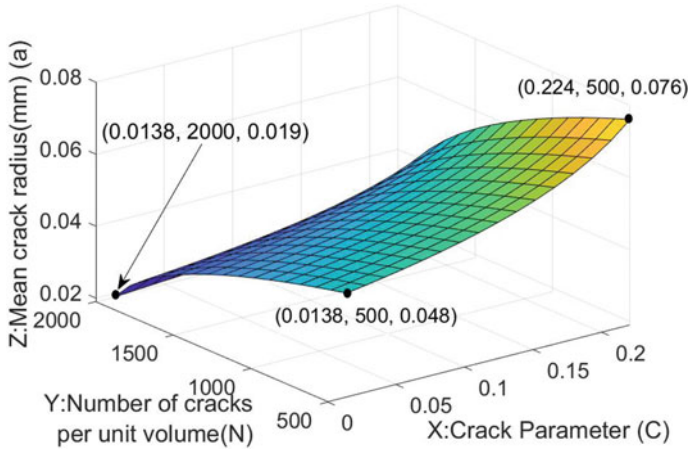
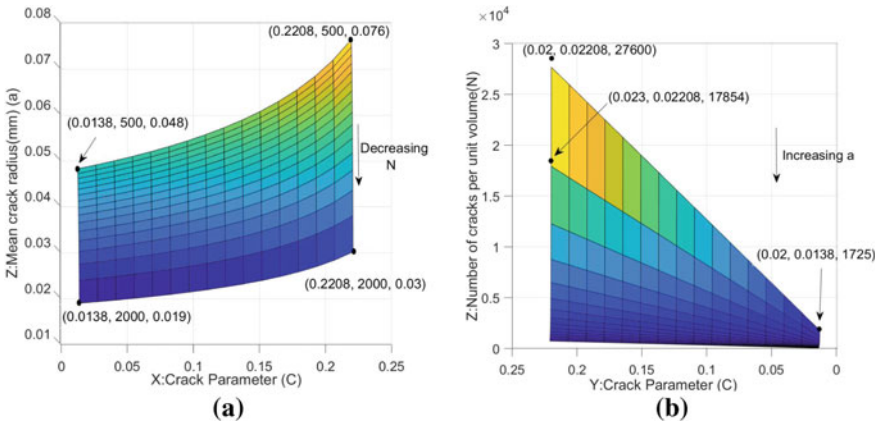**Fig. 6** 3D variation of number of cracks per unit volume (N), mean radius of crack (a), and crack parameter (C)

Fig. 7 **a** Variation of mean crack radius (a) with respect to crack parameter along with decreasing number of cracks per unit volume (N). **b** Variation of the number of crack per unit volume (N) with respect to crack parameter (C) along with an increase in crack mean radius (a)

From the above analysis, the crack parameter (C) value for the concrete specimen is 0.0138. Crack parameter (C) depends on two variables: number of cracks per unit volume (N) and the crack mean radius (a) [16]. Thus, a 3D plot is generated to understand the variation of N and mean radius (a) with crack parameter (C).

$$C = 0.0138$$

$$N\langle a \rangle^3 = 0.0138 \tag{9}$$

From Figs. 6 and 7, we can observe that:

(i) For the constant value of N as 2000 mean crack radius of cracks increases from 0.019 mm to 0.03 mm at the point of failure. No new cracks are generated for this case, but the cracks initiated further increase in size.

(ii) For the constant value of mean radius of crack (a) as 0.02 mm, the number of cracks is increased from 1725 to 27,600 per unit volume at the time of failure. For this case, new cracks are formed at each load step, assuming no increase in their size.

(iii) For considering variation in both the parameters simultaneously, it can be observed from Fig. 7 that initially, the number of cracks is 2000 with 0.019 mm mean radius size, and at the point of failure number of cracks is reduced to 500, but the crack size has increased up to 0.224 mm. This reduction in the number of cracks can be attributed to the merger of smaller cracks into larger ones.

7 Parametric Analysis

The behavior of heterogeneous concrete is dependent on various parameters. Thus, to get better insight and sensitivity on each parameter, it is crucial to study the variation on each of them. Hence, this section of the report deals with the parametric analysis of all such parameters. The parameters include volume fraction of aggregate, ITZ layer strength, aggregate size, and ITZ layer thickness.

7.1 Volume Fraction of Aggregates

The analysis is conducted for three-volume fraction of aggregate, 0.35, 0.45, 0.7. The volume fraction is varied by keeping the aggregate diameter constant, i.e., 24 mm. An increase in aggregate volume fraction also tends to increase the amount of ITZ layer in the specimen. The volume fraction ITZ layer for each aggregate volume fraction is computed using Appendix 2. Also, the change in volume fraction of the ITZ layer affects the value of crack parameter C, computed using Appendix 2 for each of the volume fractions of the ITZ layer. The results are presented in Fig. 8. The initial increase in the curve slope is attributed to the higher stiffness of concrete. Increased aggregate content enhances overall stiffness because aggregate has a greater elastic modulus in all three stages. The material's final strain is reduced by increasing the aggregate volume percentage from 0.35 to 0.7. This is because the amount of ITZ layer in the concrete has increased. The larger ultimate stress value is due to the fact that higher the material's strength, greater the strength of the heterogeneous medium.

**Fig. 8** Variation of aggregate volume fraction on concrete response
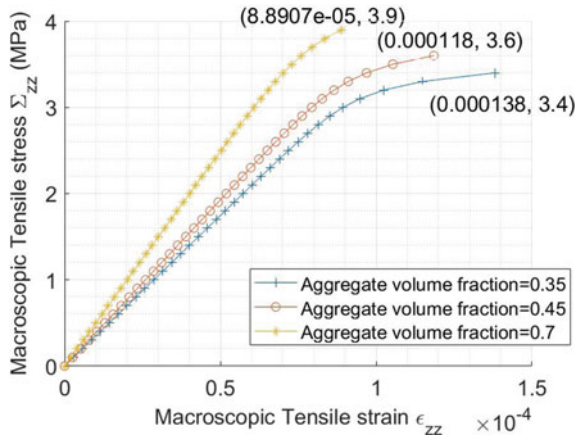
7.2 ITZ Strength

The initial strength of the ITZ layer is varied as 2.5, 3, 3.5 MPa, and corresponding 3, 3.5, 4 MPa as final strength. The variation will also lead to a change in the values of mortar strength. Thus, the values of mortar strengths are also modified in the model. The ITZ strength indicates the point of generation of microcrack and failure stress. For an increase in value of ITZ strength, both the points are achieved at higher strain values. Also, the failure is achieved at higher final macro stress, and observed change is 20–22% (Fig. 9).

7.3 Aggregate Size

The variation of aggregate diameter is understood by varying the aggregate diameters in the model keeping volume fraction as constant. Figure 10 shows the variation of aggregate size on the stress–strain curve of concrete. Three diameters of aggregates are considered, 16, 24, 32 mm. It affects the volume fraction of the ITZ layer also. The concrete with lower diameter aggregates have more number of aggregates to make constant volume fraction in all cases. Thus, a high volume fraction of the ITZ layer is observed for small size aggregates. For the corresponding change in volume fraction of the ITZ layer, crack parameter is modified from Appendix 2. The results (Fig. 10) suggest no change in the linear regime of the curve as the ITZ layer does not affect the response until microcracks are initiated. When microcracks start, low strains are observed in smaller size aggregates. This is because the aggregates are tightly packed in smaller size aggregate specimens resulting in better stiffness.

Fig. 9 Variation of ITZ strength on concrete response
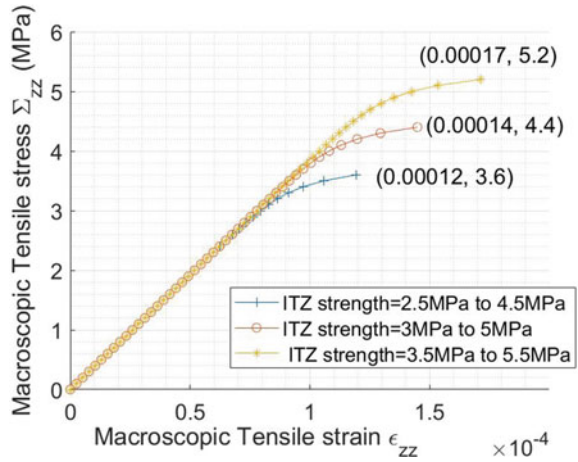
7.4 ITZ Thickness

The literature [1] suggests the thickness of the ITZ layer lies between 0.01 and 0.02 mm. The results are presented with the variation of ITZ thickness as 0.01, 0.015, 0.02 mm (Fig. 11). This results in change in the volume fraction of ITZ. The specimen with a small thickness posse less amount of the ITZ layer. Thus, large final strains are observed in the specimen. Hence, specimens with small thickness possess high ductility. From changing the thickness from 0.01 to 0.015 mm reduction in final strain is higher. But, as the thickness is further increased to 0.02 mm, the reduction factor decreases.

Fig. 10 Variation of aggregate size on concrete response
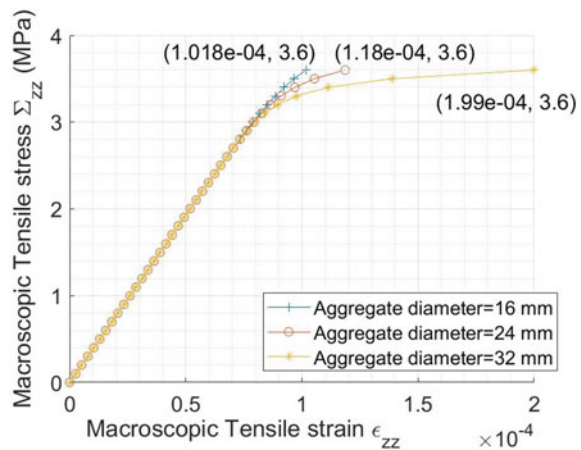
8 Conclusion

Analytical equations are developed to understand Interfacial Transition Zone's role using micromechanism concepts under uniaxial tension. At the micro-level, concrete is viewed as three-phase material; hence, concrete is modeled by keeping the ITZ layer with small thickness and different material properties. The aggregates are considered spherical embedded in the mortar matrix. The micro-level stresses are upscaled to macro-level, and a constitutive relation is obtained for the material. Nonlinearity in the model is captured by reducing Elastic modulus and Poisson's ratio of the phases as the microcracks are generated in the corresponding phase. Also, the volume fraction of the cavity is introduced as microcracks propagate. The model captures the response of the concrete perfectly. The non-linear regime helps us to understand the change in material properties when microcracks are generated in the material. The results also comment on the number and size of microcracks generated at each load step. Various parameters like volume fraction of aggregate, ITZ strength, aggregate size, ITZ layer thickness are varied to understand their effect on concrete response. The research result can help us fulfill the uncertain future human and nature demands along with economic consideration. Hence the study leads us closer to performance-based engineering. The research findings can also be used to design improved material and overcome the material's shortcomings.

9 Limitations and Future Scope of Work

The proposed model uses the equations of stresses derived for spherical-shaped aggregates. However, as aggregates are generally random in shapes, the model needs to be modified for other shapes. Since aggregate shapes are defined on different factors such as angularity, elongation, sphericity, thus a proper relation among these factors is required to counter its effect. Moreover, further experiments are needed to validate the result to account for these effects. In the proposed model stress control test is being initiated. The model can be modified using the strain control approach to counter the post-peak response. Hence, the model would be capable of capturing the softening behavior of concrete.

Appendix 1

Microscopic Stress at surface of aggregate [3] (Fig. 12).
    The microscopic stress generated at the surface of aggregate or interface:

$$T_r(\theta, \phi) = \frac{1}{3} B_{vol} \left(\Sigma_{xx} + \Sigma_{yy} + \Sigma_{zz} \right)$$

Fig. 11 Variation of ITZ layer thickness on concrete response
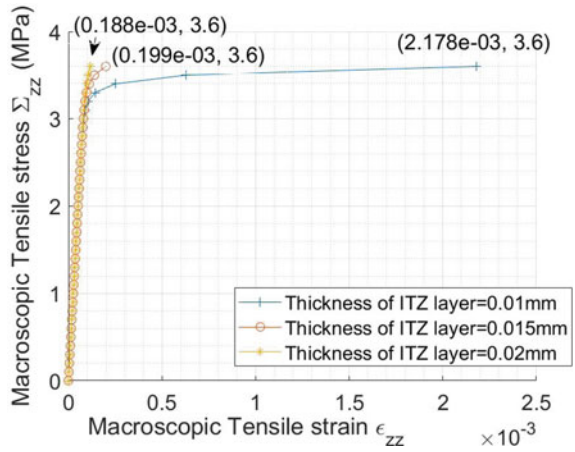
Fig. 12 Spherical base frame (ϕ is the azimuth angle, and θ is the zenith angle)
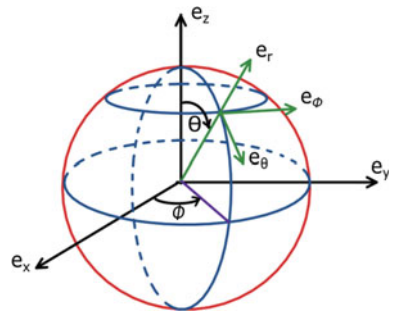
$$+ B_{dev}\left[\Sigma_{xx}\left(\cos^2\phi\,\sin^2\theta - \frac{1}{3}\right) + \Sigma_{yy}\left(\frac{2}{3} - \cos^2\theta\,\sin^2\phi - \cos^2\phi\right)\right.$$
$$\left. + \Sigma_{zz}\left(\cos^2\theta - \frac{1}{3}\right)\right]$$

$$T_\theta(\theta, \phi) = \frac{1}{2}B_{dev}\sin(2\theta)\left(\Sigma_{xx}\cos^2\phi + \Sigma_{yy}\sin^2\phi - \Sigma_{zz}\right)$$

$$T_\phi(\theta, \phi) = \frac{1}{2}B_{dev}\sin(2\phi)\sin\theta\left(-\Sigma_{xx} + \Sigma_{yy}\right) \tag{10}$$

Appendix 2

Volume fraction and crack parameter

Fig. 13 Microscopic view
of one aggregate
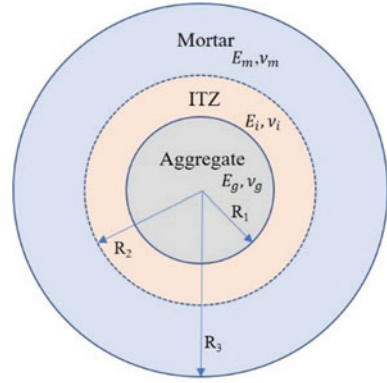
Volume Fraction of ITZ Layer

See Fig. 13.

$$f_{ITZ} = \frac{n_a 4\pi R_1^2 t}{V_T}$$

$$f_a = \frac{n_a \frac{4}{3}\pi R_1^3}{V_T}$$

$$f_{ITZ} = \frac{3t f_a}{R_1} \tag{11}$$

f_a and f_{ITZ} are the volume fraction of aggregate and ITZ layer respectively. t is the thickness of the ITZ layer around the Aggregate R_1 is the radius of the aggregate used in the specimen n_a is the number of aggregates in the specimen, and V_T is the total volume of concrete specimen.

Crack Parameter

Volume of cavity $= f_c *$ Total Volume (V_T)

$$\frac{4}{3}\pi \langle a \rangle^3 N V_{ITZ} = f_c * V_T \tag{12}$$

N is the number of microcracks per unit volume of the ITZ layer.

$$V_{ITZ} = f_{ITZ} * V_T \tag{13}$$

Thus, Crack parameter

$$C = N \langle a \rangle^3 = \frac{3f_c}{4\pi f_{ITZ}} \tag{14}$$

where, f_c is the volume fraction of the cavity formed when microcracks are generated. The value of f_c is calibrated from the experimental data.

References

1. Scrivener KL, Crumbie AK, Laugesen P (2004) The interfacial transition zone (itz) between cement paste and aggregate in concrete. Interface Sci 12(4):411–421
2. Ollivier JP, Maso JC, Bourdette B (1995) Interfacial transition zone in concrete. Adv Cem Based Mater 2(1):30–38
3. Königsberger M, Pichler B, Hellmich C (2014) Micromechanics of itz–aggregate interaction in concrete part i: stress concentration. J Am Ceram Soc 97(2):535–542
4. Benveniste Y (1987) A new approach to the application of mori-tanaka's theory in composite materials. Mech Mater 6(2):147–157
5. Lott JL (1964) Crack propagation in plain concrete. University of Illinois aUrbana-Champaign
6. Königsberger M, Pichler B, Hellmich C (2014) Micromechanics of itz-aggregate interaction in concrete part ii: strength upscaling. J Am Ceram Soc 97(2):543–551
7. Simon KM, Chandra Kishen JM (2018) A multiscale model for post-peak softening response of concrete and the role of microcracks in the interfacial transition zone. Archive Appl Mech 88(7):1105–1119
8. Zhang Y, Wang Z, Zhang J, Zhou F, Wang Z, Li Z (2019) Validation and investigation on the mechanical behavior of concrete using a novel 3d mesoscale method. Materials 12(16):2647
9. Keinde D, Kamali-Bernard S, Bernard F, Cisse I (2014) Effect of the interfacial transition zone and the nature of the matrix-aggregate interface on the overall elastic and inelastic behaviour of concrete under compression: a 3d numerical study. Eur J Environ Civ Eng 18(10):1167–1176
10. Kim JJ, Taha MR (2014) Experimental and numerical evaluation of direct tension test for cylindrical concrete specimens. Adv Civil Eng 2014
11. Reinhardt HW (1984) Fracture mechanics of an elastic softening material like concrete. HERON 29(2):1984
12. López CM, Carol I, Aguado A (2008) Meso-structural study of concrete fracture using interface elements. i: numerical model and tensile behavior. Mater Struct 41(3):583–599
13. Dutta S, Chandra Kishen JM (2018) Role of aggregate debonding on the tensile response of concrete: a micromechanical approach. Eng Fract Mech 199:518–531
14. Chen H, Sun W, Stroeven P, Sluys LJ (2007) Overestimation of the interface thickness around convex-shaped grain by sectional analysis. Acta Materialia 55(11):3943–3949
15. Case ED (1984) The effect of microcracking upon the poisson's ratio for brittle materials. J Mater Sci 19(11):3702–3712
16. Zimmerman RW (1985) The effect of microcracks on the elastic moduli of brittle materials. J Mater Sci Lett 4(12):1457–1460

Effective Management and Implementation of a PRA Project for a Safety Critical System

Saily Varde and Prabhakar V. Varde

1 Introduction

Initiation, performance, and execution of a Probabilistic Risk Assessment (PRA) project for a complex system requires an organized approach for ensuring application of state-of-the-art tools and methods, high quality of data/information and deliverables that are in line with the scope and objective of the project [1]. Information, resource management and review are crucial for efficient and effective utilization of resources and completion of the project activities in coordinated and timely manner. An effective management framework is a key to any project success, in terms of deliverables within given time frame. It is also expected that the study is effectively utilized for addressing and managing real-time safety and other performance related issues.

PRA and its extension as risk-based/risk-informed are finding wider applications in many safety-critical systems, like nuclear plants, space systems, process and chemical plants etc. [2]. Further, there is an increasing interest in application of PRA methods in industries which have hazard potentials, like waste processing and management, aviation, thermal power plants, railways, and other industries. PRA is being considered for addressing issues in operations and maintenance management as well.

PRA studies have become an establish tool complementing or supplementing the traditional deterministic approach as part of integrated approach to safety analysis study to complement or supplement the relatively traditional deterministic approach.

S. Varde (✉)
Westinghouse Electric, Mumbai, India
e-mail: saily23varde@gmail.com

P. V. Varde
Bhabha Atomic Research Centre, Mumbai, India

Safety Critical Lab, IIT Madras, Chennai, India

However, in recent times PRA applications are finding real-time applications in siting, design, operations, maintenance and regulatory reviews and even life extension and regulatory licensing [3]. For developing a PRA model that caters to wide range of application, requires an approach wherein, during early project stages initiations itself the potential areas of applications are identified, such that analysis go beyond demonstrating the safety objective. The PRA development experience suggested that scope, objective and future applications should be identified well before initiating a project such that the resources spent on the project are more effectively utilized.

2   The Challenge

There are many references on PRA methodology that can be utilized as PRA guide [4], however, the open source hardly provides a reference that help develop a PRA project charter or project report. For example, the IAEA Safety Guide SSG-3 on development and application of Level 1 Probabilistic Safety Assessment is one of the major source that provides guidance on the conduct of a PRA project [5]. The NASA document on Probabilistic Risk Assessment of Space systems provides for a guidance document on PRA application to space systems [6] (Fig. 1).

The Safety Critical System Lab, at IIT Madras has PRA activities as one of the major thrust areas. Even though the primary focus has been R&D (on development of

Fig. 1   A nuclear power plant site image [7]

Fig. 2 Typical level 1 PRA report for a nuclear plant runs into over 1200 pages

advanced tools and methods, primarily to reduce uncertainty in the results, conclusion and recommendation of a PRA study), efforts are also on hand to provide risk assessment and management services to industry in general and safety critical systems (like aviation, space, chemical and process, shipping, nuclear industry, etc.). It is recognized fact that PRA projects are resource intensive—an expensive preposition. Often the uncertainty involved with initial projection in respect of objective, scope, process, methodological framework, source of data and associated analysis, in general and use of PRA in risk-informed applications [8], hamper the project management activities. The net results are, adverse effect on project in terms of frequent change applications and their management that might lead to repeated extension requirement for the completion of the project, compromised quality of the study, often limited or no application potential at more than one level and eventually higher uncertainties in the end results etc. These situations may prohibit application potential of the project (Fig. 2).

This can better be appreciated with one single observation that a Level 1 PRA reports, for instance a nuclear power plant, often runs in a couple of thousand pages, comprised of an executive summary, Vol 1—Main report containing major features of the project strategies and approaches, Vol 2 General Facility Description, Vol 3 Accident Sequence Analysis, Vol 4 System Analysis, Vol 5 Data collection, Analysis and Quantification, Vol 6 Human Reliability Analysis, Vol 7 Uncertainty and Sensitivity Analysis, Vol 8 List of Cut-sets, Vol 9 Major Assumptions, Discussion, results and interpretation of the results. Appendixes. The above description is for a PSA of a plant having ~ Initiating Events, over 10 Safety Systems and over 35 human actions at plant and system level. It is worthwhile to mention that if there is requirement to develop a PRA essentially using plant specific data, then a heuristic can be considered that a significant resources in terms of time and human efforts—at least 50% of total project resources might require for generating and plugging as part of quantification of the PRA model.

This is just to convey complexity of handling, a PRA project. Data and information development and integration of models might run into pages. Although performed in

a professional software environment, documentation, change and upgrade management rationale to name a few makes the project development and management activities a complex task. Needless to say, these activities have challenges in an organization when a new model is developed for the first time. As the learning enriches the project duration also reduces on one hand, while the new insights and compliance in due course of time keep the project team on tow.

The experience gained on development of PRA management model was thought proper to develop a management framework for PRA projects such that the project can be completed meeting the objective in targeted timeline, while sticking to scope and objective of the project. Further, the framework must ensure provisions for project scope expansion and considerations for any change requests (Fig. 3).

3   Major Features of a PRA Project—A Brief Overview

It is a well-recognized fact that 'Risk' is an integral component of any activity be it social, engineering, healthcare, transport or even social service and politics, etc. This paper focuses on complex engineering systems. PRA project for complex engineering system deals with development of a PRA model of the plant towards providing the statement of 'risk potential' from the plant. PRA is performed at three levels.

   (i) *Level 1 PRA*—Plant system analysis towards providing the statement of core damage frequency (CDF/year) estimates,
  (ii) *Level 2 PRA*—Deals with takes plant damage states as seeds and extend this input for containment scenario modelling for evaluation of various source terms towards providing the frequency of release/year.
 (iii) *Level 3 PRA*—Environment modelling to evaluate the overall risk by postulating fatalities and health impact in public domain. i.e.

The modelling activities involve graphical tools like fault tree and event tree analysis [9]. Generally, event tree and fault tree modelling are employed for accident sequence modelling respectively. Since the developmental activities involve modelling of complex and large event and fault tree methods, professional and bench marked software environment that include, some of the popular PRA tools, like Isograph, Item and RiskSpectrum, CAFTA, etc.) while extensive work is being performed to facilitate advanced features that include dynamic PRA, simulation platform etc. where the physics-of-failure/mechanistic approach is integrated with probabilistic approach, web-based features are facilitate improved environment for uncertainty modeling and analysis.

There are major procedural steps for development of complete PRA as follows.

  (1) Development of Project report/charter.
  (2) System familiarization, and identification of resources.
  (3) Hazard identification of applicable initiating event and safety systems.
  (4) Development of event tree.
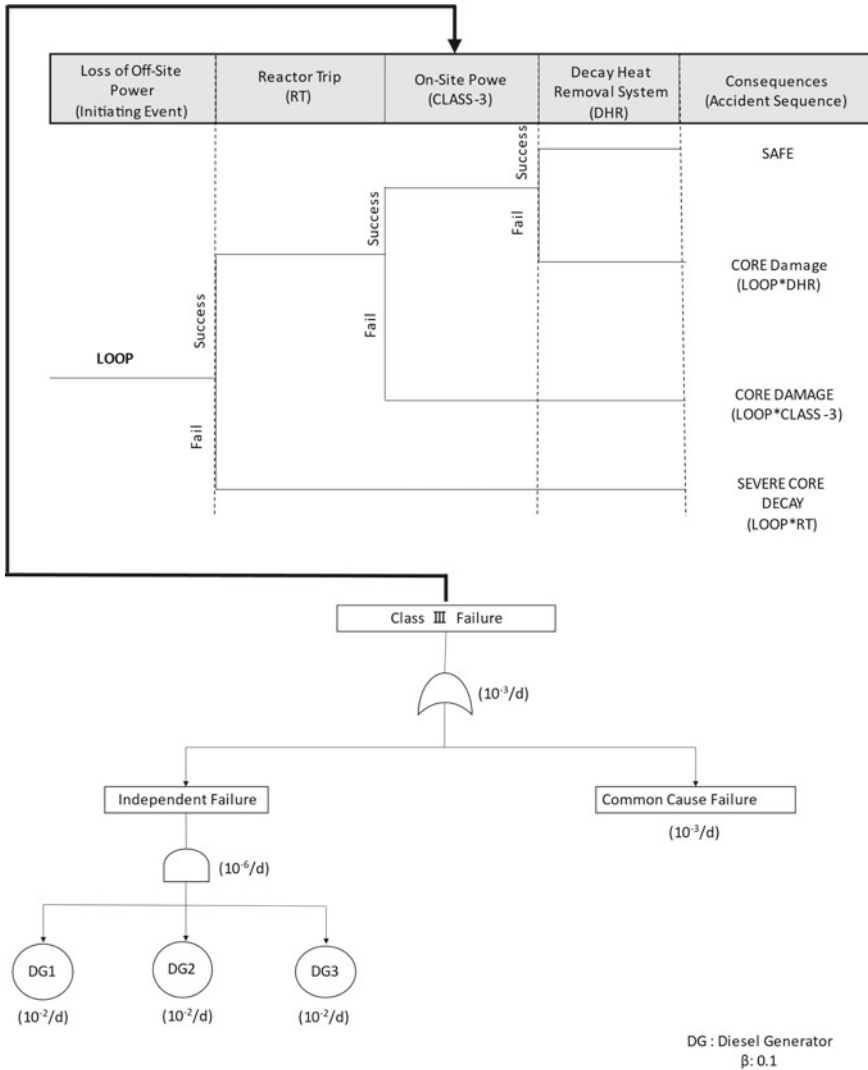
Fig. 3 Event tree and fault tree integration in PRA—a simplified illustration of loss of offsite power in nuclear power plant

(5) Development of fault tree for safety and safety support systems.
(6) Data collection and analysis for generating the failure probability analysis.
(7) Qualitative analysis and identification of minimal cut-sets.
(8) Identification and modelling for special features like common cause failure (CCF), human reliability as part of event sequence and system modelling.
(9) Quantification of the model.
(10) Uncertainty and sensitivity analysis.

(11)   Documentation and preparation of the PRA report.

Some of these activities and their dependencies as also relations have been shown in Fig. 5.

4   Major Considerations Before Initiating a PRA Project

The project complexity is a function of various factors like (a) Use and application of the level of innovation using advance technologies like passive systems, digital technologies, simulations, human reliability, uncertainty analysis, etc., that directly require research and development input and thereby additional time for scheduling and fallback provisions, if the results are not as intended, (b) System complexities in terms of number of systems and their interactions, for instance, modelling it for power in the range of from tens of MW research reactor is relatively not as complex as modelling for thousands of MW PWR as there are additional cooling systems, steam, turbine and feedwater system, requirement for cooling tower or ultimate heat sink (c) Team expertise level: A team of freshers will certainly require training and time even if the team leader is experienced person, (d) Dependability on the data and information—this aspect often determines the uncertainty level in final results. For instance, if the plant is in design stage, then it is given that the PRA model will be built using generic data (either available in national and international handbook or data from other plant), but if the PRA is being done during the operational phase of the plant, then considerable effort will go into data collection and analysis. However, the adequacy of the data will determine the requirement of data from other sources and thereby application of mathematical technique like Bayesian updating [10] for obtaining the best estimate of the available limited data, (e) Availability of an efficient and effective PRA software—this requires software capability to address PRA requirements. For example, software provision with efficient data assessment and management modules, option for Common Cause Failure (CCF) analysis and suggestions of CCF factor based on Physics of Failure (PoF) [11] modelling, its dependency on system design, layout and human interaction is expected to save modelling effort and chances of error. Further, the scope of the project for example, has been found to affect the project not only to its time and scheduling complexity but might require expertise depending on the scope of the project. Generally, during initial stages, PRA is performed considering the Limited Scope Level 1 PRA, that deals with creation of Level 1 PRA[] with consideration for internal initiating event, full power operation and reactor core as the source of radioactivity while giving due considerations for human factor [12], uncertainty and sensitivity [8] modelling towards a primary aim to identify the strength and weakness in the design and operation of the plant. However, more recent experience has been on requirement on performing full scope Level 1 PRA [13] by extending its scope from limited scope PRA to including low power and shutdown, and external events viz, seismic, Flood PRA etc.

Often regulatory authority makes Level 1 as mandatory and Level 2 PRA desirable—the case in point is regulatory requirement in India [14]. The available literature shows that Level 1 PRA has been performed for most of the plant as also Level 2 PRA are being actively completed. There are very few countries actively working on Level 3 PRA.

As can be the PRA project scope is a major factor that determines, time, resources, expertise, and other factors. Further, a typical lifecycle of an engineering plant, in terms of timeline or progress of work, might start from siting, conceptual, preliminary design, regulatory approval, commissioning, operation, ageing studies to support life extension Programme and finally decommissioning. At the outset it is recommended that a PRA project should be started as early as possible, i.e., during the siting/conceptual stages itself as site characteristics have significant impact on safety of the plant and its effect on the public domain during potential accident cases. Therefore, the objective of the project should be set very clearly and unambiguously right during initiation of the project.

The best strategy is to have clarity on requirements in respect of scope, objective, resource, timeline, schedule, coordination and communication of activities within and outside the PSA task group. This can be done by developing a PRA project charter or project report. This charter/report helps not only task group members but also the management, the field staff, design team and operation, safety agencies to better appreciate the project and what is expected from an agency (which is not directly involved in the project but having role to support the work).

5 Project Charter for Implementation of Integrated Management Approach to PRA

The following section will present an overview and salient features of a project charter as a prerequisite for a PRA project. As can be seen from the discussion that the process of developing a PRA study involves implementation of technical, R&D support, organizational framework and human resource management, particularly expert services, quality assurance, services support and coordination and communication with internal as well as with outside groups agencies.

For ensuring effective and efficient implementation of project activities of PRA project an Integrated Management System is required to be established by development of a project charter entitled an Integrated Management approach which may include aspects like project objectives, project scope, risk, quality criteria, and goals during the initiation of the project itself. In the following section, the experience and insight on development of PRA projects has been discussed.

The motivation for proposing the integrated management approach for PRA is based on the experience with not only PRA projects but also a range of scientific and developmental projects. The formulation of an integrated management framework is part of the Detailed Project Report of a PRA project. Accordingly, Fig. 4 shows

the major elements of Integrated Management Framework. The following discussion talks about the major feature of the projects that explains the dynamics of the project towards commissioning a PRA report.

Development of project report/project charter starts once the plant/organization's management provides official consent for taking up the project along with the board scope and objective of the project. Commitment of providing required resource and logistic support also forms the part of initial authorization. Often, designating a PRA expert having commensurate experience to lead the project is also identified bestowing authority for choosing a team for drafting a detailed project report.

The major elements of the detailed project report include motivation, a brief definition of the scope, objectives, and a brief discussion on the salient features of the plant (e.g., number of core safety features of the plant and process systems of
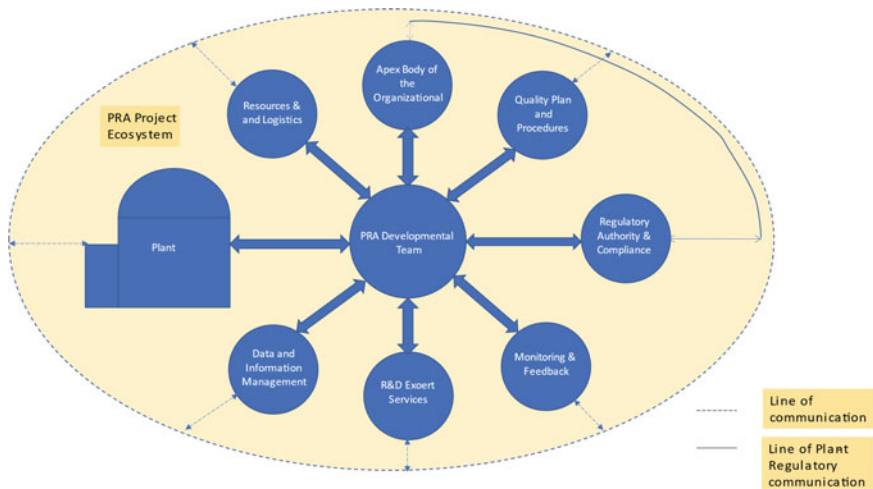

Fig. 4 PRA project integrated management charter

Fig. 5 Dependency metrics for project team efficiency

the plant, plant location and its seismic characteristics, general rainfall and flooding history, and a power failure frequency, etc.) Postulation of tentative number and size of the fault tree and event trees will be performed, plant life (if during operation) will be estimated such that an evaluation can be made regarding dependability on plant experience on reliability data, as also requirement of data from generic source. The project report also lists a preliminary list of initiating events and an approximate assessment on efforts required for detailed event tree analysis in support of accident sequence modelling. The quality control activities and criteria development should start right when the DPR (Detailed Plant Report) development starts. As mentioned, earlier there are ten major steps involved in modelling a PRA right from Initiating Event Analysis to documentation of the study and production of final report. Some additional steps are peer review and incorporation of the comments.

The DPR should also define the structure of the PRA team. The PRA team should include at least three PRA expert, one design/operation expert, Electrical and Process Control Engineer, data analyst, human reliability analyst, and a quality assurance engineer. The strength and expertise quotient of the team is critical to assessing the time required for completion of the project given the fact that many activities go in parallel, and the experience of the team also contribute to project timeline.

Based on the above information, the DPR should provide an activity chart or a bar chart that provides starting and end point relative to other activities. This chart should be revised dynamically such that an insight can be drawn on the activities that are adversely affecting the schedule. In line with project goals and objectives provision should be made for efforts required for special aspects of the project, like common cause failure, human reliability, uncertainty and sensitivity analysis.

A brief description of the software used for the analysis, that include PRA, statistical analysis, data assessment and management etc. should be provided. PRA software procurement requires time and many project activities cannot proceed in the unavailability of these software tools, therefore procurement of software, computational facility, PRA cell formation, support required from the plant on design, operation and performance assessment should be initiating immediately after submission of the project report to the plant.

The DPR should provide a format for the Executive and Main Report. Often a separate document is required for accident sequences and minimal cut-sets list and other annexure for example, a description of human reliability analysis procedure, Monte-Carlo simulation, Common Cause Failure Analysis strategies used in the project and even description of uncertainty and sensitivity analysis features should form part of the DPR.

The DPR should also provide a synopsis of the project in a brief. The report should not be more than three pages in a way that can be understood by management level such that, the DPR communicates the efforts and resources required for this project. The strength and weakness of the PRA analysis can also be discussed in brief.

The DPR is submitted to the plant's management for seeking official authorization to start the project, as also the stakeholders, like concerned plant divisions, sections such that right in the beginning of the project there is an awareness for kind of interaction and support will be expected from them. It is also recommended that

the DPR should be subjected for regulatory review so that many gap areas can be addressed right during the initiation phase of the project and provision can be made for the compliance—this aspect will reduce the project development and review time significantly.

A final project charter might run into ~ hundred pages, expected to be an asset as the project charter integrates all the PRA function and thereby sensitizes all the levels of staff regarding their possible involvement and what is expected of them.

Like any other project the activities in a project are distributed. Of course, in PRA project, the PRA team is central to development of the project. The activities are often, not only complex but also challenging in terms of interdependencies, new elements requiring scientific or technical first of kind solutions, advanced modeling in areas like human error, uncertainty analysis and finally treatment of qualitative input for final quantification. Therefore, an integrated management approach has been developed for a PRA project effective execution and completion. The following Section provides an overview of the project.

5.1 PRA Development

Dependability is one important aspect that affects all stages of the project from initiation to completion. Figure 5 shows that factors on which the functioning of the team depends, in terms of information and data, availability of qualified PRA software, Computational facility, staff (whether it is dedicated or part-time drawn from various other agencies), availability of guides and standards from national or international level, availability of quality assurance programme, regulatory expectations from the project, a system of internal review, etc. The PRA development is performed in various settings, like R&D, academic, industry, consultancy, etc., and each setting has its own pros and cons. Further, there are organizations or a group in an organization that are dedicatedly and perpetually involved in development of PRAs for similar or completely different systems.

In such organizations, if we see that new elements to a project is not significant, then development of PRA to an extent might mean employing an existing template and here the dependability of requirements of resources, are relatively less and staff involved in PRA development can be trained more effectively. But PRA project becomes challenging when the design and engineering and projected operations are much different compared to existing plant since new plant will have different level of science, engineering, fuel type, fluid characteristics, system enthalpies, and various safety provisions including shutdown and cooling modes. A case in point is Fast Breeder Reactor which is different compared to a thermal reactor, like PWR or BWR even though both are nuclear power plants—generating power. Even if considerable experience is available, PRA of a Fast reactor poses challenges, in terms of mode of cooling (active to passive mode of cooling), physical design and consequently core reactivity response evaluation, dependability on safety system, meaning of redundancy and diversity, and the definition of failure criterion. One of the

major insights is, relatively a greater number of assumptions made due to lack of data and information, new design and its postulated behavioral uncertainty. This requires a commensurate representation of uncertainty and robust sensitivity analysis such that operational technical specification captures and translates into safety limits—that need not be reached during the life of the plant, limiting condition of operation—if it reaches then plant should be shutdown, limiting safety systems settings that requires regulatory review, etc. The PRA model should be capable to address the capability for technical specification evaluation for new as well as existing plants.

5.2 Apex Organization

There are two important aspects where the apex body of the organization must play active role (as the success of the PRA project depends on the higher role of the apex body). First, to provide the official mandate to perform the PRA often by defining the objective, scope, and purpose for which the PRA study need to be developed. Second, the PRA performance process should be integrated with the organization chart by delineating the line of authority and communication. Additionally, It should also direct the plant responsible agencies to define the role and responsibilities of the kay staff for example, PRA team leader, Operations/Design team head, maintenance and services team head such that regulatory reviews and compliance nodes are defined. The Apex organization also states the commitment to logistic and revenue provisions. Involvement or oversight of apex body is critical to success of the PRA project.

5.3 Quality Plan and Procedures

Development of quality assurance, attributes, criteria, plans, procedures and application of the same at strategic and well-defined epochs during the project is a key to not only the quality level of the product but also provides, transparency, check on compliance to the set criteria, etc. Quality assurance activities can broadly be divided into two parts, the PRA procedural and other management attributes like documentation, monitoring and software and hardware system deployed to support the project.

There are two major sources for setting and verifying or grading the procedural aspects of the PRA quality document/standards, viz., ASME/ANN PRA standard [15] and IAEA-TECDOC-1806 [13]. Both the approaches define quality attributes at two levels, viz. IAEA refer the two level as general attribute and special while the ASME refer them as high and supporting level requirements. In both the cases the lower-level attributes is a sub-set of upper-level attributes. These attributes or requirements are referred here as quality attributes. These attributes are developed for each of the procedural element of PRA.

Here we will discuss IAEA quality attributes and its application. IAEA attributes have been developed in 12 major steps in Full Scope PRA. How these attributes are implemented and how they are evaluated is a question. Further, how this insight is used are some questions to explore. First, the analysis for given procedural step identifies the applicable attributes from the IAEA reference followed by preparing a checklist. This checklist is attached at the end of the document. For example, for the task 'Initiating Event Analysis' (IE), considering the Task A, accordingly the IE-A01 is a general attribute and under this general attribute, a special attribute (S1) is identified, coded as IE-A01-S1. Finally, all the attributes along with their grading provide a statement of quality level of the procedural element of PRA, here IE. These checklists forms part of each individual document of PRA element and helps further reviews including regulatory review for a given application.

Other quality aspects are software quality, documentation quality, lab accreditation etc. For software quality assurance, vendor as well as the PRA team members should certify the quality levels by performing benchmark cases. For documentation either the internal documentation system meeting quality criteria, or other international standards like ISO-9001 system should be used. To ensure laboratory quality accreditation, the certificate of the lab and associated equipment, like calibration and certification from a recognized governmental or non-governmental service should be performed. For example, the reliability, accelerated life test, vibration testing labs should be having a valid accreditation certificate.

5.4 Monitoring and Feedback

Project progress monitoring by employing standard techniques like Gantt-chart, often supported by PERT and CPM (Programme Evaluation and Review Technique and Critical Path Method CPM) approaches provide an effective schedule monitoring, evaluation/review and correction/modification as part of project schedule and resource management. These techniques are used for to organize, schedule and monitor the progress of the project. These techniques are graphical approaches to visualize project progress, inter-dependencies among activities and monitoring of progress of work and thereby provide strategic solution by allocation of resources for improved management of resources. For instance, the CPM draws the team attention on the element falling in critical path among other parallel and dependent activities.

Keeping in view the major PRA project requirements a simplified Gantt chart has been developed and shown in Fig. 6. As can be seen this chart has been developed for Level 1 limited scope PRA that has a schedule of ~4 years. Development of project charter, plant familiarization, documentation and quality assurance—that starts with development of QA plan starts right simultaneously at start time into the project. The data collection activity can only be started after plant familiarization while hazard analysis can be started as soon as the initial information is available. Two activities, i.e. documentation and quality assurance which start with the project and almost perpetual throughout the project as every activity of the project require QA and
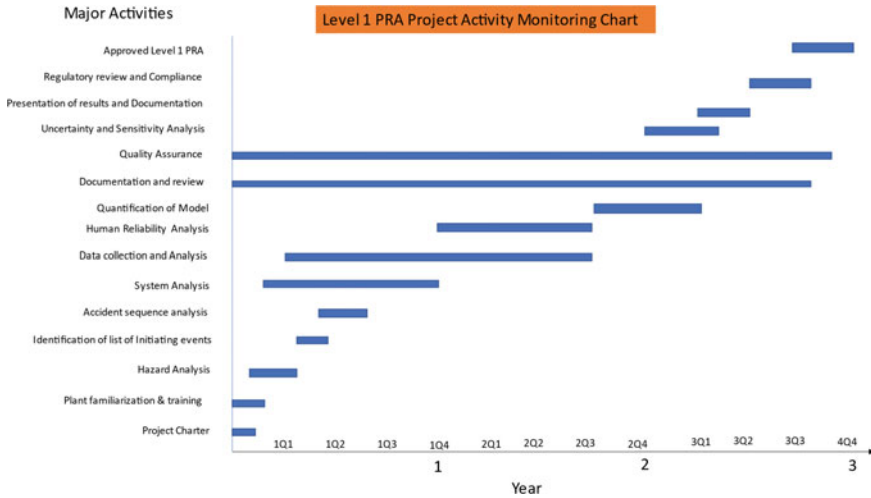
Fig. 6 Project activity scheduling and monitoring chart

Documentation. The project concludes with regulatory review approval as shown on top bar-line and marks conclusion of the project.

Along with this the project risk monitoring is vital for the success of the project. The parameters that are tracked for their risk potential are, budget and finance, tools, and methods (software limitation, credibility of test results, team motivation, compliance etc.) used in the project, human resource capability, expertise and any other factor (from inside or outside) need to be monitored.

5.5 Information and Data Collection Analysis and Management

In case, the PRA is being performed for an operating plant or if the quality criteria set higher utilization of plant specific data, then activities involved in data and information collection and analysis is time and resource consuming preposition. It is a recognized fact that converting raw information into reliability data, especially when the information is either not complete or inadequate, poses challenges. As availability of data/supporting information and background reflects in the statement of uncertainty.

Here, developing and implementing an integrated data collection and analysis system provides an effective solution. The major challenge is communicating reliability expert's wish list, or the minimum information required to translate the information/data into reliability estimates. Since, the system is being developed for operational PRA project, inputs like failure mode, failure criteria, type of failure (Independent or CCF/Safety or Operational) becomes useful for developing an application

of PRA. Therefore, a computerized data collection system can effectively meet these challenges. Another, flip side is, if too much information is requested in computerized system, then the operational staff, feels discouraged to forward to the form to PRA team, therefore, there should be a balance as also backup systems to resolve the gap. For example, monthly meetings between PRA team and data analysts with the operations staff go a long way to resolve the issue.

Certain provisions, apart from failure estimates, like characterization of associated uncertainties, mathematical solution to combining plant specific data with the generic data, e.g., *Bayesian updating* forms a vital component data management system [10]. Record of incidents and associated data, particularly the root cause analysis of human errors and common cause failure is a key to developing quality PRA.

5.6 Resource and Logistics

The availability of resources and logistics are vital requirements for successful completion of a PRA project. First and foremost, the trained human resource that include at least two members of the team should possess higher qualifications in related safety and reliability domain. PRA modelling requires knowledge of reliability and statistical tools and methods. Among these one should also be a Ph.D. in reliability, quality and/or safety or in related field. The availability of lab and computational facility along with bench marked PRA software, Statistical analysis, HAZOP, Root Cause Analysis, Risk-monitor software are must as software-based simulation for sensitivity analysis and fine tuning of the PRA model iteratively, are some of the integral activities of PRA project. A professional reliability data and information management system (either as part of PRA software or a separate self-standing module) is vital for analysis, data collection and processing activities.

The following metrics relates PRA project complexity to human resource requirement (Fig. 7):

Human resource	Project Schedule (Yr)	Project Complexity in terms of design and PRA modelling			
		Highly Complex	Complex	Modest Complexity	Low complexity
	7	6 years	5	3	2
	5	6.5	5.5	4	2.5
	3	7.5	6.0	4.5	3
	2	8.0	6.5	5.0	3.4

Fig. 7 An indicative schedule—for complexity versus available human resource

Selection of PRA software: A thorough market survey is required as part of the procurement procedure. Software requirement for the software vis-à-vis utility criteria need to be evaluated with cost, can provide an effective metrics for software evaluation. For instance, if the PRA project is only limited to safety assessment or the scope extends to application of this software for routine operational deployment, like living PRA or in support of risk monitoring, or technical specification optimization, etc. Further, the scope of PRA also dictates the software requirements (like Level 2 PRA requires thermal hydraulics, structural analysis as part of containment modelling and Level 3 PRA requires atmospheric dispersion modelling and evaluation of consequences in public domain). Similarly, when the study moves from Limited scope to full scope by extending the PRA study to include Seismic RA, External Flood PRA, impact of outside object, etc. the project software cost and complexity of the software modules also increases.

5.7   Regulatory Review Vis-a-Vis Compliance Tracking

Effectiveness of regulatory reviews, oversight and compliance quotient tracking along with corrective action programme performance management is an integral part of risk-conscious culture. Generally, regulatory review process follows defense in depth approach that implies to more than one check. Therefore, depending upon the safety significance of the case in question, there is a provision of three-tier review. PRA document depending upon the significance attached might follow three tier review.

Regulatory review is generally a time-consuming process. Here, the availability of quality attribute and the prior approval of DPR can significantly reduce the time as also overall effectiveness of the review process. Therefore, a checklist containing the items for applicable attributes and corresponding grading in fact help decide regulator about the strategy to be adopted, considering the safety significance of each item in the checklist. Often, at the outset, based on the initial review of the checklists enable regulator to take a decision whether to go for detailed review and refer back the PRA to plant with major limitations of the existing PRA study. The initial review of the DPR and checklists is a win–win strategy for both the regulator as well as for the plant as there is an understanding about the broader aspects like depth of the analysis, methodology, considerations of assumptions and use of data and information, etc., are some of the major aspects.

The regulatory teams are highly experienced in subject matters and decision making based on the facts and figures presented along with additional insights and finally ensuring compliance of the subject submission. Here, it may be noted that the facts and figures often adding adequacy or completeness of submission and taking contingence of overall state of affairs is critical to overall effectiveness of regulatory review. For example, regulatory agencies find inadequacy of data and associated uncertainty as one of the weaknesses as an issue for action or compliance. Here, the plant authority should proactively indicate this gap areas, if it exists in the study and

therefore a rather universal view (in the context of the document) of the submission for every issue pointed by regulator is the best practice towards achieving higher quality levels of the PRA document.

The experience suggests that the review of PRA is based on the comments received, actions for compliance can be implemented in parallel such that if not all, the major part of the study can stand compliant and with completion of additional efforts for remaining compliance items are available for regulatory approval.

6 Agent Based Approach to Project Management—A Proposal

6.1 General

The peer review of the work suggested exploring the potential of Agent Based approach to PRA project management. Even though the Agent Based Management approaches are increasingly being used in software [16] and control industries/ applications where all the individual agents work in a dynamic to a large extent in a closed loop and concurrent environment. Yada and Varde developed an intelligent agent based operator support and beam orbit control scheme for Indus-2 accelerator for synchrotron radiation [17]. The tuning of accelerator for getting the desired electron beam position and angle at the source point is a time consuming and regular job done during commissioning of new BL or when accelerator is operated at new operating point. This work presents a novel intelligent agent based operator support and beam orbit control scheme for accelerator control. In fact, one of the major benefit of agent based approach is that the agent based model of the project offers a platform for simulation which has potential to study impact of many project activities on its schedule, quality and resources, etc. However, the observation is that an intelligent element in an agent enhances the benefits as many computations that involve uncertainties and human factor induced elements can better be captured in intelligent approach where the formal mathematical models may not be very effective. Ourdev et. al have proposed initial steps for an Intelligent agent-based approach to adoptive project management to implement belief-desire-interaction to individual agent modeling [18]. This approach has been demonstrated on a real-time monitoring for a tunnel boring system that helped managing the project timeline.

6.2 The PRA Project Characterization

The major characteristics of a PRA project which distinguishes it from other projects are as follows:

1. Modeling requires an approach as applicable to safety critical systems.

2. The PRA project requires management of two major categories of risk, viz., the core risk estimation for the subject safety critical system and second the project management risk.
3. A PRA software environment facilitates the core modeling and simulation functions.
4. There are no closed loop operations in the project that impact its requirement or function.
5. Data modeling analysis on hardware, software, and human as also institutions impact the quality of the project.
6. The objective, apart from project risk, is evaluation and prediction of the plant/ system and component risk potential. That implies project time line, risk in terms of financial, traditional industrial even though requires attention; the accuracy of prediction in terms of acceptable risk is the major objective.
7. The knowledge base component is a dominant factor, skill-based and rule-based component is captured by the PRA software tool.
8. R&D input even though low, often impact the quality of the output.
9. The design and operations expert form the part of the project comprised of 2–10 experts depending on the nature and complexity of the project.
10. The final PRA provides the core framework for a Risk-monitor/Living PRA that supports operations and design optimization studies.
11. The PRA project requires a integrated, distributed and a concurrent with a fairly strong communication and coordination protocol for implementation.
12. Timely generation of requests for experimental and R&D component is desirable for PRA project.
13. Decision making forms part of final iterations in support of uncertainty and sensitivity analysis.

6.3 Core Modeling Formulation Elements

Keeping in view the above, the following section provides the framework of a intelligent agent based system for a PRA project.

1. The PRA framework discussed in Sect. 5 provides the reference model for implementation of agent based approach for PRA project.
2. The conflict resolution strategy to problem solving for intelligent or linear/non-linear functions are either rating through importance measures/additional input or data/deliberative based depending on the situation.
3. The common thread that runs though all the agents is use of experience in designing the basic building blocks—the agents in the architecture.
4. Capability to handle quantitative or qualitative data at agent level.
5. Project eco-system is deliberative and opinion where the qualitative information/input is at the core. A fuzzy logic approach is adopted for handling linguistic variable for obtaining the quantitative estimates in support of decision making,

6. The objective of this paper is modeling for project risk management. For modeling the project risk, modeling is performed first, for project reliability.
7. Further inference of probability of non-performance of project individual objectives/functions
8. Evaluation of consequences in terms of overall impact and
9. Decision on action required to mitigate the risk impact.
10. Feedback on the impact of the action, by surveillance, monitoring, periodic evaluation, and prediction

Implementation of PRA project management requires a highbred approach that involves development of intelligent and normal agent.

6.4 Intelligent Agent Based System Model

6.4.1 General

Even though, the agent based approach framework is complex due to size of the project, due to distributed architecture, iterative and recursive and exhaustive internal and regulatory review functions involved in development of a PRA study, this section presents essential higher level functions only. PRA project is a data intensive work and might involve ANN or deep learning involving Bayesian estimation towards reducing uncertainties in data, intermediate (system level) and final (plant) level results. The following sub-sections provide a simplified approach to agent based management of PRA project.

6.4.2 Adoption of General Framework to Intelligent Agent Based Modeling

The agent-based approach gets its power from software tools that can model and an environment, process, or activities in an integrated manner through conventional or intelligent program such that business can be performed through a more transparent, deliberative and integrated manner. Intelligent agent can be defined as computer program that can exhibit its behavior like human, in terms of learning and training itself the patterns, logical operations using the sets of data, and draw inference in an autonomous manner to meet the objective function. The outcome is agent-based approach makes the industries and R&D environment very effective and efficient. Apart from input and output functions the agent has memory short-or long-term memory as also learning capability facilitated by intelligent modules involving machine learning approaches ranging from simple Artificial Neural Network to deep learning that might include more than one hidden layer to cater to complex computational or prediction capabilities. In this paper the major input to the intelligent agent-based framework has been derived from the PRA.

Project Integrated Management Charter given in Fig. 4. The modules in this chart have been shown as integrated at the central module dealing with PRA team. However, keeping in view the formalism involved in an agent-based approach, the special characteristic of each agent along with its connection and communication have been covered at higher level only. All the agents do not require to be having intelligent capability. Communication and coordination protocol requires facility to implement the iterative approach as also recording of each session particularly the set. For demonstration of development approach for agent-based approach, Fig. 4 has been considered as representation architecture of the agent- based approach to PRA risk management along with their communication and coordination protocol.

The Intelligent Agent Based Framework shown in Fig. 8. The major advantage of distributed as also integrated framework is that the major administrative, planning and monitoring function that require cognitive component like perception, reasoning and diagnosis can be allocated to one Apex agent. The PERT approach for scheduling tasks, fuzzy algorithm for natural language processing and ANN for prediction of evolving scenario for complex non-linear functions provide an effective mechanism for implementing the corrective action or mitigation activities. The information flow and periodic updates keep the PRA team focused on the critical paths as also for other teams. The facility is the source of data and based on the feedback the agent objective is to provide quality input to avoid uncertainty and inaccuracy in data collection and further in analysis.

The following section will provide information on essential structure of a typical agent various function and processing as also storage of information.

6.4.3 Typical Agent

Unlike in an industrial environment, in a PRA project management the project and technical activities for the plant can be seen working like an integrated eco-system. Therefore, an agent function can be divided into two major categories, viz, project risk management and technical risk management [19].

The common component of a typical agent are input, processing, validation, Output, risk and uncertainty and operator-agent-interface module and connecting internal threads for intra-module connection and communication module. Further, there are core or process functions and evaluations, e.g. for a PRA technical activities, after data analysis and verification, the PRA modeling forms the process/core i.e. modeling activities as can be seen in Fig. 9. The processing/analysis function could be analytical, logical, computational or even intelligent to a complex set of operations involving one or many of these functions Agent also offers working platform for an experienced as also a freshly trained staff. For example, the agent offers default functions, data, assumptions for training the fresh staff. The validation function might cater to the quality of data, of reference, session specific input and output as also assumptions for final assessment of sensitivity analysis.

The project progress monitoring at agent level is defined by agent reliability metrics as follows:
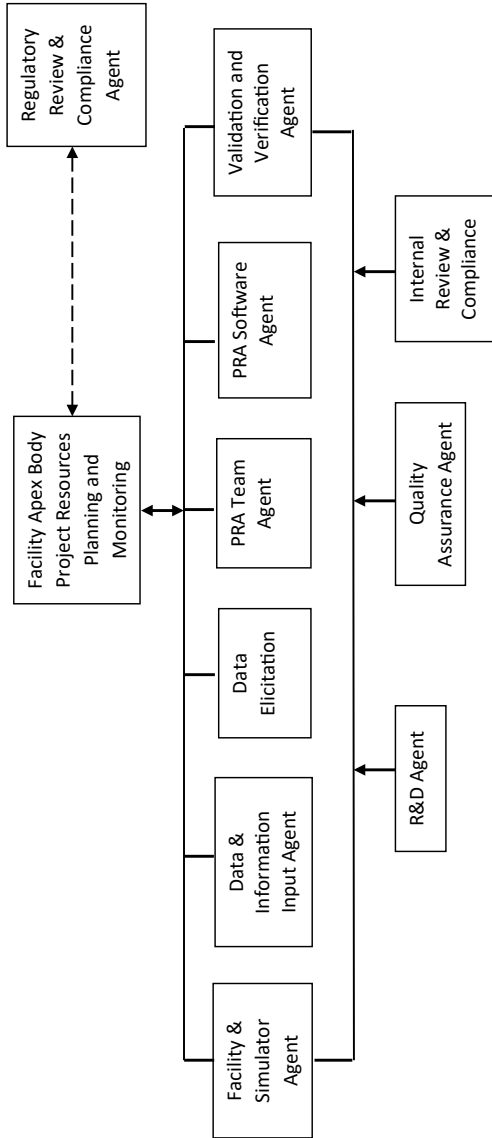
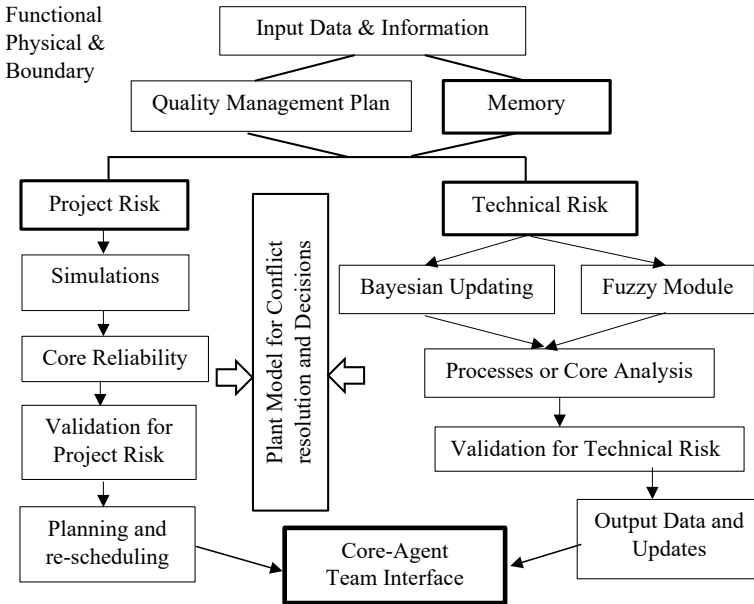**Fig. 8** Typical framework for an agent-based approach to PRA project

Fig. 9 Typical agent configuration module

$$R_A = f(q, t, s)$$

Agent reliability R_A is a function of

q ratio of achieved quality to desired quality of work;
t ratio of time required to completion of the project to projected time-line.
s   Ratio of available resources to desired resources.

Agent level failure probability can be given by

$$F_A = (1 - R_A)$$

This formulation can be used for estimating the reliability for independent agent module and aggregating the agent reliability to project reliability or conversely the project failure probability. Project unreliability or failure instances introduces a penalty in terms of deliverables or compromised quality or delay in development of plant or design applications. It is desired that Project risk due to not meeting the schedule comprised quality, etc. should be evaluated, to a great extent in a dynamic manner as follows:

$$P_R = \sum_{i=1}^{n} (F_{Ai} * C_{Ai})$$

Conflict resolution in a project scenario is a complex function, unlike in technical risk modeling, therefore a deliberative or an intelligent approach like Machine learning approach with appropriate rating and additional input are considered adequate for resolution.

7   Final Remark

PRA projects deal with work at many levels, that include general activities like information and data collection, plant walkdown, reference to deterministic analysis, design, and operational documents, as well as modelling of the plant, employing risk and reliability methods, R&D activities often with new elements, like modelling of passive system or digital system modelling, challenges modeling related to structural systems that might include reactor core and fuel etc., and finally communication and coordination of various aspects of the activities. Given this background a distributed and integrated management approach is required for not only successful completion of the project but also to achieve higher quality levels in the PRA project.

The experience suggests that a PRA project is a complex activity that requires additional elements like all or higher component of skilled manpower, R&D support as also a dynamic interface with the plant requires special attention for project. As an project management framework requires dealing with project as well as technical component. Application of an Intelligent Agent Based approach requires an attention as the agent-based approach has worked very well in other typical project environment. Therefore, this paper develops a basic framework for application of intelligent agent based approach to a PRA Project. The authors could not find any literature on PRA project management through an intelligent agent based approach, this paper develops a framework for application of intelligent agent based approach to risk management. The initial experience has been that agent-based approach has potential to cover the gap areas in the conventional or traditional approach to project management, like lack or communication, limitation of deliberations, inadequate procedures to use qualitative input, and handling of non-linear or conventional mathematical functions.

References

1. IAEA (2010) Development and application of level 1 probabilistic safety assessment for nuclear power plants, SSG, IAEA, Vienna
2. Varde PV, Pecht M (2018) Risk-based engineering—an integrated approach for complex engineering systems. Springer, Singapore
3. Varde PV (2012) Development of an integrated approach for life extension and licensing of ISOMED—a Co-60 Based Irradiator. Nuclear Engineering and Design
4. Stewart MG, Robert EM (1997) Probabilistic risk assessment of engineering systems. Chapman & Hall, London

5. International Atomic Energy Agency (2010)Development and application of level 1 probabilistic safety assessment for nuclear power plants, Specific Safety Guide SSG-3, IAEA, Vienna

6. NASA (2011) Probabilistic risk assessment procedures guide for NASA managers and practitioners, NASA/SP-2011-3421, 2nd edn. NASA headquarters, Washington DC

7. https://1.bp.blogspot.com/-7wvCcgZ2TCI/X5FBDMW76KI/AAAAAAAABJY/AtSolMorz mMVx4SDLwxTKsdrvpsT9AZpACLcBGAsYHQ/s650/Nuclear%2BPower%2BPlants% 2Bof%2BIndia.jpg

8. U.S. NRC (2009) Guidance on the treatment of uncertainties associated with PRAs in risk-informed decision making, NUREG-1855 vol 1. NRC, Washington D.C.

9. Modarres M (1993) What every engineer should know about reliability and risk analysis. CRC Press, College Park

10. El-Shanawany AB (2011) A comparison of Bayesian analysis methods for reliability parameter estimation in PSA. IET, Manchester

11. Lindsey NJ (2021) OSMA digital evolution: R&M physics of failure (PoF) handbook. National Auronautics and Space Administration, 14 June 2021. Available: https://nepp.nasa.gov/wor kshops/etw2021/talks/14-JUN-21_Mon/1030_Lindsey-NASA-OSMA-PoF-Handbook-202 10017119.pdf. Accessed 28 Feb 2022

12. International Atomic Energy Agency (1992) Procedures for conducting common cause failure analysis, IAEA-TECDOC-648. IAEA, Vienna

13. International Atomic Energy Agency (2016) Attributes of full scope level 1 probabilistic safety assessment (Psa) for applications in nuclear power plants: IAEA Tecdoc No 1804. IAEA, Vienna

14. Solanki RB, Prasad M (2007) Probabilistic safety assessment of nuclear plants—a monograph. Atomic Energy Regulatory Board, 2005, 2007

15. ASME/ANS (2009) Standard for level 1/large early release ferquency probabilistic risk assessment for nuclear power plant applications. ASME/ANS RA-S-2008, The American Society of Mechanical Engineers, New York

16. Isakov D (2022) anylogic.com, 24 Nov 2022. Available: https://www.anylogic.com/blog/an-agent-based-approach-to-software-development-project-modeling. Accessed 14 Feb 2023

17. Yadav RP, Varde PV (2013) Intelligent agent based operator support and beam orbit control scheme for synchrotron radiation sources. Int J Adv Sci Technol 52:11–34

18. Xie OH, Abourizk S (2008) An intelligent agent approach to adoptive project management. Tsinghua Science and Technology, vol 13, no S1

19. Khoo YB, Zhou M, Kayis B, Savci S, Ahmed A, Kusumo R (2008) An agent-based risk management tool for concurrent engineering projects. Compl Int 12

Application of Probabilistic Risk Assessment Approach in Nuclear Power and Space Sectors

Janaki Devi Kompella, Karthik Ravichandran, and Vignesh Anandan

1 PRA and Historical Perspective

1.1 Introduction

Probabilistic Risk/Safety Assessment (PRA/PSA) is a comprehensive, structured, logical, and quantitative analysis technique to identify and assess risks in complex technological systems, to improve their safety and performance in a cost-effective manner [1]. PRA involves development of a fully integrated model of the facility, for identification of accident sequences that can originate from a broad range of initiating events (IEs), and determination of their frequencies and consequences. The event sequence progressions following different IEs are modelled using Event Trees considering success and failure of various safety and safety support systems that are required to actuate for mitigating the consequences of initiating events. The unavailability/unreliability of these systems is evaluated using Fault Tree Analysis (FTA) technique (a top-down deductive approach) wherein the undesired state of a system is identified and all possible basic faults such as component random failures, human errors, or other causes and their combinations that can cause the undesired state are determined. Software tools such as RiskSpectrum® PSA, CAFTA, etc. are used for development of event trees and fault trees and the overall PRA model of a facility.

J. D. Kompella (✉) · K. Ravichandran · V. Anandan
RELSAFE PRA Consulting Private Limited, Thane, Maharashtra 400607, India
e-mail: devi.kompella@relsafe.co.in

K. Ravichandran
e-mail: karthik.ravichandran@relsafe.co.in

V. Anandan
e-mail: vignesh.anandan@relsafe.co.in

A PRA study typically answers the three questions in the risk triplet shown in Fig. 1. These provide qualitative and quantitative insights into the operational risk and safety of a facility. Figures 2 and 3 provide a simplified illustration of the event tree and fault tree for an IE that can occur in a Nuclear Power Plant (NPP) and Spacecraft, and how these elements are linked.

The probabilistic approach uses realistic and best-estimate assumptions, combines expert judgement, and provides an integrated framework for addressing the uncertainties explicitly. The nuclear industry uses PRA and Deterministic Safety Assessment (DSA) as complementary studies to assess the level of safety throughout the life cycle of a NPP [3]—from conceptual design until end of service/decommissioning.

PRA is also actively used in Aviation, Space, Oil and Gas, Chemical, Transportation, Marine/Shipping industries, where safety and risk assessment are of paramount importance. While the fundamental concepts and methodological aspects of PRA remain industry neutral, the differences in technological aspects such as design of the facility/systems/components, site characteristics, types of hazards/initiating events, failure events, event progression, reliability data, choice of risk metrics, etc. must be
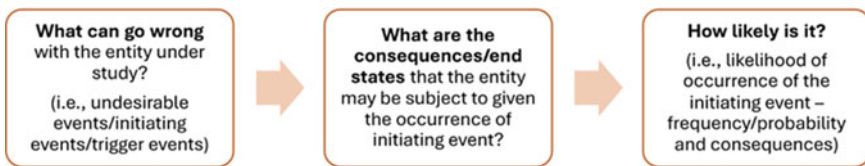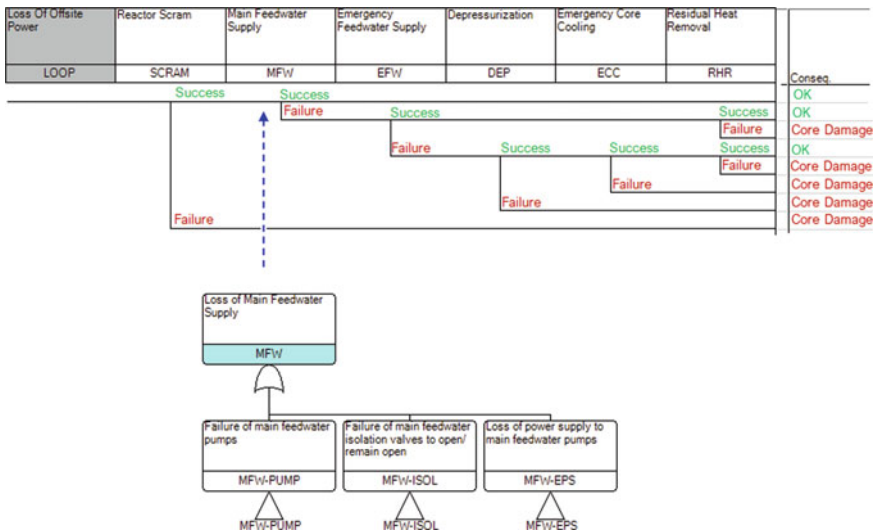

Fig. 1 Risk triplet in PRA

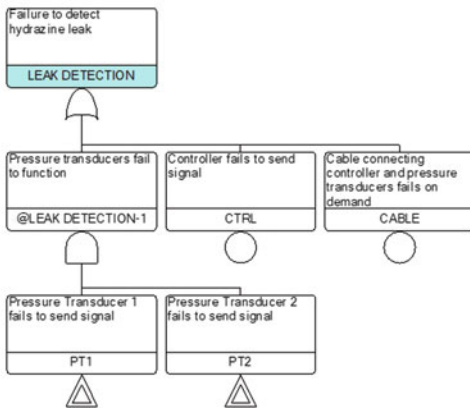**Fig. 2** Event tree for loss of offsite power IE in NPP facility

Fig. 3 Event tree for hydrazine leak IE in a spacecraft (Credits: NASA PRA guide [2])

aptly conceived in the industry specific PRA study. These elements play a crucial role in determining the scope, approach, outcomes and quality of a PRA study.

Successful implementation of PRA model for any engineering facility helps to identify the inherent risks and main contributors to risk, foresee the adverse consequences, evaluate and manage these effectively. PRA plays an important role in presenting the safety level of a plant to regulators/utilities/government agencies/public and in supporting risk informed decision making.

1.2 Historical Perspective

PRA has its roots from the aviation and aerospace industry. Boeing company and Bell laboratories conceived the FTA technique in 1960s which provided a deductive, systematic and holistic assessment of the airplane systems along with their interconnections and dependencies and highlighted critical faults that can occur in an airplane. This method gained popularity in 1970s and 1980s when the US Federal Aviation Agency (FAA) recommended FTA for new aircraft designs to identify and

reduce the occurrences of single failures to less than one-in-a-billion flight hours. This aided in understanding the risk in a quantitative perspective.

The National Aeronautical Space Administration (NASA) began to use conservative PRA methods in 1967 after the Apollo 1 cabin fire that resulted in three fatalities. It is after the Challenger space shuttle incident in 1986 and Columbia space shuttle incident in 2003, PRA gained significant momentum because earlier studies predicted such incidents and PRA methodologies started to mature significantly producing highly useful insights on design and operational improvements; this reinforced the need for PRA analysis in future missions.

Within the nuclear industry, the philosophy of risk assessment was conceived as early as 1950s based on maximum plausible accident that can occur in a facility. The known risks of plausible accident scenarios were normally covered by adequate safety margins in plant design, but the unknown risks were estimated by considering hypothetical worst-case/incredible accident scenarios. Later, when the civilian nuclear power programme began to expand and evolve with proposals to build large NPPs (in the range of 200–500 MWe), there was a desire to evaluate all possible risks from the facility including the effects of radioactive releases to the environment and public. This led to an idea to adapt the PRA concepts of aerospace industry to nuclear industry.

The reactor safety study, famously known as the Rasmussen study/WASH-1400 was the first full-fledged application of PRA to a large modern light water reactor, published by the United States Nuclear Regulatory Commission (USNRC) in 1975. Though the study was appreciated for its pioneering efforts in risk assessment, it had methodological gaps in several areas which demanded a more robust methodology. In 1979, after the TMI plant suffered a partial core meltdown due to small loss of coolant accident (LOCA), the post-accident investigations of NRC observed that such accidents were infact predicted by WASH-1400 study and recommended that greater importance should be given to PRA studies with improved methods in assessing the risk of NPPs. Over 75 PRA studies were completed in the US by mid-1990s. USNRC and International Atomic Energy Agency (IAEA) promoted the technique all over the world by developing various standards and guidelines. Since then, PRA has become the mainstay to overall plant safety assessment not only for commercial NPPs but also for research reactors and other nuclear facilities worldwide.

Today, PRA is mandated by all nuclear regulatory authorities around the world. The assessments performed by different countries are driven by the evolution of PRA methodologies, data, modelling approaches and NPP operating experience. In India, Bhabha Atomic Research Centre (BARC) and Nuclear Power Corporation of India Limited (NPCIL) have been carrying out PRA studies since the late 1980s and have developed dedicated teams for conducting such studies for all operating NPPs and new builds.

Post Fukushima accident, international organizations such as the IAEA, USNRC, Western European Nuclear Regulatory Association (WENRA), Nuclear Energy Agency (OECD-NEA), World Association of Nuclear Operators (WANO), European Nuclear Safety Regulators Group (ENSREG) have strengthened their advocacy on safety assessments. In particular, the existing regulatory requirements and standards
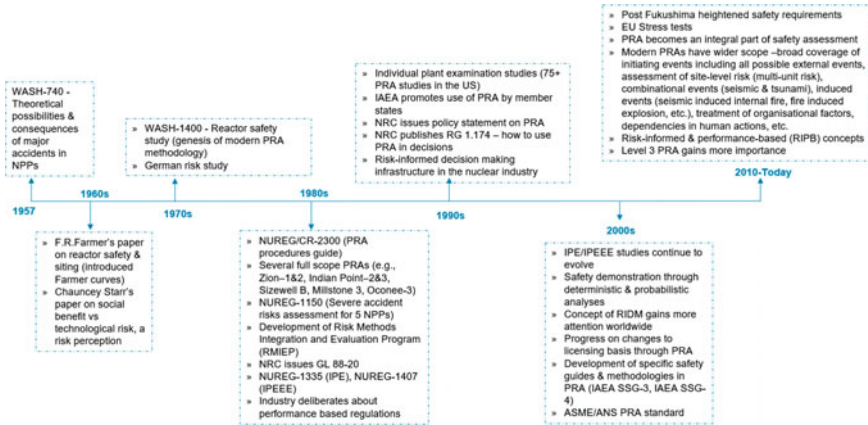
Fig. 4 Evolution and advancement of PRA in the nuclear industry

on safety in US, UK, India, Japan, Switzerland, France, Spain, Finland, and other European countries have been significantly enhanced due to which the scope of PRA study has also increased (wider coverage of initiating events, detailed plant response models and system fault trees, etc.). PRA supports several useful applications and is extensively used for risk-informed decision making in NPPs, aiming to increase the safety in a cost-effective manner.

Figure 4 shows the evolution and advancement of PRA in the nuclear industry.

2 PRA in Nuclear Industry

2.1 Definition of Risk in Nuclear Industry

The definition of risk encompasses two aspects: the likelihood (probability/ frequency) of an event to occur and its consequences on the health and safety of the facility personnel, public and the environment. NPP utilities/organizations are exposed to different sources of risk, which can be categorized into one of the following: Safety-related, Operation/Production, Commercial or Strategic.

All risks to an NPP (radiological, chemical, and industrial related risks) that can occur during its lifetime must be analysed using deterministic and probabilistic approaches to ensure that they do not pose undue threat to the plant, plant personnel, public and the environment. For demonstration of plant safety, the risk analysis should consider all sources of radioactivity in the NPP including spent fuel pools, and a wide range of events such as internal events, internal hazards, external hazards, and combinational hazards in all plant operating modes.
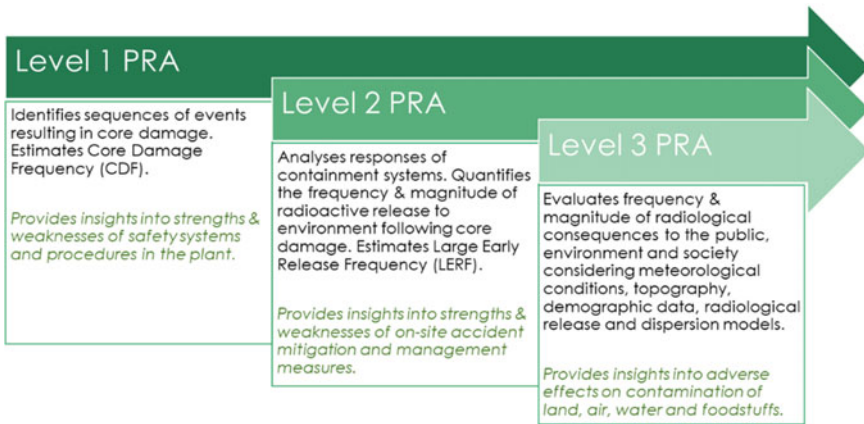
Fig. 5 Levels of PRA (Credits: IAEA and USNRC)
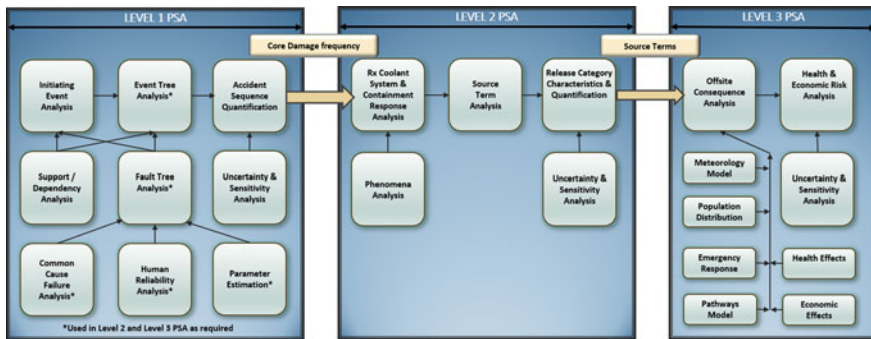
Fig. 6 Generic framework and tasks of PRA (Credits: INL, US)

2.2 PRA Framework in Nuclear Industry

The overall PRA framework is executed in three levels as depicted in Fig. 5, and the specific tasks/elements are shown in Fig. 6. Typically, it takes about 3–5 years to perform a full scope Level 1 and Level 2 PRA study from scratch covering all initiating events for all plant operating modes [1, 4].

2.3 Regulations, Standards and Guidance on PRA in Nuclear Industry

The safety regulations in the nuclear industry are largely harmonized, with major initiatives taken by US Nuclear Regulatory Commission (USNRC), International

Atomic Energy Agency (IAEA), Electric Power Research Institute (EPRI), American Society of Mechanical Engineers (ASME), Western European Nuclear Regulators' Association (WENRA), Nuclear energy Agency (NEA), European Nuclear Safety Regulators Group (ENSREG), et al. In addition, the regulatory authority in each country provides specific requirements on safety assessments for e.g., the Swiss Federal Nuclear Safety Inspectorate (ENSI) provides detailed and prescriptive requirements on the quality and scope of PRA. There are several regulations, standards and safety guides on PRA; USNRC RG 1.200, IAEA SSG-3, IAEA SSG-4, ASME/ANS RA-Sb, ASME/ANS 58.21, ASME/ANS 58.22, AERB/NPP&RR/SM/O-1, ENSI-A05, WENRA Safety Reference Levels to name a few, and other topic specific guides/literatures on PRA tasks such as IE definition, data analysis, HRA, etc., required for full scope PRA study and PRA applications.

2.4 Important Objectives of Risk Assessment in Nuclear Industry

The high-level objectives of a PRA study for an NPP are:

  i. To determine factors that contribute significantly to the radiation risks from a facility by considering various internal and external events that can affect the plant (such as transient events, loss of coolant accident, fire, flooding, earthquakes, etc.);
 ii. To evaluate the extent to which the plant is designed such that no postulated initiating event contributes largely/disproportionately to the risk;
iii. To provide assessments of the frequency of occurrence of core damage states, plant damage states and risks of off-site releases across all plant operating states;
 iv. To identify systems and components for which design improvements and/or modifications to operational procedures could reduce the likelihood and/or severity of accidents;
  v. To assess the adequacy of plant emergency operating procedures and severe accident management procedures and recommend modifications to reduce the likelihood and/or severity of accidents;
 vi. To provide confidence that cliff edge effects[1] will be minimised or prevented;
vii. To verify compliance with quantitative/probabilistic safety targets set by the regulator.

---

[1] Small deviation in plant parameters that could give rise to abnormal consequences.

2.5 Significant Benefits Brought by PRA in the Nuclear Industry

The use of PRA over the last four decades has brought significant benefits to the nuclear industry right from strengthening the regulatory policies on safety, to specific plant/design modifications and development of bespoke methodologies and handbooks to increase the realism in PRA results and to support risk-informed decision making. Below are some examples of the uses/benefits of PRA in the nuclear industry:

i. Identification and resolution of plant vulnerabilities by enhancing existing design aspects;

ii. Evaluation of risk benefits of different design options to strike a balance between safety and cost;

iii. Supports upgrades, backfitting activities and plant modifications by identifying the system-level safety, overall plant safety and risk benefits of the proposed modifications;

iv. Risk-informed rationale for changes to plant technical specifications—controls/optimisation to allowed outage time and surveillance test interval programs;

v. Alternative regulatory approaches to safety classification and categorisation of SSCs;

vi. Supports reliability centered maintenance (RCM) program in the facility—identifying equipment requiring different levels of preventive and corrective maintenance, thereby focussing resources to enhance overall system reliability;

vii. Provides perspectives and alternatives for severe accident management and mitigation, enhancing plant emergency/accident management procedures, and improve operator training;

viii. Provides risk-based safety indicators for operations and maintenance through integration with risk monitor models—to provide instantaneous and average risk profile for the complete set of maintenance activities;

ix. Other targeted applications like significant determination programs, precursor studies, trip risk analysis, changes to licensing basis, changes to fire protection programs, inspection of critical pipe segments in the plant and much more;

x. PRA constantly supports regulatory decisions and regulatory policy making. Some of the key regulatory changes brought by PRA in Code of Federal Regulations (CFR) of USNRC are:

(a) 10 CFR 50.63—development of station blackout (SBO) rule prompted by PRA findings concerning the risk significance of SBO scenarios

(b) 10 CFR 50.109—backfit rule—new requirements based on PRA insights would lead to substantial safety improvement in the plant

(c) RG 1.174—changes to plant licensing basis

(d) 10 CFR 50.65—maintenance rule—monitoring the effectiveness of maintenance at NPP, manage the risk of maintenance activities through PRA, improvement of shutdown risk through effective maintenance strategies

Concept Design	Evaluates the robustness of the design - operational, safety systems & support systems and the layout of the plant
Detailed design/construction	Uncovers design weaknesses, proposes changes to system design, redundancy aspects, decisions regarding final design changes before commissioning and plant start-up
Operation and maintenance	Maintained as Living PSA using the particularities of the plant and operational experience. Living PSA is continuously updated in view of annual safety reviews, periodic safety reviews, regulatory requirements, methodological and data advancements, etc. PSA is used to perform several useful applications.
Refurbishment	Evaluate plant modifications, safety upgrades, capability of the design to meet long term operation
Decommissioning	Evaluate safety of decommissioning activities

Fig. 7 Role of PRA throughout NPP lifecycle

    (e) 10 CFR 50.48 I—fire protection rule—option to use fire PRA to support risk-informed performance based (RIPB) fire protection program as an alternative non-deterministic approach to achieve NRC's fire protection goals

    (f) 10 CFR 50.69- Risk-informed categorization and treatment of structures, systems, and components (SSCs)

Figure 7 shows the vital role played by PRA throughout the lifecycle of an NPP.

2.6 Limitations of Current PRA Framework

One of the main limitations of the conventional PRA models is the 'static' modelling of accident progression and system interactions. For example, the success or failure of systems determines the accident progression and related end states, which is a binary process driven by analysts' understanding of the plant and systems. In certain areas, such as human reliability analysis, accident sequence modelling for external hazards, extended mission time modelling, etc. the static style of modelling could reduce the realism in PRAs.

There is increasing interest in recent years towards use of dynamic modelling approaches, which extends the traditional PRA framework by incorporating dynamic and physics-based outcomes and variations. Such a dynamic approach enables modelling of various scenarios (e.g., with and without system degradation) and can more realistically reflect the time-dependent system interactions and human responses. It is also possible to depict the recurrence of a particular event in the event tree. Although the dynamic approach decreases uncertainty in conventional PRAs and improves depiction of accident evolution and system interactions, it is resource-intensive; verifying the dynamic models can be difficult. More details about the limitations of traditional PRA and prospects of dynamic PRA are discussed in [5, 6].

3   PRA in Space Industry

3.1   Definition of Risk in Space Industry

Space missions are challenging endeavors with unique hazards, risks, and technical challenges. Space safety includes protection of human life and/or spacecraft during all phases of the mission regardless of whether it is a 'manned' or 'unmanned'.

In a space mission, a risk is a potential failure that can take place during the design, build, transportation, and launch stages of a spacecraft or during its operation in orbit. Depending on the severity of failure, this can lead loss of mission, loss of vehicle or loss of crew (for manned missions) or a reduction in the performance or lifetime of the spacecraft (degraded condition) or loss of/damage to critical assets, infrastructure, or surrounding population near the launch site. The concept of space safety also extends to planetary protection (e.g., forward contamination to solar system bodies by earth and backward contamination considering vice-versa), protection from space debris, environmental effects of space operations such as long-term impact of solid fueled rockets on the protective ozone layer and the effects of perchlorate contaminants from rocket fuels that can pollute drinking water supplies.

3.2   PRA Framework in Space Industry

There are different challenges to assessing safety/risk in space missions. Worldwide, at least 200 people have lost lives during processing, testing, launch preparations, launch operations and other spaceflight related incidents; out of these 31 fatalities are related to human spaceflight. In addition, there are 35+ space missions that resulted in very near misses and some training related accidents that nearly resulted in deaths.

The space industry is growing rapidly with a variety of mission objectives and wider international cooperative efforts. There is an interest and need in the global community to undertake space missions in accordance with harmonized safety regulations and standards which keep evolving with increased number of space missions and international participation. The International Standards Organization (ISO) under the technical committee group TC20 has developed several internationally accepted standards that create a foundation for carrying out space missions. For e.g.,

- ISO 14620 [7] covers the safety requirements for space systems, including system safety, launch site operations and flight safety systems
- ISO 14624 [8] covers the safety and compatibility of materials for space systems
- ISO 17666 [9] covers the principles of integrated risk management framework for space projects

- ISO 11231 [10] covers the principles, processes, and requirements for conducting a probabilistic risk assessment for space missions

NASA has pioneered the space safety regulations, standards, requirements, and risk assessment methods (both qualitative and quantitative such as PRA). They publish several policy directives (NPD), procedural requirements (NPR), standards (STD), handbooks (HDBK) and other guidance under the safety and mission assurance framework (SMA) [2, 11, 12]. NASA has embedded risk management techniques into its program management policy and uses Continuous Risk Management (CRM) as well as Risk-Informed Decision Making (RIDM) processes to manage project risk and achieve improved safety and performance of their space missions.

The national space programs have their own regulations and requirements which are currently controlled by government agencies. For e.g., NASA, FAA, US Air Force in the US; European Space Agency (ESA), European Aviation Safety Agency (EASA) in Europe; Russian State Space Corporation, Roscosmos in Russia; Japan Aerospace Exploration Agency (Jaxa) in Japan; and Indian Space Research Organisation (ISRO) in India. Though implementation of ISO standards and other widely acknowledged standards (from NASA) is desirable, they are treated as voluntary. The effective implementation of such international requirements require support from national and private space agencies. The International Astronautical Federation (IAF) and International Association for the Advancement of Space Safety (IAASS) have developed several proposals to create internationally accepted space standards and safety requirements [13–16].

Figure 8 shows the risk management framework and where/how safety assessment (and mainly PRA) fits in this framework.
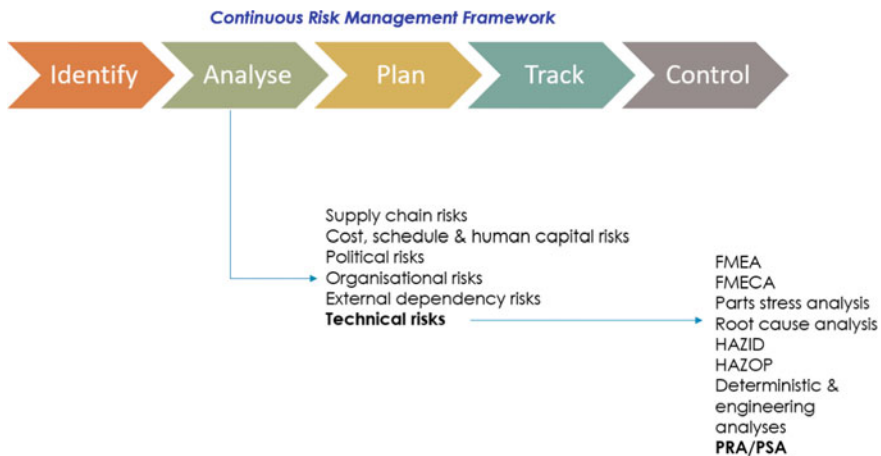

Fig. 8 NASA's continuous risk management framework

3.3   Objectives of PRA in Space Industry

The requirements as explained below form the objectives for PRA in space industry.

The requirements to conduct safety assessments are either explicitly defined as in the case of NASA, ESA and JAXA, or implicitly covered as part of the engineering design and safety assurance program in other agencies. There are explicit requirements as to when a PRA study is necessary and when other risk/safety assessment methods are acceptable, depending on the mission criticality. Though there are different interpretations made by the space agencies with respect to safety assessment, when it comes to PRA, the industry requirements are harmonized. For e.g., ISO 11231, NASA guides NASA/SP-2011-3421, NASA/SP-2014-612, European Cooperation for Space Standardisation (ECSS) guide ECSS-Q-ST-40C [17], JAXA guides JMR-001, JMR-002 provide perspectives on when a PRA undertaking is required. For instance, NASA mandates PRA study for all their crewed/manned space missions, complex/high-priority robotic missions, next generation science missions, missions involving planetary protection, etc. The United Nations Office for Outer Space Affairs (UNOOSA) mandates that any use of nuclear power sources in outer space should be based on a thorough safety assessment including probabilistic risk analysis in accordance with IAEA guidelines.

The international space agencies and the ISO standards state the type of space missions where a PRA study is required. Some examples are given below:

- Transportation of humans to space (International Space Station, Low Earth Orbit missions, etc.)
- Design of space/planetary stations to be inhabited by humans
- Launch vehicles carrying nuclear materials
- Demonstration of a novel technology for a first-of-a-kind space mission
- Transfer of existing design technology and adaptation/integration into a new design
- Planetary protections (e.g., mars sample return mission)
- Projects that are of critical importance to national safety and security
- Risky space missions (such as flyby missions)

All these project activities involve scenarios that can result in death of/serious injury to humans, agency workforce and public, loss of proprietary national property/critical scientific data. For other type of projects, the choice of risk assessment technique is at the discretion of the national agency.

Regardless of the nature of mission, NASA recommends a PRA study if the lifecycle cost exceeds \$1 billion. Available literatures indicate that safety assessments require only a small fraction of the mission cost, so this must be seen as an essential investment in space industry.

3.4 Significant Benefits of PRA in Space Industry

Following are some examples of uses/benefits of PRA in space sector:

- Validate conceptual designs (e.g., crew exploration vehicle, crew module, robotic landers, etc.) and identify the elements of the design that are the greatest detractors of system reliability;
- Evaluate alternative design concepts, design modifications and upgrades (e.g., space capsule/crew module, launch abort system, using parts/systems of existing launch vehicle on a new launch vehicle, etc.);
- Identify those potential mission limiting components and other elements that will require special operations/attention to testing/environmental isolation, etc.;
- Fulfil safety compliance for special missions (mars sample return—planetary protection, missions carrying nuclear payloads, etc.);
- Evaluate the impact of proposed engineering change;
- Enhance system engineering, design, and reliability for future missions.

Over the last three decades, NASA has been extensively using PRA as the baseline method to achieve integrated systems safety. The study has become the mainstay for improving the safety, technical performance, and cost reduction of space missions. ESA has detailed requirements on safety analysis, which have a careful consideration of deterministic and probabilistic methods for safety demonstration. For e.g., hazard analysis, FMECA, fault tree analysis, etc., are used for regular missions while PRA is recommended for manned spacecrafts and safety critical systems. JAXA's guidelines specify integrated requirements for safety assessment of unmanned payload vehicle. The safety assessment requirements for manned space projects are compliant with NASA's requirement wherein PRA plays a major role. Roscosmos's special technical regulations on space technology safety define a detailed reliability program to be implemented across all stages of a life cycle. Robust engineering analysis techniques and deterministic methods are used for safety demonstration. PRA scope is limited as noted from literature survey of publicly available sources.

In India, PRA study for Gaganyaan mission is in the making by ISRO, as indicated in their annual report. ISRO has a long-term vision to use PRA as an effective risk management tool for other space missions. Soon, ISRO plans to use nuclear thermal propulsion/radioisotope thermoelectric generator (RTG) for power generation and thermal management of deep space mission projects, wherein PRA could become a beneficial study for safety demonstration.

3.5 Regulations, Standards and Guidance on PRA in Space Industry

There is only limited literature available on PRA studies for space missions; some technical papers discuss only the high-level methodology and insights from
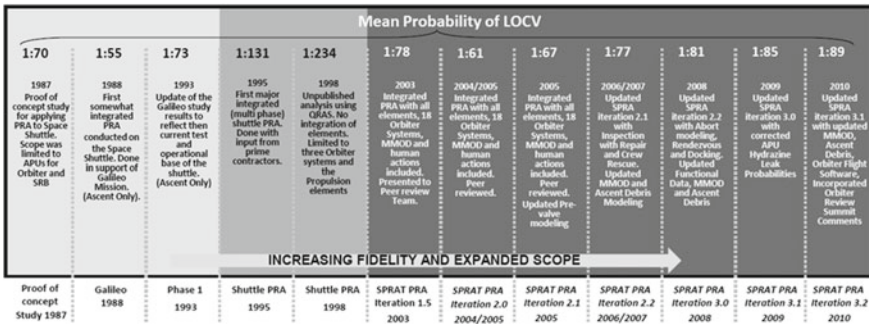
Fig. 9 Evolution of NASA's space shuttle PRA study [19]

PRA studies of specific space missions (mostly from NASA) without mentioning the details of PRA. The Space Shuttle PRA report (NASA-CR-197808-12 [18]) published in 1995 was the first major integrated multi-phase PRA study. Subsequent PRA studies were incrementally developed over the next decade until NASA retired the space shuttle program permanently in 2011. The initial shuttle PRA studies did not model failures within thermal protection system, human errors and possible recovery actions, abort scenarios, collision during rendezvous and docking, collision from space debris (such as MMODs), software failures, etc. However, these have been incorporated in the later models with Iteration 3.2 being the full scope shuttle PRA developed till date [19].

Figure 9 shows the evolution of space shuttle PRA model. With the repeated developments in NASA safety requirements, standards, PRA guides and computational tools, the risk estimates proved to be realistic.

NASA published a detailed PRA guide NASA/SP-2011-3421 [2], systems safety handbook NASA/SP-2014-612 [11] and fault tree handbook with aerospace applications which are widely used by the space industry to develop PRA models. The Space Shuttle PRA study published in 1995 (NASA-CR-197808-12 [18]) by Science Applications International Corporation documents the potential risk of loss of vehicle and provides a good context to understand the PRA modelling for space missions. Space PRA practitioners use these as valuable guidance documents, however, most of the PRA models are built based on experience gained from previous space missions and expertise of the individual/team working on various PRAs [20].

3.6 Challenges in Development of Space PRA Models

There are limited or no specific guidance on the details of PRA such as initiating event definition, accident sequence/scenario modelling, data analysis, etc., in the space industry. Component failure data is based on past mission experience, testing experience and generic data sources. Other specific data sources remain proprietary to

the national agency and are not available in the public domain. The main difficulty for development of a common knowledge base on PRA is each space mission is unique with respect to the choice of technology (for instance launch vehicle, crew module), which is indigenously designed by the respective national agencies. The technology/ design drives the scope of PRA and mission risk analysis, for instance, the initiating events during launch, orbit insertion and re-entry and the accident progression can be unique, the failure experience can be different, human errors can be different in a fully autonomous spacecraft as compared to semi-autonomous spacecraft, etc., and the specificities are much more. Due to these reasons, it is imperative that PRA practitioners and space mission design team work together and develop the PRA models with due consideration to the specificities of the space missions. Some of the critical and challenge areas of contemplation by space PRA practitioners are:

(a) Understanding the complexities of system in a dynamic environment
(b) Validating the coverage of initiating events across all mission phases
(c) Event tree modelling approaches (single large event tree depicting the entire mission or multiple event trees)
(d) Modelling the accident progression and constructing phenomenological models/ performing simulations for the unknowns (modelling failure progression of a mission phase affecting another mission phase, modelling diverse scenario possibilities, etc.)
(e) Modelling software failures, and how to ensure that critical functional failures are addressed appropriately in PRA
(f) Modelling structural failures, human errors and uncertainties
(g) PRA project management (managing a PRA project for the first time)
(h) Integration of PRA model (integration of system models and scenarios from different departments)
(i) Interpretation of PRA results and communication of risk insights to the management

3.7 NASA's Recent Experience

The learnings from previous space shuttle accidents and insights from shuttle PRA studies have helped to rethink the safety concepts in recent and upcoming space missions. For e.g., the Orion spacecraft as part of the Artemis project has multiple safety measures focusing on human safety, namely: (i) Redesigned hatch and its opening mechanism to allow rapid escape, (ii) changes to spacecraft atmosphere to prevent/minimize fire hazards whilst maintaining crew safety, (iii) enhanced launch abort and crew escape system, special ablative heat shields that can withstand high re-entry speeds, (iv) powerful flight avionics and mission control software, (v) strict technical specifications, inspection and quality controls for spacecraft design. NASA requires a system-centric approach to address the safety and reliability requirements for their current and future space missions wherein the individual system level and overall reliability requirements must be verified through detailed PRA studies. The

safety and engineering panel reviews the PRA models and reports in detail and examines every component on the spacecraft and assesses the effect of those components failing independently or in combination with other components to make necessary adjustments in the design process. Thus, PRA serves as an integral part right from early design until the design is finalised and approved for the actual mission [21].

4   Comparison of Nuclear PRA and Space PRA

An attempt has been made to compare some aspects/elements of Nuclear PRA and Space PRA, shown in Table 1. While the PRA is well matured in the nuclear sector, it continues to evolve in the space sector. Except for the aspects that are technology specific, these sectors can complement one another on the conceptual fronts of PRA.

5   Concluding Remarks

PRA for Nuclear Power Plants have advanced considerably since its first application in 1970s. It has reached a reasonable state of maturity over the years and is constantly evolving. Modern PRAs have wider scope with broader coverage of initiating events including all possible external events, assessment of site-level risk (multi-unit risk), combinational events, treatment of human errors and associated dependencies, etc.

Insights from PRA studies have helped to strengthen the regulatory policies on safety assessment and brought numerous benefits to the industry such as development of station blackout rule, changes to plant licensing basis, fire protection rule, risk-informed categorization of structures, systems, and components, strengthening the accident management and operator's response to severe accidents and much more.

Besides safety demonstration, PRA is used today to support several useful applications such as Significance Determination Process, Risk-informed optimization of plant technical specifications, online/real time risk monitoring of maintenance activities, inspection of critical pipe segments in the plant and so on. Post Fukushima, PRA has increasingly gained importance in safe design and operation of NPPs worldwide and complements the deterministic safety analysis throughout the life of an NPP.

Safety and reliability demonstration is of paramount importance is the Space industry, which is growing rapidly with increasing interest in the global community to devise space missions based on harmonized safety regulations and standards. International organizations/agencies such as ISO, NASA, ESA, JAXA have published several safety standards, technical standards, and detailed guides for risk assessment. There are explicit requirements in these standards as to when a PRA study is mandatory (for instance in human spaceflight and high priority robotic missions) and when other risk/safety assessment methods are acceptable, depending on the mission criticality and life cycle cost.

NASA made a pioneering effort to integrate risks from both Spacecraft (SC) and Ground Segment (GS) through application of PRA in supporting the design of the Geostationary Operational Environmental Satellite R-Series, a high-priority operational space mission. Effective collaboration between the design team and PRA analysts is very well described in papers related to this PRA project [21]. PRA

Table 1 Comparison of nuclear and space PRA task elements

PRA task area/ element	Nuclear	Space
General	Clear guidance and requirements are available on the scope and level of details expected in a PRA study, including specific attributes a PRA should fulfil to support risk-informed applications	Exact requirements and scope of a space PRA study need to be decided by the agency undertaking the PRA development activity. The PRA study is mission specific
	Detailed reference PRA studies, guidance/ methodologies and literature available, for instance for initiating event frequencies, component reliability data and CCFs	Lack of guidance on specific PRA topics such as initiating event analysis, scenario modelling and data analysis, which largely drives the PRA efforts
	Vast knowledgebase on PRA topics, shared through international communities like IAEA, ANS et al., and international working groups engaged for continuous methodological enhancements	Attempts ongoing to harmonize the PRA framework, international bodies have more to do on knowledge sharing and development of more specific guidance
PRA scope, risk metrics and data	The typical scope involves Level 1, Level 2 and Level 3 PRA for all plant operating states (internal events, internal hazards, external hazards, and combination hazards)	The typical scope includes all types of hazards in each mission phase (Ascent, Orbit, Deboost, Re-entry, Descent, Landing). Specific PRAs may be developed for ground centres, launch pads or other facilities supporting the mission

(continued)

Table 1 (continued)

PRA task area/ element	Nuclear	Space
	Core damage frequency (CDF), fuel damage frequency (FDF), large early release frequency (LERF) and large release frequency (LRF)	Loss of vehicle (LOV), loss of mission (LOM), loss of crew (LOC), expected casualty (EC), ABORT
	Dedicated generic databases exist for IE frequencies, component failures and CCFs	Component failure data is largely developed using historical mission data. Existing information from Shuttle PRA study, NWSC, MIL, aerospace failure data handbooks, published papers, etc. could be utilized
Scenario modelling/ event tree modelling	Two approaches used for PRA model development, namely: (a) Small event tree and large fault tree, and (b) Large event tree and small fault tree	The PRA models can be developed based on: (a) single event tree or (b) multiple event tree approaches. For instance, in the context of a crewed mission, the single event tree approach models mission timeline from launch till landing by propagating the end states to relevant mission phases (the idea of scenario gets discarded). Whereas the multiple event tree approach decomposes each phase of the mission separately (scenario definition becomes an intensive process)
Mission times	The nominal mission time considered for components/systems is 24 h. Extended mission time requirements vary from 48 to 72 h	Mission time for components/systems vary between few minutes to few days/years
Modelling component failures	Component failure modes are represented in a straightforward manner (e.g., fails to start, fails to run, fails to open, etc.)	Defect models need to be constructed for leaks, cracks, process errors, etc. to identify how these propagate to component failures. Component failure models are not always straightforward
Modelling maintenance and repairs	Maintenance and repairs are explicitly modelled as per plant practices	Maintenance/repairs may not be possible in short term crewed missions (e.g., to low earth orbit). These may be modelled in PRAs developed for orbiting space station, lunar base or ground based facilities

Table 1 (continued)

PRA task area/ element	Nuclear	Space
CCF modelling	Scope of CCF modelling is vast due to a greater number of redundancies in the design	Scope of CCF modelling is limited due to the limited redundancies
Modelling phenomenological events	Phenomenological events are mostly modelled in Level 2 PRA	Phenomenological progression of events is modelled in all mission phases (and can get complex owing to the dynamic nature of mission events). More emphasis is given to time dependent evolution of scenarios
Supporting studies/ Analyses for PRA model development	Supporting analyses such as thermal hydraulic analysis, severe accident modelling (e.g., MELCOR analysis) are required to support the success criteria formulation	Physics of failure, probabilistic mechanistic analysis, thermal design analysis and structural reliability analysis are required as support studies, for the PRA model development

Analysts were actively involved in system engineering and design engineering to ensure that a comprehensive set of technical risks were correctly identified. Findings from PRA study led to design changes in several subsystems of SC to reduce the risk from micro-meteoroids. This resulted in a more robust design thereby influencing the program's concept of operations. Integration of PRA with system and design engineering earlier in the process was reported to have provided a well-managed approach for risk assessment that increased reliability and availability, optimized lifecycle costs, and harmonized the SC and GS developments [21].

NASA's detailed PRA methods guide, systems safety and fault tree handbooks cover a general framework for development of PRA studies in the space industry. Due to the diversity among space missions and technological differences, standalone guides on specific PRA tasks such as IE definition, systems modelling, data analysis, etc. have been difficult to develop/envision compared to those available in the nuclear industry. Thus, while the NASA guide and other standards help in formulating the general PRA basis, most PRA models are developed largely based on the experience gained from previous space missions and the expertise of the team consisting of PRA practitioners and space scientists/mission designers. Effective and highly useful space PRAs can be developed with good collaboration between PRA practitioners and the space scientists.

This paper attempted to highlight the importance and mandatory nature of PRA in the nuclear industry, which experienced various safety benefits through PRA studies. Indian nuclear industry is part of the fraternity widely applying PRA techniques for assessing the safety of NPPs. The paper also endeavors to highlight the benefits of

PRA experienced in the space industry internationally. Like in the nuclear industry, PRA must be seen as an important requirement by space regulatory bodies and space agencies to analyse the mission risk in a holistic manner and gain the numerous benefits of PRA to strengthen safety and reliability of space missions.

References

1. International Atomic Energy Agency (2010) Development and application of level 1 probabilistic safety assessment for nuclear power plants, IAEA Specific Safety Guide SSG-3
2. National Aeronautics and Space Administration (2011) Probabilistic risk assessment procedures guide for NASA managers and practitioners, 2nd edn. NASA/SP-2011-3421, Dec 2011
3. International Atomic Energy Agency (2016) Safety of nuclear power plants: design. IAEA Specific Safety Requirements SSR-2/1 Rev. 1
4. International Atomic Energy Agency (2010) Development and application of level 2 probabilistic safety assessment for nuclear power plants, IAEA Specific Safety Guide SSG-4
5. Mosleh A (2014) PRA: a perspective on strengths, current limitations, and possible improvements, vol 46, no 1. Nuclear Engineering and Technology
6. Wiltbank NE, Palmer CJ (2021) Dynamic PRA prospects for the nuclear industry. Front Energy Res 9:750453. https://doi.org/10.3389/fenrg.2021.750453,November
7. International Organization for Standardization (2019) Space systems-safety requirements, part 2: launch site operations, 3rd edn. ISO 14620: 2019, Dec 2019
8. International Organization for Standardization (2006) Space systems-safety and compatibility of materials, part 6: determination of reactivity of processing materials with aerospace fluids. ISO 14624: 2006, Apr 2006
9. International Organization for Standardization (2016) Space systems-risk management, 2nd edn. ISO 17666: 2016, Nov 2016
10. International Organization for Standardization (2019) Space systems-probabilistic risk assessment, 2nd edn. ISO 11231: 2019, May 2019
11. National Aeronautics and Space Administration (2014), NASA system safety handbook, vol 2. System safety concepts, guidelines, and implementation examples, NASA/SP-2014-612, Version 1.0, Nov 2014
12. National Aeronautics and Space Administration (2017) NASA agency risk management procedural requirements. NPR 8000.4, Dec 2017
13. Musgrave G, Larsen A, Sgobba T (2009) Safety design for space systems (sponsored by the International Association for the Advancement of Space Safety). ISBN 978-0-7506-8580-1
14. Independent Space Safety Board (2010) Space safety standard commercial human-rated system. IAASS-ISSB-S-1700-D310806 (Rev-B3), Mar 2010
15. International Space Safety Foundation (2021) Making space safe and sustainable. IAASS vision, proposals and initiatives to organize and regulate outer space, Dec 2021
16. Pelton JN, Jakhu RS (2010) IAASS book series on space safety—space safety regulations and standards. ISBN 978-1-85617-752-8
17. European Cooperation for Space Standardization (2009) ECSS-Q-ST-40C (Rev. 1), safety standard, Mar 2009
18. Probabilistic Risk Assessment of the Space Shuttle (1995) Phase 3: a study of the potential of losing the vehicle during nominal operation, NASA-CR-197808, vol 1 to 5, Feb 1995
19. Boyer RL (2010) Space shuttle probabilistic risk assessment (SPRA) iteration 3.2, NASA Johnson Space Center. In: Presented at TRISMAC 2010 conference, Oct 2010
20. RAND Corporation (2016) Developing a risk assessment methodology for NASA, RAND_RR1537. ISBN: 978-0-8330-9563-3

21. Kalia P, Pair R, Uhlenbrock J, Quaney V, Shi Y (2013) Use of a PRA in supporting the design of a GEOS weather satellite and ground system. Int J Perform Eng 9(6)

An Innovative Method for Ranking Generalized Trapezoidal Fuzzy Number Using Euler Line of the Triangle Formed by Joining the Centroids-Application to Replacement Models

S. Poomagal and R. Sujatha

1 Introduction

Ranking fuzzy numbers plays a remarkable role in decision analysis, most of the real-time problems that exists in nature are fuzzy. An enormous defuzzification method has been developed by various research groups. On the whole the ranking methods provide an association from the set of fuzzy numbers to a set of real numbers. It is made clear that, to obtain a natural order each fuzzy set can be replaced by a real number from the effect of defuzzification methods. A wide range of ranking procedures has been developed later than the initiation of fuzzy sets by Zadeh [1] in 1965. For decision analysis with fuzzy background, Jain [2] was initiated the method of ranking fuzzy numbers by representing the vague quantity as a fuzzy set. Later on various research groups were extended the ranking procedures, some among them were investigated and compared by Chen and Hwang [3], Bortolan and Degani [4]. Yager [5] put in the concept of centroid, to obtain the ranking measure for fuzzy numbers. The horizontal and vertical coordinates of the centroid point as the index of ranking was first portrayed by Murakami et al. [6]. Ranking of singleton fuzzy numbers was not made with the above mentioned methods; to overcome this limitation Cheng [7] proposed an approach based on the distance method for ranking fuzzy numbers. This method computes the distance from the original point to the centroid point, however this measure does not ranks the positive and negative fuzzy numbers

S. Poomagal (✉)
Department of Mathematics, University College of Engineering Kancheepuram, Anna University Chennai, Kanchipuram, India
e-mail: poomagal777@gmail.com

R. Sujatha
Department of Mathematics, Shiv Nadar University, Chennai, India

simultaneously. To rectify this limitation Chu and Tsao [8] presented a ranking function root on the Centroids and original point's area. Shieh [9] proposed the precise and accurate procedure for illustrating the centroid point's vertical and horizontal coordinates. Later Wang et al. [10] revised the Chu and Tsao [8] to eradicate the limitations of the ranking measure. Recently Phani Bushan Rao and others [11–17], and formulated and find out the center of gravity point using centroids of centroids, circumcenter of the centroids, incenter of centroids and orthocentre of centroids. Recently Rouhparvar and Panahi [18] come up with a ranking index based on the incenter point for the generalised fuzzy numbers.

In this paper, the authors have proposed a new method based on the Euler line of the centroids to rank fuzzy quantities. Finally a ranking procedure is defined which is the distance between the intersection points of line joining the center point of the two parallel sides of the trapezoidal fuzzy number and the Euler line of the triangle formed by the Centroids, to the original point.

The paper is prearranged as follows: Sect. 2, we recalled some of the essential results on fuzzy numbers. Proposed ranking function for generalised trapezoidal fuzzy numbers has been elaborated in Sect. 3. Numerical examples and comparison of this work with other methods are carried out in Sect. 4 and the application to the proposed method is given in Sect. 5. The paper ends up with the conclusions in Sect. 6.

2 Preliminaries

In this section some standard definitions of fuzzy set theory is given [11, 12, 14].

2.1 Definition

Let U be a universal set. A fuzzy set A of U is defined by the membership function f_A (x): U → [0,1] where f_A (x) is the degree of x in A, $\forall$x ∈ U.

2.2 Definition

A real fuzzy number "A" is described as any fuzzy subset of the real line R with membership function $f_A(x)$ possessing the following properties:

 i. $f_A(x)$ is a continuous mapping from R to the closed interval $[0, \omega]$; $0 < \omega \leq 1$
 ii. $f_A(x) = 0$ for all $x \in (-\infty, a] \cup [d, \infty)$
 iii. $f_A(x)$ is strictly increasing on [a, b] and strictly decreasing on [c, d]
 iv. $f_A(x) = 1$, for all $x \in [b, c]$ where a, b, c and d are real numbers.

2.3 Definition

The membership function of the real fuzzy number A is given by

$$f_A(x) = \begin{cases} f_A^L(x), & x_1 \leq x \leq x_2, \\ \omega, & x_2 \leq x \leq x_3, \\ f_A^R(x), & x_3 \leq x \leq x_4, \\ 0, & otherwise \end{cases}$$

where $0 < \omega \leq 1$ is a constant, x_1, x_2, x_3 and x_4 are real numbers and $f_A^L : [x_1, x_2] \to [0, \omega]$, $f_A^R(x) : [x_3, x_4] \to [0, \omega]$, are two strictly monotonic continuous function from R to the closed interval $[0, \omega]$. It is customary to write a fuzzy number as $A = (x_1, x_2, x_3, x_4 : \omega)$. If w = 1 then $A = (x_1, x_2, x_3, x_4 : 1)$ is a normalised fuzzy number, otherwise A is said to be a generalised or non-normal fuzzy number. If the membership function $f_A(x)$ is piecewise linear, then A is said to be a trapezoidal fuzzy number.

2.4 Definition

The membership function of a generalised trapezoidal fuzzy number $A = (x_1, x_2, x_3, x_4 : \omega)$ is given as

$$f_A(x) = \begin{cases} \frac{\omega(x-x_1)}{x_2-x_1}, & x_1 \leq x \leq x_2, \\ \omega, & x_2 \leq x \leq x_3, \\ \frac{\omega(x_4-x)}{x_4-x_3}, & x_3 \leq x \leq x_4, \\ 0, & otherwise \end{cases}$$

If w = 1 then $A = (x_1, x_2, x_3, x_4 : 1)$ is a normalised trapezoidal fuzzy number and A is said to be a generalised or non-normal trapezoidal fuzzy number if $0 < \omega < 1$. The image of $A = (x_1, x_2, x_3, x_4 : 1)$ is given by $-A = (-x_4, -x_3, -x_2, -x_1 : 1)$. As a particular case if $x_2 = x_3$ the trapezoidal fuzzy number reduces to a triangular fuzzy number given by $A = (x_1, x_2, x_4 : \omega)$. The value of '$x_2$' corresponds with the mode or core and $[x_1, x_4]$ with the support. If w = 1 then $A = (x_1, x_2, x_4 : 1)$ is a normalised triangular fuzzy number and $\tilde{A}$ is said to be a generalised or non-normal.

3 Proposed Method

By considering a generalised trapezoidal fuzzy number $A = (x_1, x_2, x_3, x_4 : 1)$ and divide the trapezoid in to three partitioned plane figures as shown in Fig. 1. The centroid points of the three plane figures (AEB), (BEFC) and (CFD) be C1, C2 and C3. These centroid points were calculated $C1\left(\frac{x_1+2x_2}{3}, \frac{\omega}{3}\right), C2\left(\frac{x_2+x_3}{2}, \frac{\omega}{2}\right)$ and $C3\left(\frac{x_4+2x_3}{3}, \frac{\omega}{3}\right)$ and is observed that these Centroids are non-collinear, they may form a triangle by joining them. And by the property of analytical geometry it is known that all the centres of the triangle lie in the line and named Euler Line [19]. With this idea the equation of the line joining the orthocentre and circumcenter of the triangle with vertices C1, C2 and C3 has been calculated, which is an Euler line.

The equation of Euler line is calculated as

$$y + \left\{\frac{[3\alpha_1\alpha_2 + \omega^2]}{2\omega(\alpha_5 - \alpha_4)}\right\}x = \frac{\alpha_1\alpha_2\alpha_3 + \omega^2(7\alpha_5 - 4\alpha_4)}{12\omega(x_2 + x_3 - x_1 - x_4)} \tag{1}$$

where $\alpha_1 = (2x_1 + x_2 - 3x_3)$, $\alpha_2 = (x_3 + 2x_4 - 3x_2)$, $\alpha_3 = (7x_2 + 7x_3 + 2x_1 + 2x_4)$, $\alpha_4 = (x_1 + x_4)$ and $\alpha_5 = (x_2 + x_3)$.

The equation of the line joining the middle points of the parallel lines of the generalised trapezoidal fuzzy number $G\left(\frac{x_2+x_3}{2}, \omega\right)$ and $H\left(\frac{x_1+x_4}{2}, 0\right)$ is
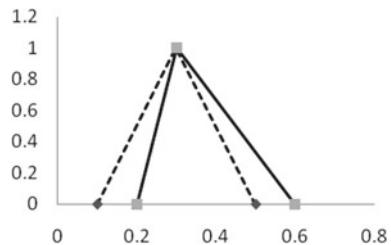
$$y + \frac{2\omega x}{\alpha_4 - \alpha_5} = \frac{\alpha_4\omega}{\alpha_4 - \alpha_5} \tag{2}$$

The point of intersection (x, y) of Eqs. 1 and 2 is evaluated as

$$x = \frac{\alpha_1\alpha_2\alpha_3 + \omega^2(7\alpha_5 + 8\alpha_4)}{6(3\alpha_1\alpha_2 + 5\omega^2)} \text{ and } y = \frac{7\omega}{3}\left(\frac{\alpha_1\alpha_2 + \omega^2}{3\alpha_1\alpha_2 + 5\omega^2}\right) \tag{3}$$

A triangular fuzzy number $A = (x_1, x_2, x_4 : \omega)$ which is a particular case of trapezoidal fuzzy number, the coordinates has been evaluated by equating $x_3 = x_2$ in (Eq. 3).

Fig. 1 Generalized trapezoidal fuzzy number

The ranking measure of the generalised trapezoidal fuzzy number $A = (x_1, x_2, x_3, x_4 : \omega)$ which associates fuzzy numbers to real numbers has been defined as

$$R(A) = \sqrt{x^2 + y^2} = \sqrt{\left(\frac{\alpha_1 \alpha_2 \alpha_3 + \omega^2(7\alpha_5 + 8\alpha_4)}{6(3\alpha_1\alpha_2 + 5\omega^2)}\right)^2 + \left(\frac{7\omega}{3}\left(\frac{\alpha_1\alpha_2 + \omega^2}{3\alpha_1\alpha_2 + 5\omega^2}\right)\right)^2}$$

(4)

which is the distance between the original point and the intersection point of the line joining the mid points of the parallel lines of the trapezoidal fuzzy number and the Euler line. The basis for choosing this point as a point of reference is that each centroid point C1, C2 and C3 are the balancing points of each individual plane figure. Since the Euler line have all the centers of the triangle lies on it, it may be considered as the balancing line of the triangle formed by joining the centroids of the three plane figures of trapezoid. The line joining the midpoints of the two parallel sides of the trapezoidal fuzzy number can also be treated as a balancing line of the trapezoidal [10]. Since these two lines are considered as a balancing lines, the intersection point of these two balancing lines may considered as the enhanced point of reference of the Trapezoidal. We have categorize the ranking between the fuzzy numbers as follows.

If $A = (x_1, x_2, x_3, x_4 : \omega_1)$ and $B = (x'_1, x'_2, x'_3, x'_4 : \omega_2)$ be two different generalised trapezoidal fuzzy number then.

(i) $R(A) < R(B) \Leftrightarrow A < B$
(ii) $R(A) > R(B) \Leftrightarrow A > B$
(iii) $R(A) = R(B) \Leftrightarrow A = B$

The sufficient condition has been proved in detail by Wang and Kerre [20, 21]. Here R(A) represents the distance between the original point and the intersection point of the line joining the mid points of the parallel lines of the trapezoidal fuzzy number and the Euler line of the Fuzzy number A. Since the ranking depends on the distance, the larger the distance is, the larger the Fuzzy number.

4 Numerical Examples

In this section some standard definitions of fuzzy set theory is given [11, 12, 14].

4.1 Example

Let A = $(0.1, 0.3, 0.3, 0.5; 1)$ and B = $(0.2, 0.3, 0.3, 0.4; 1)$ Then R(A) = 0.527 and R(B) = 0.548. Since R(A) < R(B) $\Rightarrow$ A < B (Fig. 2).

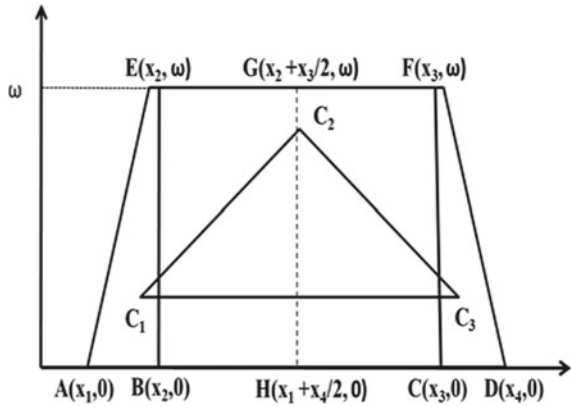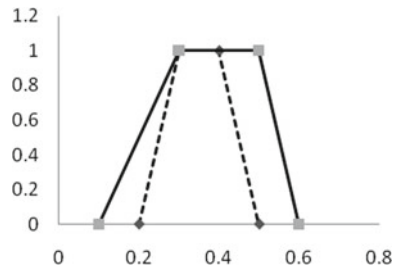**Fig. 2** Fuzzy number A and
B of Example 4.1

Fig. 3 Fuzzy number A and
B of Example 4.3

4.2 Example

Let $A = (0.1, 0.3, 0.3, 0.5; 1) \Rightarrow -A = (-0.5, -0.3, -0.3, -0.1; 1)$ and $B = (0.2, 0.3, 0.3, 0.4; 1) \Rightarrow -B = (-0.4, -0.3, -0.3, -0.2; 1)$ then $R(-A) = 0.527$ and $R(-B) = 0.548$ as $R(-A) < R(-B) \Rightarrow -A < -B$.

4.3 Example

Let $A = (0.2, 0.3, 0.4, 0.5, 1)$ and $B = (0.1, 0.3, 0.5, 0.6; 1)$ then $R(A) = 0.54$ and $R(B) = 0.41$ since $R(A) > R(B) \Rightarrow A > B$ (Fig. 3).

4.4 Example

Let $A = (0.2, 0.3, 0.4, 0.5; 0.8)$ and $B = (0.1, 0.2, 0.3, 0.6; 0.7)$ then $R(A) = 0.46$ and $R(B) = 0.35$. Since $R(A) > R(B) \Rightarrow A > B$ (Fig. 4).
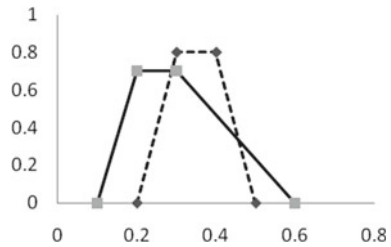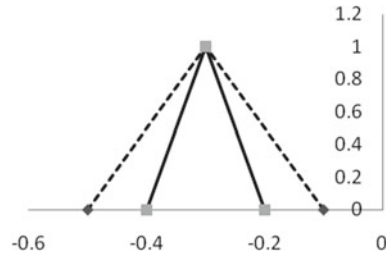
Fig. 4 Fuzzy number A and B of Example 4.4

Fig. 5 Fuzzy number A and B of Example 4.5

4.5 Example

Let $A = (-0.1, -0.2, -0.3, -0.4; 1)$ and $B = (-0.2, -0.3, -0.4, -0.7; 1)$ then $R(A) = 0.482$ and $R(B) = 0.544$. Since $R(A) < R(B) \Rightarrow A < B$ (Fig. 5).

4.6 Example

$A = (-0.1, -0.3, -0.5, -0.6; 1)$ and $B = (0.2, 0.3, 0.4, 0.5; 1)$, Since $R(A) < R(B) \Rightarrow A < B$ as a result $R(A) = -0.402$ and $R(B) = 0.54$.

4.7 Example

Consider four fuzzy numbers A1 = (0.1,0.2,0.3:1); A2 = (0.2,0.5,0.8;1); A3 = (0.3,0.4,0.9;1); A4 = (0.6,0.7,0.8;1) defined as in Fig. 6, which were ranked earlier by Yager, Fortemps and Roubens, Liou and Wang, PhaniBushanRao and Ravi Shankar, N and Chen and Lu and the comparison were made with the proposed method and depicted in Table 1.

It can be made clear from Table 1 that no methods discriminate the fuzzy numbers A2 and A3 whereas the methods of Liou and Wang [24], Chen [25] cannot discriminate the fuzzy numbers A2, A3 and A1, A4. It's clear that Phani Bushan Rao and Ravi Shankar [12, 17] formulae lead to an incorrect ranking order: A2 > A3, which is
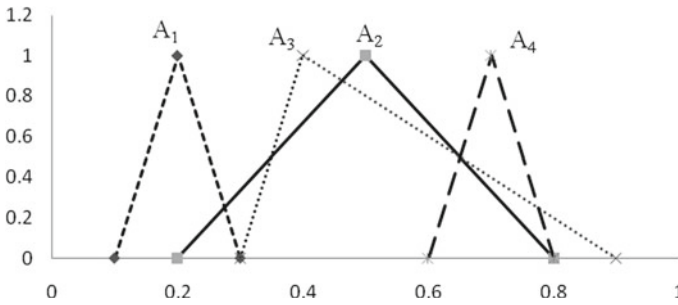
Fig. 6 Triangular fuzzy numbers A_1, A_2, A_3 and A_4

Table 1 Comparison of various ranking methods

Method\fuzzy Number		A_1	A_2	A_3	A_4	Ranking order
Yager [22]		0.20	0.5	0.50	0.70	$A_4 > A_3 = A_2 > A_1$
Fortemps and Roubens [23]		0.20	0.5	0.50	0.70	$A_4 > A_3 = A_2 > A_1$
Liou and Wang [24]	$\alpha = 1$	0.25	0.65	0.65	0.75	$A_4 > A_3 = A_2 > A_1$
	$\alpha = 0.5$	0.20	0.50	0.50	0.70	$A_4 > A_3 = A_2 > A_1$
	$\alpha = 0$	0.15	0.35	0.35	0.65	$A_4 > A_3 = A_2 > A_1$
Chen [25]	$\beta = 1$	–0.2	0.00	0.00	–0.20	$A_2 = A_3 > A_1 = A_4$
	$\beta = 0.5$	–0.20	0.00	0.00	–0.20	$A_2 = A_3 > A_1 = A_4$
	$\beta = 0$	–0.20	0.00	0.00	–0.20	$A_2 = A_3 > A_1 = A_4$
Phani Bushan Rao and Ravi Shankar [12]		0.4591	0.632	0.6146	0.8129	$A_4 > A_2 > A_3 > A_1$
Proposed method		0.501	0.629	0.667	0.837	$A_4 > A_3 > A_2 > A_1$

contrary to the ranking order: A2 < A3 obtained by by means of the correct centroid formula in Eq. 4. This shows the fact that incorrect centroid formulae can lead to an incorrect ranking orders which may lead to take a wrong decision by the decision maker. Hence while ranking the fuzzy numbers, using an appropriate centroid formulae is much better.

5 Application

In every part of our real life situations we cope with a replacement problem. In decision analysis it is used to determine an optimal decision for maintenance and replacement. The replacement problems treats with the situations that arise when some components necessitate replacement because of reduced efficiency, or breakdown or complete failure. Such decreased efficiency or complete failure may be either gradual or it occurs all of a unexpected.

In general, replacement problems are of three types.

Replacement of items that deteriorate with time and the value of money changes with time or does not change with time.

Replacement of items that entirely breakdown, and

Replacement of outdated items moving to further more developments.

We have considered an example to show how the proposed method of ranking is adopted for estimating economic life of fuzzy replacement problem where the value of money changes as time changes. The data considered in this example was attained as of Biswas and Pramanik [26]. The fuzzy cost of a machine is US$(5900, 5950, 6050, 6100). The fuzzy maintenance cost of a machine and its salvage value at the end of each year is given in the Table 2. The authors have assumed that the rate of interest as 10% per annum. To solve this problem we have considered 1000$ = 1$.

Table 2 Fuzzy maintenance cost and salvage value

Year	Fuzzy maintenance cost	Fuzzy salvage value
1	[1100, 1150, 1200, 1270]	[3800, 3900, 3950, 4000]
2	[1300, 1360, 1400, 1450]	[2600, 2650, 2700, 2760]
3	[1500, 1580, 1600, 1650]	[1900, 1950, 2000, 2060]
4	[1800, 1840, 1850, 1870]	[1450, 1470, 1480, 1500]
5	[2000, 2030, 2050, 2070]	[950, 980, 1000, 1050]
6	[2350, 2400, 2460, 2500]	[550, 570, 590, 600]
7	[2900, 2920, 2950, 3000]	[500, 530, 540, 550]

Using the proposed method the defuzzified value of capital cost is calculated as 2.602. Similarly the defuzzified value of the fuzzy maintenance cost and salvage value for every year is calculated and given in the Table 3. The annual equivalent amount [AEA_t] is calculated as in [27] and is given in Table 3. It is clear from the table that the value of annual equivalent amount of cost is confided with the ranking method. The year analogous to the minimum value is the year of replacement and it will epitomize the economic life of the equipment. Since the minimum value obtained at the 7th year, the equipment must be replaced at this year.

Table 3 Defuzzified values and annual equivalent amount of cost

Year	Defuzzified values		Annual equivalent amount of cost
	Maintenance cost	Salvage value	
1	0.486	1.598	2.663
2	0.520	1.004	2.164
3	0.547	0.674	1.800
4	0.585	0.469	1.560
5	0.587	0.286	1.403
6	0.620	0.152	1.282
7	0.698	0.127	1.158

6 Conclusion

This research work proposes an effective method that ranks generalized Trapezoidal fuzzy numbers which is simple and accurate. This method ranks normal and non-normal Trapezoidal fuzzy numbers. This method which is simple and easier in calculation though it gives acceptable results to well defined problems, it also presents a correct ranking order to the problems which are not well defined, this method also match with human perceptivite results. Comparative examples and application to replacement problem is used to interpret the advantages and efficiency of the proposed methodology. To apply this ranking procedure for various decision making problems and incorporation of defuzzification to various real time problems is left for future work.

References

1. Zadeh LA (1965) Fuzzy sets. Inf Control 8(3):338–353
2. Jain R (1976) Decision making in the presence of fuzzy variable. IEEE Trans Syst Man Cybern 6:698–703
3. Chen SJ, Hwang CL (1992) Fuzzy multiple attribute decision making. Springer, Berlin
4. Bortolan G, Degani R (1985) A review of some methods for ranking fuzzy subsets. Fuzzy Sets Syst 15(1):1–99
5. Yager RR (1980) On a general class of fuzzy connectives. Fuzzy Sets Syst 4(3):235–242
6. Murakami S, Maeda H, Lmamura S (1983) Fuzzy decision analysis on the development of centralized regional energy control system. IFAC Proc 16:363–368
7. Cheng CH (1998) A new approach for ranking fuzzy numbers by distance method. Fuzzy Sets Syst 95(3):307–317
8. Chu TC, Tsao CT (2002) Ranking fuzzy numbers with an area between the centroid point and original point. Comput Math Appl 43:111–117
9. Shieh BS (2007) An approach to centroids of fuzzy numbers. Int J Fuzzy Syst 9(1):51–54
10. Wang YM et al (2006) On the centroids of fuzzy numbers. Fuzzy Sets Syst 157:919–926
11. Phani Bushan Rao P, Ravi Shankar N (2011) Ranking Fuzzy Numbers with a distance method using circumcenter of centroids and an index of modality. Adv Fuzzy Syst 1–7

12. Ravi Shankar N, Thorani YLP, Phani Bushan Rao P (2012) Fuzzy risk analysis based on a new approach of ranking fuzzy numbers using orthocenter of centroids. Int J Comput Appl 42(3):24–36
13. Suresh Babu S et al (2012) Ranking generalized fuzzy numbers using centroid of centroids. Int J Fuzzy Logic Syst (IJFLS) 2(3):17–32
14. Thorani YLP et al (2012) Ordering generalized trapezoidal fuzzy numbers. Int J Contemp Math Sci 7(12):555–573
15. Thorani YLP, Phani Bushan Rao P, Ravi Shankar N (2012) Ordering generalised trapezoidal fuzzy numbers using orthocenter of centroids. Int J Algebra 6(22):1069–1085
16. Rao PPB, Shankar NR (2012) Ranking generalized fuzzy numbers using area, mode, spreads and weights. Int J Appl Sci Eng 10(1):41–57
17. Phani Bushan Rao P, Ravi Shankar N (2013) Ranking fuzzy numbers with an area method using circumcenter of centroids. Fuzzy Inf Eng 1:3–18
18. Rouhparvar H, Panahi A (2015) A new definition for defuzzification of generalised fuzzy numbers and its applications. Appl Soft Comput 30:577–584
19. Tabachnikov S, Tsukerman E (2014) Circumcenter of mass and generalized Euler line. Discrete Comput Geom 51:815–836
20. Wang X, Kerre EE (2001) Reasonable properties for the ordering of fuzzy quantities (I). Fuzzy Sets Syst 118:375–385
21. Wang X, Kerre EE (2001) Reasonable properties for the ordering of fuzzy quantities (I). Fuzzy Sets Syst 118:387–405
22. Yager RR (1981) A procedure for ordering fuzzy subsets of the unit interval. Inf Sci 24:143–161
23. Fortemps P, Roubens M (1996) Ranking and defuzzification methods based on area compensation. Fuzzy Sets Syst 82:319–330
24. Liou TS, Wang MJ (1992) Ranking fuzzy numbers with integral value. Fuzzy Sets Syst 50:247–255
25. Chen SH (1985) Ranking fuzzy numbers with maximizing set and minimizing set. Fuzzy Sets Syst 17(1):113–129
26. Biswas P, Pramanik S (2011) Fuzzy approach to replacement problem with value of money changes with time. Int J Comp Appl 30(10):28–33
27. El-kholy AM, Abdelalim AM (2016) A comparative study for fuzzy ranking methods in determining economic life of equipment. Int J Const Eng Manag 5(2):42–54